NORTHWESTERN UNIVERSITY

Understanding Photophysics of Rylene Diimides and Tetrapyrroles in the Solid State for Enhancement of Organic Photovoltaic Performance

A DISSERTATION

SUBMITTED TO THE GRADUATE SCHOOL
IN PARTIAL FULFILLMENT OF THE REQUIREMENTS

for the degree

DOCTOR OF PHILOSOPHY

Chemical Engineering

By

Carolyn E. Ramírez

EVANSTON, ILLINOIS

September 2022

Abstract

Organic photovoltaics offer an opportunity to make solar cells more affordable and widely accessible using cheap, solution-processable light-absorbing layers. In order to realize new technologies, a fundamental understanding of organic chromophore photophysics is required to overcome efficiency limitations. Throughout this doctoral work, I investigated the kinetic and physical characteristics of various rylene diimide and tetrapyrrole macrocycles to gain insight into their individual suitability for use in energy technologies.

I investigated many fundamental phenomena including symmetry-breaking charge separation in polycrystalline thin films of 1,6,7,12-tetra(phenoxy)perylene-3,4:9,10-bis-(dicarboximide) having either n-octyl groups (octyl-tpPDI) or hydrogen atoms (H-tpPDI) attached to its imide nitrogen atoms. We found that H-tpPDI films undergo rapid symmetry-breaking charge separation with a long-lived charge separated state, providing a new route to increase the open-circuit voltage and reduce recombination losses in organic solar cells. We also found that bis(3′-aminopentyl)-perylene-(3,4:9,10)-bis(dicarboximide) (C_5PDI) undergoes quantitative singlet exciton fission in the solid-state despite lacking longitudinal slip-stacking in its crystal structure. Enhancement of the crystallinity of C_5PDI films will improve the triplet quantum yield of this material for use in photovoltaic devices.

I also studied various macrocycles including Zinc 2,11,20,29-tetra-*tert*-butyl-2,3-naphthalocyanine (*t*-Bu-ZnNc) and 13,23-diacetyl-8,8,18,18-tetra-methyl-12,22-diphenyl-bacteriochlorin (B-189) in the solid state and found that aggregation of such molecules slows internal conversion and enhances radiative decay from higher lying singlet excited states and allows faster intersystem crossing. Overall, these findings indicate a significant difference in dilute

monomeric and aggregated molecular behavior, opening new pathways for energy technology applications.

Acknowledgements

Thank you especially to Prof. Michael R. Wasielewski, my research supervisor and mentor, for support, expertise, mentorship, and collaboration. Thank you to Dr. Ryan M. Young, Research Professor in the Wasielewski Research Group, for your mentorship, expertise, encouragement, and endless support. Thank you to my committee members: Prof. Michael R. Wasielewski (Chair), Prof. Randall Q. Snurr, Prof. Mark C. Hersam, Prof. Linsey C. Seitz, and Prof. Jeffrey Lopez for your mentorship and expertise.

This work was supported by the U.S. Department of Energy, Office of Science, Office of Basic Energy Sciences under Award DE-FG02-99ER14999 (awarded to Prof. Michael R. Wasielewski). This work made use of the IMSERC at Northwestern University, which has received support from the Soft and Hybrid Nanotechnology Experimental (SHyNE) Resource (NSF ECCS-1542205), the State of Illinois, and the International Institute for Nanotechnology (IIN). This work also made use of the Keck-II facility of Northwestern University's NUANCE Center, which has received support from the Soft and Hybrid Nanotechnology Experimental (SHyNE) Resource (NSF ECCS-1542205); the MRSEC program (NSF DMR-1720139) at the Materials Research Center; the International Institute for Nanotechnology (IIN); the Keck Foundation; and the State of Illinois, through the IIN. X-ray scattering measurements were performed using Beamline 8-ID-E at the Advanced Photon Source, a U.S. Department of Energy (DOE) Office of Science User Facility operated for the DOE Office of Science by Argonne National Laboratory under Contract DE-AC02-06CH11357. I would like to specifically thank Dr. Joe Strzalka for his collaboration and expertise. X-ray diffraction measurements were performed using the Jerome B. Cohen X-ray Diffraction Facility supported by the MRSEC program of the National Science Foundation (DMR-1720139) at the Materials Research Center of Northwestern University and the Soft and Hybrid

Nanotechnology Experimental (SHyNE) Resource (NSF ECCS-1542205). I would like to specifically thank Jerrold A. Carsello for his collaboration and expertise with XRD. Thank you additionally to Dr. Stephen A. Miller with the Northwestern University Laser & Electronics Design Core Facility for his optics expertise and support.

Thank you to the Wasielewski lab members all of whom have created a welcoming and collaborative environment. Specifically, thank you Dr. Michelle Chen, Dr. Joaquin Alzola, Dr. Younjue Bae, Dr. Adam Coleman, Dr. Robert Jacobberger, Dr. Itai Schlesinger, Dr. Su Chen, Dr. Natalia Powers-Riggs, Malik Williams, Paige Brown, Laura Bancroft, and Colin Tichvon for research/experimental support, synthesis of compounds, and sharing expertise. Additionally, thank you to Prof. Jonathan Lindsey from the North Carolina State University Department of Chemistry for collaboration and synthetic support for the bacteriochlorin project.

Thank you to the Northwestern University Chemical & Biological Engineering (ChBE) Department for providing a challenging and rewarding atmosphere during my five years of graduate school. Thank you specifically to Department Chair, Prof. Randall Snurr, and Associate Department Chair, Prof. Julius Lucks, for your leadership and championship of the ChBE Anti-racism, Diversity, Equity, and Inclusion (ARDEI) Committee. Thank you to my friends and colleagues who co-founded and led this work with me and also shared many laughs and cathartic conversations: Kavitha Chintam, Dr. Alex Prybutok, and Jonathan Chan. Thank you to all of the ARDEI committee members over the last two years for your energy, determination, and hard work to make the ChBE department a more equitable place for all.

I extend heartfelt gratitude and appreciation to all of my friends and family who have provided me with an irreplaceable community that supported me through my doctoral work. Specifically, thank you to my Texas fam, especially Kirsten, Sophie, Julia, Diana, Holly, and Megan for the fun

times, countless Zoom calls, laughs, visits, and encouragement. I love y'all. Thank you to my Chicagoland friends for respite from the stress of grad school, especially Nilou, Ally, Benedict, Leslie, Dr. DJ LP, Abby, Ranya, Dr. Mena, Maggie, Rose, Dr. Carrie, Sam L., and many, many more amazing people I have had the privilege of meeting here. Thank you all for the support, friendship, coalition-building, and accountability as we navigate early adulthood. I love you all dearly.

Thank you to my loyal and loving pets: my guinea pigs Iggy and Lola and our precious pup Milo. Lastly, I want to express my loudest and largest thanks to my family, without whom I would not be where nor who I am. Thank you Mom and Dad for being my biggest champions and for always encouraging me to follow my dreams even when you had no idea what I was talking about. Thank you to my brother and best friend, Ricky, for always being supportive, critical, and funny (in that order). Thank you to the three of you, the three most important people in my world, for growing with me, learning with me, and loving me. I love you so much. This accomplishment is ours. Thank you to my Bigmama for being an icon and a role model as a strong woman I have looked up to my whole life. Thank you for sharing laughs and stories with me and for always showing interest in my work even when it could have bored you to tears. I love you so much and am elated to share this accomplishment with you.

Gracias a mis antepasados por la fuerza, la inspiración, la orgulla Boricua, y la compasión por nuestra gente. Esto es para los sueños que parecieron imposibles. ¡Pa'lante!

For my family,

mi Casita Ramírez:

Mom, Dad, Ricky, Milo, Tony, and Cleo

Table of Contents

List of Tables & Figures 11

Introduction & Literature Review 14

- Motivation for organic solar cells 14
- Kinetic pathways resultant from photoexcitation 16
- Rylene diimides 19
- Description of primary techniques 20
- Path forward for singlet fission and related photophysical processes 21

Chapter 1: Symmetry-Breaking Charge Separation in the Solid State: Tetra(phenoxy)perylenediimide Polycrystalline Films[54] 23

- ABSTRACT 23
- INTRODUCTION 23
- EXPERIMENTAL METHODS 25
- RESULTS & DISCUSSION 28
  - Solid state packing. 28
  - Energetics from steady-state spectroscopy. 30
  - Energy of the triplet state. 35
  - Stabilization of the CT state. 36
- CONCLUSIONS 37

Chapter 2: Effect of Crystallinity on Endoergic Singlet Fission in Perylenediimide Single Crystals and Polycrystalline Films 39

- ABSTRACT 39
- INTRODUCTION 40
- EXPERIMENTAL METHODS 42
- RESULTS & DISCUSSION 47
  - Crystal structure and film morphology. 47
  - Steady-state absorption and emission spectroscopy 49
  - Singlet fission dynamics 52
  - SF mechanism in single crystals and polycrystalline films 57
- CONCLUSIONS 59

Chapter 3: Photophysics of Zinc 2,11,20,29-tetra-*tert*-butyl-2,3-naphthalocyanine: Aggregation-Induced S_2 Emission and Rapid Intersystem Crossing in the Solid State 62

- ABSTRACT 62
- INTRODUCTION 62
- EXPERIMENTAL METHODS 66
- RESULTS & DISCUSSION 69
  - Film packing and structure 69
  - Singlet excited-state dynamics: Aggregation-induced anti-Kasha emission 70
  - Triplet excited-state dynamics: Aggregation-induced intersystem crossing 73

Effects of aggregation on *t*-Bu-ZnNc photophysics 78

CONCLUSIONS 81

Chapter 4: Rapid Intersystem Crossing and Subsequent Photophysics in the Solid-state of 13,23-diacetyl-8,8,18,18-tetra-methyl-12,22-diphenyl-bacteriochlorin 83

ABSTRACT 83

INTRODUCTION 83

EXPERIMENTAL METHODS 85

RESULTS & DISCUSSION 88
- Morphological data: X-ray diffraction of single crystal and thin film 88
- Excited state dynamics of B-189 90
- Energetics of dilute and aggregated B-189 95

CONCLUSIONS 97

Chapter 5: The Saga of Triplet Transfer in Films of Perylene Diimide 98

ABSTRACT 98

INTRODUCTION 98
- Förster energy transfer 98
- Dexter energy transfer 99
- Solid-state triplet transfer 99

EXPERIMENTAL METHODS 100

RESULTS & DISCUSSION 100
- PDI-PhEt/QDI-C_{15} films 100
- PDI-PhEt/Pc$(OBu)_8$ films 103
- PDI-PhEt/*t*-Bu-ZnNc films 106
- Ph_4-C_8-PDI/*t*-Bu-ZnNc films 111

CONCLUSIONS 115

Chapter 6: Policy Position - Without Environmental Justice, the Renewable Energy Transition Will Leave Low-Income and BIPOC Communities Behind[207] 118

EXECUTIVE SUMMARY 118

INTRODUCTION 118

POLICY RECOMMENDATIONS 123
- Recommendation 1: Need for consumer protections and utility weatherization upgrades 123
- Recommendation 2: Household weatherization upgrades for equitable electricity access 125
- Recommendation 3: Environmental Justice Task Forces to ensure equity in the renewable energy transition 127

CONCLUSIONS 129

Conclusions and Outlook 131

APPENDIX A: SUPPLEMENTAL INFORMATION FOR CH. 1 134

APPENDIX B: SUPPLEMENTAL INFORMATION FOR CH. 2 153

APPENDIX C: SUPPLEMENTAL INFORMATION FOR CH. 3 172

APPENDIX D: SUPPLEMENTAL INFORMATION FOR CH. 4 192

References 204

List of Tables & Figures

Figure 1. Projected solar energy growth from U.S. DOE AEO..12
Figure 2. Structure of Si solar cell..12
Figure 3. Benefits of down-conversion of high energy photons via singlet fission...............13
Figure 4. Jablonski diagram showing different photophysical pathways after absorption.....13
Figure 5. Vibronic peaks correlating with different vibrational levels.................................14
Figure 6. Singlet fission diagram...15
Figure 7. Mechanism of SB-CS...16
Figure 8. Rylene diimide molecules studied..16
Figure 9. Transient absorption (TA) spectroscopy schematic..17
Scheme 1. Structures of tpPDI molecules...22
Figure 10. C_8-tpPDI and H-tpPDI crystal structures... 25
Figure 11. GIXRD data for C_8-tpPDI and H-tpPDI films...27
Figure 12. Steady-state absorption and emission spectra for tpPDI.....................................28
Figure 13. FsTA spectra of C_8-tpPDI and H-tpPDI films...29
Figure 14. Generalized kinetic models for C_8-tpPDI and H-tpPDI.......................................32
Table 1. Rate constants for generalized kinetic models...33
Figure 15. Chemical and crystal structure of C_5PDI...43
Figure 16. GIXRD data for C_5PDI films...44
Figure 17. C_5PDI crystal steady-state absorption and emission data....................................45
Figure 18. C_5PDI film steady-state absorption and emission data...47
Figure 19. FsTAM and nsTAM data for C_5PDI crystal...48
Figure 20. TREPR data for C_5PDI crystals...49
Figure 21. FsTA and nsTA data for C_5PDI SVA film..50
Figure 22. Steady-state absorption data of *t*-Bu-ZnNc films..63
Figure 23. Steady-state emission data of *t*-Bu-ZnNc films...64
Figure 24. FsTA data of *t*-Bu-ZnNc in toluene excited at 400 nm.. 65
Figure 25. FsTA data of *t*-Bu-ZnNc films excited at 712 nm...67
Figure 26. TREPR spectrum of *t*-Bu-ZnNc film..68
Figure 27. Triplet quantum yield calculations for *t*-Bu-ZnNc film..69
Figure 28. Energy diagrams for *t*-Bu-ZnNc...70
Figure 29. Molecular and single crystal structure of B-189...80
Figure 30. GIWAXS data of B-189 film...81
Figure 31. GIXRD data of B-189 films...82
Figure 32. Steady-state absorption and emission data of B-189...83
Figure 33. FsTA and nsTA data of B-189 in solution...84
Figure 34. FsTA and nsTA data of B-189 film...85
Figure 35. Energy diagrams for B-189...87
Table 2. Attempted triplet donor and acceptor molecules...91
Figure 36. QDI-C_{15}/PDI-PhEt film absorption data and diagram...92
Figure 37. GIWAXS data of QDI-C_{15}/PDI-PhEt films...93
Figure 38. FsTA data for QDI-C_{15}/PDI-PhEt unannealed film..93
Figure 39. FsTA data for QDI-C_{15}/PDI-PhEt thermally annealed film................................. 94
Figure 40. PDI-PhEt, $H_2Pc(OBu)_8$, $PdPc(OBu)_8$ film schematics..95
Figure 41. UV-vis absorption data for PDI-PhEt/$PdPc(OBu)_8$ film..96

Figure 42. FsTA data for PdPc(OBu)$_8$ film..........97

Figure 43. FsTA data for PDI-PhEt/PdPc(OBu)$_8$ film..........98

Figure 44. Steady-state absorption data for PDI-PhEt/*t*-Bu-ZnNc films..........99

Figure 45. GIWAXS data for PDI-PhEt/*t*-Bu-ZnNc films..........100

Figure 46. FsTA data for unannealed PDI-PhEt/*t*-Bu-ZnNc film..........101

Figure 47. FsTA data for annealed PDI-PhEt/*t*-Bu-ZnNc film..........101

Figure 48. Ph$_4$-C$_8$-PDI:*t*-Bu-ZnNc film diagram..........102

Figure 49. Steady-state absorbance and emission data for Ph$_4$-C$_8$-PDI:*t*-Bu-ZnNc films....103

Figure 50. FsTA data of neat Ph$_4$-C$_8$-PDI film..........104

Figure 51. FsTA data of 1:1 Ph$_4$-C$_8$-PDI:*t*-Bu-ZnNc film..........105

Figure 52. FsTA data of 5:1 Ph$_4$-C$_8$-PDI:*t*-Bu-ZnNc film..........106

Figure 53. FsTA data of 8:1 Ph$_4$-C$_8$-PDI:*t*-Bu-ZnNc film..........106

Figure A1. Additional tpPDI single crystal images..........122

Figure A2. GIWAXS data for tpPDI films..........122

Figure A3. AFM images of tpPDI films..........123

Figure A4. UV-vis of tpPDI film annealing..........124

Figure A5. Steady-state absorbance and emission data plotted vs. wavenumber..........124

Figure A6. FsTA data for tpPDI films plotted vs. wavenumber..........125

Figure A7. NsTA data for tpPDI films..........125

Figure A8. NsTA data kinetic fits..........126

Figure A9. FsTA data kinetic fits..........127

Figure A10. tpPDI molar extinction coefficient measurements..........128

Figure A11. Absorbance and emission data of octyl-tpPDI in solution..........130

Figure A12. Solution sample UV-vis for tpPDI triplet sensitization..........131

Figure A13. Normalized overlay of nsTA spectra for triplet sensitized H-tpPDI..........131

Figure A14. Raw nsTA spectra of triplet sensitized H-tpPDI..........132

Figure A15. Steady-state absorption and emission data of fresh H-tpPDI film..........133

Figure A16. FsTA data for H-tpPDI thermally annealed film at 300 K..........135

Figure A17. FsTA data for H-tpPDI thermally annealed film at 250 K..........135

Figure A18. FsTA data for H-tpPDI thermally annealed film at 200 K..........136

Figure A19. FsTA data for H-tpPDI thermally annealed film at 150 K..........136

Figure A20. FsTA data for H-tpPDI thermally annealed film at 100 K..........137

Figure A21. Arrhenius plot of SB-CS kinetic rate constants..........137

Figure B1. Light polarization dependence of C$_5$PDI absorption..........140

Figure B2. Vibronic absorption band Gaussian fits with emission data for C$_5$PDI films.....141

Figure B3. Near-infrared emission of C$_5$PDI films..........141

Figure B4. Data for triplet sensitization of C$_5$PDI film with PdPc(OBu)$_8$..........142

Figure B5. FsTA and nsTA data for SVA C$_5$PDI film on low fluence system..........144

Figure B6. FsTA and nsTA data for unannealed C$_5$PDI film on low fluence system..........144

Figure B7. FsTA and nsTA data for unannealed C$_5$PDI film on high fluence system..........145

Figure B8. Temperature-dependent UV-vis of unannealed C$_5$PDI film..........145

Figure B9. Temperature-dependent absorption compared with raw fsTA data at 300 K.....146

Figure B10. TRF data of SVA C$_5$PDI film in 1 ns window..........147

Figure B11. TRF data of SVA C$_5$PDI film in 10 ns window..........148

Figure B12. TRF data of unannealed C$_5$PDI film in 1 ns window..........148

Figure B13. TRF data of unannealed C$_5$PDI film in 10 ns window..........149

Figure B14. Triplet quantum yield for C_5PDI film...149
Figure B15. Triplet quantum yield for C_5PDI crystal..150
Figure B16. AFM images of C_5PDI films..153
Figure C1. GIXRD data for *t*-Bu-ZnNc films...154
Figure C2. GIWAXS data for *t*-Bu-ZnNc films...154
Figure C3. GIWAXS linecuts for *t*-Bu-ZnNc films...155
Figure C4. Abs. and emission data plotted vs. wavenumber for *t*-Bu-ZnNc films...............155
Figure C5. Steady-state absorption and emission data in toluene (300 K)..........................156
Figure C6. Steady-state absorption and emission data of films...156
Figure C7. Emission spectra of *t*-Bu-ZnNc in toluene RT vs. frozen.................................157
Figure C8. Temperature-dependent emission of *t*-Bu-ZnNc..158
Table C1. Data and calculations for Arrhenius plot...159
Figure C9. Arrhenius plot of temperature-dependent fluorescence.....................................159
Figure C10. FsTA data of *t*-Bu-ZnNc in toluene ex. 765 nm...160
Figure C11. NsTA data of *t*-Bu-ZnNc in toluene ex. 765 nm...160
Figure C12. FsTA data of *t*-Bu-ZnNc unannealed film ex. 410 nm....................................161
Figure C13. FsTA data of *t*-Bu-ZnNc annealed film ex. 410 nm..162
Figure C14. NsTA data of *t*-Bu-ZnNc unannealed film ex. 712 nm....................................162
Figure C15. NsTA data of *t*-Bu-ZnNc annealed film ex. 712 nm..163
Figure C16. Temperature-dependent UV-vis of *t*-Bu-ZnNc film.......................................163
Figure C17. Triplet-sensitization data of *t*-Bu-ZnNc doped w/ $Pd(PPh_3)_2Cl_2$.....................164
Figure D1. Steady-state absorption and emission data for B-189 in toluene.......................169
Figure D2. Steady-state absorption and emission data for B-189 film................................169
Figure D3. FsTA and nsTA kinetic fits of B-189 in toluene..170
Figure D4. FsTA and nsTA kinetic fits of B-189 film...171
Figure D5. TRF data for B-189 film in 2 ns window...171
Figure D6. TRF data for B-189 film in 5 ns window...172
Figure D7. Spectral deconvolution of B-189 film fsTA data...172
Figure D8. DFT optimized geometry of B-189 monomer...173

Introduction & Literature Review

Motivation for organic solar cells

As the global and national populations continue to grow, so will energy demand. According to the United States Department of Energy 2022 Annual Energy Outlook, the portion of U.S. energy consumption composed of renewable energy sources is projected to double from 21% in 2021 to 44% by 2050. Solar energy is expected to increase from 19% of renewable energy production to 51% by 2050, translating to 22% of total U.S. energy production coming from solar by 2050, shown in Figure 1.[1] In order to meet those demands and achieve larger consumer buy-in to solar energy, the cost of solar cells must decrease.

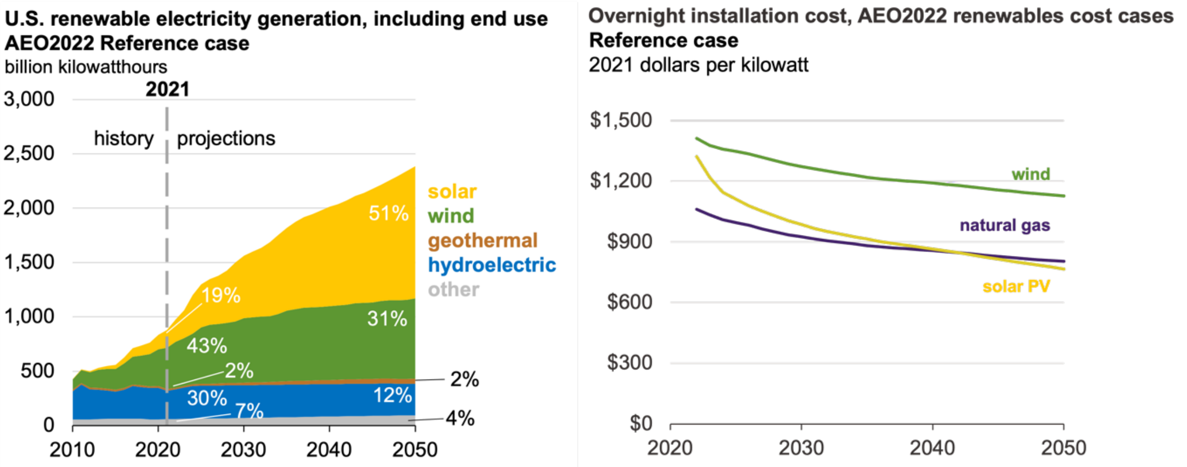

Figure 1. Projected solar energy growth from U.S. DOE AEO[1] *(reproduced with permission from source: 2022 AEO, U.S. Energy Information Administration, published March 3, 2022)*

Current state-of-the-art commercially available solar cells are composed of silicon active layers (shown in Figure 2).[2] Inorganic silicon-based devices are expensive to produce due to energy-intensive deposition processes required to manufacture them, and resultant devices are relatively brittle and inflexible, limiting their applications.[3]

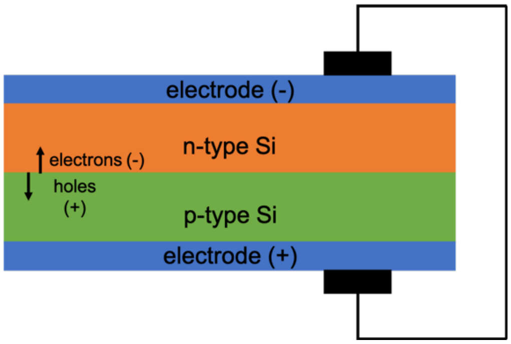

Figure 2. Structure of Si solar cell.[2]

Organic materials (both small organic molecules and semiconducting polymers) offer advantages to silicon because they are solution-processable and cheaper to produce.[4] Due to the relative ease of synthesis of new molecules with different optoelectronic properties, their absorption profiles can span from deep ultraviolet (UV) to near-infrared (IR). This is an additional advantage over silicon which is limited to some UV, visible, and near-IR absorption as shown in Figure 3. High energy photons are wasted.[5, 6-7] For a single junction solar cell, the theoretical maximum efficiency, known as the Shockley-Queisser limit, is 33.7%.[8] High energy photons can be down-converted to useable energy via processes like singlet fission in organic chromophores, a process which can increase the maximum efficiency of a solar cell to ~45%.[9]

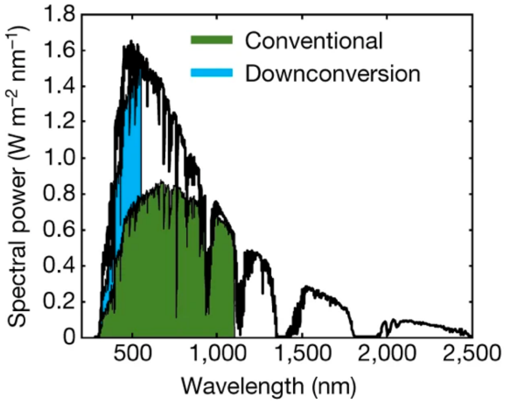

Figure 3. Benefits of down-conversion of high energy photons via singlet fission[5, 6, 7] *(reproduced with permission from Nature 571, 90–94 (2019). Copyright 2019 Springer Nature Limited)*

Kinetic pathways resultant from photoexcitation

Absorbance

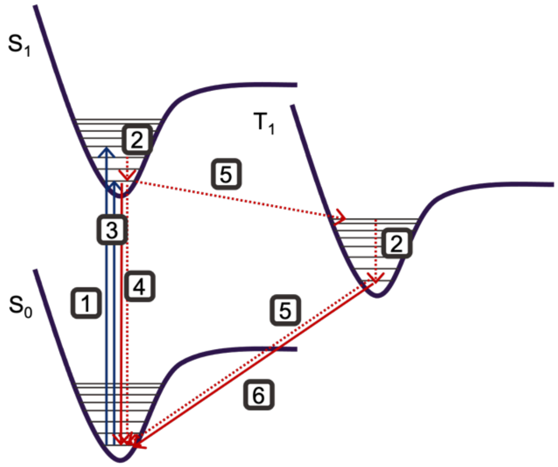

Figure 4. Jablonski diagram showing different photophysical pathways after absorption:[10] 1) absorbance; 2) internal conversion; 3) fluorescence; 4) internal conversion; 5) intersystem crossing; 6) phosphorescence; solid lines = radiative; dashed lines = non-radiative

When light is incident on an organic chromophore, electrons are initially excited from the ground state to the singlet excited state. This is shown in Figure 4 in a Jablonski diagram which shows various typical energy surfaces depicted as Morse potentials. This absorption is attributed to the $S_1 \leftarrow S_0$ transition, which is also known as the HOMO (highest occupied molecular orbital) to LUMO (lowest unoccupied molecular orbital) transition.[10] This $S_1 \leftarrow S_0$ transition can be examined using UV-vis spectroscopy. As shown in Figure 5, there are multiple vibrational energy levels that can be involved in the initial excitation, resulting in multiple vibronic peaks in absorption spectra. There are also higher energy singlet states, $S_n \leftarrow S_0$, that could be involved in excitation.[10]

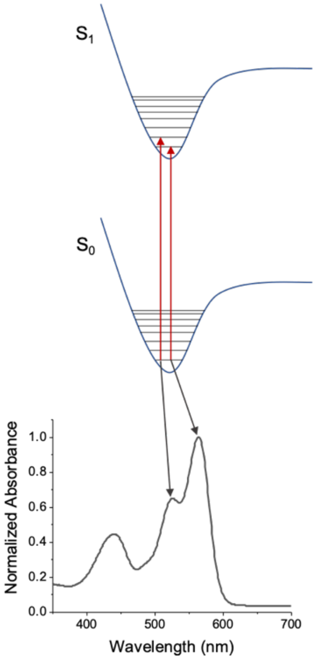

Figure 5. Vibronic peaks correlating with different vibrational levels[10] shown for H-tpPDI absorption in CH_2Cl_2

Fluorescence

When excited singlet excitons radiatively recombine to the ground state, they **fluoresce**.[10] An excited electron can relax to any bound vibrational level within the S_0 state, resulting in multiple vibronic peaks in fluorescence spectra. The difference between S_1 wavelengths of absorbance and fluorescence spectra is known as the Stokes shift.[10]

Phosphorescence

In order for the triplet to relax back to the ground (S_0) state, it must undergo ISC again. It can either radiatively decay via a process called **phosphorescence** or undergo non-radiative ISC. Due to the required spin-orbit coupling, this is very slow (on the order of 10^{-9} to 1 s).[10]

Internal conversion

Per Kasha's rule, any higher-lying states (S_n or T_n, n>1) of the same spin multiplicity generally non-radiatively relax to the lowest vibrational level of S_1 or T_1, respectively, before undergoing any sequential photophysics, a form of **internal conversion** (IC).[10] Excited singlet excitons in the lowest vibronic state can also non-radiatively relax to the ground state, undergoing another form of IC that quenches fluorescence by emitting energy as heat.[10]

Intersystem crossing

The excited singlet could also **spin intersystem cross** (ISC) and form triplet (T_1 or T_n). This process is spin-forbidden in the quantum mechanical sense because the spin must flip to become triplet.[10] ISC is typically an unlikely, and therefore slow, kinetic process. In order for ISC to happen, overall angular momentum must be conserved in the molecule. When the spin flips, there is an associated change in spin angular momentum. Therefore, in order to promote this process, the spin angular momentum change must be coupled to a change in orbital angular momentum, meaning there is a geometric rearrangement in the molecule.[10]

Excimer formation

When an excited (S_1) organic chromophore is very close to a neighboring molecule, this can result in strong coupling and subsequent formation of a distributed excitation on a dimer unit, which is called an **excimer**.[10-11] The excimer can emit to give a broad, red-shifted feature separate from the monomeric $S_1 \rightarrow S_0$ transition, or it can mediate other kinetic transitions including triplet formation through ISC/singlet fission or induce charge separation.[12,13]

Singlet exciton fission

Singlet exciton fission (SF) is a bimolecular process by which a singlet exciton can down-convert into two triplet excitons via coupling with a nearby molecule. Unlike triplet formation via ISC, SF is spin-allowed because the coupled triplets maintain singlet character.[14] Translated to kinetics, spin-allowed means this process can happen rapidly, typically on the order of 10^{-15}-10^{-12} s. As shown in Figure 6, in order for SF to occur, the triplet energy of a molecule must be approximately half that of the singlet.

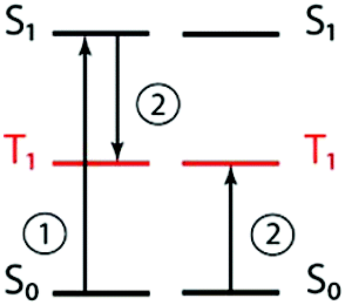

Figure 6. Singlet fission involves down-conversion of one singlet exciton into two triplet excitons[14] *(reproduced with permission from Chem. Rev. 2010, 110, 11, 6891–6936. Copyright 2010 American Chemical Society)*

The general kinetic mechanism is: $S_0 + S_1 \leftrightarrow {}^1(TT) \leftrightarrow T_1 + T_1$ where there are individual forward and reverse rate constants (k) that govern both kinetic steps. ${}^1(TT)$ is the "multiexciton correlated triplet pair" intermediate. The kinetics of SF are much more complicated than the simplified scheme shown, as there are multiple pathways proven to access SF including coupling between singlet and triplet states as well as charge transfer-mediated SF.[14-15] Overall, the primary benefit of this kinetic process is two excitons from one photon, resulting in external quantum efficiencies greater than 100% in photovoltaics.[16]

Symmetry-breaking charge separation

Symmetry-breaking charge separation (SB-CS) occurs when one molecule is photoexcited ($S_1 \leftarrow S_0$) while coupled to a neighboring (S_0) molecule. The complex undergoes charge transfer where one molecule is oxidized while the other is reduced, breaking the charge-neutral symmetry and resulting in an anion-cation pair, depicted in Figure 7.[17-18] This phenomenon has been observed in many solution studies, but is much less studied in the solid state, as it generally is energetically not favored in nonpolar environments.[13, 17, 19-20] To achieve exciton dissociation with organic molecules in OPVs, separate electron donor and acceptor molecules are needed. With SB-CS, only one material is needed to both generate and separate opposite charges.[20] From the charge-separated state, excitons can form an excimer, undergo charge recombination, or intersystem cross to form triplet.[17, 19]

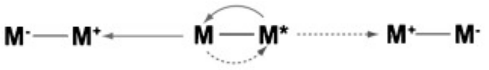

Figure 7. Mechanism of SB-CS[18] *(reproduced with permission from ChemPhysChem (2012) 13: 2001-2011 Copyright 2012 WILEY-VCH Verlag GmbH & Co. KGaA, Weinheim)*

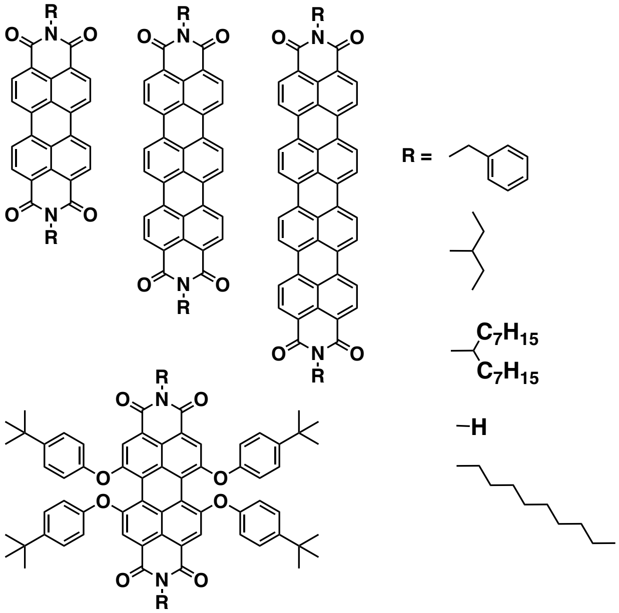

Figure 8. Rylene diimide molecules studied: PDI, TDI, QDI, and tetraphenoxy-PDI with various **R** groups at the imide positions.

Rylene diimides

Rylene diimides are a class of organic molecules composed of naphthalene cores and imide ends. These chromophores are robust dyes used in many industrial applications. They can have very high extinction coefficients and can easily be modified with core substituents and aromatic or alkyl tails to alter packing in the solid state.[21] As shown in Figure 8, this report will deal with perylene-3,4:9,10-bis-(dicarboximide) (**PDI**), terrylene-3,4:11,12-bis(dicarboximide) (**TDI**), and quaterrylene-3,4:13,14-bis(dicarboximide) (**QDI**).

Description of primary techniques

Transient absorption (TA) spectroscopy

Transient absorption spectroscopy is used to study how excited molecules evolve over time by pumping a sample with monochromatic light at a wavelength resonant with maximum absorption in the steady-state absorbance measurement and probing the sample with a white light continuum, shown in Figure 9.[22] Multiple spectra are taken at different time delays between the pump and probe to get a full temporal picture (ranging from fs to μs) of electron dynamics.

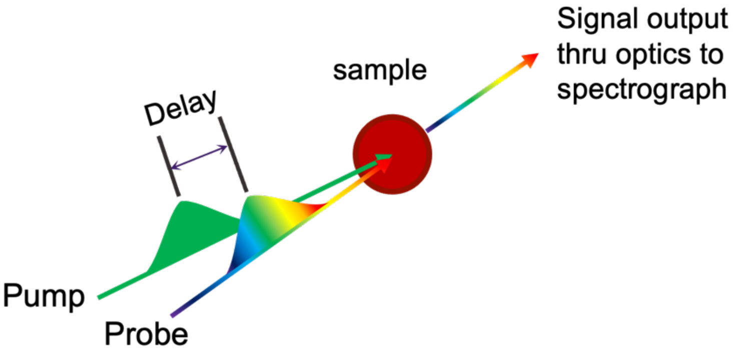

Figure 9. Transient absorption (TA) spectroscopy schematic[22]

In the Wasielewski lab, two primary TA setups are used for the following experiments. One system has a high pulse energy (~1 μJ/pulse) with a low repetition rate (1 kHz), which gives high signal to noise data.[23] For solid state samples, the high pulse energy can cause too high of an excitation density resulting in undesirable singlet-singlet annihilation and optical damage to the sample. The other setup with low pulse energies (~20 nJ/pulse) and a high repetition rate (100 kHz) is more useful for solid-state samples.[24]

Time-resolved fluorescence (TRF)

To monitor how emission changes over time, a streak camera is used for transient fluorescence spectra which measures the emitted light as a function of wavelength and time simultaneously after pumping with monochromatic light.

X-ray diffraction (XRD)

To understand how molecules are packing in the solid-state, the most useful techniques are x-ray diffraction and scattering. When x-rays penetrate the film, they are diffracted by the molecules in the molecular lattice. The angle of diffraction gives information on molecular packing through Bragg's law: $n\lambda = 2dsin(\theta)$ where λ is the wavelength of the x-ray source, *d* is lattice spacing, and θ is half of 2θ, the angle of diffraction.[25]

Grazing incidence wide angle x-ray scattering (GIWAXS)

Using the Argonne Advanced Photon Source Synchrotron, static GIWAXS can be measured and the resultant pattern plotted in reciprocal space can give information about long range order like grain size as well as short range order like packing using the relationship $q = \frac{2\pi}{d}$, where d (defined above) is measured in Å and q is in Å^{-1}.[26, 27]

Path forward for singlet fission and related photophysical processes

Singlet fission (SF) has taken on new life in the last decade as researchers realized its theoretical potential to improve the efficiency of photovoltaics to surpass the Shockley-Quiesser limit for a single junction solar cell of 33% to an efficiency of 44%.[9, 14, 28-29] SF chromophores can be used in multiple ways to improve solar cell devices. Acenes, a class of molecules which undergo SF rapidly, have been shown to successfully down convert high energy photons outside of the absorption range of silicon to lower energy triplets that can then be used in silicon devices.[30-31] SF molecules have also demonstrated high quantum efficiencies above 100% in organic, dye-sensitized, and hybrid inorganic nanocrystal/organic chromophore solar cells.[16, 32-38]

While these applied results are promising, there remains much to be understood about fundamental aspects of SF. Our group has been working in this space for many years trying to better understand the mechanisms behind SF in rylene diimide and some modified acene molecules of many different conjugations and substitutions.[39-42] These studies range from understanding the photophysics of newly synthesized monomers, dimers, and trimers in solution to studying monomers in solid-state films as the next steps towards device applications. Our group’s studies show that the more delocalized the electrons are (more naphthalene units on the core) in rylene diimides, the more exoergic and rapid SF is.[43-45] Additional studies in our group have elucidated spin dynamics between different vibrational manifolds of spin multiplicities as well as the mysterious nature of the correlated triplet pair state and state mixing during SF.[12, 15, 46-48] The SF community has continued to dig deeper into fundamental aspects of this phenomenon,[49-50] especially working to understand the kinetics of competing mechanisms like excimer formation, charge transfer, and fluorescence in acenes and rylenes alike and further studying coherence of the correlated triplet pair.[51-53] My goal during my doctoral work has been to use this fundamental understanding of SF and other photoactivated processes to better understand dynamics of rylene diimides and tetrapyrroles in thin films.

Chapter 1: Symmetry-Breaking Charge Separation in the Solid State: Tetra(phenoxy)perylenediimide Polycrystalline Films[54]

Carolyn E. Ramírez, Su Chen, Natalia E. Powers-Riggs, Itai Schlesinger, Ryan M. Young, and Michael R. Wasielewski

Published: *J. Am. Chem. Soc.* 2020 Oct. 06, 142, 42, 18243–18250 https://doi.org/10.1021/jacs.0c09185

Reproduced with permission: *Copyright © 2020, American Chemical Society*

ABSTRACT

Generation of electron-hole pairs via symmetry-breaking charge separation (SB-CS) in photoexcited assemblies of organic chromophores is a potentially important route to enhancing the open-circuit voltage of organic photovoltaics. While most reports of SB-CS have focused on molecular dimers in solution where the environmental polarity can be manipulated, here we investigate SB-CS in polycrystalline thin films of 1,6,7,12-tetra(phenoxy)perylene-3,4:9,10-bis-(dicarboximide) having either n-octyl groups (octyl-tpPDI) or hydrogen atoms (H-tpPDI) attached to its imide nitrogen atoms. Structural analyses using various X-ray techniques reveal that while both compounds show π-π stacking in thin films, H-tpPDI is more slip-stacked than octyl-tpPDI and has intermolecular hydrogen bonds to its neighboring molecules. Transient absorption spectroscopy shows that octyl-tpPDI exhibits strong mixing between its singlet excited state and a charge transfer state, yielding an excimer-like state, while H-tpPDI undergoes nearly quantitative SB-CS, making the latter a promising candidate for use in organic photovoltaic devices.

INTRODUCTION

In order to meet the growing global demand for energy with minimal cost to the environment, cheaper and more efficient solar cell technology is key. Solution-processable organic photovoltaics (OPVs) present an opportunity for more affordable device production compared with conventional silicon devices.[4] However, OPV efficiencies are often limited by low open-circuit voltages (V_{OC}). The V_{OC} in a photovoltaic device depends on the dark current, and is thus a measure of recombination losses.[55] This parameter is also related to the energy difference between the highest occupied molecular orbital (HOMO) of the electron donor molecule and the lowest unoccupied molecular orbital (LUMO) of the electron acceptor molecule, ΔE_{DA}.[55-56] The value of ΔE_{DA}, and thus V_{OC}, is maximized in OPV systems in which the donor and acceptor molecules have the same band gap, as the case where the same compound generates both holes and electrons. However, under these conditions, the free energy change for charge separation is approximately zero, $\Delta G_{\mathrm{CS}} \sim 0$, so this process may not compete with singlet exciton recombination back to the ground state. Nevertheless, depending on local environmental fluctuations or those within the chromophores themselves, symmetry-breaking charge separation (SB-CS) can occur when one molecule is photoexcited ($S_1 \leftarrow S_0$) while electronically coupled to an identical neighboring molecule in the ground state (S_0).[20] The excited complex then undergoes charge transfer where one molecule is oxidized while the other is reduced, breaking the charge-neutral symmetry and resulting in a radical ion pair.[17-18] This phenomenon has been observed primarily in solution, but is much less studied in the solid-state, as it is generally energetically disfavored by nonpolar environments.[13, 17, 19-20, 57] Bartynski, *et al.*, showed that the use of an organic chromophore which undergoes SB-CS in an OPV can significantly increase the V_{OC}, but at the cost of lower short circuit current density (J_{SC}).[20]

Our group has studied the fundamental mechanism of SB-CS in several rylene diimide systems.[58] Recently, we demonstrated SB-CS in crystalline aggregates of hydrogen-bonded guanine-quadruplexes of terrylenediimide,[59] supporting the existence of SB-CS in noncovalent rylene diimide aggregates. We have also observed SB-CS in solutions of 1,6,7,12-tetra(phenoxy)-perylene-3,4:9,10-bis-(dicarboximide) (tpPDI) triangular trimers and cyclophane dimers in solution,[13, 19] including in the non-polar solvent toluene.[60] SB-CS in nonpolar solution is thought to occur in part due to the appreciable quadrupole moment of solvents like toluene,[60-61] while SB-CS in solid-state and aggregated crystalline systems is likely due to the quadrupolar nature of rylene diimides themselves due to their large conjugated π systems.[59, 62] The quadrupole moment of the solvent, or self-solvating rylene diimide in the solid-state, helps to stabilize the charge transfer (CT) state, making this state thermodynamically more accessible.

Here we analyze how the crystal structures of two different tpPDI derivatives influence their photophysics in the solid state. Specifically, we study polycrystalline films of two different tpPDI derivatives, octyl-tpPDI and H-tpPDI shown in Scheme 1. A mixture of excited-state and CT character is observed by transient absorption spectroscopy in both films. Formation of an excimer-like state with CT character is evident in the octyl-tpPDI film, while the H-tpPDI film shows clear evidence of SB-CS. This distinction is primarily due to the differences in crystal morphology between the two derivatives that directly influence the effective electrostatic environment that the molecules experience, which in turn controls the fate of the excited states in these systems.

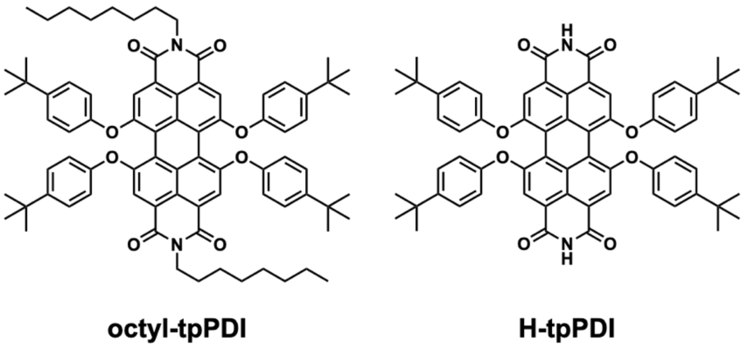

Scheme 1. Structures of the molecules studied here.

EXPERIMENTAL METHODS

Synthesis. The compounds in this study were synthesized following published procedures.[63-65] The starting material, 1,6,7,12-tetrachloroperylene-3,4,9,10-tetracarboxy dianhydride, was purchased from Fisher Scientific.

Crystallography. Octyl-tpPDI and H-tpPDI single crystals were grown using a vapor diffusion method. Octyl-tpPDI (0.5 mg) was dissolved in 4 mL of $CHCl_3$. The octyl-tpPDI solution (0.5 mL) was then transferred into a 1 mL culture tube, which was placed inside of a 20 mL vial filled with 8 mL of CH_3OH. The 20 mL vial was sealed and left in the dark. As CH_3OH slowly diffused into the octyl-tpPDI solution, crystals gradually appeared. Crystals suitable for single-crystal X-ray diffraction analysis were obtained after three days. A suitable crystal was selected and mounted on a microsource loop affixed with paratone oil on a 'Bruker APEX-II CCD' diffractometer. The crystal was kept at 100 K via a liquid N_2 stream during data collection. Using Olex2,[66] the structure was solved with the XT[67] structure solution program using Intrinsic Phasing and refined with the XL[68] refinement package using Least Squares minimization.

The single crystal of H-tpPDI was grown following the same method, but CH_3OH was replaced with heptane. A suitable crystal was selected and mounted on a microsource on a 'Bruker APEX-II CCD' diffractometer. The crystal was kept at 100 K during data collection. Using Olex2,[66] the structure was solved with the XS[68] structure solution program using Direct Methods and refined with the XL[68] refinement package using Least Squares minimization.

Film Preparation. Films of each compound were made by spin-coating 100 µL of 20 mg/mL octyl-tpPDI or 15 mg/mL H-tpPDI solution in $CHCl_3$ at 700 rpm on sapphire substrates (purchased from Ted Pella, Inc.) that were first sonicated for 10 minutes in water, methanol, and acetone and dried with nitrogen. The films were then thermally annealed at 115 ^{o}C for 90 minutes in a nitrogen-filled (oxygen/moisture-free) glovebox. Film thicknesses were measured using a high-resolution Dektak 150 Stylus Surface Profilometer. The octyl-tpPDI film had a thickness of 161 ± 75 nm while the H-tpPDI film had a thickness of 221 ± 102 nm.

X-ray Characterization. Both films were characterized with grazing-incidence X-ray diffraction (GIXRD) using a Rigaku ATX-G. Films were analyzed using out of plane GIXRD with an incident angle of 0.25º. Grazing-incidence wide-angle X-ray scattering (GIWAXS) was also done on both films at the Advanced Photon Source at Argonne National Laboratory using beamline 8-ID-E (reserved for high signal to noise GIWAXS measurements). Measurements were taken with 10.92 keV/1.1354 Å X-rays produced from the synchrotron incident on the sample at an angle of 0.140º. A Pilatus 1 M detector was used to gather all scattered X-rays and the resultant GIWAXS images were analyzed and corrected with the GIXSGUI MATLAB program.[69]

Steady-State Spectroscopy. All solution steady-state absorption measurements were measured in CH_2Cl_2 using a Shimadzu 1800 UV-Vis spectrophotometer. All film steady-state absorption measurements were collected using a Shimadzu UV-3600 UV/Vis/NIR spectrometer with an integrating sphere to correct for scatter and reflectance. Steady-state emission measurements were acquired with a Horiba Nanolog fluorimeter. Films were excited in a front-face geometry while the solution sample was excited in a right-angle geometry. The octyl-tpPDI film was excited at 550 nm while the H-tpPDI solution and film samples were excited at 500 nm.

Transient Absorption Spectroscopy. Femtosecond transient absorption (fsTA) data were collected on a high repetition rate, low fluence system described previously.[24] Nanosecond transient absorption (nsTA) data were collected on a lower repetition rate, high fluence system published previously.[23] All film samples were excited at 580 nm, while the solution samples used to determine the triplet transient absorption spectra were excited at wavelengths resonant with the maximum absorption of the triplet sensitizer (see Appendix A). All data were fit and modeled using a previously described MATLAB fitting program.[70] Data were globally fit to a first order kinetic model.

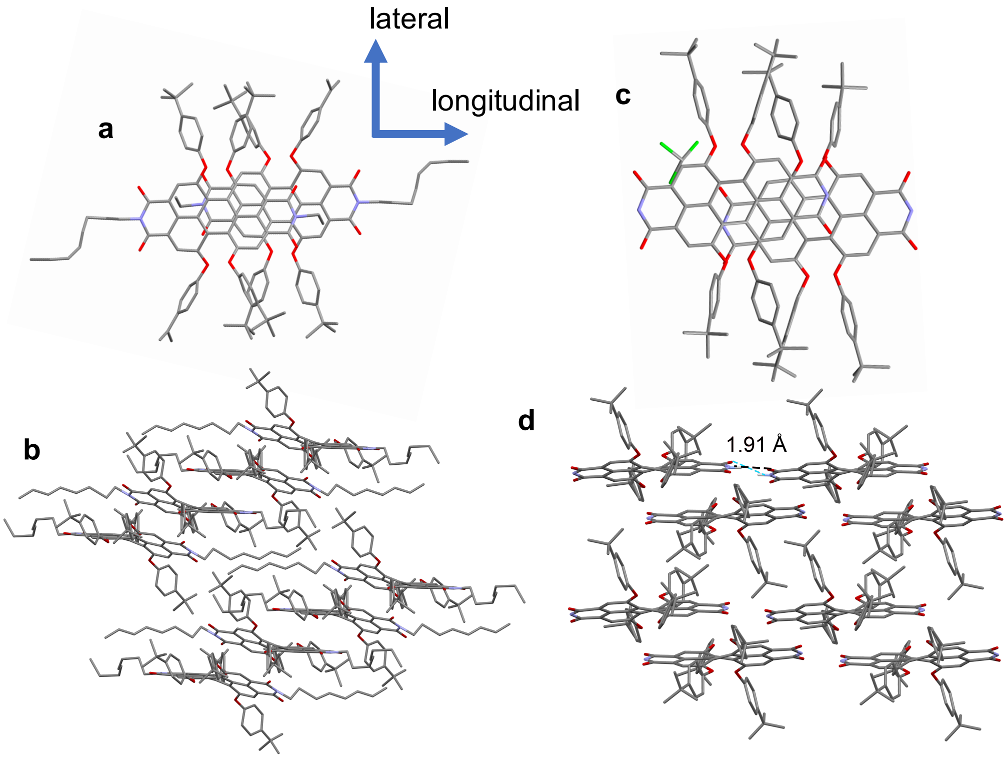

Figure 10. (a) Octyl-tpPDI dimer showing slip-stacking and (b) long range order in octyl-tpPDI crystal showing *π*-*π* stacking and slip-stacking. (c) H-tpPDI dimer showing slip-stacking and (d) long range order in H-tpPDI crystal showing hydrogen bonding, π-π stacking, and slip-stacking.

RESULTS & DISCUSSION

Solid state packing. The crystal structure of octyl-tpPDI shown in Figure 10a,b obtained with single crystal X-ray diffraction (XRD) reveals significant *π*-*π* slip-stacking. The tetraphenoxy groups at the bay positions cause core twisting in the molecule, but the *π*-*π* interactions maintain the overlapping planes parallel to each other as shown in Figure A1a. The molecules have an average *π*-*π* distance of 3.46 Å and are slipped relative to one another by 4.44 Å longitudinally (along the long axis) and 1.47 Å laterally.

The crystal structure of H-tpPDI shown in Figure 10c,d also shows evidence of significant *π*-*π* slip-stacking between neighboring molecules. The *π*-*π* distance is 3.28 Å, which is slightly smaller than in octyl-tpPDI, with a longitudinal slip distance of 5.48 Å and a lateral slip distance of 1.22 Å. H-tpPDI shows a significantly larger longitudinal slip distance than octyl-tpPDI, suggesting that the octyl-tpPDI molecules should exhibit stronger dipolar coupling of their transition moments. H-tpPDI has an additional ordering parameter that influences the structure and resultant electronic coupling. Figures 10d and A1c show a pair of hydrogen bonds between the hydrogen attached at the imide position of one molecule and the carbonyl oxygen on a neighboring molecule with a distance of about 1.9-2.0 Å. Hydrogen bonding in PDIs has been observed previously at similar intermolecular distances,[71] and has been shown to introduce sufficient order in stacked rylene diimides to induce SB-CS, as seen in guanine- terrylenediimide quadruplexes.[59] The role of hydrogen bonding on the excited-state dynamics will be discussed in detail below.

Grazing incidence X-ray diffraction (GIXRD) data were also collected on all films in order to confirm similar packing patterns of tpPDI compounds in both thin films and single crystals. As shown in Figure 11, GIXRD data are overlaid with simulated powder patterns generated from the single crystal XRD data and show generally good agreement. In the GIXRD spectra for octyl-tpPDI films (Figure 11a), there are three intense powder pattern peaks that generally line up with the GIXRD spectrum at 2θ values of 5º, 6º, and 7º, which correspond to the (001), (010), and (01-1) planes, respectively. The clear alignment between the experimental film GIXRD data and the peaks predicted in the simulated powder pattern indicates that the film exhibits packing concordant with that observed in the solved single-crystal structures. While no π-π stacking peak is evident in the GIXRD data, grazing incidence wide angle X-ray scattering (GIWAXS) data (shown in Figure A2) for the octyl-tpPDI film show a strong band along the q_{xy} axis between 1 and 1.5 Å^{-1}, which likely corresponds to edge-on π-π stacking between slip-stacked molecules.

In the H-tpPDI data shown in Figure 11b, there are simulated powder pattern peaks at 2θ values of 5° and 8°, which correspond to the (001) and (10-1) planes, respectively. Similar to the octyl-tpPDI spectra, these peaks match well with the GIXRD data for the H-tpPDI film, confirming that the molecules in the film pack as indicated in the solved crystal structure. Additionally, there is a broad peak from 20-26° corresponding to 3.4-4.4 Å *d*-spacing attributed to π-π stacking. GIWAXS data collected on the H-tpPDI film (Figure A2) show an intense feature near 1.5 Å^{-1} on the q_z axis which corresponds to face-on 4.2 Å π-π stacking. These data confirm the π-π stacking evidenced by GIXRD and more specifically show its orientation to the substrate surface. Face-on π-π stacking is favorable for photovoltaic applications because the molecules pack parallel to the substrate, promoting light absorption and also enabling easier charge transport/extraction by surrounding layers.[72-73]

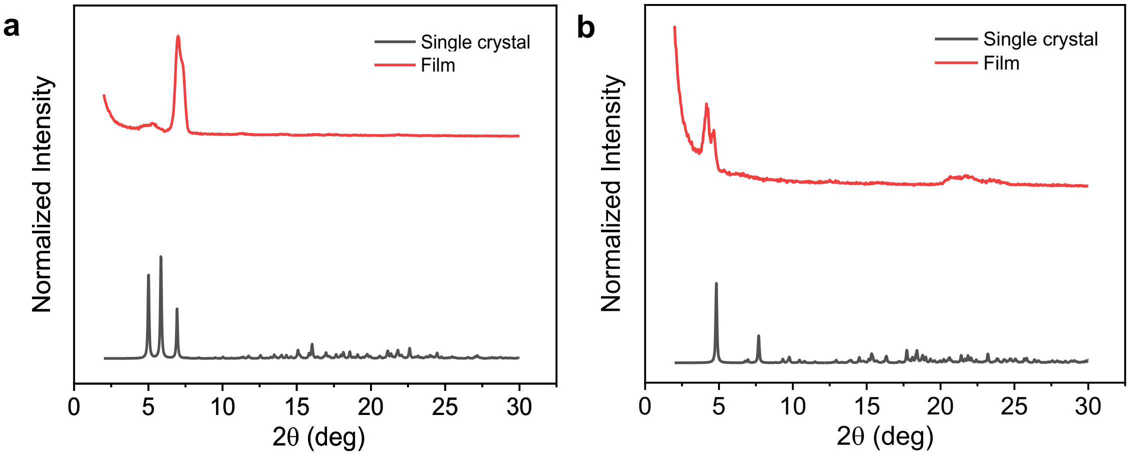

Figure 11. Grazing incidence XRD spectra of (a) octyl-tpPDI and (b) H-tpPDI films overlaid with simulated powder patterns generated from single crystal structures.

Energetics from steady-state spectroscopy. In Figure 12, the steady-state absorption and emission data for both films are shown overlaid with the solution spectra of H-tpPDI in CH_2Cl_2. These data are shown plotted versus wavenumber in Figure A5, while the data for octyl-tpPDI in solution are shown in Figure A11. All solution samples were prepared with a concentration of

0.008 mM. Because of the low concentration and narrow absorption and emission spectra for the solution sample evident in Figure 12, there is likely no aggregation or hydrogen bonding of H-tpPDI molecules. The film absorption spectra appear to have the same primary vibronic peaks at 590 and 540 nm, but show a bathochromic shift compared to the solution spectrum. The ratio between the two primary vibronic peaks differs, especially in the octyl-tpPDI film, indicating increased dipolar coupling between molecules in both films on average[74-75] and suggesting that the coupling assertions made from the single crystal data also apply to the polycrystalline films.

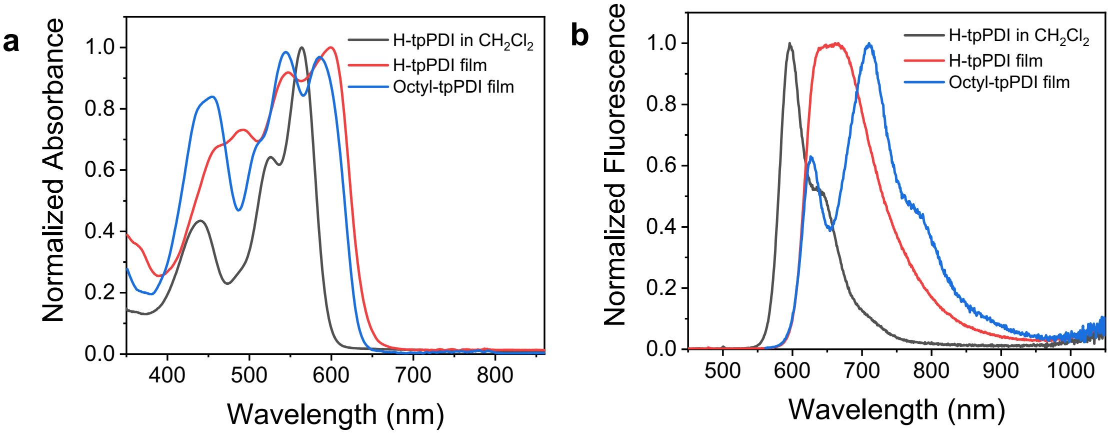

Figure 12. Steady-state (a) absorption and (b) emission spectra for tpPDI films and solution.

The steady-state fluorescence spectra of both H-tpPDI and octyl-tpPDI in the films are shown in Figure 12b and are broadened and red-shifted compared to the monomer. While this pronounced shifting and broadening is typical of PDI excimer formation,[74-76] given that both H-tpPDI and octyl-tpPDI show significant CT character in the films (see below), the observed emission is largely CT in nature. From these data, the singlet excited state energies of both H-tpPDI and octyl-tpPDI in solution determined from the intersection of the normalized absorption and emission spectra are 2.13 eV, while the corresponding energies in the film are 2.01 eV and 2.04 eV, respectively. The energies of the lower energy states of H-tpPDI and octyl-tpPDI having CT character in the films are 1.85 eV and 1.74 eV, respectively.

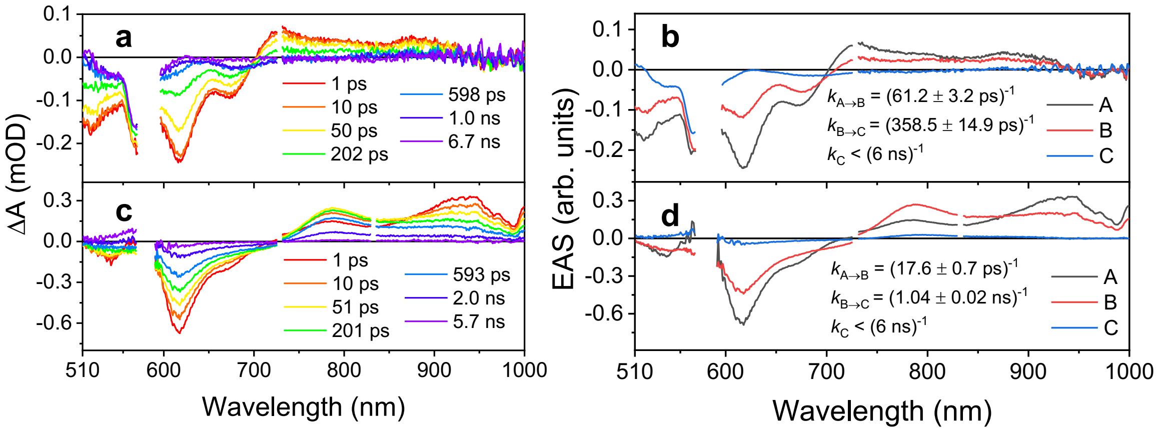

Figure 13. FsTA of both films: (a) raw data for octyl-tpPDI, (b) EAS for octyl-tpPDI, (c) raw data for H-tpPDI, (d) EAS for H-tpPDI.

Excited State Dynamics in Solid-State Films. In order to further probe the photophysics of these films, femtosecond (fs) and nanosecond (ns) transient absorption (TA) spectra were acquired by exciting the samples at 580 nm. FsTA spectra and evolution-associated spectra (EAS) for both films are shown in Figure 13. These data are shown plotted versus wavenumber in Figure A6. The EAS were obtained from a fit to an A → B → C first-order kinetic model. The states are not discrete chemical species as a consequence of intrinsic disorder in polycrystalline films; there are likely multiple populations contributing to the same signal. Mixing of discrete energy states is also possible in these systems but cannot be determined conclusively in polycrystalline films with inherent disorder. The octyl-tpPDI film data shown in Figure 13a,b start with state A composed of ground state bleach (GSB) from 510-650 nm, stimulated emission (SE) from 650-700 nm, and singlet excited state absorption (ESA) at 710 and 875 nm. State B forms in $\tau_{A\to B} = 61$ ps and shows broad, flat absorption, which is characteristic of PDI excimer formation.[74, 76-77] A weak band near 800 nm, a feature typical of the tpPDI anion,[13] may indicate some CT contribution to the excimer state. Such excimer-like states are common in strongly coupled rylene aggregates.[78-80] The excimer-like state acts as an energy trap state that prevents complete charge separation, as seen in

PDI dimers used as electron acceptors in OPVs.[81] The excimer-like state B then decays to form a low yield of state C in $\tau_{B\rightarrow C}$ = 359 ps, which the nsTA data given in Figure A7a,b show is the octyl-tpPDI triplet state that lives for τ_C = 50 ns.

The H-tpPDI film fsTA spectra shown in Figure 13c,d begin with state A exhibiting GSB at 550, 610, and 640 nm, SE from 680-710 nm, singlet ESA at 925 nm, and the H-tpPDI anion absorption at 785 nm. The immediate appearance of this anion feature shows that ultrafast charge separation occurs for some populations within the ~300 fs instrument response. State B evolves in $\tau_{A\rightarrow B}$ = 17.6 ps as the singlet absorption largely decays and the anion peak intensifies and red shifts slightly to 790 nm. This spectral evolution to primarily CT character indicates that a majority of the excited state population undergoes SB-CS with this time constant. The cation feature, typically observed around 620 nm in tpPDI,[13] is obscured by the GSB in both film spectra. Finally, state C forms in $\tau_{B\rightarrow C}$ = 1.04 ns, showing complete absence of the singlet ESA. The triplet ESA grows in at 510 and 560 nm and notably, the anion feature is still present at 790 nm. The disappearance of the singlet ESA suggests that the remaining excited populations undergo SB-CS, though with a slower rate, possibly due to being in a less favorable local geometry within the film. The presence of the triplet features at long times alongside the anion indicates that some populations that have already charge separated are also recombining to the triplet state on this timescale.

While the solid-state environment of these films is fairly nonpolar, PDI has been shown to have a strong quadrupole moment that increases as the length of the alkyl group attached at the imide position decreases.[62] This alkyl tail effect arises from the difference in molecular packing in the solid state. The tpPDI molecules can essentially “solvate” each other, and thus, octyl-tpPDI may experience an overall less polar environment than H-tpPDI, partially rationalizing why SB-

CS occurs more readily in H-tpPDI than in octyl-tpPDI films. This self-solvation stabilizes the CT state and enables ultrafast SB-CS.[60]

Despite the fact that there is considerable through-space electronic interaction between the tpPDI molecules in both crystals via π-π interactions, it is important to note that intermolecular hydrogen bonding presents an opportunity for through-bond coupling,[82] as seen in perylene monoimide "foldamers."[83] Hydrogen bonding may also improve hole mobilities in organic photovoltaic devices. Gsänger, *et al.*, have shown that PDIs with unsubstituted nitrogen atoms exhibit enhanced hole mobilities compared to their anhydride analogues in transistors, which they attributed to the combination of imide-carbonyl hydrogen bonding and perylene core π-π stacking.[71] However, due to the strong evidence of π-π interactions in both tpPDI films, the coupling contributions are likely much higher from through-space than through-bond interactions.

The charge-separated state in the H-tpPDI film lives nearly three times longer than the excimer-like state in the octyl-tpPDI film as evidenced by slower decay into the triplet state, which is advantageous for potential photovoltaic applications because the charge carriers need to be extracted from the active layer to generate current before they recombine. The longer-lived, charge-separated state results from order induced by π-π stacking and hydrogen bonding,[84] enabling more facile charge extraction as well as enhanced stabilization of the CT state by the H-tpPDI quadrupole moment. NsTA data (Figure A7c,d) show that the triplet state lives for about 2.5 μs in the H-tpPDI film, suggesting that intersystem crossing (ISC) back to the ground state takes much longer in H-tpPDI than in octyl-tpPDI. The long triplet lifetime may also result from a combination of π-π stacking and hydrogen bonding in H-tpPDI.[84-85] In contrast, the short triplet lifetime in the octyl-tpPDI system could be explained by larger and more densely packed domains shown in atomic force microscopy images in Figure S3. These larger domains provide more opportunities for triplet exciton annihilation.

Energy of the triplet state. In order to confirm the assignment of the triplet spectrum seen in film TA data and estimate the energy of the triplet state, nsTA spectroscopy was performed in solution using two different triplet sensitizers with experimentally known triplet energies that bracket the calculated triplet energy of tpPDI, 1.17 eV (calculated using TDDFT, see the Appendix A), following a protocol used previously.[39] Palladium naphthalenediimide porphyrin (Pd-NDP)[86] has a triplet energy, $E(T_1)$, of 1.30 eV,[39] determined previously by phosphorescence spectroscopy. Palladium octabutoxyphthalocyanine ($PdPc(OBu)_8$) has a triplet energy, $E(T_1)$, of 1.12 eV.[39, 87] Additionally, in order to obtain an accurate triplet spectrum, H-tpPDI was sensitized with anthracene (known $E(T_1) = 1.84$ eV).[88] All three samples were prepared in CH_2Cl_2 containing both H-tpPDI and the sensitizer. NsTA spectra of all samples are overlaid and normalized in Figure A13. As expected, the Pd-NDP sensitized sample shows a H-tpPDI triplet spectrum that matches the anthracene-sensitized sample because triplet energy transfer from the sensitizer to H-tpPDI is energetically downhill in both systems. In contrast, the $PdPc(OBu)_8$ sensitized sample does not show signatures of the H-tpPDI triplet, which indicates its 1.12 eV triplet energy is too low to sensitize H-tpPDI triplet state formation. The resultant kinetic schemes for both solid-state systems are summarized in Figure 14 and Table 1.

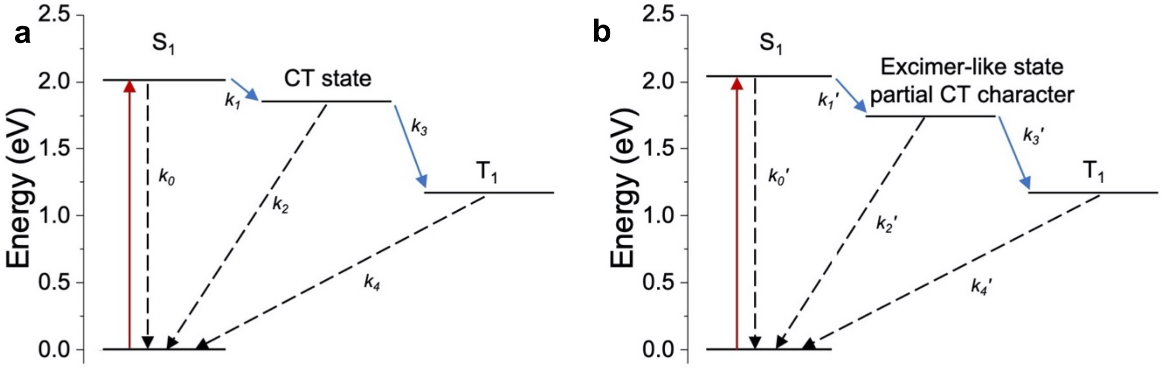

Figure 14. Generalized kinetic models for (a) H-tpPDI and (b) octyl-tpPDI. Rate constants are based on the TA data.

Table 1. Rate constants for generalized kinetic models.

H-tpPDI		Octyl-tpPDI	
$k_0 + k_1$	$(17.6 \pm 0.7\ \text{ps})^{-1}$	$k_0' + k_1'$	$(61 \pm 3\ \text{ps})^{-1}$
$k_2 + k_3$	$(1.04 \pm 0.02\ \text{ns})^{-1}$	$k_2' + k_3'$	$(359 \pm 15\ \text{ps})^{-1}$
k_4	$(2.5 \pm 0.1\ \mu\text{s})^{-1}$	k_4'	$(50 \pm 2\ \text{ns})^{-1}$

Stabilization of the CT state. These two contrasting systems provide insights into the SB-CS mechanism and design strategies to maximize charge separation in the solid state via control of molecular packing through intermolecular interactions like hydrogen bonding. One criterion for SB-CS to occur requires the CT state energy to be lower than the singlet excited state energy of the system. We have demonstrated that standard methods for estimating the energy of the CT state do not work well for these systems.[60] In this case, the low energy states of H-tpPDI and octyl-tpPDI having CT character are both emissive. Moreover, since the TA spectra of H-tpPDI show that it forms a nearly pure CT state by SB-CS, while those of octyl-tpPDI indicate that it has partial CT character, the emission spectra provide the approximate CT state energies for these molecules in the polycrystalline films. While the quadrupole moments of neighboring molecules can stabilize the CT states of both H-tpPDI and octyl-tpPDI in the polycrystalline solids,[62] this effect is likely higher in H-tpPDI based on a comparison of its π-π stacking structure with that of octyl-tpPDI. In addition, SB-CS may be triggered by fluctuations that result from vibrations in the tpPDI core, which in turn, can modulate the effective quadrupole moment experienced by the molecules.

The charge separation rate is modulated by the competition between Coulombic and CT/exchange coupling. Coulombic coupling is a long-range electrostatic interaction that can include quadrupolar effects in molecules like PDI,[81, 89] while charge transfer/exchange coupling is a short range interaction that depends on orbital overlap, which can occur through-space by π-π stacking or through the bonds.[89] The influence of π-π stacking is evident from the crystal structures and film packing of both compounds. In addition, the fact that formation of the CT state in H-tpPDI is faster than in octyl-tpPDI indicates that the electronic coupling between H-tpPDI molecules is larger than between octyl-tpPDI molecules in the solid state. This is most likely a consequence of the hydrogen bonds between H-tpPDI molecules controlling π-π stacking that enhances the electronic coupling.

CONCLUSIONS

We have shown that SB-CS can occur in the solid-state, as evidenced from TA spectra of octyl-tpPDI and H-tpPDI films, which show clear evidence of anion formation, particularly in H-tpPDI. Structural characterization indicates that both molecules pack in polycrystalline films similarly to their single crystal structures. The difference in slip-stacking between the two crystal structures suggests that the interchromophore dipolar coupling should be greater in octyl-tpPDI than in H-tpPDI, which is evidenced by formation of the octyl-tpPDI excimer-like state having partial CT character. SB-CS in the H-tpPDI film leading to nearly complete charge transfer is attributed to the strong quadrupole moment of PDI[62] as well as electronic coupling to neighboring molecules as a result of favorable π-π interactions in its hydrogen-bonded solid state structure. The observation of SB-CS in the solid-state is promising for potential optoelectronic applications including OPVs. Minimizing the need for band gap engineering by using SB-CS chromophores as single-layer active materials could alleviate V_{OC} limitations in current OPVs.

Attributions:

- Carolyn E. Ramírez: film fabrication, steady-state film spectroscopy, non-linear spectroscopy data collection and analysis, X-ray data acquisition and analysis, analysis of crystal structure characteristics, made figures, wrote manuscript
- Su Chen: synthesized molecules, grew crystals, conducted solution steady-state measurements and extinction coefficient calculation, solved for TD-DFT triplet energy
- Natalia E. Powers-Riggs: solved crystal structures
- Itai Schlesinger: AFM measurements and grain-size discussion of films
- Ryan M. Young: high fluence nsTA and solution fsTA/nsTA measurements, discussion, manuscript revisions and content
- Michael R. Wasielewski: funding, oversight, manuscript revisions and content

Chapter 2: Effect of Crystallinity on Endoergic Singlet Fission in Perylenediimide Single Crystals and Polycrystalline Films

Malik Williams, Itai Schlesinger, Carolyn E. Ramírez, Robert Jacobberger, Paige J. Brown, Ryan M. Young, and Michael R. Wasielewski

Published: *J. Phys. Chem. C.* 2022, June 22, XXXX, XXX, XXX-XXX. https://doi.org/10.1021/acs.jpcc.2c02298

Reproduced with permission: *Copyright © 2022, American Chemical Society*

ABSTRACT

The triplet state energy of bis(3′-aminopentyl)-perylene-(3,4:9,10)-bis(dicarboximide) (C_5PDI) in the solid state is 1.1 eV, so that achieving singlet fission (SF) in crystalline films of C_5PDI can provide a potential means of delivering triplet excitons to silicon-based solar cells, whose bandgap is also 1.1 eV, to enhance their performance by utilizing blue light in the solar spectrum. Here, we use transient absorption spectroscopy and microscopy to assess the effect of solid-state order on SF dynamics by comparing C_5PDI single crystals and thin polycrystalline films. The x-ray single crystal structure of C_5PDI shows that it forms π-stacked dimers, wherein the PDIs are twisted ~51° relative to one another. Formation of the correlated triplet pair state $^1(T_1T_1)$ in the C_5PDI single crystals occurs in $\tau = 56 \pm 4$ ps mediated by a mixed state having both excited singlet and charge transfer character, while in a solvent-vapor-annealed C_5PDI polycrystalline thin film, $^1(T_1T_1)$ formation occurs in $\tau = 169 \pm 6$ ps. The quantum yield of the $^1(T_1T_1)$ state formation in each case is nearly quantitative, yet the free triplet exciton quantum yield in the single crystals is 70%, while that in the annealed polycrystalline film is only 29%. Steady-state and time-resolved photoluminescence measurements indicate that the disorder in the polycrystalline film hinders free triplet excitons via long-lived excimer trap states at sites with suboptimal electronic coupling. The higher free triplet yield in the single crystal also clearly shows that the high degree of molecular

order in the crystal enables competition between triplet annihilation and diffusional escape, which is critical for utilizing the triplet excitons to enhance solar cell performance.

INTRODUCTION

Singlet fission (SF) is a spin-allowed process in which a molecule that has been photoexcited to its excited singlet state (S_1) interacts with a neighboring molecule in its ground state (S_0) to produce a correlated triplet pair state $^1(T_1T_1)$ followed by decorrelation to form two free triplet excitons (T_1).[14] SF continues to attract considerable interest because pairing an ideal blue-light absorbing SF chromophore with a complementary red-light absorber raises the Shockley-Queisser limit for photovoltaic efficiency from 33 to 45%.[90-91] Many organic chromophores exhibit SF, ranging from small molecules to polymers, and from polycrystalline films to single crystals.[28, 92-96] One essential criterion for a useful SF chromophore is that it produces triplet excitons rapidly[97] and in high yield.[98-100] Equally important, the energy of the triplet excitons should be high enough to match the bandgap of silicon, thus capturing the blue photons of the solar spectrum that are degraded to heat in typical silicon solar cells. The SF rate in a chromophoric organic solid depends both on the SF energetics, where rapid rates are achieved when the energies of the singlet and triplet excitons, E_S and E_T, respectively, are such that $E_S \geq 2E_T$, and the electronic coupling between adjacent chromophores is favorable. This dependence has been the subject of several theoretical[97, 101] and experimental[99, 102-103] investigations. For example, SF dynamics in polyacene crystals, like pentacene[104-106] and tetracene,[107-108] have shown that crystallite size impacts their SF rates, and that variable SF rates reported for the same molecules may result from variable crystallite size and/or from polymorphism.[108-110] When $E_S \geq 2E_T$, as in the case of pentacene,[111] sub-picosecond SF often occurs, so that the subtle effects of intermolecular coupling may become more challenging to discern. In contrast, when $E_S \cong 2E_T$ or even when $E_S \leq 2E_T$ as is the case in tetracene, the SF rate is slower, so that the effects of intermolecular coupling become more apparent.

Among organic semiconductors, perylene-(3,4:9,10)-bis(dicarboximide) (perylenediimide, PBI, PDI) has attracted much attention because of its robust photochemical and thermal stability as well as the synthetic tunability of its photophysical and redox properties.[112] Moreover, PDI derivatives form well-ordered, π-stacked structures with a stacking geometry that can be tuned by functionalizing the PDI.[113] Substituents at the imide nitrogen atoms have only weak effects on the electronic properties of PDI derivatives, but strongly affect their intermolecular interactions as a result of varying steric demand.[114] In general, molecular packing in the solid has been shown to impact both the SF rate and the free triplet exciton yield.[50, 108-110, 115-116] Moreover, it has been noted that a packing motif having parallel and longitudinally slip-stacked PDIs is the most favorable arrangement for SF;[49, 97, 113-114, 117] however, the effect of rotating the N-N axis of two PDIs relative to one another, while maintaining π-stacking, has not been studied. In contrast, such a structural change in the homologous terrylenediimides, for which $E_S \geq 2E_T$, has been shown to maintain a high triplet exciton yield.[70]

Here, we compare the impact of crystallinity on the SF rate and free triplet exciton yield in C_5PDI single crystals to that in polycrystalline thin films. As shown below, the triplet state energy of bis-*N,N*-(3′-aminopentyl)-PDI (C_5PDI) in the solid state is about 1.1 eV, so that achieving SF in crystalline films of C_5PDI can provide a potential means of delivering triplet excitons to silicon-based solar cells having a 1.1 eV bandgap to enhance their performance. Using ultrafast transient absorption spectroscopy and microscopy we show that formation of the correlated triplet pair state $^1(T_1T_1)$ in the C_5PDI single crystal occurs in $\tau = 57 \pm 4$ ps, while $^1(T_1T_1)$ formation is slower in a solvent-vapor annealed (SVA) polycrystalline C_5PDI thin film, where $\tau = 169 \pm 6$ ps. The quantum yield of the $^1(T_1T_1)$ state formation in each case is nearly quantitative, yet the free triplet exciton quantum yield in the single crystals is 70%, while that in the annealed polycrystalline films is only 29%, showing that molecular order has a strong impact on the escape of free triplets from this highly correlated state, which is critical for utilizing these excitons to enhance solar cell performance. These results inform the prospects of future SF-based enhancements to silicon photovoltaics.[118]

EXPERIMENTAL METHODS

Synthesis, crystal growth, and characterization. C_5PDI was synthesized as reported previously[119] and C_5PDI single crystals were grown by slow vapor diffusion of methanol into solution prepared in dichloromethane over the course of 3-5 days. A suitable crystal was selected and affixed to a loop using Paratone oil on a Rigaku XtaLAB Synergy-DW diffractometer. The crystal was cooled and kept at 100 K during data collection. Using Olex2,[66] the structure was solved with the XT structure solution program using intrinsic phasing and refined with the XL refinement package using least squares minimization. The C_5PDI crystal structure has been deposited in the Cambridge Crystallographic Data Centre database (CCDC #2108992).

Film preparation and morphological characterization. C_5PDI films were grown by vapor depositing C_5PDI onto cleaned sapphire substrates (purchased from Ted Pella, Inc.) that were first sonicated in deionized water, methanol, and then acetone for 10 minutes each and dried with a stream of nitrogen. The annealed film was solvent-vapor annealed (SVA) in acetone for 15 minutes in air. Film thicknesses were measured using a high-resolution Dektak 150 Stylus Surface Profilometer. The unannealed film was found to be 79 ± 19 nm thick and the SVA film was found to be 64 ± 21 nm thick. The films were characterized using grazing incidence X-ray diffraction

(GIXRD) using a Rigaku SmartLab Thin-film Diffraction Workstation. Films were analyzed using in-plane and out-of-plane GIXRD with X-rays at incident angles of 0.5^{o} and 0.25^{o}, respectively.

Single-crystal steady-state absorption spectroscopy. Steady-state absorption spectra were collected on the crystals using a continuous wave Xenon arc lamp (Oriel Instruments, model 66902). The beam was spatially filtered through a pinhole, polarized using a Glan-Thompson polarizer and a motorized (ELL14K, Thorlabs) achromatic half-wave plate (SAQWP05M-700, Thorlabs) to rotate the linear polarization. The beam was then sent into the back port of an upright microscope (Eclipse Ti-U, Nikon). The beam was directed through an internal mirror to a 15x reflective objective lens (LMM15X, Thorlabs) to focus on the sample. The transmitted light was collected using a second objective lens and then sent to a home-built spectrometer (grating: 52A15BK-224C, Richardson Gratings) and focused onto a fast line-scan camera (OctoPlus, Teledyne e2v), sampling at 100,000 lines/s. For absorption measurements, a reference spectrum (on bare glass), and a transmission spectrum (through a single crystal) were collected for each polarization in the range 0-360° in steps of 10°. A dark spectrum, with no light on the sample was subtracted from all reference and transmission spectra.

For emission measurements, the output of an optical parametric amplifier (see femtosecond transient absorption microscopy section) was set to 450 nm and ~1 μW using a neutral density filter. The beam was focused on the sample and recollected using the same setup used for steady-state absorption measurements. To resolve the weak emission the integration time on the line-scan camera was set to the maximum of 655 ms.

Film steady-state absorption and emission spectroscopy. All film steady-state absorption measurements were collected using a Shimadzu UV-3600 UV/vis/NIR spectrometer with an integrating sphere to correct for scatter and reflectance. Steady-state emission measurements were acquired with a Horiba Nanolog fluorimeter. Films were excited in a front-face geometry at 350 nm. All steady-state spectroscopy measurements on films were acquired in air at room temperature.

Femtosecond transient absorption microscopy. Visible femtosecond transient absorption microscopy (fsTAM) was performed using a commercial Yb:KGW, 4 W, 100 kHz repetition rate, 300 fs, amplified laser system (Spirit-One, Spectra-Physics). The 1040 nm fundamental was separated into two portions. One beam was directed to an optical parametric amplifier (OPA) (Spirit-OPA-8, Light Conversion) to generate a 450 nm pump beam. This linearly polarized pump was directed to a quarter-wave plate, which converted it to a circularly polarized beam, and then into an electro-optic amplitude modulator (EO-AM-NR-C4, Thorlabs), which was phase-synchronized to the laser output. The EOM output was sent through a linear polarizer resulting in a linearly polarized beam amplitude-modulated at 50 kHz. A laboratory-built two-prism compressor was used to compensate for the severe pulse stretching (up to several ps) induced by the EOM. The pulses were compressed to ~200 fs as measured using a laboratory-built autocorrelator. The other 1040 nm beam was directed to a double-pass linear delay line (IMS600LM, Newport), and then focused into an 8 mm thick undoped YAG crystal for white light continuum generation. The beam was then recollimated and the fundamental was removed using a 1000 nm short-pass filter. The pump and probe beams were co-axially combined using a 50:50 beam splitter and sent into the microscope system and spectrometer described above. The polarizations of the pump and the probe beams were varied independently using two achromatic half-wave plates. The pump and probe power on the sample were each set to 2 μW using two neutral density filters. The pump and probe focused spot size (4σ of Gaussian) on the sample were 2.1 μm, giving pump and probe energy densities of 288 μJ/cm^2 and 144 μJ/cm^2, respectively. To mitigate systematic baseline shifts during the measurement, the TA spectrum at each delay point was individually referenced to a fixed negative delay point (-10 ps).

Nanosecond transient absorption microscopy. Visible nanosecond transient absorption microscopy (nsTAM) was performed using the same probe source as for the fsTAM described above. A nanosecond-pulsed 405 nm diode laser (NPL41B, Thorlabs), synchronized at 50 kHz to the Spirit-One, was used as a pump. The laser output was combined with the same white light continuum beam used in the fsTA experiment and both beams were sent to the microscope through the same optical path as described previously. The pump/probe delay was electronically controlled using a digital delay generator (DG645, Stanford Research).

Film transient absorption spectroscopy. Femtosecond and nanosecond transient absorption (fsTA/nsTA) data were collected on films exciting at 500 nm using a low repetition rate (1 kHz), high fluence amplified laser system published previously.[23] The pump energy density was ~200-500 μJ/cm^2. Low-fluence fsTA data were also collected on films exciting at 590 nm as a control using a high repetition rate (100 kHz) laser system also described previously,[24] with a pump energy density of ~5 μJ/cm^2 to eliminate singlet-singlet annihilation and thermal effects in the TA data. All data were fit and modeled using a previously described MATLAB fitting program.[70] High-repetition rate data were fitted using first-order kinetic models, while low-repetition rate data were fitted using higher-order kinetic models to account for singlet exciton annihilation and bimolecular triplet exciton decay. All film measurements were acquired with the films placed in an evacuated cryostat to remove the influence of ambient oxygen on the dynamics. Triplet-sensitized solution data were collected exciting anthracene at 355 nm.

Time-resolved fluorescence spectroscopy. Picosecond time-resolved fluorescence (TRF) data were collected on thin films of C_5PDI in air using a Hamamatsu C4780 streak camera described previously.[15] The excitation pulses at 100 kHz were tuned to 500 nm and attenuated to ~300 pJ/pulse to minimize pump scatter, with an excitation density of ~0.2 μJ/cm^2. Data were collected using 1, 2, 10, and 20 ns windows; the instrument response function (IRF) was ~2-3% of the acquisition window, with the shortest time resolution being ~20 ps. The optical density of the samples was ~0.1 at the excitation wavelength in 1 mm cuvettes. A 650 nm long-pass filter was installed for the longer time windows to better capture the weaker, long-lived, redshifted emission and avoid detector saturation. All data were acquired in the single-photon counting mode using the Hamamatsu HPD-TA software.

Data analysis and global fitting. The TA data on each crystal were smoothed using a Gaussian kernel filter; film nsTA data were spectrally smoothed using a 5-point adjacent average. Each time-resolved dataset was then chirp corrected in software by fitting time-zero to a 4th-order polynomial and globally fit to the kinetic models described in the text.

Time-resolved electron paramagnetic resonance spectroscopy. Time-resolved electron paramagnetic resonance (TREPR) spectroscopy was conducted at X-band (~9.6 GHz) using a Bruker Elexsys E680-X/W EPR spectrometer with a split-ring resonator (ER4118X-MS3). The C_5PDI crystals were sealed in a quartz tube under a vacuum of 10^{-3} Torr. Spectra were collected at 85 K by flowing liquid nitrogen through an optical cryostat (Oxford Instruments CF935). The sample was photoexcited with 625 nm, 7 ns, 2 mJ pulses generated by an optical parametric oscillator (Basi-scan, Spectra-Physics), which was pumped with the output of a frequency-tripled Nd:YAG laser (Quanta-Ray Lab 170, Spectra-Physics) operating at a repetition rate of 10 Hz. Kinetic traces of the transient magnetization were acquired as a function of the magnetic field using quadrature detection under continuous microwave irradiation of 5.0 mW. The data were processed by first subtracting the background signal prior to the laser pulse for each kinetic trace and then subtracting the signal at off-resonance magnetic fields for each spectrum. The spectra were fit using the *pepper* function in EasySpin 5.2.33.[120] The experimental TREPR spectrum for the triplet ($S = 1$) species is modeled using the Hamiltonian:

$$H = \mu_B g \sum_{i=x,y,z} \boldsymbol{B_i} \cdot \hat{\boldsymbol{S}}_{\boldsymbol{i}} + hD\left(\hat{S}_z{}^2 - \hat{\boldsymbol{S}}_{\boldsymbol{i}}{}^2/3\right) + hE\left(\hat{S}_x{}^2 - \hat{S}_y{}^2\right) \tag{2.1}$$

where μ_B is the Bohr magneton, g is the isotropic g-factor, $\boldsymbol{B}$ is the magnetic field vector, $\boldsymbol{S}$ is the spin vector, and D and E are the zero-field splitting parameters.

RESULTS & DISCUSSION

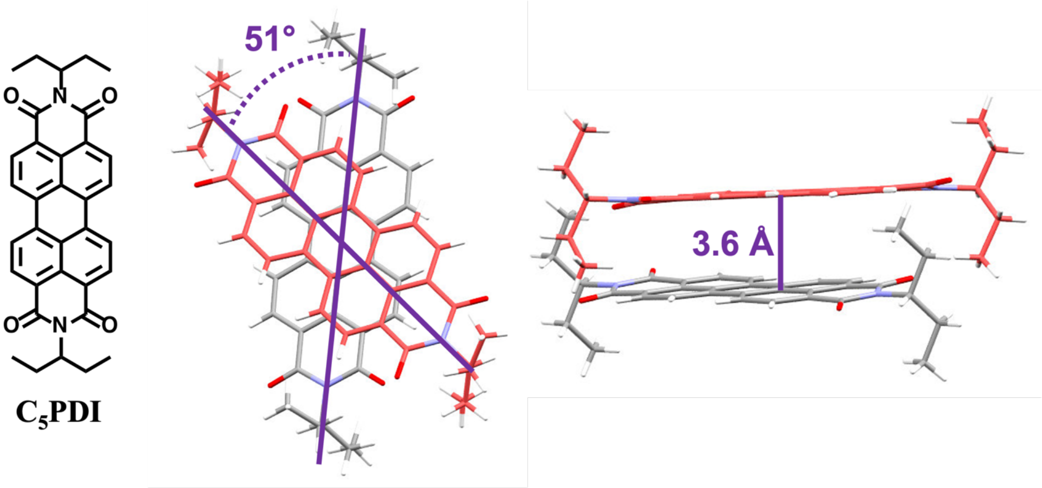

Figure 15. Chemical and single-crystal X-ray diffraction structure of C$_5$PDI

Crystal structure and film morphology. X-ray diffraction was used to obtain the structure of a red, rod-like single crystal (Figure 15). The single crystal is in a monoclinic $P2_1/C$ space group with unit-cell dimensions of a = 33.89 Å, b = 7.34 Å, c = 21.14 Å. There are four half C$_5$PDI molecules in the unit cell that form a π-stacked assembly with a 3.6 Å π-π distance. All π-stacks are found to be oriented in the same direction, along the major crystal axis. Additionally, due to the steric bulk introduced by the 3-aminopentyl groups, a completely cofacial PDI-PDI orientation is inhibited, resulting in the long axes of the π-stacked PDIs being rotated by $\alpha = 51°$. For noncoplanar, non-collinear transition dipole moments such as in this case, the Coulombic coupling between nearest neighbors is given by:[121]

$$V_{Coul} = \frac{2|\mu_{AB}|^2}{r^3}[\cos\alpha - 3\cos^2\theta] \tag{2.2}$$

where α is the angle between the transition dipole moments μ_{AB}, and θ is the angle between the PDI planes and the line connecting their centers of mass, and r is the distance between these centers. From the structure in Figure 15, $\theta \sim 77°$, meaning that together with the 51° twist the coupling from an ideal H-aggregate is reduced by 52% for the same distance and transition dipole strength. This may have significant impact on inhibiting excimer formation, which is a common parasitic deactivation channel for excited states in H-aggregated PDI dimers.[11, 78, 122-123] The axial rotation will also alter the charge-transfer coupling (V_{CT}), which is highly sensitive to molecular orbital overlap.[49, 97, 117, 124-125]

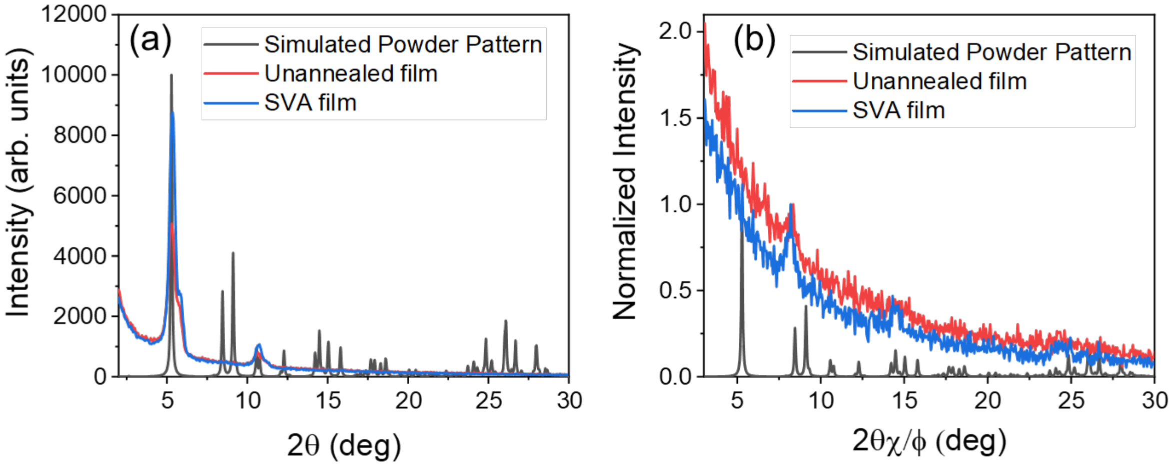

Figure 16. (a) Out-of-plane GIXRD data for C_5PDI; (b) normalized In-plane GIXRD data for C_5PDI films; film pattern compared to simulated powder pattern generated from the single crystal structure.

To determine how the C_5PDI molecules pack in the thin films on the sapphire substrates, we collected GIXRD data both in- and out-of-plane (Figure 16) and compared it to the simulated powder XRD pattern generated from the single crystal structure. The out-of-plane data (Figure 16a) show agreement with the peaks at 5 and 12° values of 2θ. The in-plane GIXRD data (Figure

16b), while much weaker, show agreement with the powder patter at 8, 13, and 23° 2θχ/φ. The 23° peak, while very weak, corresponds to a *d*-spacing of 3.9 Å, which is likely π-stacking between the C_5PDI molecules. Interestingly, π-stacking in-plane would correspond to face-on stacking of the C_5PDI molecules on the sapphire substrates, which is favorable for charge extraction in solar cell applications. These GIXRD data show reasonable agreement with the simulated powder pattern, suggesting that while the films are polycrystalline in nature, the packing is similar to the single crystal structure.

Atomic force microscopy images (Figure B16) show that the height variation and the grain boundaries are an order of magnitude larger in the unannealed film compared to the SVA film, which is likely to impact the dynamics in the triplet state. Fitting the images collected on two representative locations on these samples to Gaussian height distributions yielded widths of 22 nm and 2 nm on these films, respectively. Interestingly, the 22 nm width on the unannealed film also agrees with the thickness uncertainty obtained from the profilometry. The lateral extent of these boundaries is only visible in the unannealed film whereas the SVA film shows mostly a flat surface with occasional contaminants. AFM images were analyzed using Gwyddion.[126]

Steady-state absorption and emission spectroscopy. Figure 17a shows the steady-state absorption spectra of a typical C_5PDI crystal when the incoming beam polarization is

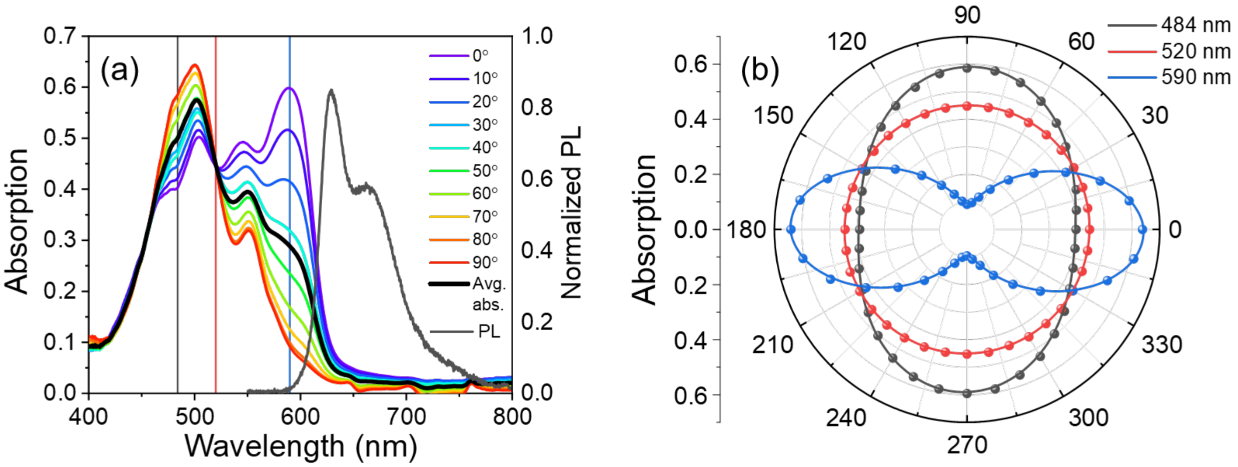

Figure 17. (a) Polarization dependence of the steady-state absorption spectrum of a C_5PDI crystal from 0° – 90° and the unpolarized photoluminescence spectrum (black). (b) The radial absorption plot for three key wavelengths with fits (see SI), where the plot colors in (b) match the vertical line colors in (a).

incrementally changed between 0° and 90°. This is representative of a larger data set collected over the full angular range of 0° to 360° (Figure B1) and depicted as a radial plot in Figure 17b. Similar results on C_5PDI single crystals were reported earlier,[127] so here we only review these results briefly. The C_5PDI absorption shows two prominent, orthogonally polarized Davydov bands. The largest dichroic ratio is observed with the lowest energy band at 590 nm, while the high-energy Davydov band has a lowest energy absorption peak at 550 nm. This amounts to about a 150 meV splitting between the bands. Austin *et al.* were able to spectrally model these two Davydov bands including the vibronic detail for these crystals.[127] Their results suggest that to fully capture the spectral shape of these bands, both Coulombic (neutral dipole-dipole interaction) and charge transfer (CT) character must be invoked. CT character results from symmetry-breaking charge separation in the crystal, and has been observed previously in varying degrees, including complete charge separation, in other PDI systems including covalently linked dimers and partially ordered films.[54, 60, 128-130] The photoluminescence spectrum of the C_5PDI single crystal has a maximum at 629 nm and displays vibronic structure. The intersection of the 0° absorption and (unpolarized) emission spectra of the C_5PDI single crystals gives the S_1 energy $E_S = 2.02$ eV.

The steady-state absorption spectra for the unannealed and SVA films are shown in Figure 18a. After annealing for 15 minutes in acetone, a strong, lower energy vibronic band grows in at 585 nm and the other primary vibronic bands at 500 and 540 nm red shift slightly. The absorption spectrum of the SVA film resembles an average of the polarized absorption spectra of the single crystal (Figure B2), which agrees with the polycrystalline nature of the SVA film as indicated in Figure 16b. The steady-state emission spectra of the unannealed and SVA films both show an emission band at 615 nm and lower energy bands at 700 and 710 nm, respectively. The values of E_S for the unannealed and SVA C_5PDI films obtained from the intersection of their absorption and emission spectra are both 2.07 eV (Figure B2). This energy is close to the single crystal value given above, while both values are significantly smaller than the corresponding C_5PDI monomer S_1 energy in solution (2.36 eV).[49] These data show that while solvent-vapor annealing does not largely alter the S_1 energy in the film, the transformation of the absorption spectra indicates that the interaction between the PDIs is changing significantly, as the Franck-Condon overlap at the ground state configuration changes to resemble that of the single crystal.

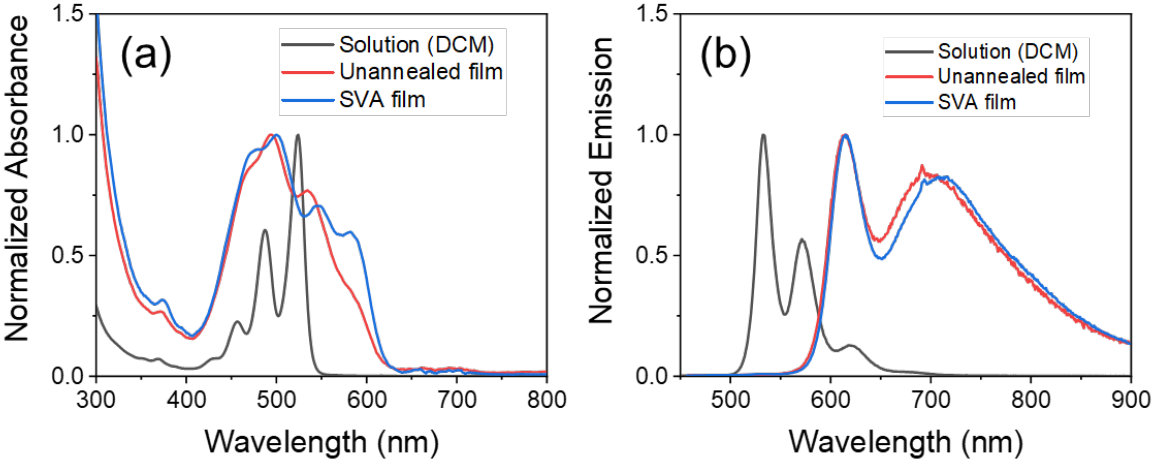

Figure 18. (a) Steady-state absorption and (b) emission spectra for C_5PDI films overlaid with solution spectra.

In contrast, the emission spectra of both films exhibit a strong vibronic feature at 613 nm (2.02 eV), and a second, broad feature of similar intensity that extends beyond 900 nm (Figure 18b). This feature peaks at 700 nm (1.77 eV) and 710 nm (1.75 eV) in the unannealed and the SVA films, respectively. While the single crystal showed no indication of excimer emission, the lower energy peak in the films shows broad, featureless, and strongly red-shifted features characteristic of an organic excimer.[58] The role of this excimer will be discussed in detail below.

The triplet energy of C_5PDI in the solid state was determined using phosphorescence spectroscopy of the thin films (Figure B3). Both spectra show an onset of emission at 1160 nm, indicating that the $^{3*}C_5$PDI energy is about 1.1 eV, which is slightly lower than the 1.2 eV triplet energy of monomeric PDI in a frozen glass,[49] most likely resulting from intermolecular electronic interactions due to C_5PDI π-stacking.[44] While phosphorescence from the C_5PDI single crystal was too weak to measure, we assume that the $^{3*}C_5$PDI energy in the single crystal is similar to that in the SVA polycrystalline film.

Singlet fission dynamics. Figures 19a-c show fsTAM spectra and kinetics on a typical C_5PDI single crystal. The probe polarization was set to coincide with the lower energy Davydov band polarization, while the 450 nm pump was linearly polarized at an arbitrary angle. We did not observe any spectral changes in the fsTAM spectra when changing the pump polarization because the single crystals have negligible polarization dependence at 450 nm. Immediately following photoexcitation, the lower Davydov band at 590 nm bleaches, which is accompanied by the appearance of a broad excited-state absorption (ESA) at 727 nm (Figure 19a). The bleach and ESA both decrease in the first few picoseconds and the ESA blue shifts to 720 nm, along with apparent loss of stimulated emission. This behavior has been observed previously in π-stacked PDI derivatives and is assigned to formation of a mixed state having excited singlet and CT character

(S_1-CT).[74-76, 80] The broad ESA still maintains a peak around 700 nm that is characteristic of the PDI anion,[131] indicating significant CT character in the S_1-CT mixed state, followed by SF from that state to state C.[54, 60, 76] At intermediate delay times (10-100 ps) the near-infrared ESA feature decreases, while at the same time a new ESA appears at 570 nm. This new absorption as well as the bleach remain constant during the remaining 7 ns pump-probe delay time window. At long times, the transient spectrum exhibits concomitant $T_n \leftarrow T_1$ ESA peaks obtained by doping a C_5PDI film with PdPc(OBu)$_8$ (E_T = 1.12 eV[87]) (Figure B4).

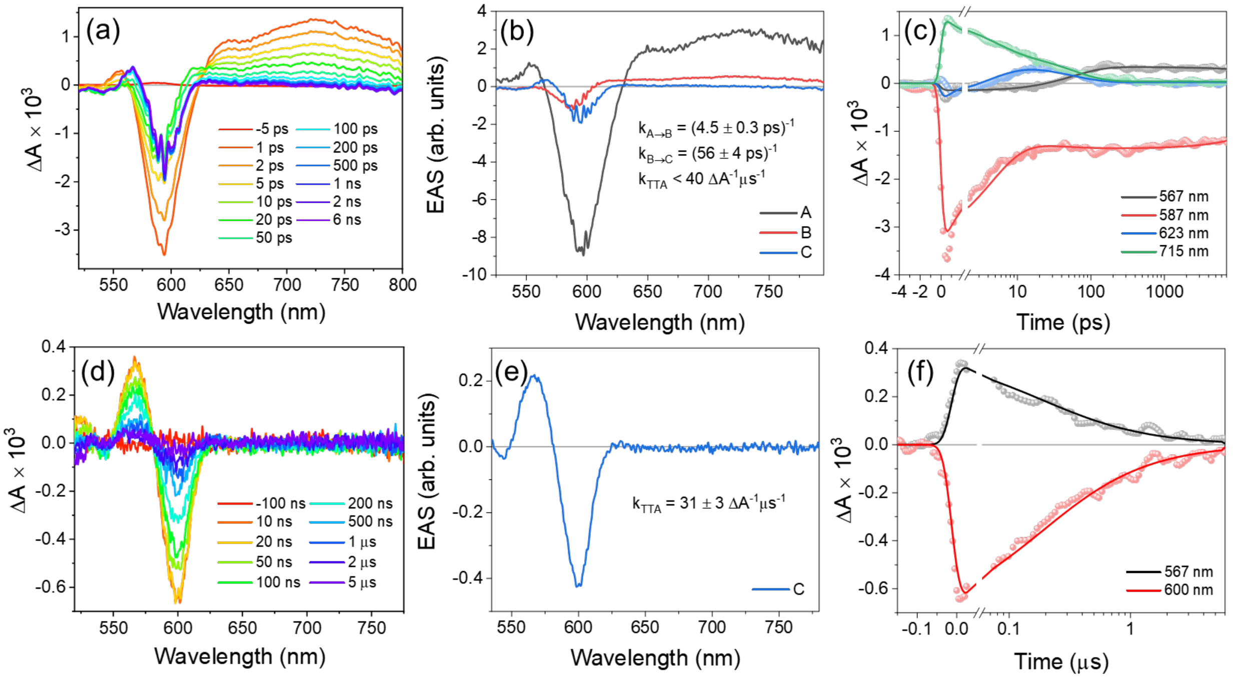

Figure 19. (a)-(c) fs-TAM and (d)-(f) ns-TAM of a C_5PDI single crystal. (a) and (d): spectral evolution of transient absorption signals. (b) and (e): Evolution-associated spectra. (c) and (f): Kinetic traces and fits at several key wavelengths.

The fsTAM data were globally fit using a sequential model, A → B → C, with rate constants $k_{A\rightarrow B}$ and $k_{B\rightarrow C}$, for the A → B and B → C first-order processes ($k_i = 1/\tau_i$), respectively, and with C decaying to the ground state via bimolecular triplet-triplet annihilation (TTA) on a much slower timescale. The resulting evolution-associated spectra (EAS) and the corresponding kinetic fits for four key wavelengths are shown in Figures 19b and 19c, respectively, which yield $k_{A\rightarrow B}$ = (4.5 ±

0.3 ps)$^{-1}$ and $k_{\mathrm{B}\rightarrow\mathrm{C}}$ = (56 ± 4 ps)$^{-1}$. NsTAM (Figures 19d-f) reveals that the triplet excitons almost completely decay to the ground state slowly over the 6 μs experimental time window and are not simply described by a single first-order decay. From the crystal structure, it is apparent that the π-stacks do not easily facilitate the one-dimensional ordering previously seen in other single crystals of SF chromophores such as *N,N*-bis(3′-aminopentyl)terrylenediimide (C_5TDI),[132] and thus the long-time decay is treated as a generic bimolecular biexciton decay. Fits to this model show excellent agreement with a single species that decays bimolecularly to the ground state via TTA with k_{TTA} = 31 ± 3 ΔA^{-1} μs^{-1}.

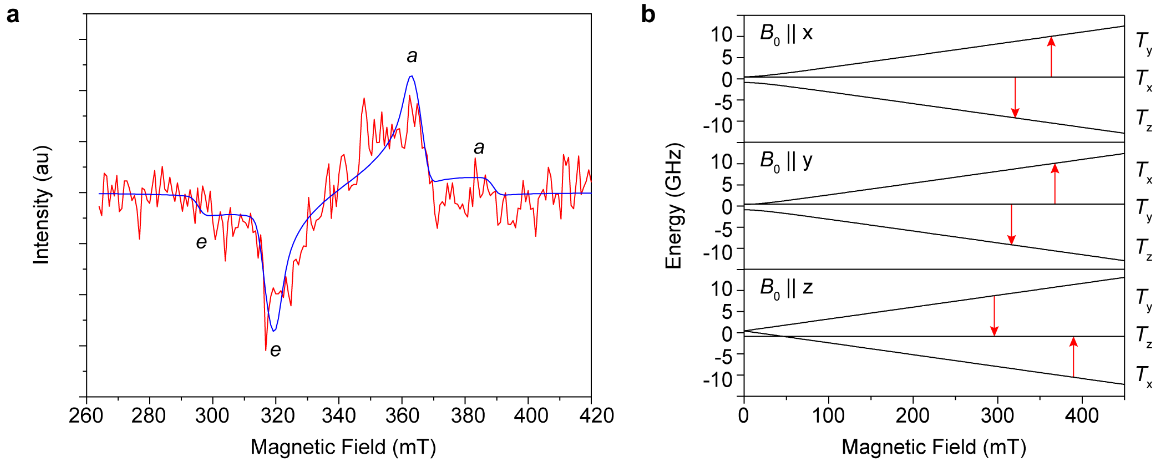

Figure 20. (a) TREPR experimental (red line) and simulated (blue line) spectrum of the C_5PDI crystals after photoexcitation with a 625 nm laser pulse at 85 K and at X band. The spectrum is an average of data collected between 50 and 250 ns after photoexcitation. (b) Plot of energy vs. magnetic field in the three canonical orientations relative to the magnetic field, B_0, in which the T_x and T_y sublevels in the zero-field limit are selectively populated. Upward and downward arrows indicate absorptive and emissive transitions, respectively.

Time-resolved electron paramagnetic resonance (TREPR) spectroscopy provides further evidence for the assignment of the long-lived species in the C_5PDI crystals to triplet excitons. The TREPR spectrum shown in Figure 20a exhibits an (*e*,*e*,*e*,*a*,*a*,*a*) polarization pattern from low to high magnetic field, where *a* is enhanced absorption and *e* is emission, and is fit with zero-field splitting parameters, |*D*| = 1340 MHz and |*E*| = 40 MHz, which are consistent with those reported previously for other PDI derivatives,[133-134] confirming the formation of triplet excitons in the C_5PDI crystals. Six state-to-state transitions are present in the triplet spectrum, in which two pairs of transitions are nearly degenerate due to $|E| << |D|$ in the zero-field splitting tensor. The spin polarization pattern is consistent with triplets generated via SF that subsequently undergo spin-selective decay to the ground state via intersystem crossing that occurs preferentially through the T_z zero-field spin sublevel.[135] Figure 20b shows the transitions within the triplet energy manifold in the three canonical orientations with respect to the magnetic field, corresponding to peaks in the TREPR spectrum.

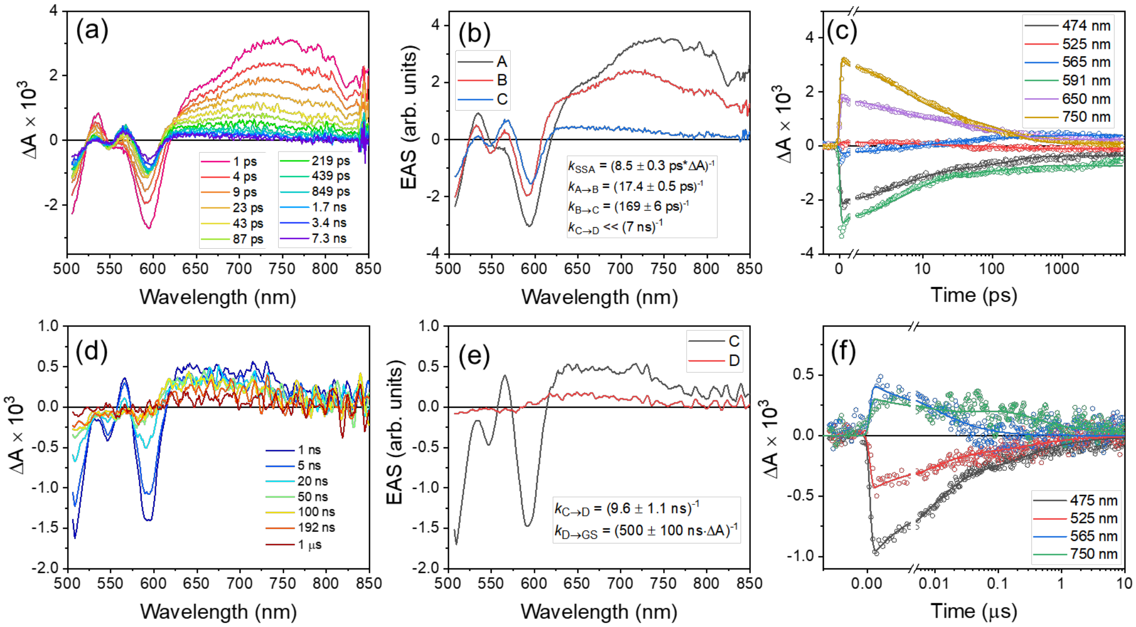

Figure 21. (a)-(c) fs-TA and (d)-(f) ns-TA of the SVA annealed C_5PDI film photoexcited at 500 nm. (a) and (d): spectral evolution of transient absorption signals. (b) and (e): Evolution-associated spectra. (c) and (f): Kinetic traces and fits at several key wavelengths.

The fsTA and nsTA data for the SVA C_5PDI polycrystalline film excited at 500 nm shown in Figure 21 closely resemble the fsTAM and nsTAM data for the C_5PDI single crystal shown in Figure 19. The higher pump energy density of this apparatus results in the presence of nonlinear singlet-singlet annihilation (SSA) decay, which is accounted for in our kinetic model. Analogous to the single crystal data, global fitting of the data results in three distinct states. Following photoexcitation, the SVA film shows an immediate GSB accompanied by formation of a broad 700 nm ESA band, which is assigned to an $S_n \leftarrow S_1$ transition. The initial state transforms to a similar S_1-CT mixed state along with vibrational relaxation in $k_{A\rightarrow B} = (17.4 \pm 0.5 \text{ ps})^{-1}$, which exhibits a decreased GSB and an ESA at 720 nm. This state evolves with $k_{B\rightarrow C} = (169 \pm 6 \text{ ps})^{-1}$ to form an ESA at 570 nm and little or no ESA between 600 and 800 nm, once again indicative of triplet exciton formation. The fsTA and nsTA data for the SVA and unannealed films using low fluence excitation pulses at a 50 kHz repetition rate are given in Figures B5-B7. The spectra of the unannealed film show that very few long-lived triplet excitons are formed.

It is important to note, however, that thermal heating from the deposition of phonons following SSA as well as direct heating by the laser during fsTA spectroscopy is evident in the film samples at these pump energy densities, including in the crystal. The dynamics of the films in the absence of significant SSA were obtained using a much lower excitation density and exciting at the lowest energy (590 nm) transition (Figure B5) and are in good agreement with the data shown in Figure 21. To assess the effect of heating on the spectra, temperature-dependent steady-state UV-Vis absorption measurements were obtained on the unannealed C_5PDI film (Figures B8 and B9). The spectra show that most of the thermal effects present as negative ΔA features. The thermal distortion present at 560 nm overlaps somewhat with the main triplet absorptive feature; however, it does not change with increasing temperature and the triplet ESA is broader than the thermally induced absorption.

The nature of the S_1-CT mixed state observed in the fsTA and the excimer emission seen in the steady-state fluorescence spectra of the films is not immediately clear, so we performed time-resolved fluorescence spectroscopy on the films, as shown in Figures B10-B13. In the SVA C_5PDI film, the TRF data are dominated by the vibronic feature peaking at 613 nm that decays with a lifetime of $\tau = 165 \pm 20$ ps, in excellent agreement with the fsTA data in Figure 21. We note that the initial S_1-CT mixed state formation occurs within the ~20 ps instrument response and thus is not resolvable. In contrast, the emission at redder wavelengths lives significantly longer. By spectrally filtering the bright, short-lived emission, we see that the feature peaking at ~710 nm in the steady-state emission spectrum has a lifetime of $\tau = 3.7 \pm 0.2$ ns, which does not match any of the observed lifetimes in the transient absorption data. Similar results are seen for the unannealed film. This long lifetime suggests that the reddest emission feature originates from states that are not involved in the SF dynamics, such as defect or trap states at grain boundaries. The ~170 ps state with a maximum at 613 nm (2.03 eV) in the SVA films is therefore assigned to the S_1-CT mixed state from which SF occurs, while the lowest energy state seen in the steady-state emission spectra is assigned as the excimer trap state. Notably the unannealed film also shows this feature at 613 nm; however, the emission quenching is biexponential with ~100 and ~500 ps lifetimes, which are similar to the values seen in the transient absorption data for those films. The discrepancy may be due to the available probe time windows and resolution, as well as the inherent heterogeneity in the unannealed film.

SF mechanism in single crystals and polycrystalline films. In both the single crystal and the SVA film, the initial S_1/Frenkel exciton state rapidly transforms into a state that shows the transient features of the PDI anion,[136] as well as those of the excited state. From the time-resolved photoluminescence data for the SVA film, the first emissive state observed has a 165 ps lifetime commensurate with the SF process and the decay of the intermediate observed in the transient absorption experiments. This implies that the emission spectrum of that species is that of the intermediate, and any localized S_1 emission decays prior to the instrument response. Hence, we assign the energy of the S_1-CT mixed state to the peak of this feature at 2.02 eV (613 nm). Because state mixing requires the energies of the S_1 and CT states to be similar, [58, 137] the energy of this mixed intermediate state in the film is taken to be approximately the same as that of the S_1 state (2.07 eV). If the emission of the crystal also arises mostly from this mixed state, which is reasonable considering the significantly longer lifetime of this state compared to the pure vertical S_1 state (56 vs 4.5 ps, respectively), then the mixed state energy is taken as 2.02 eV (Figure B2). Together with the 1.1 eV T_1 energy, this makes SF endoergic by 130 and 180 meV in the SVA film and single crystal, respectively, which is consistent with SF rates seen previously in molecules that are known to undergo endoergic SF like other PDI derivatives and tetracene.[44, 49 44, 98, 103, 108-109] In contrast, SF from the emissive excimer state of the films would be endoergic by about 450 meV, indicating a significant kinetic barrier to triplet formation, which is consistent with the lack of observed triplet formation in the unannealed film.

The residual long-lived, strongly red-shifted photoluminescence from the films is thus assigned to excimer traps sites with unfavorable electronic couplings that do not permit competitive SF. These couplings dominate in the unannealed film resulting in little or no SF. In contrast, the GIXRD data show that the SVA film is more crystalline and less heterogeneous than the as-deposited film, leading to a higher SF rate, which more closely approximates that of the single crystal. The lack of strongly red-shifted photoluminescence from the single crystal is consistent with the high degree of ordering characteristic of single crystals, which minimizes the number of defect trap sites that lead to exciton decay by pathways other than SF. We have previously demonstrated SF mediated by the mixed S_1-CT state leading to triplet yield of 190% in thin films of C_5TDI.[70] Moreover, SF mediated by the S_1-CT mixed state has been observed in tetracene and 3,6-bis(thiophen-2-yl)diketopyrrolopyrrole, where the mixed S_1-CT state forms within picoseconds from S_1,[12, 138] and subsequently fissions into triplet excitons, similar to what is observed here for C_5PDI.

Despite the near-unity efficiency of the primary SF event in the single crystal and SVA films, the free triplet exciton (T_1+T_1) yields in both cases are surprisingly small. Spectral deconvolution was used to obtain lower-bounded triplet yields of 70 ± 2% for the crystal and 29 ± 8% for the film (Figures B14-B15). Thus, if nearly 100 % of the singlet population reaches the S_1-CT mixed state as indicated by the kinetics, the low yield of uncorrelated T_1 may be due to either rapid recovery of the ground state from this intermediate, or fast triplet-triplet annihilation *within* the correlated ^{1}(TT) state following SF. In either case, the strong electronic coupling provided by the close packing of C_5PDI in the crystal and polycrystalline film is both an advantage and disadvantage, as it leads to fast deactivation of both the S_1 and ^{1}(TT) states, and a reduced triplet yield. Modulating the twist and the lateral displacement of the PDI cores may allow for direct tuning of the triplet-triplet annihilation, while preserving the S_1-CT mixed state mediation process. Indeed, our C_5TDI film work shows that it is completely possible to have a rapidly forming S_1-CT mixed state that still leads to near the ideal 200% free triplet exciton yield,[70] suggesting that both processes can be tuned independently.

CONCLUSIONS

Due to their high stability, synthetic tunability, and visible light absorption, PDIs are potentially useful SF materials. Using single-crystal X-ray diffraction, we found that the C_5PDI forms pairs of twisted π-π dimers that minimize any steric hindrance between the alkyl groups in the imide position. We have studied the excited state dynamics of C_5PDI in a single crystal and in a polycrystalline thin film by transient absorption spectroscopy, microscopy, fluorescence and time-resolved electron paramagnetic resonance spectroscopy. Upon excitation of both samples, rapid formation of triplet excitons is observed from the strong transient absorption signal and further confirmed by TREPR spectroscopy. We conclude that the triplet exciton formation mechanism is SF from a S_1-CT mixed state that forms in high yield, with SF occurring with $\tau = 56 \pm 4$ ps and 169 ± 6 ps lifetimes for the single crystal and polycrystalline thin film, respectively. Time-resolved emission data support the assignment of a S_1-CT mixed state-mediated SF process. The triplet exciton quantum yield in the single crystals is 70%, while that in the SVA polycrystalline film is only 29%. This study affords a better understanding of not only the impact of crystalline order on triplet yield but also the impact different packing motifs have on SF. In addition, the observation of similar SF rates in both the single crystal and SVA polycrystalline films of this molecule suggests that new architectures should be further explored in SF chromophores, especially given that C_5PDI molecules pack face-on to the substrate, making potential triplet exciton or charge extraction more facile.

Attributions:

- Malik Williams: synthesized molecule, grew crystal, solved crystal structure, collected some steady-state spectroscopy on the crystal, fsTAM of crystal, data analysis, wrote part of manuscript
- Itai Schlesinger: steady-state spectroscopy of crystal, fsTAM/nsTAM of crystal, data analysis, triplet yield calculation for crystal, AFM data acquisition and analysis, wrote part of manuscript
- Carolyn E. Ramírez: film fabrication, steady-state film spectroscopy, non-linear spectroscopy data collection and analysis for films, film X-ray data acquisition and analysis, triplet yield calculations for film, wrote part of manuscript
- Robert Jacobberger: TR-EPR acquisition and analysis
- Paige J. Brown: TRF data acquisition
- Ryan M. Young: high fluence nsTA and solution fsTA/nsTA measurements, TRF data analysis, discussion, manuscript revisions and content

- Michael R. Wasielewski: funding, oversight, manuscript revisions and content

Chapter 3: Photophysics of Zinc 2,11,20,29-tetra-*tert*-butyl-2,3-naphthalocyanine: Aggregation-Induced S_2 Emission and Rapid Intersystem Crossing in the Solid State

Carolyn E. Ramírez, Robert Jacobberger, Ryan M. Young, and Michael R. Wasielewski - Manuscript accepted with minor revisions (JPC C 2022)

ABSTRACT

Aggregation can dramatically alter the photophysics of organic chromophores by modulating their electronic properties. Zinc 2,11,20,29-tetra-*tert*-butyl-2,3-naphthalocyanine (***t*-Bu-ZnNc**) in thin films emits primarily from its second excited singlet state (S_2), while ***t*-Bu-ZnNc** in solution obeys the well-known Kasha rule and emits from S_1. This behavior most likely results from the hindered motion of the *t*-butyl groups in the rigid, closely packed thin films. This is corroborated by the observation of enhanced S_2 emission in low-temperature glassy solutions. The ***t*-Bu-ZnNc** films also show rapid intersystem crossing to form a long-lived triplet excited state an order of magnitude faster than in solution due to the enhanced density of triplet states and the concomitant reduced singlet-triplet energy gap between the broadened excited state manifolds in the closely packed solid.

INTRODUCTION

The competition between photophysical decay pathways is highly sensitive to the electronic/vibronic coupling between the initial and final states as well as the energy difference between them. A principal consideration in the design of molecular photoactive materials is how to control the competition between these pathways to produce the desired product state. The various decay processes available for a photoexcited organic chromophore, such as fluorescence, internal conversion, intersystem crossing, and charge transfer, all depend on the energy differences between their target states, and thus allow a means to control the fate of the excited state. Aggregation in organic systems offers a route to modulate both the coupling and the energy gap, with dramatic effects progressing from dimers to disordered solids and single crystals.

Kasha's Rule is one direct manifestation of the kinetic competition between excited state decay processes. In the context of fluorescence emission, it specifies that an electronically excited molecule of a given spin multiplicity will emit from the lowest electronic state within that manifold, after first decaying to this state via internal conversion (IC).[139] For example, if a molecule in its singlet ground state (S_0) is photoexcited to its second excited singlet state (S_2), it typically relaxes rapidly to S_1 by IC before decaying from S_1 to S_0, possibly by emission of a photon. This rule follows as a consequence of the large difference between typical internal conversion and emission rates, which scale very differently depending on the energy differences involved.[140-144] Specifically, non-radiative IC depends exponentially on the energy as described by the energy gap law:[145]

$$k_{IC} \propto e^{-\Delta E/k_B T} \tag{3.1}$$

where ΔE is the energy gap, k_B is the Boltzmann constant, and T is the temperature. Microscopically, this is due to the inability of the bath to quickly dissipate large energy releases through phonons or molecular vibrations. Fluctuations in the instantaneous energies from vibrations or other motions of flexible groups can bring two electronic states transiently closer in energy and trigger internal conversion. In contrast, the fluorescence emission rate in simple systems tends to scale as the cube of this gap (ΔE^3), so there is the propensity for competition between these processes depending on the scale of the gaps involved.[10, 146]

For most chromophores, the $S_1 - S_2$ energy gap is sufficiently small to allow ultrafast IC to compete effectively with emission from S_2. A well-known exception is azulene, which exhibits substantial emission from its S_2 energy level.[143-144, 147-149] This higher-state emission occurs because of the large $S_1 – S_2$ energy gap (1.74 eV),[148] which slows the rate of IC according to the discussion above compared to that of emission. Other cases of anti-Kasha emission involve systems studied specifically in the gas phase,[150] as well as more complicated mechanisms including aggregation-induced emission,[151-153] where compounds that do not intrinsically exhibit higher-state emission in dilute solution will emit from higher states when subject to strong intermolecular interactions in the solid state. For example, Qi *et al.* found that aggregation of a rhodamine-naphthalimide compound resulted in anti-Kasha bright emission from the S_2 energy level, while S_1 remained a dark state.[154] In addition, Guo *et al.* showed that materials that show aggregation-induced delayed fluorescence can help enhance organic light emitting diode technologies. The molecules in the study of Guo *et al.* were not strongly luminescent in solution because of high IC rates, but upon aggregation, IC slowed and triplet formation dominated.[152]

Triplet formation via intersystem crossing (ISC) can also be significantly enhanced in the solid state due to strong molecular interactions. So-called "Aggregation-Induced intersystem crossing" (AI-ISC) has been found in chromophores whose phosphorescence can be exploited.[151, 155-158] In general, the ISC rate depends both on spin-orbit coupling, H_{SO}, and the energy gap between the triplet and the S_1 state, $\Delta E_{S\text{-}T}$:[145]

$$k_{ISC} \propto \frac{|\langle T|H_{SO}|S_1\rangle|^2}{\Delta E_{S-T}^2} \tag{3.2}$$

Only the lowest singlet excited state is considered because ISC is generally slow and is expected to obey Kasha's rule. Both spin-orbit coupling and $\Delta E_{S\text{-}T}$ are highly sensitive to molecular packing.[145] Upon aggregation and ultimately moving to the solid state, the discrete, well-defined energy levels in an isolated molecule broaden, eventually becoming band-like, which effectively decreases $\Delta E_{S\text{-}T}$ and increases the ISC rate. Similarly, in organic compounds with metal centers, like porphyrins and phthalocyanines, aggregation will increase the total spin-orbit coupling experienced by an excited chromophore due to the closer proximity to the heavy-atom metal centers of the neighboring units.[159] We note that other efficient triplet formation processes can be enabled by aggregation, specifically singlet exciton fission, provided that the triplet energy of the chromophore is approximately half that of the singlet energy and the interchromophore electronic coupling is favorable.[14, 160] Thus, chromophore aggregation can be used as a powerful tool to modulate triplet formation in organic solids.[158]

In this study, we explore the effects of aggregation on the singlet and triplet excited state dynamics of zinc 2,11,20,29-tetra-*tert*-butyl-2,3-naphthalocyanine (***t*-Bu-ZnNc**), shown in Scheme 1. Because of their expanded π-structure resulting in extensive electron delocalization,[161] naphthalocyanines are interesting for many electronic applications requiring near-infrared absorbing chromophores. Both ***t*-Bu-ZnNc** and unsubstituted **ZnNc** have been studied in solution in donor-acceptor systems as well as in the solid-state in single crystals and highly ordered films.[162-166] The **ZnNc** molecules in single crystals are slip-stacked, which reduces their π-π overlap somewhat.[163] In addition, **ZnNc** forms polycrystalline films when vacuum-deposited on various heated substrates, including glass, highly oriented pyrolytic graphite, MoS_2, indium tin oxide, NaCl, and other alkali halides.[164-166] These studies show that the **ZnNc** molecular orientation and stacking can be manipulated with the choice of substrate. ***t*-Bu-ZnNc** has been shown to form amorphous films that possess different properties upon thermal annealing.[167]

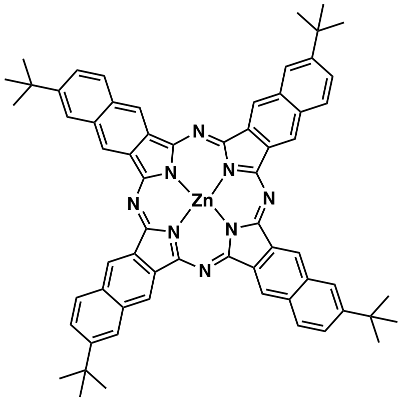

Scheme 1. Molecular structure of ***t*-Bu-ZnNc**

The optical properties of **ZnNc** and those of its *tert*-butyl-modified derivative ***t*-Bu-ZnNc** have received much less attention.[168] To exploit **ZnNc** and its derivatives as near-infrared-absorbing chromophores in electronic and electro-optic applications, a deeper understanding of their excited-states is needed. Here, we examine the excited-state dynamics and emission behavior of spin-coated amorphous films of ***t*-Bu-ZnNc** on sapphire substrates. We observe significant emission from the S_2 state of ***t*-Bu-ZnNc** in the film that does not occur in room temperature solution, which we attribute to lowering the $S_2 \rightarrow S_1$ IC rate due to hindered *t*-Bu group rotation in the solid state. ISC rates and associated triplet yields also increase upon aggregation, which we attribute to AI-ISC due to the decreased singlet-triplet energy gap. The slowing of the $S_2 \rightarrow S_1$ IC rate in the solid state leads to a complete change in the overall emission characteristics of ***t*-Bu-ZnNc** and demonstrates how aggregation can be used to manipulate the complicated kinetic interplay between these photophysical processes.

EXPERIMENTAL METHODS

Materials. Zinc 2,11,20,29-tetra-*tert*-butyl-2,3-naphthalocyanine (***t*-Bu-ZnNc**) was purchased from Sigma Aldrich and used as received.

Film Preparation. Films were prepared by first dissolving ***t*-Bu-ZnNc** in $CHCl_3$ or CH_2Cl_2 at a concentration of 20 mg/mL (40 mg/mL for Electron Paramagnetic Resonance (EPR) spectroscopy samples) and spin-coating the solution on clean sapphire (quartz for EPR measurements) substrates. The substrates were cleaned before deposition by sonication in water, methanol, and acetone for 10 minutes each and dried with N_2. One film was thermally annealed in an N_2-filled glovebox at 250 ^{o}C for 3 hours and one remained unannealed. The thicknesses of both films were measured using a high-resolution Dektak 150 Stylus Surface Profilometer. The unannealed film was 88 ± 18 nm thick and the thermally annealed film was 82 ± 29 nm thick.

X-ray Characterization. Both films were characterized with grazing-incidence X-ray diffraction (GIXRD) using a Rigaku ATX-G. Films were analyzed using out of plane GIXRD with an incident angle of 0.5°. Grazing-incidence wide-angle X-ray scattering (GIWAXS) was also done on both films at the Advanced Photon Source at Argonne National Laboratory using beamline 8-ID-E (reserved for high signal-to-noise GIWAXS measurements). Measurements were taken with 10.92 keV/1.1354 Å X-rays produced from the synchrotron incident on the sample at an angle of 0.140°. A Pilatus 1 M detector was used to gather all scattered X-rays and the resultant GIWAXS images were analyzed and corrected with the GIXSGUI MATLAB program.[69]

Steady-State Optical Spectroscopy. Solution steady-state absorption spectra were measured in toluene using a Shimadzu 1800 UV−vis spectrophotometer. All film steady-state absorption measurements were performed using a Shimadzu UV-3600 UV/vis/NIR spectrometer with an integrating sphere to correct for scatter and reflectance. Steady-state emission data were acquired with a Horiba Nanolog fluorimeter. Films were excited in a front-face geometry while the solution sample was excited in a right-angle geometry. Solution samples were excited at 350 nm at 295 K for standard measurements. The low-temperature emission measurements were taken by mounting a sample cell with two quartz windows separated by a 2 mm PTFE spacer containing ***t*-Bu-ZnNc** in toluene in a Janis VNF-100 cryostat (Janis Research Co. LLC) coupled to a Cryo-Con 32B (cryogenics Control Systems, Inc.) temperature controller. Emission measurements were then conducted ramping the temperature down between 220-108 K. Film samples were excited at 350 nm at 295 K.

Transient Absorption Spectroscopy. Femtosecond transient absorption (fsTA) data on films were collected on a high repetition rate, low fluence system described previously.[24] All nanosecond transient absorption (nsTA) data and the fsTA data on solution samples were collected on a lower repetition rate, high fluence system published previously.[23] Samples were excited separately at two wavelengths: samples were pumped exciting the $S_1 \leftarrow S_0$ transition (765 nm for solution, 712 nm for films) and the $S_2 \leftarrow S_0$ transition (400-410 nm for both). All data were fit and modeled using a previously described MATLAB fitting program.[70] Femtosecond TA data were globally fit to a first order kinetic model while nanosecond TA data were fit to a second order kinetic model.

Electron Paramagnetic Resonance Spectroscopy. Time-resolved electron paramagnetic resonance (TREPR) spectroscopy was conducted at X-band microwave frequency (~9.6 GHz) using a Bruker Elexsys E680-X/W EPR spectrometer with a split-ring resonator (ER4118X-MS3). The ***t*-Bu-ZnNc** film was flame-sealed in a quartz tube under a vacuum of 10^{-3} Torr. The sample was photoexcited with 690 nm, 7 ns, 3.5 mJ pulses generated by an optical parametric oscillator (Spectra-Physics, BasiScan) pumped with the frequency-tripled output of a Nd:YAG laser (Spectra-Physics. Quanta-Ray Lab-170-10H) at a repetition rate of 10 Hz. Following photoexcitation at 10 K, kinetic traces of the transient magnetization were acquired as a function of magnetic field using quadrature detection under continuous microwave irradiation of 3.1 mW. The data were processed by subtracting the background signal prior to the laser pulse for each kinetic trace and then subtracting the signal at off-resonance magnetic fields for each spectrum. The spectrum for the triplet ($S = 1$) species was fit using the pepper function in EasySpin 5.2.33[120] and was modeled using the Hamiltonian:

$$\mathcal{H} = g\mu_B \boldsymbol{B_0} \cdot \boldsymbol{\hat{S}} + D\left(\hat{S}_z{}^2 - \frac{S(S+1)}{3}\right) + E\left(\hat{S}_x{}^2 - \hat{S}_y{}^2\right) \tag{3.3}$$

where g is the isotropic g-factor, μ_B is the Bohr magneton, $\boldsymbol{B_0}$ is the magnetic field vector, $\boldsymbol{S}$ is the spin vector, and D and E are the zero-field splitting parameters.

TD-DFT Calculations. Time-dependent density functional methods and computational results are given in the Appendix C.

RESULTS & DISCUSSION

Film packing and structure

Spin-coated films of ***t*-Bu-ZnNc** studied in this work were relatively amorphous as cast with minimally enhanced crystallinity upon annealing. Figures C1-C3 show both the grazing incidence X-ray diffraction (GIXRD) and grazing incidence wide angle X-ray scattering (GIWAXS) data for both the unannealed and thermally annealed ***t*-Bu-ZnNc** films. The GIXRD data of the annealed film in Figure C1 show very few peaks compared with many strong features in the simulated powder pattern of the **ZnNc** crystal structure. The reported crystal structure of the bare **ZnNc** shows a π-π distance of 3.23 Å and center-center distance of 6.85 Å.[163] The crystal structure of ***t*-Bu-ZnNc** is unavailable, but we hypothesize that the *t*-Bu groups added to enhance solubility also impact the crystal structure packing and directly influence its optoelectronic properties.

Singlet excited-state dynamics: Aggregation-induced anti-Kasha emission

The steady-state UV-vis absorption data shown in Figure 22 reveal a change in the ratio of the vibronic Q-band peaks in solution versus the film. In toluene, the lowest energy vibronic peak at 760 nm dominates the absorption, while a Gaussian fit of absorbance spectra[169] reveals that the lowest energy bands of the unannealed and annealed films (Figure C6d,e) occur at 820 and 810 nm, respectively. After thermally annealing, the ratio of the third to second vibronic bands in the film increases, showing enhanced absorption to the higher excitonic state in the more ordered solid-state structures. Additionally, the relative absorption from the Soret band ($S_2 \leftarrow S_0$) increases in the film, likely due to excitonic coupling of the transition dipole moments between adjacent chromophores.[170] This phenomenon has been seen previously in anti-Kasha chromophores like azulene, where the higher energy absorption is attributed to non-Condon behavior. In order to accurately model the S_2 absorption and emission of azulene, Prlj *et al*. employed Herzberg-Teller coupling beyond the Franck-Condon approximation because the excitonic vibrations could not be treated independently from the nuclear coordinate of the vibration, as is the core assumption in the

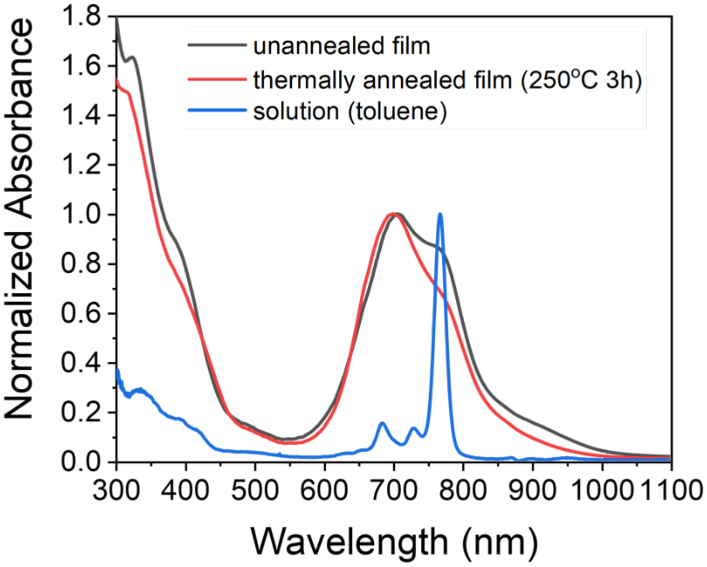

Figure 22. Steady-state UV-vis absorption spectra of both unannealed and annealed ***t*-Bu-ZnNc** films overlaid with ***t*-Bu-ZnNc** dissolved in toluene.

Franck-Condon approximation.[171-172] The absorption in the films is also significantly broadened compared to the solution spectrum, which is a generic phenomenon in disordered solids.[44, 70, 173]

The steady-state emission spectra of the ***t*-Bu-ZnNc** films are compared to that in solution at 295 K in Figure 23. The steady-state absorption and emission spectra are plotted versus wavenumber in Figure C4. In Figure 23a, the visible light emission is shown for all three samples. As expected per Kasha's rule, ***t*-Bu-ZnNc** in solution shows strong S_1 emission at 767 nm. However, upon close inspection S_2 emission is evident in the solution sample near 400 nm (see inset). The emission from the films occurs at 500 nm, which is below the wavelength of the $S_1 \leftarrow S_0$ absorption (600-900 nm), indicating that this emission originates from S_2. This band is significantly red shifted and broadened compared to that of the solution sample. The near-infrared (NIR) emission data for the films shown in Figure 23b shows S_1 emission at 1000 1000 nm. The fluorescence quantum yield of both films is <0.5% between 350 and 850 nm.

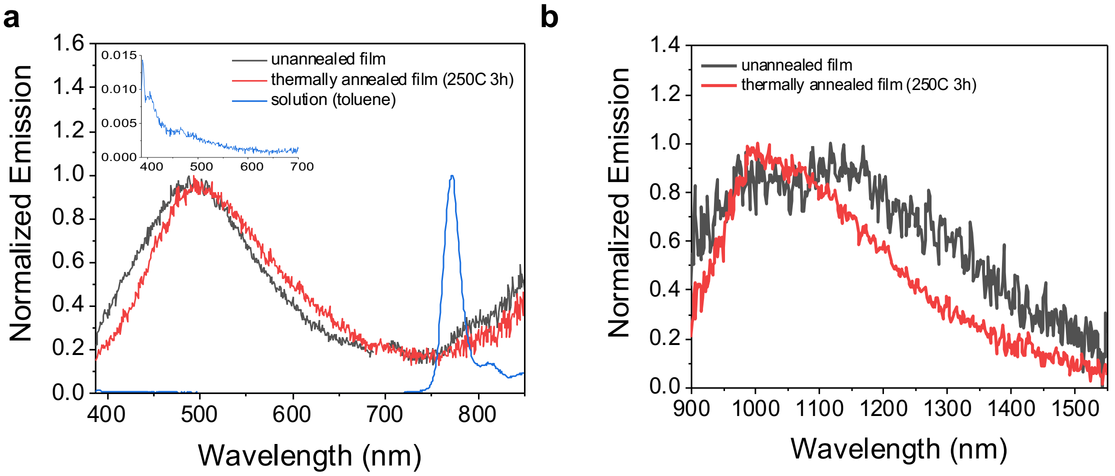

Figure 23. Steady-state emission spectra of (a) both unannealed and annealed ***t*-Bu-ZnNc** films overlaid with ***t*-Bu-ZnNc** dissolved in toluene; Inset: zoomed-in view of S_2 emission of ***t*-Bu-ZnNc** in toluene; (b) unannealed and annealed film NIR emission.

This violation of Kasha's rule is likely a consequence of significant alteration in the energy landscape in the solid state.[151-153] From the intersection of the absorbance and emission data for solution and films shown in Figures C5 and C6a,b,d,e, we find the S_2 and S_1 energies in solution are $E(S_2) \cong 3.3$ eV and $E(S_1) = 1.61$ eV. Likewise for the film, $E(S_2) = 2.92$ eV and $E(S_1) = 1.36$ eV. The energy gap between S_1 and S_2 is quite large, leading to the possibility that the energy gap law results in a slow internal conversion/vibrational relaxation rate that results in enhanced S_2 emission.[145] The lower overall quantum yield of emission in the films compared to solution also indicates that the emission of S_2 is enhanced relative to S_1. This can result from extending the S_2 lifetime and/or decreasing the S_1 lifetime. To further clarify this point, we probed the lifetimes of each state with femtosecond transient absorption (fsTA) spectroscopy.

The fsTA spectra for ***t*-Bu-ZnNc** in toluene excited at 400 nm are shown in Figure 24. The data were modeled using sequential kinetics. The absorption changes are dominated by a ground-state bleach at 765 nm, which persists throughout the experiment, as well as excited-state absorption peaks at 450 and 500 nm that are assigned to $S_n \leftarrow S_2$ transitions (state A). These signals

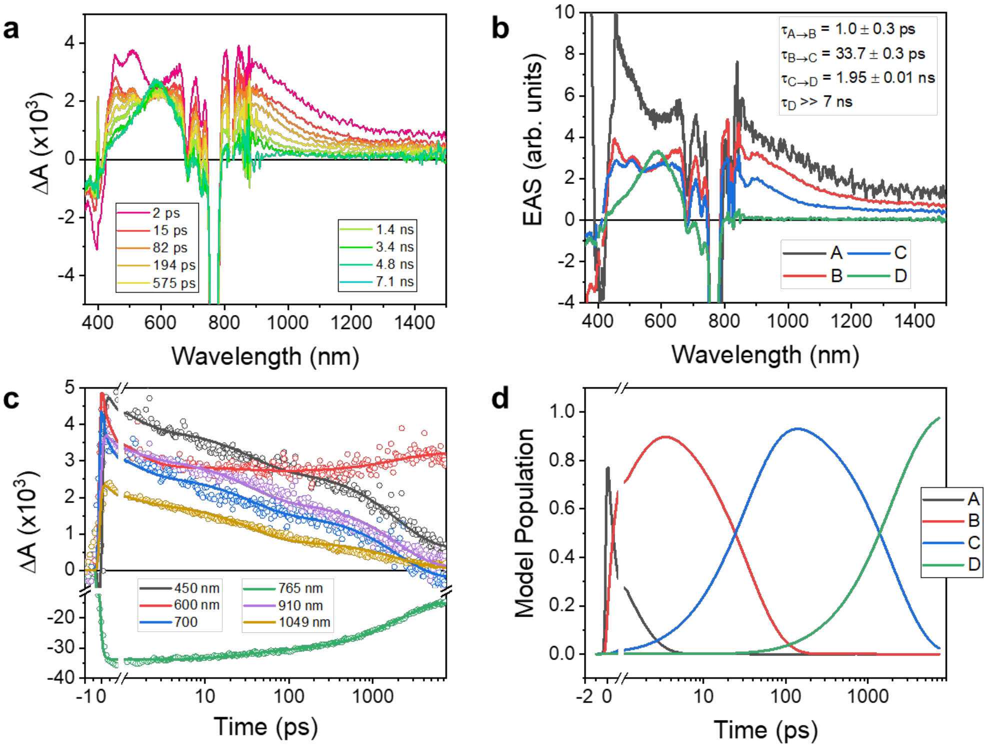

Figure 24. Femtosecond transient absorption spectroscopy of t-Bu-ZnNc in toluene excited at 400 nm: (a) raw spectra, (b) evolution-associated spectra, (c) quality of kinetic fit, (d) population of states versus time.

decay with a time constant τ = 1.0 ± 0.3 ps via IC to a vibrationally hot S_1 state (B) with the appearance of a new peak at 508 nm and sharpening of the feature near 900 nm. The singlet state relaxes with a time constant of 33.7 ± 0.3 ps with some spectral evolution near 450 nm indicating that this relaxation process most likely occurs on the same electronic excited state surface and leads to the vibrationally cooled S_1 (state C). The $S_n \leftarrow S_1$ absorptions then slowly transform with a time constant of τ = 1.95 ± 0.01 ns to a single broad feature at 600 nm that is assigned to $T_n \leftarrow T_1$ absorption (state D).[162] These features and dynamics are very similar to those observed exciting the $S_1 \leftarrow S_0$ band (*vide infra*), with no new features appearing at early times. The relaxation process is slower when pumping at 400 nm compared to 765 nm (33.7 ± 0.3 vs 22.0 ± 0.5 ps, respectively) likely due to additional vibrational cooling associated with the excess energy deposited into S_1 following rapid IC.

Excitation of the films at 400 nm yields spectra that initially do not show dramatic spectral evolution. Relaxation processes prior to ISC (see below) with some spectral evolution in the 500-800 nm range do occur in the films in the 5-30 ps time range with the decay times lengthening upon thermal annealing (Figures 24 and C12-C13). This may be a result of a decreased internal conversion rate from S_2 to S_1 upon annealing; however, direct observation of the IC process in the films were not possible because the most substantive spectral differences between the $S_n \leftarrow S_2$ and $S_n \leftarrow S_1$ transitions are on the edges or beyond the 500-900 nm spectral range of the high repetition rate TA instrument used to measure the films.

Triplet excited-state dynamics: Aggregation-induced intersystem crossing

Femtosecond and nanosecond transient absorption spectra were collected on both the unannealed and annealed ***t*-Bu-ZnNc** films and compared to those of ***t*-Bu-ZnNc** in solution to explore the effects of aggregation on the triplet excited state following excitation to S_1 at 712 nm.

As shown in Figures 25b and 25e, the singlet excited state (state A) produced following photoexcitation structurally relaxes to state B prior to ISC to the triplet (state C). Intersystem crossing occurs in τ = 53 ± 2 ps and 113 ± 7 ps in the unannealed and thermally annealed films, respectively, representing a substantial rate increase over solution. Thus, the increased ISC rate in the films dramatically decreases the S_1 lifetime, and hence quenches the S_1-based emission. This is discussed in depth below.

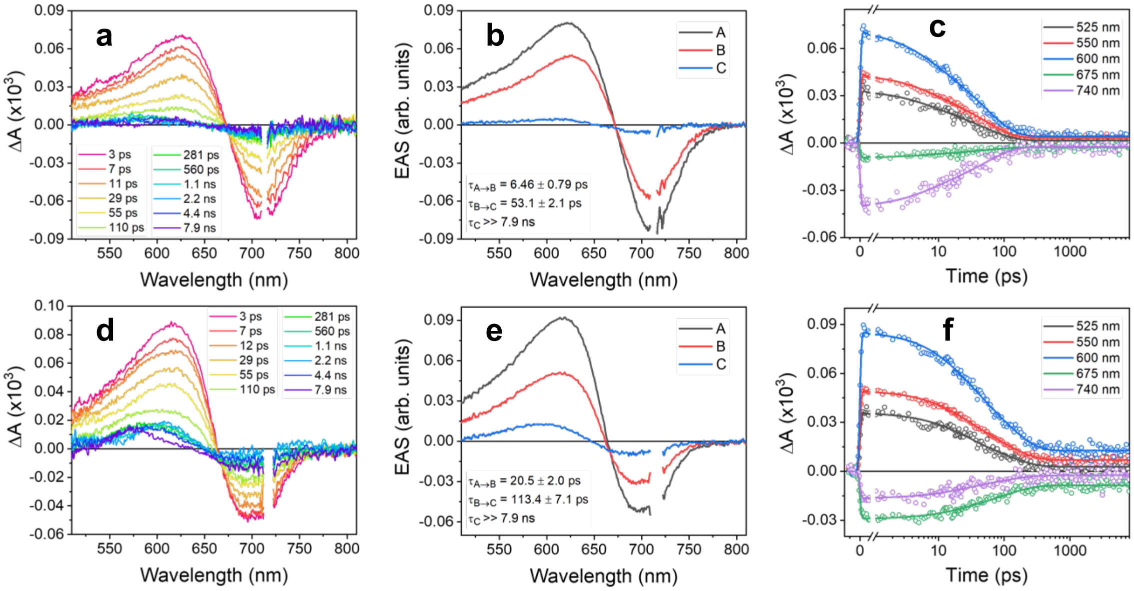

Figure 25. FsTA spectroscopy of (a)-(c) unannealed ***t*-Bu-ZnNc** film and (d)-(f) thermally annealed ***t*-Bu-ZnNc** film; (a) and (d): spectral evolution of transient absorption signals; (b) and (e): Evolution-associated spectra; (c) and (f): Kinetic traces and fits at several key wavelengths.

We observe qualitatively that the triplet yield appears significantly higher in the annealed film. Further discussion of the triplet yield can be found in Appendix C. Notably, the singlet excited state decays twice as fast in the unannealed film compared with the annealed film and shows a larger triplet absorption change, implying a potentially complicated interplay between the ISC and possibly IC rates upon annealing (see below). The triplet state lives beyond the temporal range of the instrument in both the solution and film samples. The nsTA data for ***t*-Bu-ZnNc** both in solution and in the films following $S_1 \leftarrow S_0$ excitation are shown in Figures C10, C14, and C15, and show that the long-lived state in the fsTA data agrees well with the triplet species observed in nsTA spectroscopy, with an excited-state absorption peak at 600 nm and ground-state bleach at 720 nm that decays within the nsTA temporal window. Decay of the triplet state by triplet-triplet annihilation (TTA) occurs more rapidly in the annealed film than the unannealed film, presumably as a consequence of the higher crystallinity of the annealed film leading to more rapid triplet migration. Notably, the nsTA data for the ***t*-Bu-ZnNc** films show faster triplet decay than in solution, possibly resulting from triplet diffusion.[174-175] The triplet decays in the films also require two bimolecular TTA processes to fit the data, possibly resulting from contributions to the TA at long times due to thermal effects of the pump excitation, most notably between 700-850 nm (Figure C16), which may also contribute to rapid triplet decay. The two bimolecular processes also suggest that TTA might be occurring within crystalline domains first and then annihilating at the interfaces of other domains following three-dimensional exciton diffusion, which is plausible in a heterogeneous film with defects.[176-177]

To confirm the assignment of the long-lived TA signals in the films to the triplet state and not to thermal distortions,[50, 178] transient absorption spectra were acquired on a thin film of ***t*-Bu-ZnNc** doped with $Pd(PPh_3)_2Cl_2$ and excited at 740 nm (Figure C17). Here, the palladium provides additional spin-orbit coupling via the heavy-atom effect, leading to rapid ISC in the neighboring ***t*-Bu-ZnNc** within the doped film.[12, 40] The resulting spectrum is the same as that produced in the undoped films at long times, confirming the assignment of the triplet species in the ***t*-Bu-ZnNc** films.

Additional evidence for the assignment of the long-lived TA signals to the triplet state was provided by TREPR spectroscopy on the ***t*-Bu-ZnNc** films. Following photoexcitation at 690 nm, an (*a*,*e*) spectral pattern from low to high magnetic field, where (*a*) and (*e*) correspond to absorptive and emissive signals, respectively, is observed at 100 ns after the laser pulse (Figure 5, red line). The simulated triplet spectrum (Figure 26, blue line) agrees well with the experimental spectrum when the zero-field splitting parameters of the triplet state are D = 507 MHz and E = 6 MHz and the T_Z spin sublevel of the triplet manifold is selectively populated. The D value of ***t*-Bu-ZnNc** is slightly smaller than that previously measured for the corresponding Zn phthalocyanine and Zn tetra-*t*-butylphthalocyanine of ~720 MHz,[179-180] which is consistent with the larger size of the naphthalocyanines relative to phthalocyanines.

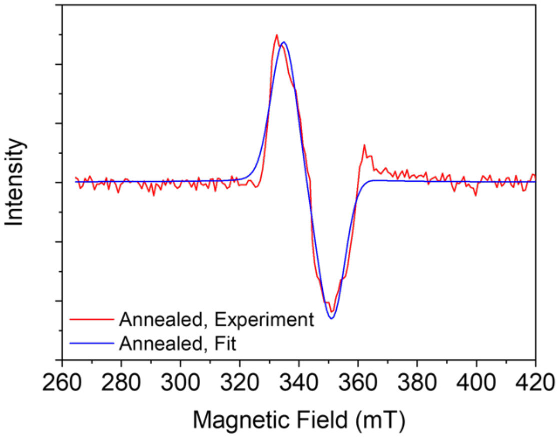

Figure 26. TREPR spectrum (red) and simulated spectrum (blue) of a ***t*-Bu-ZnNc** film ~100 ns after optical excitation at 690 nm.

With the identity of the triplet state established we performed spectral deconvolution[40, 42] on the fsTA data for the thermally annealed ***t*-Bu-ZnNc** film excited at 712 nm to obtain the time-dependent populations of the S_1 and T_1 states and determine the yield of the AI-ISC process. Details are given in the Supporting Information. Basis spectra are shown in Figure 27a, and the extracted populations are shown in Figure 27b. The resulting triplet yield in the annealed ***t*-Bu-ZnNc** film is 10 ± 2%. The annealed film produces nine times more triplet-state-excited molecules than the unannealed film (see App. C). Interestingly, while the GIXRD and GIWAXS data shown in Figures C1-C3 do not show very high crystallinity, the difference between the disordered unannealed spin-coated film and the slightly ordered thermally annealed spin-coated film is evident in the higher triplet quantum yield between the two samples. This difference indicates that in addition to aggregation inducing rapid ISC in the films, annealing appears to enhance this effect. While these differences are not readily apparent in the X-ray spectra (GIWAXS, GIXRD, Figures C1-C3), there are a few possible explanations including some highly localized reordering to favor

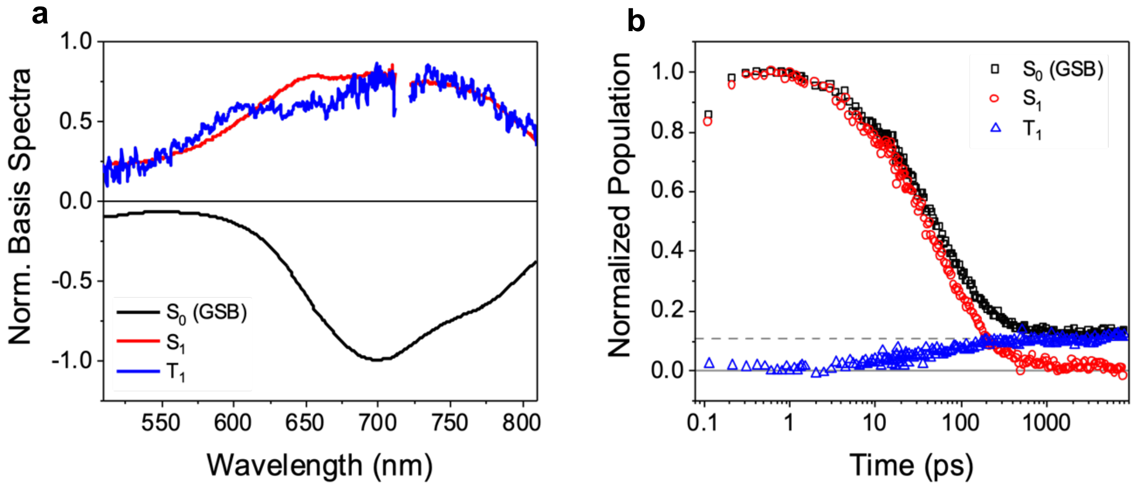

Figure 27. Triplet quantum yield calculations for ***t*-Bu-ZnNc** thermally annealed film: (a) basis spectra calculated from raw fsTA data and (b) populations of each species calculated via spectral deconvolution of raw fsTA data.

ISC. The X-ray data show the average order at different length scales throughout the film. While the GIWAXS data shown in Figure C2 show relatively amorphous packing, there may be some microcrystalline re-ordering upon thermal annealing that is not detected by GIWAXS but serves to enhance ISC. Local order could also be affected by thermal annealing including smoothing/annihilation of defects/trap sites in the amorphous film. This small enhancement in local order could enable stronger heavy-atom ISC effects with neighboring Zn atoms, resulting in a higher AI-ISC yield in the annealed film.

Effects of aggregation on *t*-Bu-ZnNc photophysics

The energetics of ***t*-Bu-ZnNc** calculated in the gas phase using time-dependent density functional theory (TD-DFT) as well as experimentally determined values from both solution and solid-state samples are shown in Figure 28. The energy gap between the S_2 and S_1 energy levels is very large (1.4-1.7 eV) in both solution and the films, so IC is expected to slow substantially in this system per the energy gap law,[145] allowing fluorescence from S_2 to outcompete IC to S_1 to an appreciable amount. The almost equal energy spacing between $S_2 \rightarrow S_1$ and $S_1 \rightarrow S_0$ is also strongly reminiscent of azulene.[143, 147] The S_1 energy decreases by 0.25 eV from solution to film, while the S_2 energy decreases by 0.38 eV. Clustering into more *J*-like aggregates results in energy level splitting and lowering.[158, 181] Aggregation induces a more significant lowering of the S_2 energy

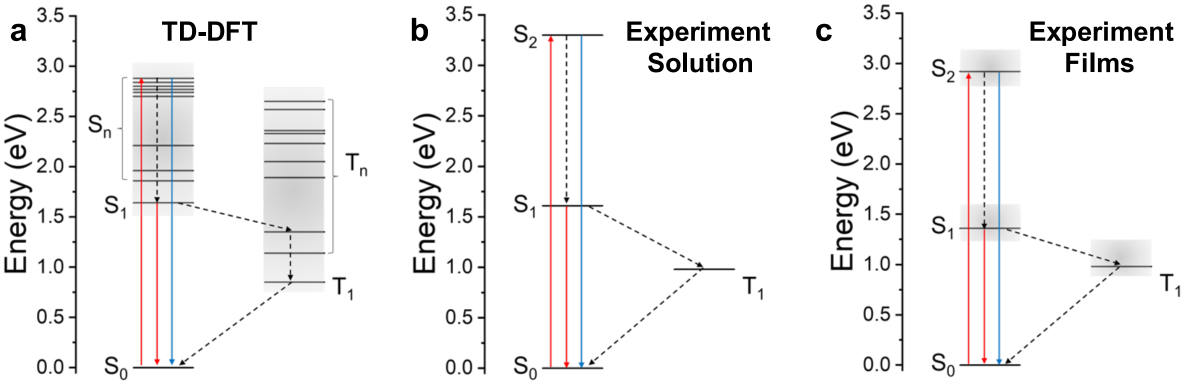

Figure 28. Jablonski diagrams showing: (a) energy splitting and density of states of singlet and triplet energy levels from TD-DFT calculations of **ZnNc** (gas phase calculation); (b),(c) proposed kinetic mechanisms for S_2 excitation and subsequent emission of ***t*-Bu-ZnNc** in (b) toluene [solution] and (c) film [solid-state] with experimentally determined S_n and T_n values. Solid and dashed arrows indicate radiative and non-radiative transitions, respectively.

level, perhaps owing to the non-Condon nature of this vibronic state discussed previously. The experimentally reported **ZnNc** triplet energy in a frozen solution is $E(T_1)$ = 0.98 eV,[162] and the addition of the *t*-butyl groups is not expected to alter that energy significantly.

As discussed above, IC is facilitated by fluctuations in the electronic state energies, which are influenced by the motions of non-rigid groups and solvent molecules within the first solvation shell, implying that the emission should be strongly temperature dependent. Therefore, we examined the steady-state emission of a dilute solution of ***t*-Bu-ZnNc** in toluene as a function of temperature above and below the freezing point of toluene (178 K). Figure C8b shows that as temperature decreases, emission from S_2 increases. An Arrhenius plot of the integrated emission exhibits a linear relationship with the inverse of the temperature, as shown in Figure C9, indicating the excited-state dynamics of ***t*-Bu-ZnNc** do obey the energy gap law. The low-temperature solution measurements show that in the absence of aggregation, diminished structural fluctuations lower the IC rate and consequently increase S_2 emission. Given the rigid nature of the naphthalocyanine core, it is reasonable to assign the origin of the fluctuations to hindered rotation of the *t*-Bu groups. Thus, in the solid-state films, the stacking of the ZnNc cores impedes the motion of the *t*-Bu groups and reduces the energy fluctuations that drive the IC process, ultimately enhancing S_2 emission, despite the larger energy gap between $S_2 \rightarrow S_1$ in solution than in the film. It is well known that molecules in the solid-state may possess different excited state energies relative to solution because bulky substituents that have no effect in solution may significantly affect the crystal packing in the solid-state.[39, 44, 151-154, 182]

Following competitive IC from S_2 to S_1, ^{1*}***t*-Bu-ZnNc** undergoes ISC to the T_1 state in competition with IC and fluorescence decay back to the S_0 state (Figure 28). In the solid state, the S_1 lifetime of ***t*-Bu-ZnNc** decreases relative to that in solution by factors of 36 and 18 in the unannealed and annealed films, respectively. This leads to a dramatic reduction of the S_1 emission, and in concert with the decreased $S_2 \rightarrow S_1$ IC rate, allows the S_2 emission to dominate in the film. While the S_1 lifetime in the solid state increased by a factor of ~2 upon annealing, the corresponding triplet yield increases nine times (see App. C for details). These two seemingly contradictory findings ultimately mean that thermal annealing is changing the ratio of ISC and IC rates. Since the observed lifetime is the result of the sum of all of the decay rates that deactivate the singlet excited state, i.e. $\tau_{obs} = (k_{IC} + k_{rad} + k_{ISC})^{-1}$, the longer S_1 lifetime in the annealed film thus suggests that $S_1 \rightarrow S_0$ IC is slowed upon annealing to a larger degree than the ISC rate constant increases, resulting in an overall longer observed time constant. The radiative decay rate may also be increasing, as shown by the stronger S_1 emission (> 800 nm) in the annealed film compared with the unannealed film (Figure C6f). However, the radiative rate constant must still be small due to the low emission quantum yield and any increase must still be much less than the decrease in k_{IC} to maintain the longer excited-state lifetime.

Rapid ISC in naphthalocyanines may be especially pronounced owing to the close energetic proximity of several low-lying excited singlet and triplet states of ***t*-Bu-ZnNc** (Figure 28). Exciton coupling between multiple chromophores will split these energy levels resulting in quasi-continuous bands of electronic states in the solid state with the resulting Franck-Condon overlap favoring rapid ISC.[170,181] The width of these bands narrows the energy gaps compared to those of the corresponding discrete electronic states in the isolated molecules. The bands provide a large density of final states for the ISC transition, which with eq (3.2) predicts will dramatically increase the overall ISC rate. Additional ISC pathways are also available to the higher-lying triplet excited states, which will then decay rapidly to T_1 via IC within the triplet manifold. Changes in the spin-orbit coupling upon annealing may also be contributing to the increased ISC rate from the same rate expression: the added presence of nearby Zn atoms could enhance spin-orbit coupling between the S_1 and T states due to the number of Zn atoms in close proximity to the ^{1*}***t*-Bu-ZnNc**. The impact of this effect should be sensitive to changes in the local chromophore density and order within the solid.

TTA is also sensitive to changes in the local order. The triplet state in the films lives for hundreds of nanoseconds compared to tens of microseconds in solution. Triplet lifetimes in the solid state will be determined primarily by triplet exciton diffusion, which is largely limited by order and the sizes of local crystalline domains.[174-175] Therefore, we attribute the difference in triplet lifetimes between the films and solution to the increased proximity of ***t*-Bu-ZnNc** molecules in the film and the enhanced order gained from thermal annealing. As aggregation and order increase, the ISC rate increases, likely due to the increased proximity to neighboring Zn atoms. This increased heavy-atom effect accelerates SO-ISC to form the triplet state.[159] While, in principle, this should also accelerate ISC back to the ground state, the increased order in the thermally annealed film could possibly allow for triplet diffusion over larger distances, which may allow more triplets to escape annihilation and give the triplet excitons in that film a longer lifetime.

CONCLUSIONS

Aggregation of ***t*-Bu-ZnNc** in the solid state has marked effects on its excited-state dynamics. Immediately upon excitation, polycrystalline films of ***t*-Bu-ZnNc** violate Kasha's rule by emitting from the higher S_2 energy level as a consequence of the various changes in excited state decay rates that occur upon aggregation. Specifically, this aggregation-induced effect is attributed in part to a decrease in the $S_2 \rightarrow S_1$ internal conversion rate due to steric hindrance in the solid state hindering of *t*-butyl group rotations. Transient absorption spectroscopy shows that the long-lived triplet excited state in the films is rapidly populated via aggregation-enhanced ISC from the S_1

state. The ISC rate is up to 36 times faster in the solid state than in solution, and the triplet yield in the annealed film is nine times larger compared to the unannealed film. Thus, the rapid deactivation of the S_1 state in the films together with the slowed $S_2 \rightarrow S_1$ IC rate allows the S_2 emission to dominate in the films, despite the overall lower emission yield. These results show that aggregation is a powerful tool with a wide range of effects on different excited-state manifolds for modulating the behavior of organic chromophores for potential optoelectronic device applications.

Attributions:

- Carolyn E. Ramírez: film fabrication, steady-state film spectroscopy, non-linear spectroscopy data collection and analysis (fsTA), X-ray data acquisition and analysis, analysis of crystal structure characteristics, triplet yield calculations, TD-DFT calculations, made figures, wrote manuscript
- Robert Jaccobberger: TR-EPR data acquisition and analysis
- Ryan M. Young: high fluence nsTA and solution fsTA/nsTA measurements, discussion, manuscript revisions and content
- Michael R. Wasielewski: funding, oversight, manuscript revisions and content

Chapter 4: Rapid Intersystem Crossing and Subsequent Photophysics in the Solid-state of 13,23-diacetyl-8,8,18,18-tetra-methyl-12,22-diphenyl-bacteriochlorin

Carolyn E. Ramírez, Vy-Phuong Tran, Nobuyuki Matsumoto, Paige J. Brown, Ryan M. Young, Jonathan S. Lindsey, and Michael R. Wasielewski - Manuscript in prep

ABSTRACT

13,23-Diacetyl-8,8,18,18-tetra-methyl-12,22-diphenyl-bacteriochlorin exhibits markedly different photophysical properties in solution versus solid state. Aggregation of 13,23-diacetyl-8,8,18,18-tetra-methyl-12,22-diphenyl-bacteriochlorin molecules in thin films induces rapid triplet formation via spin-orbit intersystem crossing that proceeds two orders of magnitude faster than in dilute solution. From X-ray diffraction data, we find that polycrystalline thin films resemble the single crystal structure of this molecule, suggesting a high degree of crystallinity even without post-deposition annealing. Overall, aggregation-induced intersystem crossing provides a strategy to manipulate and exploit triplet production in tetrapyrroles like bacteriochlorins for potential use in light harvesting devices.

INTRODUCTION

Tetrapyrroles are an interesting class of molecules with many naturally occurring derivatives including hemes, chlorophylls, and bacteriochlorophylls.[183] They also offer a variety of synthetic pathways to new molecules.[184] Porphyrins, chlorins, and bacteriochlorins are three categories of tetrapyrroles and have numerous applications in energy harvesting, medicine, and photocatalysis,[184-187] largely due to their synthetic tunability and wide range of photoactive properties including high triplet quantum yields. Bacteriochlorins specifically are interesting as deep-red absorbing chromophores due to the large extent of electron delocalization within the macrocycle.[161, 185-186, 188-191] Bacteriochlorin analogues with different substituents radically alter the molecules' excited state properties and chemical stability. For example, common bacteriochlorins with tetra-methyl and ethyl acetoxy substituents have a fluorescence quantum yield (Φ_F) of around 0.14 and singlet excited-state lifetimes on the order of 10^{-9} s.[185] Conversely, *β*,meso-annulated bacteriochlorins have largely quenched fluorescence, low triplet quantum yields, and singlet excited-state lifetimes on the order of 10^{-12}-10^{-14} s, indicating that most of the excited singlet state population decays via nonradiative internal conversion.[185] Electrons excited to the singlet excited state in bacteriochlorins typically take one of three different kinetic paths: radiative recombination (fluorescence) back to the ground state ($S_1 \rightarrow S_0$), nonradiative internal conversion (IC) back to the ground state ($S_1 \rightarrow S_0$), or spin-orbit intersystem crossing (SO-ISC) to a lower energy triplet excited state ($S_1 \rightarrow T_1$). Thus, their quantum yields should sum to unity per eq. 1 below:

$$\Phi_F + \Phi_{IC} + \Phi_{ISC} = 1 \tag{4.1}$$

By experimentally determining two of these quantum yields (usually Φ_F and Φ_{ISC}) we can fully establish the kinetic decay pathways for bacteriochlorin molecules as a function of their substituent patterns.

SO-ISC is spin-forbidden and thus tends to proceed over longer time scales (> 10^{-9} s), which makes it very easy for this pathway to be outcompeted by rapid IC and fluorescence.[10] The intersystem crossing rate constant depends on the energy gap between the excited singlet (S_1) and triplet (T_1) states (ΔE_{S-T}) as well as the spin-orbit coupling Hamiltonian between the singlet (*S*) and triplet (*T*) states, H_{SO}, which are both heavily influenced by molecular packing:[145]

$$k_{ISC} \propto \frac{|\langle T|H_{SO}|S_1\rangle|^2}{\Delta E_{S-T}^2} \tag{4.2}$$

When molecules aggregate, their energy levels can undergo splitting and broadening,[158, 181] thereby shrinking ΔE_{S-T} and increasing k_{ISC}. This phenomenon is termed aggregation-induced intersystem crossing (AI-ISC) and has been seen in numerous organic materials in the solid state and/or aggregates in solution.[151-152, 155, 158] AI-ISC offers an avenue to control the rate and yield of triplet formation, opening interesting applications for photoactive bacteriochlorin molecules.

In this report, we studied the photophysics of 13,23-diacetyl-8,8,18,18-tetra-methyl-12,22-diphenyl-bacteriochlorin (**B-189**) in solution and in thin films. We also determined its crystal structure and studied its polycrystalline packing motifs in thin films. While crystal structures of some similar molecules have been determined,[185-186, 191] the optoelectronic properties of bacteriochlorins in the solid state have received far less attention. Here, we aim to elucidate the mechanism behind the markedly different kinetic behavior of **B-189** in solution versus the solid state and establish a pathway for optimizing SO-ISC in bacteriochlorin molecules for use in light-harvesting devices.

EXPERIMENTAL METHODS

Synthesis and crystallography. Bacteriochlorin **B-189** was prepared following established methods[192-193] from the organic starting materials methyl cinnamate, tosylmethyl isocyanide, *N,N*-dimethylformamide, nitromethane, 5,5-dimethoxy-2-methylpent-2-ene-4-one. The synthesis was carried out in the Lindsey lab at NC state University by Dr. Nobuyuki Matsumoto. The crystallization was carried out by Ms. Vy-Phuong Tran. The crystals were analyzed using single-crystal X-ray diffraction and the crystal structure was solved. The crystallization from CH_2Cl_2 / CH_3CN was done as follows:

(i) a small sample (~1 mg) of bacteriochlorin powder was dissolved in CH_2Cl_2 (~100–150 microL) and placed in a small tube.

(ii) the small tube was placed in a 3-mL vial containing CH_3CN (1 mL)

(iii) the vial was capped and allowed to stand at room temperature.

(iv) within 4-5 days, crystals appeared in the inner tube.

Film fabrication. B-189 films were made by first dissolving the compound in toluene at a concentration of 20 mg/mL and then spin-coating the solution at 700 and 1500 rpm on clean sapphire substrates (purchased from Ted Pella). Substrates were cleaned by sonication in water, methanol, and acetone for 10 minutes each and dried with nitrogen. The film thickness was found to be 915 ± 270 nm using a high-resolution Dektak 150 Stylus Surface Profilometer.

X-ray Characterization. Films were characterized with grazing-incidence X-ray diffraction (GIXRD) using a Rigaku ATX-G. Films were analyzed using out of plane GIXRD with an incident angle of 0.5°. Grazing-incidence wide-angle X-ray scattering (GIWAXS) was also done on both films at the Advanced Photon Source at Argonne National Laboratory using beamline 8-ID-E (reserved for high signal-to-noise GIWAXS measurements). Measurements were taken with 10.92 keV/1.1354 Å X-rays produced from the synchrotron incident on the sample at an angle of 0.140°. A Pilatus 1 M detector was used to gather all scattered X-rays and the resultant GIWAXS images were analyzed and corrected with the GIXSGUI MATLAB program.[69]

Steady-State Optical Spectroscopy. Solution steady-state absorption spectra were measured in toluene using a Shimadzu 1800 UV/vis spectrophotometer. All film steady-state absorption measurements were performed using a Shimadzu UV-3600 UV/vis/NIR spectrometer with an integrating sphere to correct for scatter and reflectance. Steady-state emission data were acquired with a Horiba Nanolog fluorimeter. Films were excited in a front-face geometry while the solution sample was excited in a right-angle geometry. All samples were excited at 400 nm at 295 K.

Time-resolved fluorescence spectroscopy. Picosecond time-resolved fluorescence (TRF) spectroscopy data were collected on a thin film of **B-189** in air using a Hamamatsu C4780 streak camera described previously.[15] The excitation pulses at 100 kHz were tuned to 650 nm and attenuated to ∼5 nJ/pulse to minimize pump scatter. Data were collected using 2 and 5 ns windows; the instrument response function (IRF) was ∼2-3% of the acquisition window, with the shortest time resolution being ~60 ps. The optical density of the samples was < 0.1 at the excitation wavelength. A 700 nm long-pass filter was installed for the longer time windows to better capture the weaker, long-lived, redshifted emission and avoid detector saturation. All data were acquired in the single-photon counting mode using the Hamamatsu HPD-TA software.

Transient Absorption Spectroscopy. Femtosecond and nanosecond transient absorption (fsTA, nsTA) data were collected on a low repetition rate, high fluence system published previously.[23] Samples were excited at 770 nm (solution) and 780 nm (film). All data were fit to second order kinetic models using a previously described MATLAB fitting program.[70]

DFT & TDDFT calculations. Density Functional Theory (DFT) and Time-Dependent Density Functional Theory (TD-DFT) were used as implemented in QChem 5.1 with the B3LYP functional and 6-31G* basis set to determine the optimized ground-state geometry and excited-state energies, respectively, of B-189. Additional computational details are provided in Appendix D.

RESULTS & DISCUSSION

Morphological data: X-ray diffraction of single crystal and thin film

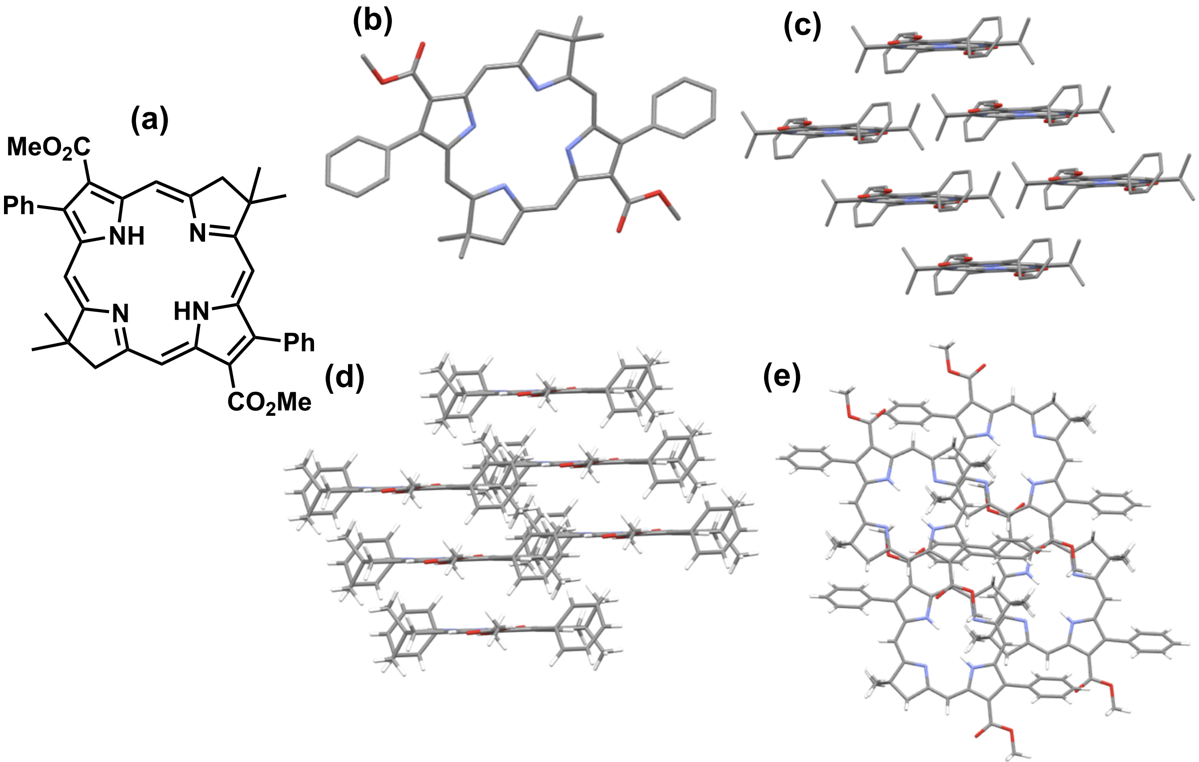

Figure 29. (a) molecular structure of **B-189**; (b)-(e) different views of **B-189** single crystal structure.

The molecular structure of the **B-189** was obtained using single-crystal X-ray diffraction. As shown in Figure 29, the phenyl functional groups are 9.19 Å apart, and the intermolecular distance between molecule cores is 3.6 Å. While the crystal structure shows the molecular stacks are slipped, there is some overlap of the electron-dense groups that can potentially support sufficient coupling for rapid exciton transfer. The cores of the molecules are not electron dense, so the lack of core overlap does not eliminate the possibility of coupling effects.

Grazing incidence wide angle X-ray scattering (GIWAXS) and grazing incidence X-ray diffraction (GIXRD) experiments were conducted on the **B-189** films to understand their degree of crystallinity as it relates to the solved single crystal structure.[69] GIWAXS data of the toluene spin-coated film shown in Figure 30a exhibit moderate polycrystallinity with a bright face-on peak at around 1.4 Å^{-1} on the q_z axis, indicating there is some amount of order parallel to the substrate at a *d*-spacing of ~4.49 Å. The sharp lines also show some isotropic polycrystallinity without a defined crystal growth direction. Linecuts in Figure 30b,c show evidence of a moderately strong 4.49 Å peak in both the q_z and q_{xy} directions. This could be related to π-stacking of the aromatic edges of the molecule, which, again, would be favorable for sufficient coupling to induce rapid exciton transfer in the films.

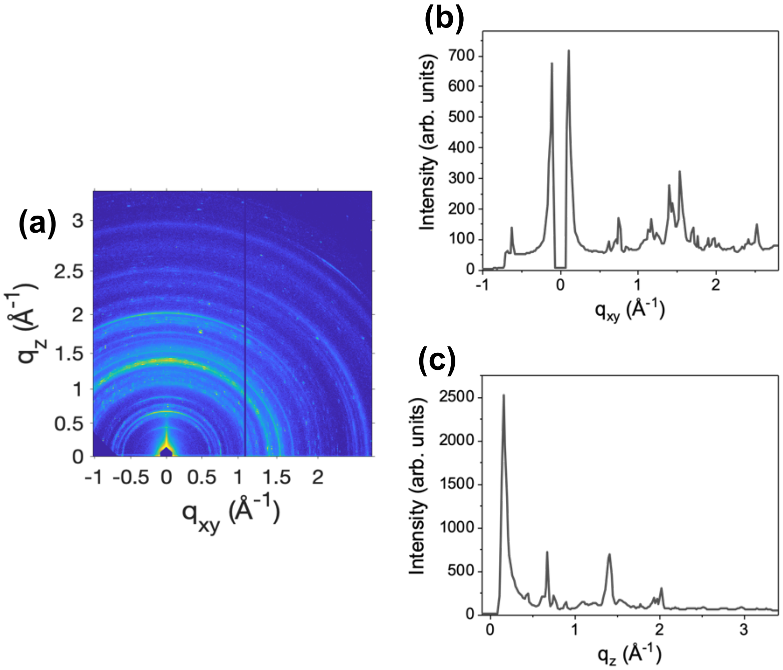

Figure 30. GIWAXS spectra of **B-189** spin-coated in toluene on sapphire (a) spectra; (b) & (c) linecuts.

GIXRD data of the films spin-coated in both toluene and chlorobenzene taken out-of-plane are overlaid with the simulated powder pattern from the single crystal X-ray data in Figure 31a. The data reveal some moderate polycrystallinity with two sharp peaks in both films at 11°, corresponding to a *d*-spacing of 8.0 Å and the (100) plane, and 21°, corresponding to *d*-spacing of 4.2 Å and the (1-12) plane. When we look at these two planes in the crystal structure, shown in

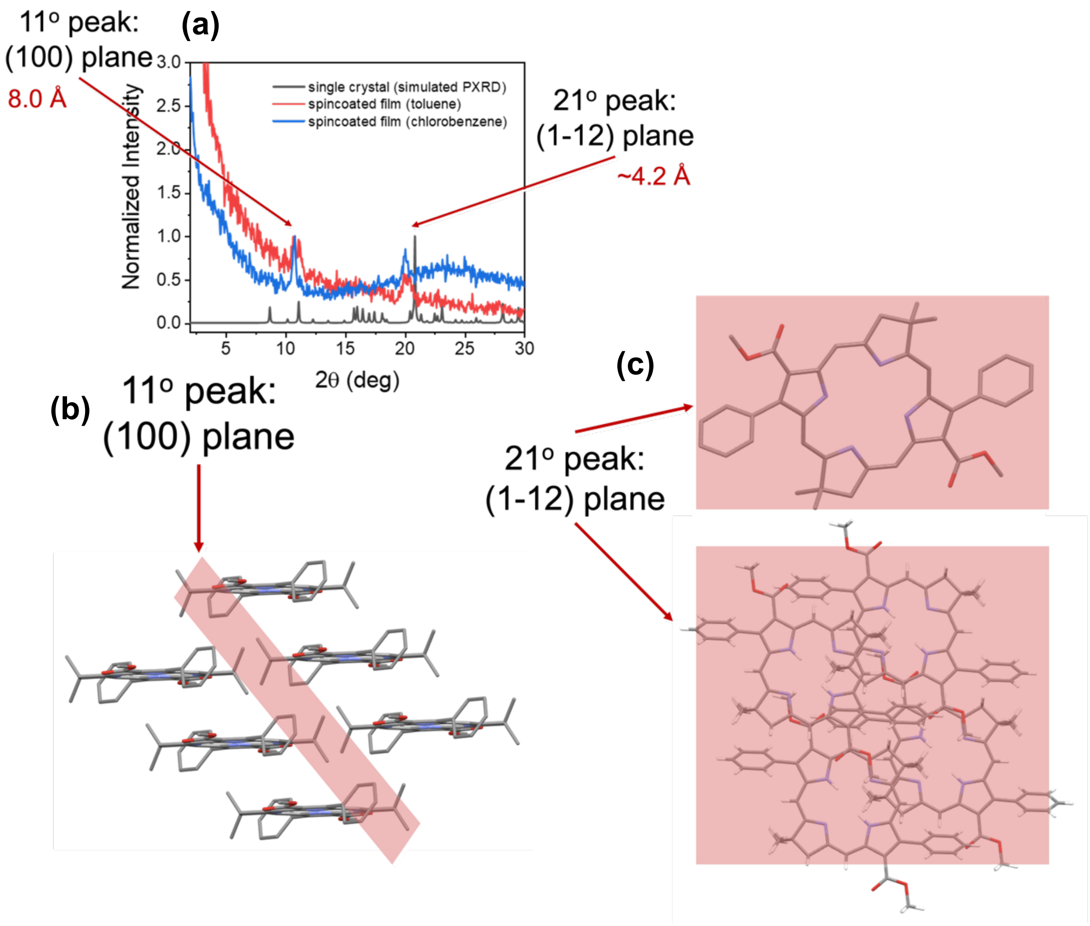

Figure 31. (a) GIXRD spectra of **B-189** films overlaid with simulated powder pattern from crystal structure; (b) visualization of (100) plane in single crystal structure; (c) visualization of (1-12) plane in crystal structure.

Figure 31b&c, we can see the (100) plane corresponds to the slip-stacked columns of molecules. We also see that the (1-12) plane corresponds to the face of the flat **B-189** molecules. These defined diffraction peaks indicate that these two crystalline structural elements are fairly consistent throughout the films suggesting a minor degree of order and polycrystallinity. The 4.2 Å feature matches that from GIWAXS at around 4.49 Å. Given the correspondence of this *d*-spacing to the (1-12) plane, this could more strongly indicate evidence of π-stacking between aromatic groups on the edges of the molecules.

Excited state dynamics of B-189

Steady-state spectroscopy

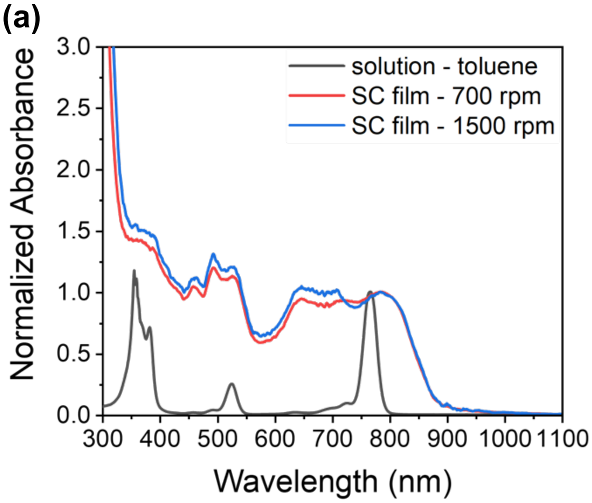

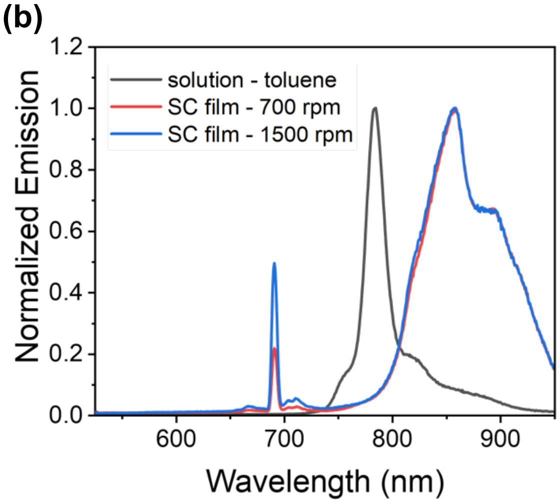

Figure 32. Steady-state (a) UV-vis absorption and (b) emission spectra of **B-189** films overlaid with solution spectra.

Steady-state absorbance data for spin-coated **B-189** films overlaid with **B-189** absorption in toluene solution are shown in Figure 32a. The spectra all possess the same general peaks with varying ratios and broadness. The film data show red-shifting and broadening, indicating significant aggregation of chromophores, as is expected in solid state films as electronic coupling increases due to closer proximity.[44, 70, 74-75, 173, 194-195] In the solution, the low energy Q-band dominates absorption. However, the film shows enhanced absorption of the higher energy Q-bands as well as the Soret band due to increased interaction of the transition dipole moments of neighboring molecules in the highly aggregated and concentrated solid state films.[170]

The emission data for the solution and two films are overlaid in Figure 32b. The emission data show one primary emissive peak representing the second vibronic band at ~780 nm in solution which is red shifted to 855 nm in the films. The highest energy vibronic band is visible as a shoulder in the solution data at 755 nm and the film data at 820 nm. The film emission spectra also show enhanced emission of a lower energy peak at 900 nm (red-shifted from ~820 nm in solution). This suggests intermediate states present in the solid state samples perhaps due to defect trapping of excitons. The film emission spectra also show emission from a higher energy state at ~690 nm, indicating Raman-active energy levels visible in the fluorescence spectra. The fluorescence quantum yield of the films was measured to be <0.5%.

From the intersection of the steady-state absorption and emission spectra shown in Figures D1 and D2, we can find the S_1 energy levels experimentally and compare to computational findings. Using TD-DFT, we found the lowest singlet excited state energy to be 1.94 eV compared to 1.60 eV in solution (experimental) and 1.49 eV in film (experimental). We calculated the lowest triplet energy to be 0.92 eV. Further discussion on energy level differences follows.

Transient Absorption Spectroscopy

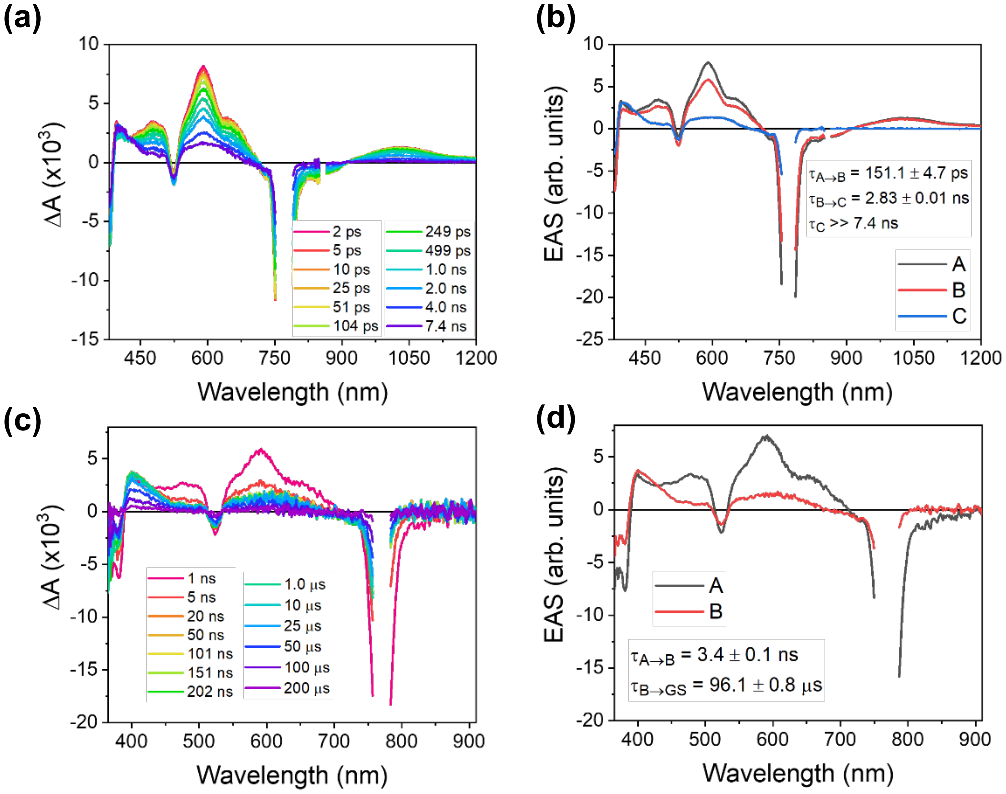

Figure 33. FsTA (a, b) and nsTA (c, d) data of **B-189** in toluene excited at 770 nm: (a, c) raw data, (b, d) evolution associated spectra.

In order to understand the photophysics of **B-189** in the solid state versus solution, we performed femtosecond and nanosecond transient absorption (fsTA & nsTA) spectroscopy. The solution fsTA data for **B-189** in toluene are shown in Figure 33a,b. The data are fit to a first order

A → B → C model where upon photoexcitation at 770 nm, the singlet excited state is populated (state A), as evidenced by the singlet absorption at 490 and 575 nm as well as the ground-state bleach (GSB) appearing red of 750 nm. After τ = 151 ± 5 ps, the system undergoes some structural relaxation into state B. State B undergoes spin-orbit intersystem crossing (SO-ISC) to state C, the long-lived triplet state, in τ = 2.83 ± 0.01 ns. The nsTA data shown in Figure 33c,d further support these kinetics showing a SO-ISC rate constant of τ = 3.4 ± 0.1 ns, very similar to that found from the fsTA experiment. The characteristic absorption features of the triplet excited state appear around 410 and 600 nm. Quality of kinetic fits for these models are shown in Figure D3.

The fsTA data for the polycrystalline thin film of **B-189** are shown in Figure 34a,b. Because these data were acquired with a high excitation fluence (2.0 mJ/cm^2), we expect singlet-singlet

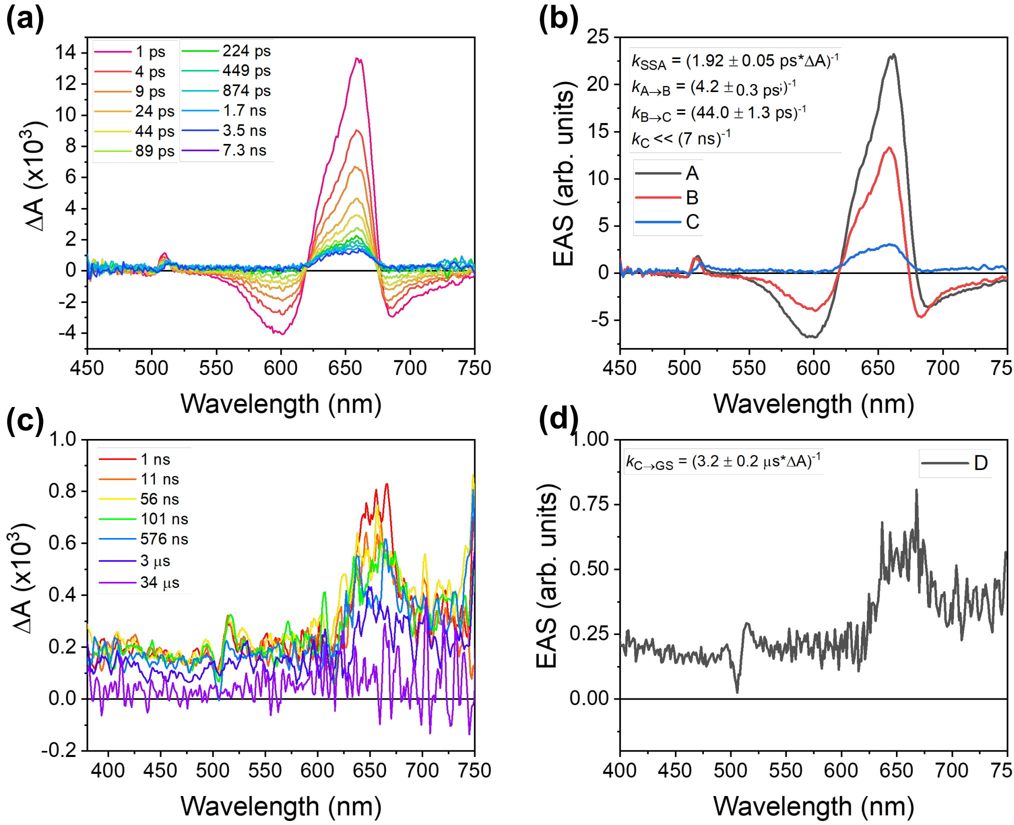

Figure 34. FsTA (a, b) and nsTA (c, d) data of **B-189** film spin-coated in toluene excited at 780 nm: (a, c) raw data, (b, d) evolution associated spectra.

annihilation (SSA) to occur, which we fit to a second-order rate constant (k_{SSA}). Like the solution data, upon excitation at 780 nm, the **B-189** film shows population of the singlet excited state, state A. State A undergoes some structural relaxation to state B in τ = 4.2 ± 0.3 ps. Surprisingly, state B undergoes a rapid τ = 44 ± 1 ps transition to state C, which appears to be the long-lived triplet state due to the disappearance of the GSB and red-shifting of the primary excited state absorption to 660 nm. Thus, triplet formation occurs two orders of magnitude faster in the film than in solution. This striking difference in triplet formation rates suggests that the mechanism of triplet formation could be aggregation-induced SO-ISC.[151-152, 157-158] The film nsTA data shown in Figure 34c,d show the triplet absorption at 660 nm has a lifetime of over 3 μs. Quality of kinetic fits for these models are shown in Figure D4. The triplet quantum yield in the **B-189** film was found to be 8.3 ± 2.2% using spectral deconvolution (shown in Figure D7) of fsTA data shown in Figure 34. This value represents a lower-bound calculation because the fsTA data are impacted by SSA which will quench the number of excited singlet excitons that can undergo SO-ISC. Given the low triplet yield, there are clearly other kinetic parameters competing with SO-ISC.

Time resolved fluorescence spectroscopy

In order to understand the effect of any emissive states, time-resolved fluorescence (TRF) spectroscopy was performed. Figures D5 and D6 show the TRF data collected on the **B-189** thin film. In the 2 ns time window, two distinct states are apparent, shown in the EAS in Figure D5b. State A has a peak energy of 1.48 eV and is shown to decay to state B within τ ~ 60 ps, in reasonable agreement with the ISC time observed by TA (state B → C in TA data). Notably, the instrument response function in this TRF time window is ca. ~60 ps and so this transition may indeed be faster. Since the film fsTA data show the SO-ISC transition occurs with a time constant of τ = 44 ± 1 ps, the TRF data suggest that this emissive state may arise from a subpopulation that does not undergo SO-ISC and instead undergoes structural relaxation to a different state B, which then relaxes back to the ground state with a lifetime of τ = 460 ± 60 ps. This ground state recovery is corroborated by the TRF data from the 5 ns window which show one state which fluoresces with a lifetime of τ = 450 ± 150 ps. Overall, the TRF data show there are no spectrally unique emissive intermediate trap states but do show that fluorescence is competing with SO-ISC, despite the low quantum yield found in the film.

Energetics of dilute and aggregated B-189

The energetics from gas-phase time-dependent density functional theory (TD-DFT) calculations and experimental steady-state spectroscopic data are shown in Figure 35. As shown by the crystal packing in Figure 29 and red-shifting in the film steady-state absorption data in Figure 32, **B-189** molecules cluster into *J*-like aggregates in the solid state, which results in energy level splitting and lowering of the lowest optically allowed absorption transition,[158, 181] hence explaining the S_1 energy level decrease from solution to film. The energy level density is represented by the gray gradients in Figure 35a,c, indicating that as energy levels split, triplet energy levels may become more readily accessible to electrons in an S_n state due to the close

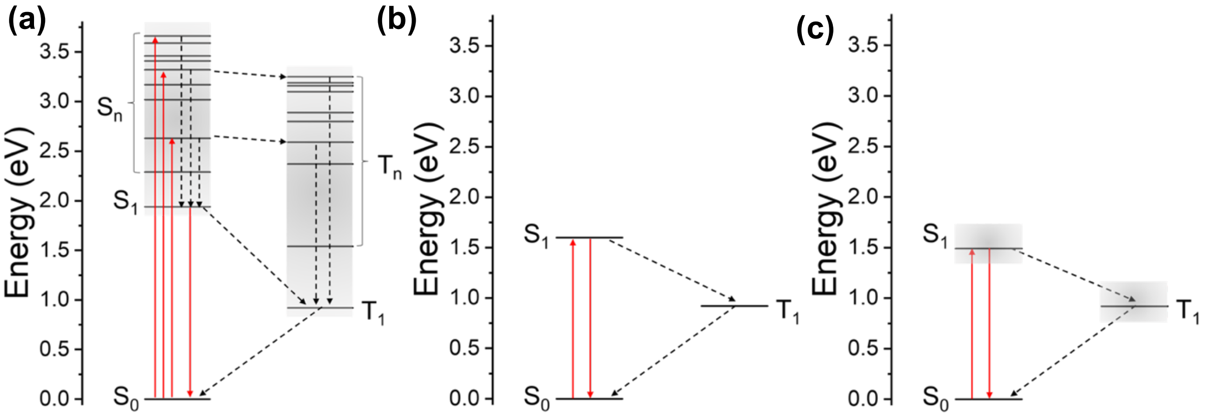

Figure 35. Energy diagrams for **B-189** showing singlet and triplet* energy levels (a) calculated from TD-DFT in gas phase; (b) determined from experiments in solution; (c) determined from experiments in thin films. Solid lines indicate photoexcitation or luminescence while dashed lines indicate non-radiative transitions.
*triplet energy level *only* found using TD-DFT

proximity of many S_n and T_n energy levels, allowing for rapid SO-ISC followed by rapid internal conversion (IC) from $T_n \rightarrow T_1$ before undergoing ISC back to the ground state. This results in a large density of triplet states, which will increase the rate of SO-ISC per eq. 4.2 and is illustrated in Figure 35a. The spin-vibronic mechanism for ISC could also be relevant in this case,[196] as Figure 35a illustrates nearly degenerate S_n and T_n energy levels, which could facilitate rapid ISC in the weak coupling limit.

In addition to energy level splitting, steric effects introduced when molecules are aggregated in the solid state can also influence the photophysics. In Figure 29, it is evident that the acetyl and phenyl functional groups are sterically hindered in the crystal structure. Vibrations and energy fluctuations in the molecule induce IC to the ground state. Steric hindrance of some of those vibrations may slow IC and allow SO-ISC to be enhanced. From the quantum yield values calculated, IC still clearly dominates per eq. 4.1: $1 - \Phi_F - \Phi_{ISC} = \Phi_{IC} \cong 0.91$. The change in rates allowing SO-ISC to compete still aligns with eq. 4.1 given the overall observed rate constant (τ_{obs}) would speed up if the rate at which k_{IC} (rate of internal conversion) increased slowed compared to the rate at which k_{ISC} (rate of SO-ISC) increased:

$$\tau_{obs} = (k_F + k_{ISC} + k_{IC})^{-1} \tag{4.3}$$

This effect of aggregation modulating the decay pathways available in the monomer is well known to occur in organic chromophores.[39, 44, 151-152, 154, 182] Aggregation also appears to affect the triplet state lifetime and rate of triplet-triplet annihilation (TTA). In solution, the triplet has a lifetime of almost 100 μs while in the film it is an order of magnitude shorter. This can most likely be attributed to aggregation and the shorter diffusion distance required for TTA to occur in the solid state versus solution. The polycrystalline nature of the films suggests that triplet diffusion and TTA will be determined by the crystalline domain sizes.[174-175]

One mechanism for enhancing k_{ISC} and Φ_{ISC} in this molecule would be via metalation because heavy metal atoms induce SO-ISC.[159] Metalated **B-189** would allow further exploitation of the AI-ISC phenomenon and make this molecule as well as similar substituents more suitable for a variety of applications requiring higher Φ_{ISC} values.

CONCLUSIONS

We studied the photophysics of a unique tetrapyrrole, **B-189**, in both solution and the solid state. With an enhanced understanding of the crystal structure and solid state packing in thin films, we can conclude that aggregation of these molecules induces rapid SO-ISC. Exploiting deep-red absorbing molecules with rapid SO-ISC is appealing for a variety of aforementioned applications. Metalating these molecules offers an additional way to modulate their photophysics and open new doors for photocatalysts and light harvesting applications.

Attributions:

- Carolyn E. Ramírez: film fabrication, steady-state film spectroscopy, non-linear spectroscopy data analysis, X-ray data acquisition and analysis, TRF data analysis, analysis of crystal structure characteristics, triplet yield calculations, TD-DFT calculations, made figures, wrote manuscript
- Vy-Phuong Tran: synthesized compound, grew crystal, solved crystal structure
- Nobuyuki Matsumoto: originally synthesized compound
- Paige J. Brown: TRF spectroscopy data acquisition
- Ryan M. Young: high fluence fsTA/nsTA data acquisition, discussion, manuscript revisions and content
- Jonathan S. Lindsey: funding and support for synthesis, discussion, coordination
- Michael R. Wasielewski: funding, oversight, manuscript revisions and content

Chapter 5: The Saga of Triplet Transfer in Films of Perylene Diimide

Carolyn E. Ramírez, Ryan M. Young, Michael R. Wasielewski

ABSTRACT

The goal of this project was to show the fundamental mechanism of triplet energy transfer of a singlet-fission born triplet exciton from the singlet-fission material, perylene diimide, to a triplet-accepting material in the solid-state in order to be one step closer to understanding the fundamental mechanisms of energy transfer in singlet-fission organic photovoltaics. Using transient absorption spectroscopy on bilayer and blend films, I attempted to visualize the singlet-fission born triplet transfer from PDI into a red-absorbing electron donor (triplet acceptor). I examined several different systems and saw qualitative but not quantitative evidence of this phenomenon.

INTRODUCTION

To realize singlet fission (SF) in organic photovoltaics, it is first important to understand how triplet energy is transferred in the solid-state and ensure that SF-born triplets are transferred faster than singlet excitons. Ample work has been done to understand singlet fission using monomers in solution and film[40, 44, 49-50, 70] and dimers or oligomers in solution,[15, 41, 45, 47-48, 197-198] but few studies have shown how triplet excitons transfer to an acceptor molecule in the solid-state through either a bilayer or bulk heterojunction architecture.[199]

Förster energy transfer. Key to understanding triplet energy transfer is the difference by which singlets and triplets exchange energy and diffuse. Singlets move via Förster resonance energy transfer (FRET), which is a form of coulombic non-radiative energy transfer via long-distance dipolar interactions between an excited and ground state molecule.[10] Typically, exciton diffusion coefficients of singlets are a few orders of magnitude higher than those of triplets in films due to defects and distances between molecules.[200] FRET is a competitor for SF, especially in films, where intermolecular distances are much shorter than in solution.[200]

Dexter energy transfer. Triplets move by directly transferring electrons between molecules. Triplets cannot exchange energy through FRET because this would involve a spin-forbidden transition of one triplet back to the ground state.[10, 201] Dexter transfer is typically short range (5-10 Å) and leads to smaller diffusion coefficients in the solid state.

Solid-state triplet transfer. A few studies have been published that successfully prove transfer of triplet excitons. In an effort to combine SF molecules with inorganic semiconductors, PbSe nanocrystals (NCs) have been shown to interface well with pentacene in a bilayer structure. The band gap (ΔE_g) of PbSe NCs is close to the triplet energy of pentacene in order to ensure efficient energy transfer, and the donor layer is thin (5 nm) to minimize diffusion losses.[202] An additional study shows successful photon down-conversion via triplet transfer from TIPS-tetracene ligands to PbS quantum dots (QD) where triplet excitons radiatively recombine within the QD to be absorbed by an additional semiconductor such as silicon.[203] Tetracene has also been shown to successfully transfer triplets to copper phthalocyanine in a bilayer film architecture because of resonant triplet energies.[204] Finally, a recent study shows triplet sensitization of silicon by tetracene using hafnium oxynitride as an interlayer to facilitate energy transfer.[7]

Table 2. Attempted triplet donor and acceptor molecules[39, 43, 45, 47, 49, 70, 96, 162, 186, 205-206]

Molecule	E(S_1) (eV)	E(T_1) (eV)
PDI	**2.2 (exp)**	**1.2 (exp)**
TDI	**1.83 (exp)**	**0.77 (exp)**
QDI	**1.6 (exp)**	**0.63 (calc’d)**
PdPc(OBu)$_8$	**1.7 (exp)**	**1.12 (exp)**
***t*-Bu-ZnNc**	**1.70 (exp)**	**0.98 (exp)**

Because all of these studies use polyacene SF chromophores, it is important to extend this study to rylene diimides. Proving triplet transfer in rylene diimide films will support the molecules' viability for use in OPV active layers.

EXPERIMENTAL METHODS

(Most experimental methods are explained in the Introduction.)

Film fabrication. Each compound was studied independently in a film made by either spin-coating or vacuum evaporating material onto a clean sapphire substrate (sonicated in water, methanol/isopropanol, and acetone; dried with N_2). I looked at a variety of systems as shown in Table 2. PDI was vacuum evaporated; TDI, QDI, and $PdPc(OBu)_8$ were spin-coated in $CHCl_3$ or CH_2Cl_2. Bilayers were made by then vacuum depositing the second layer.

RESULTS & DISCUSSION

PDI-PhEt/QDI-C_{15} films

PDI/QDI bilayer films were made in which a PDI derivative with phenethyl tails at the imide positions (PDI-PhEt), made by J. Alzola, was used as the SF triplet donor and QDI with C_{15} swallow tails, synthesized by M. Chen, was used as the triplet acceptor. The thickness of each layer was about 100 nm.

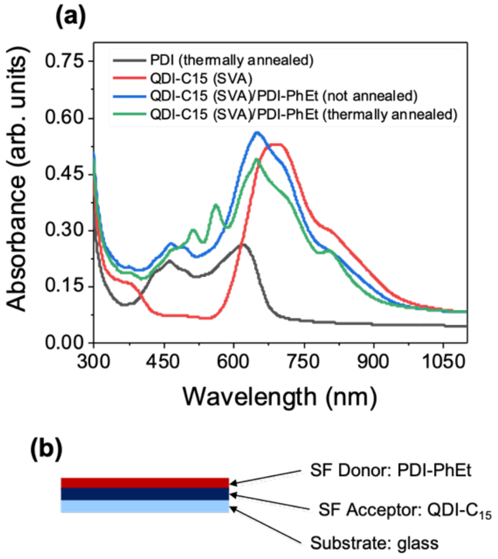

Figure 36. (a) UV-vis of QDI-C15/PDI-PhEt bilayer film components; (b) diagram of bilayer film

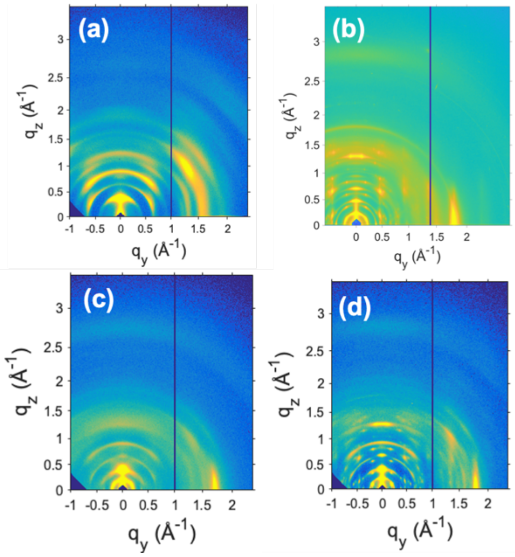

Figure 37. (a) PDI-PhEt thermally annealed; (b) QDI-C$_{15}$ thermally annealed; (c) QDI-C$_{15}$ SVA/ PDI-PhEt not annealed; (d) QDI-C$_{15}$ SVA/PDI-PhEt thermally annealed; incident angle (θ) = 0.140º in all spectra

Structural analysis. GIWAXS data were collected beginning with thermally annealed PDI-PhEt shown in Figure 37a. This film appears to be generally ordered with a strong edge-on π-π stacking peak near 1.6 Å^{-1} (3.9 Å) along the q_{xy} axis and additional larger *d*-spacing features along the q_z axis which indicate ordered spacing normal to the surface of the substrate. Figure 37b shows a thermally annealed film of QDI-C$_{15}$ with strong edge-on π-π stacking (q_{xy} =1.8 Å^{-1}). Fig. 37c shows spectra of a QDI-C$_{15}$ (SVA)/PDI-PhEt (unannealed) bilayer film. There is evidence of an edge-on π-π stacking peak at q_{xy} = 1.6 Å^{-1} and 1.8 Å^{-1} as expected from both PDI-PhEt and QDI-C$_{15}$. Fig. 37d shows spectra of a thermally annealed QDI-C$_{15}$ (SVA)/PDI-PhEt film showing clear diffraction peaks at large *d*-spacing values corresponding to QDI-C$_{15}$ with intense peaks at q_{xy} = 1.8 Å^{-1} and q_z = 1.2 Å^{-1} indicating enhanced crystallinity of QDI-C$_{15}$ from thermal annealing.

Transient absorption spectroscopy. FsTA data are shown in Figures 38-39. PDI-PhEt undergoes SF in 130 ps to form triplet,[49] and QDI-C$_{15}$ forms triplet via SF in 92 ps.[43] FsTA spectra

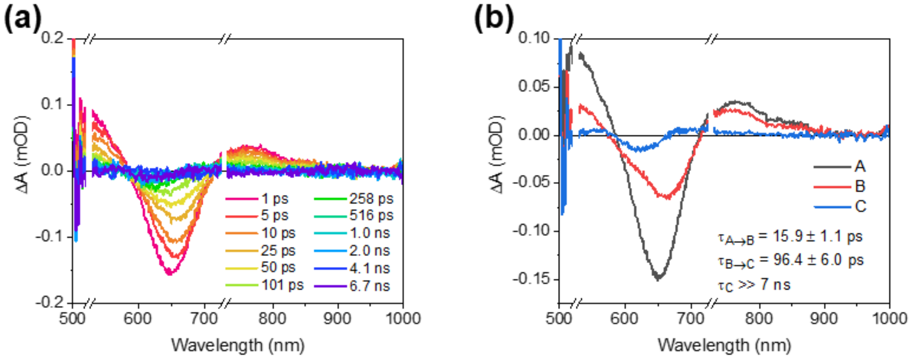

Figure 38. QDI-C$_{15}$/PDI-PhEt (not annealed) fsTA (λ_{ex} = 526 nm): (a) time evolved raw spectra, (b) kinetic model

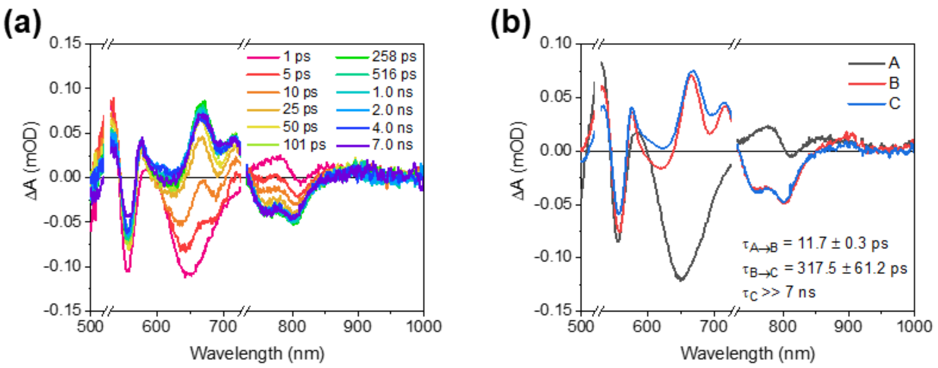

Figure 39. QDI-C_{15}/PDI-PhEt (thermally annealed) fsTA (λ_{ex} = 526 nm): (a) time evolved raw spectra, (b) kinetic model

of the QDI-C_{15} (SVA)/PDI-PhEt (not annealed) film (Figure 38) show that states A and B pertain to only the PDI-PhEt singlet excited state with absorptive features at 520, 760, and 850 nm. State C forms in 96 ps and shows PDI-PhEt and QDI-C_{15} triplet at 550 and 675 nm, respectively. No evidence of QDI-C_{15} singlet suggests Dexter transfer has occurred. Upon thermally annealing the PDI-PhEt layer, fsTA spectra of the QDI-C_{15}/PDI-PhEt film appear very different (Figure 39). The PDI-PhEt singlet peak at 780 nm is replaced by the QDI-C_{15} GSB, indicating Förster transfer from PDI-PhEt. While PDI-PhEt and QDI-C_{15} triplet still form, Förster transfer evident in state B has contaminated any potential triplet transfer. Thermal annealing likely caused intercalation of both layers, leading to undesired FRET.

PDI-PhEt/Pc(OBu)$_8$ films

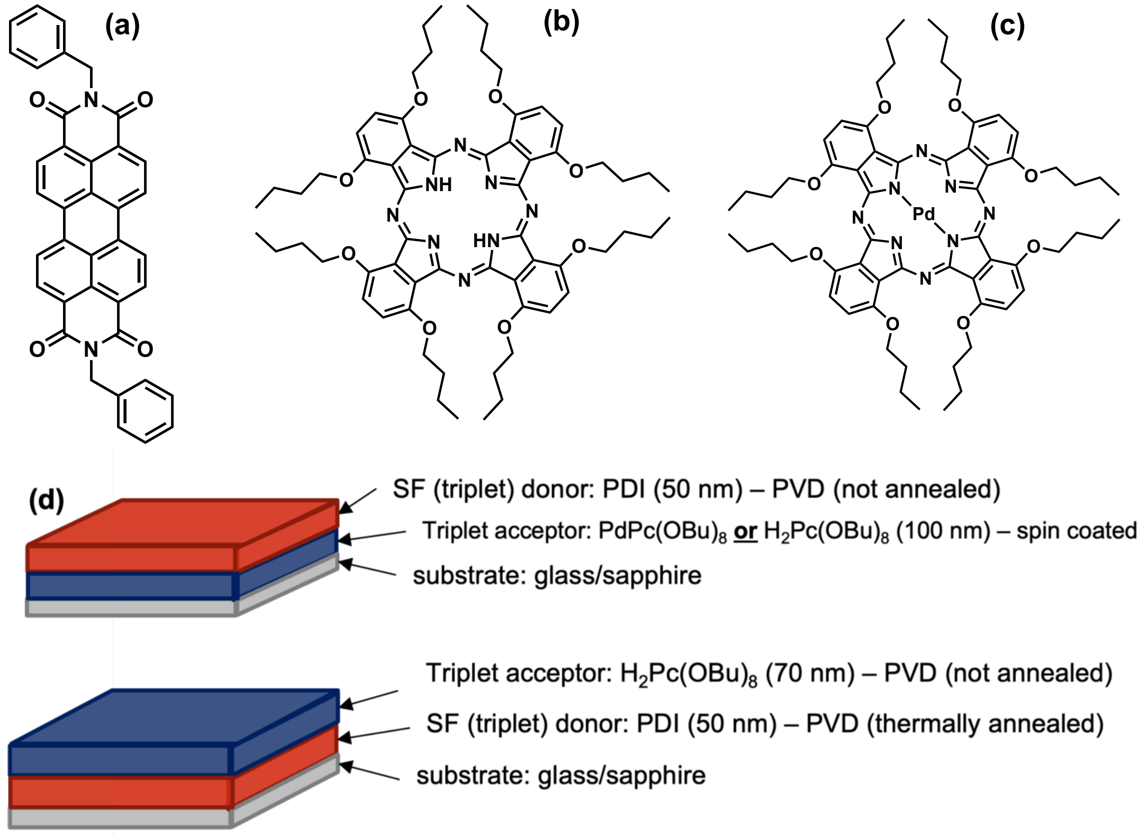
(a)
(b)
(c)
(d)
SF (triplet) donor: PDI (50 nm) – PVD (not annealed)
Triplet acceptor: PdPc(OBu)$_8$ **or** H$_2$Pc(OBu)$_8$ (100 nm) – spin coated
substrate: glass/sapphire
Triplet acceptor: H$_2$Pc(OBu)$_8$ (70 nm) – PVD (not annealed)
SF (triplet) donor: PDI (50 nm) – PVD (thermally annealed)
substrate: glass/sapphire

Figure 40. (a) PDI-PhEt (triplet donor, singlet fission chromophore), (b) H$_2$Pc(OBu)$_8$ (triplet acceptor candidate), (c) PdPc(OBu)$_8$ (triplet acceptor candidate), (d) schematics of bilayer film

Because Pc(OBu)$_8$ is commonly used as a triplet sensitizer in solution and because its triplet features are much redder compared to PDI, I examined these two molecules as interesting triplet accepting candidates. The molecules studied and the film architectures employed are shown in Figure 40.

Steady-state absorption spectroscopy. As shown in Figure 41, the PDI-PhEt and PdPc(OBu)$_8$ absorptive profiles overlap slightly, but the PDI-PhEt could be singly excited between 520-560 nm without exciting the PdPc(OBu)$_8$. PDI-PhEt exhibits Q-band absorption between 400-700 nm. PdPc(OBu)$_8$ shows Q-band absorption between 610-810 nm. Figure 41b shows that over time, the PdPc(OBu)$_8$ degrades via oxidation of the butoxy groups. The degradation is undesirable for repeated photophysical experiments, X-ray measurements in air, and other experiments, but I proceeded with transient absorption measurements to fully evaluate.

Transient absorption spectroscopy. FsTA spectroscopy was performed on the high fluence, low repetition rate laser system in order to access NIR wavelengths. Figure 42 shows the fsTA spectra of the neat PdPc(OBu)$_8$ film excited at 745 nm. The initially populated singlet excited state undergoes spin-orbit intersystem crossing (SO-ISC) to form the long-lived triplet state quantitatively in about a nanosecond. The singlet excited state absorptive features are at 500, 550, 990, and 1070 nm. The triplet absorptive peaks are 600, 645, 660, and 730 nm.

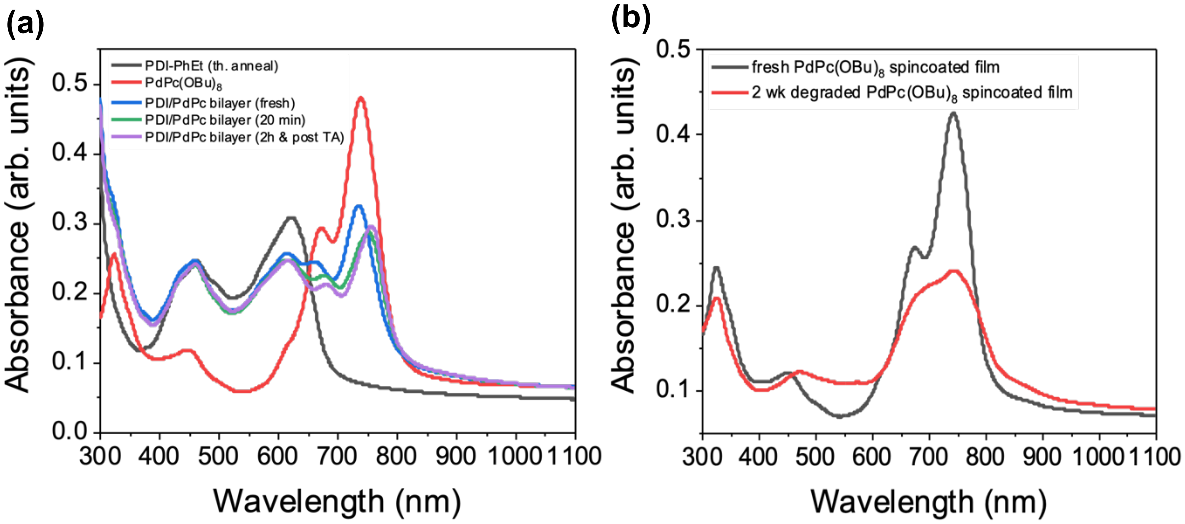

Figure 41. UV-vis absorption of PDI-PhEt and PdPc(OBu)$_8$ bilayer neat and bilayer films showing minor degradation (oxidation) of the PdPc(OBu)$_8$ layer over (a) a few hours and (b) a few weeks.

The fsTA data for the PDI-PhEt/PdPc(OBu)$_8$ film, shown in Figure 43, began with an excitation wavelength of 545 nm with the intention of only exciting the PDI-PhEt layer so that if triplets form and diffuse to the interface, they will transfer to the PdPc(OBu)$_8$ layer where we would see at later kinetic transitions signature peaks of the PdPc(OBu)$_8$ triplet but not the singlet. The notable PDI-PhEt features for the singlet are 520, 900, 110, and 1200 nm. The notable PDI-

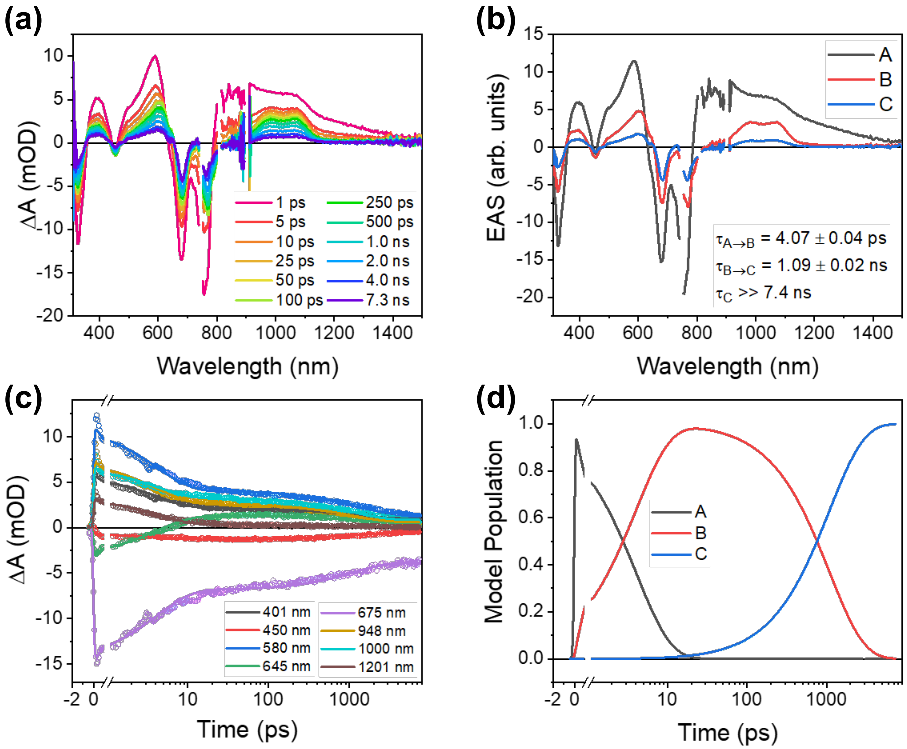

Figure 42. fsTA spectroscopy of neat PdPc(OBu)$_8$ film excited at 745 nm: (a) raw spectra; (b) evolution associated spectra; (c) quality of global kinetic fit at fitting wavelengths; (d) evolution of populations over temporal range of experiment.

PhEt triplet absorptive features are 525, 550, and 700 nm. Singlet fission happens in 130 ps in the PDI-PhEt whereupon the triplet absorptive features would be dominant. From the bilayer data, we initially see the PDI-PhEt excited state singlet absorption (states A and B). Unfortunately, state C shows clear singlet transfer from PDI-PhEt to PdPc(OBu)$_8$ from the NIR singlet feature. However, there is evidence of some small amount of triplet transfer because all the PDI-PhEt triplets are gone in <700 ps indicating they likely transferred into PdPc(OBu)$_8$. We see the PdPc(OBu)$_8$ triplet features at 645, 660, and 730 nm begin to appear in state C (after 20 ps) and more strongly in state D (after 688 ps). Considering the SO-ISC takes 1.09 ± 0.02 ns in the neat PdPc(OBu)$_8$ film, the time scale of PdPc(OBu)$_8$ formation in the bilayer film suggests that some of that triplet might result from TET from the PDI-PhEt layer.

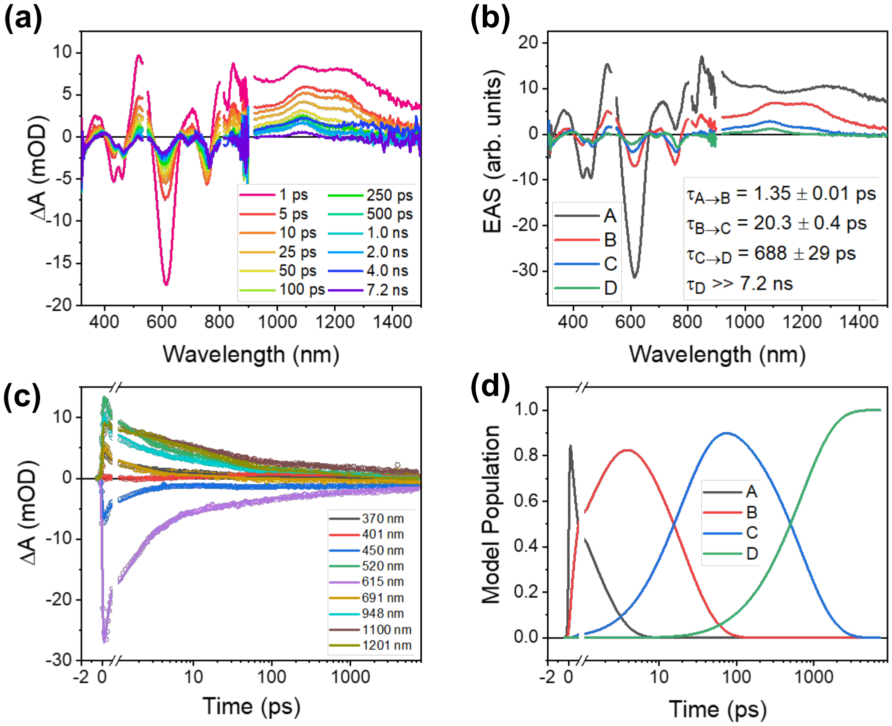

Figure 43. fsTA spectroscopy of PDI-PhEt/PdPc(OBu)$_8$ bilayer film excited at 540 nm: (a) raw spectra; (b) evolution associated spectra; (c) quality of global kinetic fit at fitting wavelengths; (d) evolution of populations over temporal range of experiment.

Overall, this bilayer system showed promise, but the degradation of the PdPc(OBu)$_8$ layer combined with the rapid Forster transfer prevented quantitative analysis of TET, which is critical for a champion donor-acceptor pairing. After studying PdPc(OBu)$_8$, I moved on to a more stable, deep-red absorbing molecule.

PDI-PhEt/*t*-Bu-ZnNc films

While PDI-PhEt remained a robust SF candidate, I needed to find a similarly robust triplet accepting (electron donating) molecule. The optoelectronic properties are discussed in detail in Chapter 3, but briefly: *t*-Bu-ZnNc shows anti-Kasha S_2 emission and rapid SO-ISC in the solid-state upon aggregation and immobilization of the *t*-Bu end groups. While the rate of triplet formation in the *t*-Bu-ZnNc films is enhanced compared to solution, due to the other favorable properties namely the photo/air-stability, lack of absorbance overlap with PDI-PhEt, this system was worth a try. From my studies in Chapter 3, I also learned that the unannealed *t*-Bu-ZnNc shows low triplet yield, favoring TET as the mechanism of potentially higher triplet yield.

Steady-state absorption spectroscopy. The steady-state absorption data are shown in Figure 44. PDI-PhEt vibronic characteristics were discussed in the previous sections and *t*-Bu-ZnNc vibronic character was discussed in great detail in Chapter 3. While the absorption profiles overlap, the PDI-PhEt can be singly excited at 560 nm.

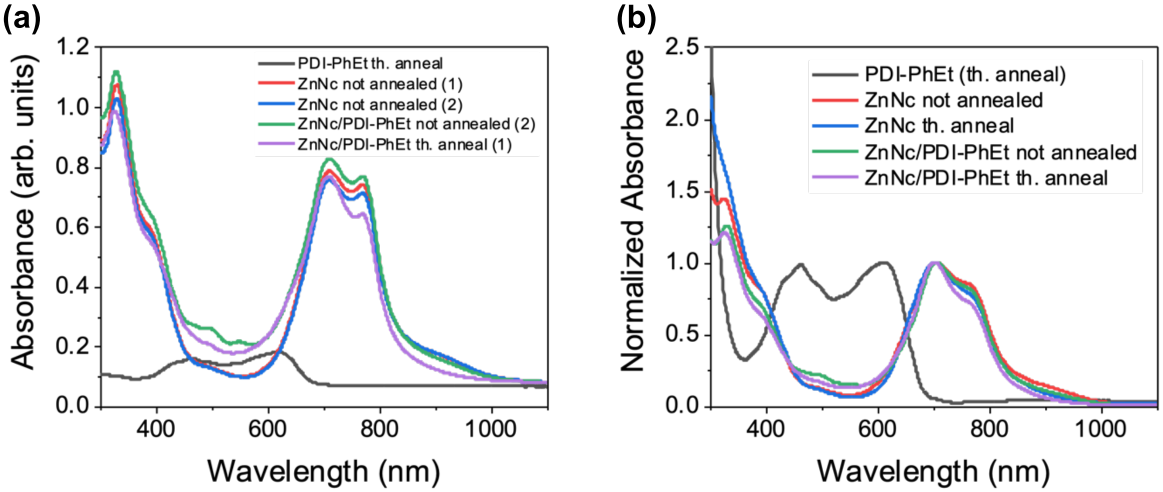

Figure 44. Steady-state absorbance of PDI-PhEt and *t*-Bu-ZnNc neat and bilayer films (a) y-axis showing film optical density and (b) y-axis showing normalized absorption.

Structural analysis. To understand how the molecules pack on top of each other, I conducted GIWAXS at various X-ray incident angles on the bilayer samples. The layer interfacing with the substrate is the spin-coated *t*-Bu-ZnNc layer, so larger angles (th = 0.160) would probe that layer and more of the interface between *t*-Bu-ZnNc and PDI-PhEt. Because the PDI-PhEt layer is vacuum deposited on top of the *t*-Bu-ZnNc layer, the smaller incident angle (th = 0.080) would probe this layer and how it packs on the *t*-Bu-ZnNc layer. In the unannealed bilayer film, the PDI-PhEt layer (shown in Figure 45a) is rather amorphous but shows a broad π-π stacking peak on both the q_{xy} and q_z axes around 1.5 Å^{-1}. Figure 45b shows the *t*-Bu-ZnNc layer spectra with a faint π-π stacking peak near 1.5 Å^{-1} on the q_{xy} axis. This is likely from the PDI-PhEt layer. In the thermally annealed bilayer shown in Figure 45c-d, we expect some intercalation of the two layers due to thermal heating of the interface. As shown in Figure 45c, the annealed PDI-PhEt appears much more crystalline with a stronger π-π stacking peak near 1.5 Å^{-1} on the q_{xy} axis. The *t*-Bu-ZnNc layer and interface do not appear to be any more ordered than in the unannealed film, but the broad peak around 1.5 Å^{-1} on both the q_{xy} and q_z axes suggests some intercalation and enhanced signal of the π-π stacking in the PDI-PhEt layer. This intercalation increases the surface area of contact between the triplet donating and accepting layers which increases the possibility of both singlet energy transfer and triplet energy transfer.

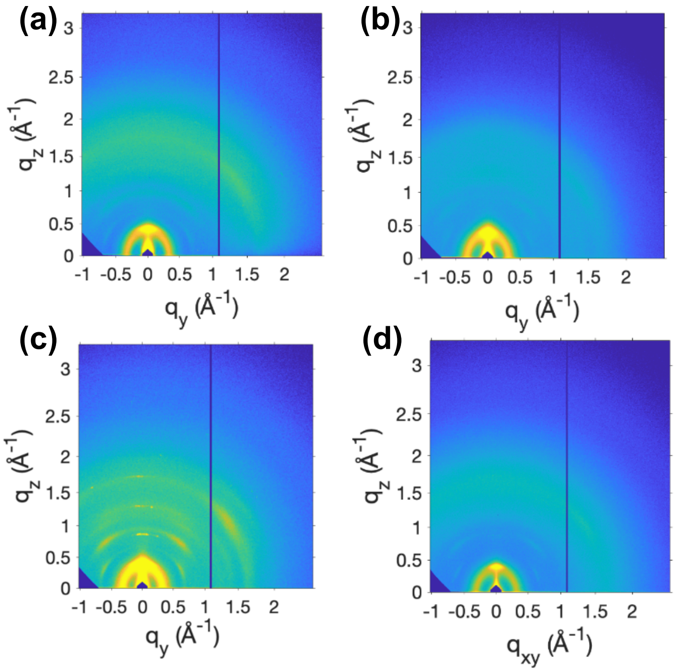

Figure 45. GIWAXS data for bilayer films of sapphire/spin-coated *t*-Bu-ZnNc/vapor-deposited PDI-PhEt: (a) unannealed film, theta = 0.080; (b) unannealed film, theta = 0.160; (c) thermally annealed film, theta = 0.080; (d) thermally annealed film, theta = 0.160.

Transient absorption spectroscopy. In order to evaluate if this bilayer system showed promise of TET, I performed fsTA on the bilayer films. Detailed fs/nsTA analysis of neat unannealed and annealed *t*-Bu-ZnNc films can be found in Chapter 3. FsTA data for the unannealed bilayer are shown in Figure 46. The film is excited at 560 nm and state A is the initially populated PDI singlet excited state. The 870 fs A → B transition is structural relaxation of the molecule remaining in the singlet excited state. The 80 ps B → C transition represents the mean of the Gaussian distribution

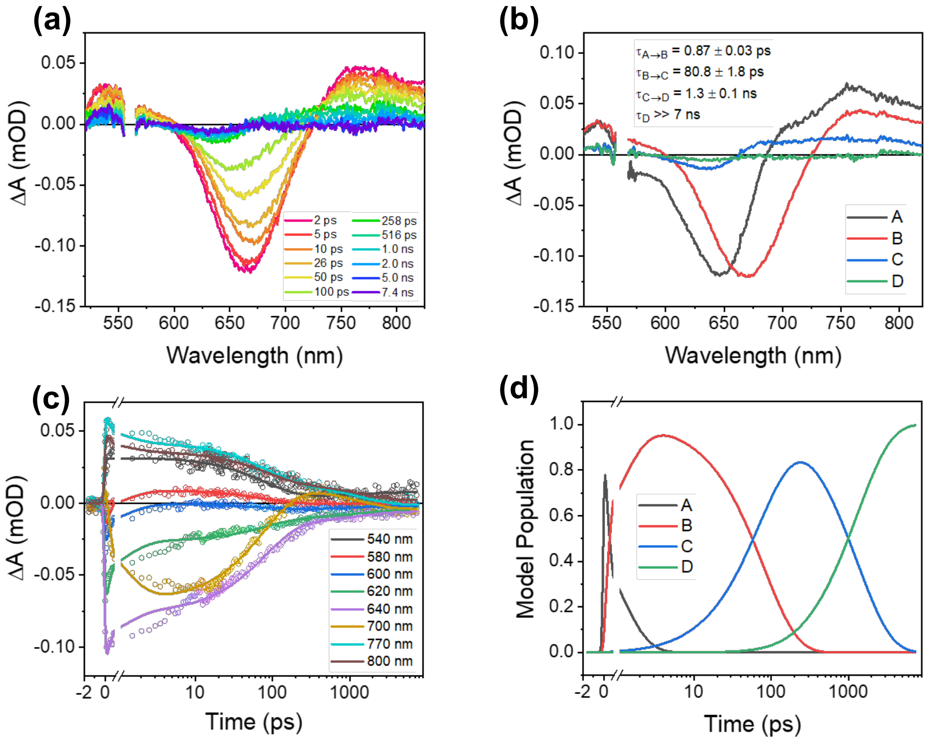

Figure 46. fsTA spectroscopy of unannealed PDI-PhEt/*t*-Bu-ZnNc bilayer film excited at 560 nm: (a) raw spectra; (b) evolution associated spectra; (c) quality of global kinetic fit at fitting wavelengths; (d) evolution of populations over temporal range of experiment.

of SF rates for the PDI-PhEt molecules. This film is not annealed, so there is extreme heterogeneity and a range of populations undergoing photophysical processes at different times. The 1.3 ns C →D transition is potentially energy transfer to *t*-Bu-ZnNc, but likely not triplet transfer because there is no evidence of the 600 nm triplet feature. The annealed film fsTA data are shown in Figure 47. The film appears to be slightly less heterogeneous with fewer states required for global fitting. The 2 ps A → B transition is still attributed to structural relaxation of the singlet excited state while the 44 ps B → C transition indicates some rapid SF happening in the PDI-PhEt layer. There is no evidence of *t*-Bu-ZnNc triplet (600 nm characteristic feature).[162] Overall, this system is unfortunately not compatible for TET.

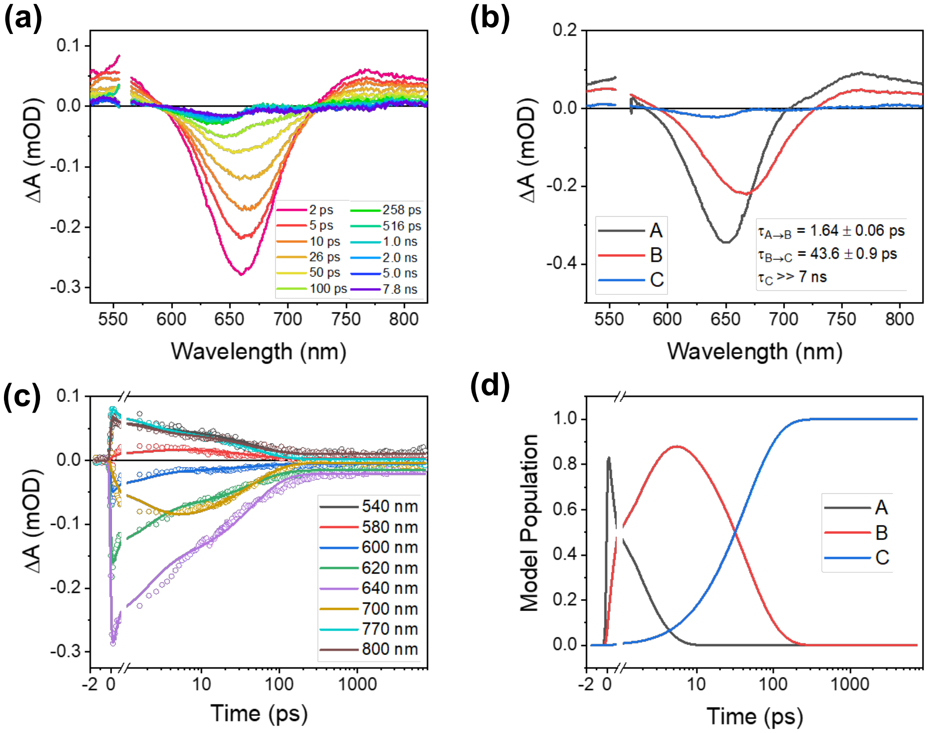

Figure 47. fsTA spectroscopy of thermally annealed PDI-PhEt/*t*-Bu-ZnNc bilayer film excited at 540 nm: (a) raw spectra; (b) evolution associated spectra; (c) quality of global kinetic fit at fitting wavelengths; (d) evolution of populations over temporal range of experiment.

Ph$_4$-C$_8$-PDI/*t*-Bu-ZnNc films

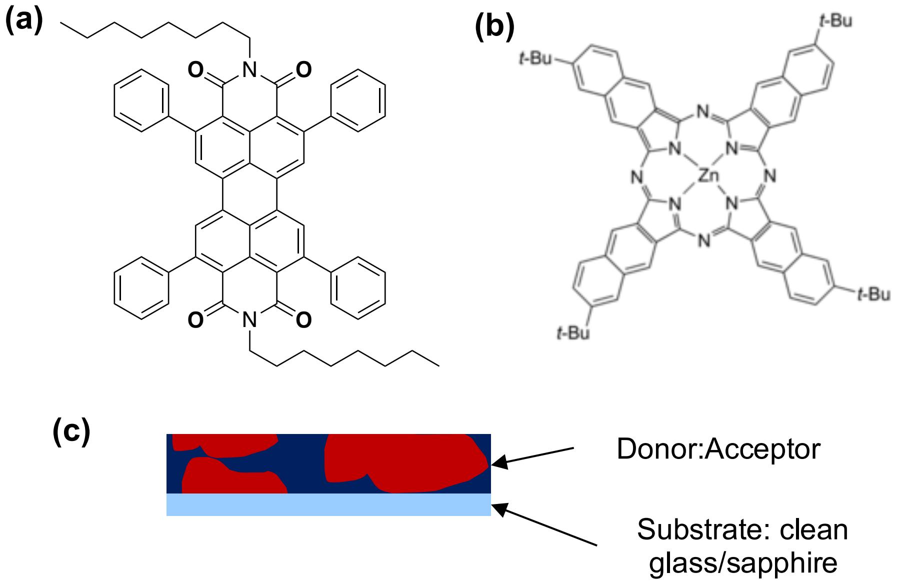
(a)
O
N
O
O
N
O
(b)
t-Bu
t-Bu
N
N
N
Zn
N
N
N
N
N
t-Bu
t-Bu
(c)
Donor:Acceptor
Substrate: clean glass/sapphire

Figure 48. (a) Ph$_4$-C$_8$-PDI (triplet donor, singlet fission chromophore), (b) *t*-Bu-ZnNc (triplet acceptor candidate), (c) bulk heterojunction blend film architecture

In order to further investigate *t*-Bu-ZnNc as a triplet accepting molecule, I studied a different SF chromophore, Ph$_4$-C$_8$-PDI, which our group has found to undergo SF within 180 ps.[44] I employed a different fabrication strategy following the lack of *t*-Bu-ZnNc signal in the previous bilayer film with PDI-PhEt. For this system, I made a series of blend bulk heterojunction (BHJ) films with varying ratios of Ph$_4$-C$_8$-PDI:*t*-Bu-ZnNc (by weight 1:1, 5:1, 8:1). Both compounds

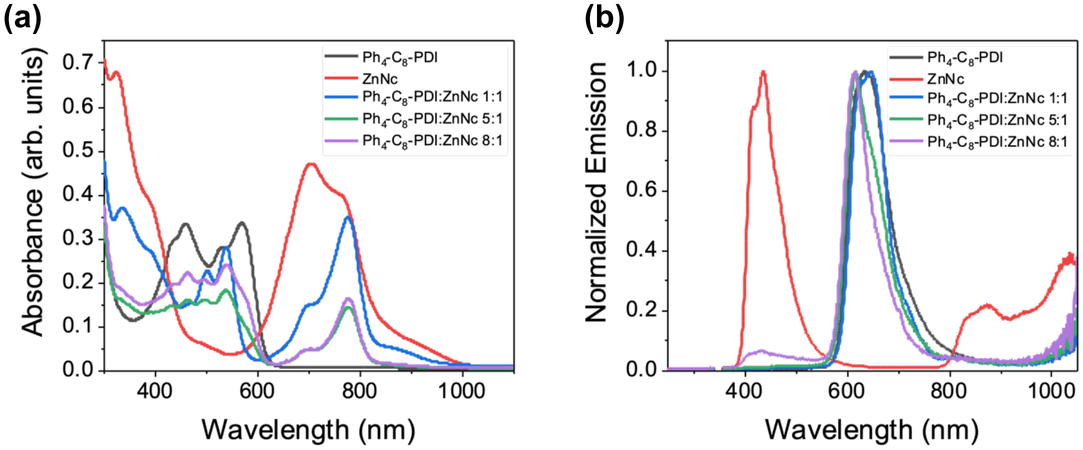

Figure 49. Steady-state (a) absorbance and (b) emission of Ph$_4$-C$_8$-PDI and *t*-Bu-ZnNc neat and bilayer films.

were co-dissolved in DCM and spin-coated on clean sapphire. The molecules involved and the BHJ structure are shown in Figure 48. The hypothesis was that by increasing surface area of contact, hopefully some triplet excitons could transfer from the SF chromophore to the *t*-Bu-ZnNc. Ph_4-C_8-PDI has an $E(S_1)$ = 2.07 eV, $E(T_1)$ = 1.19 eV, and a rate of singlet fission of 180 ± 10 ps.[37] The triplet accepting molecule, *t*-Bu-ZnNc has an $E(S_1)$ = 1.70 eV and $E(T_1)$ = 0.98 eV.

The steady-state absorption and emission data shown in Figure 49 show the neat and blend film spectra. The neat films show little overlap so that the Ph_4-C_8-PDI can be singly excited. The blend films show decreasing absorption of the *t*-Bu-ZnNc features between 650-850 nm as the Ph_4-C_8-PDI:*t*-Bu-ZnNc ratio increases. Notably the blend films show a dramatic change in the vibronic character of both the Ph_4-C_8-PDI and *t*-Bu-ZnNc spectra indicating the formation of electron donor-acceptor aggregates producing the reduced and oxidized spectra respectively. Seeing this interaction in only the steady-state absorption with just a white-light probe raises a possible problem for seeing TET in fsTA. The emission spectra shown in Figure 49b show that the blend films possess mostly PDI emissive species with minimal S_2 emission from the *t*-Bu-ZnNc.

Transient absorption spectroscopy. To evaluate how well this pairing shows quantitative TET, fsTA spectroscopy was performed. FsTA spectra of the neat Ph_4-C_8-PDI film are shown in Figure 50. This molecule undergoes SF in this film in 165.5 ± 3.1 ps. The singlet excited state absorptive

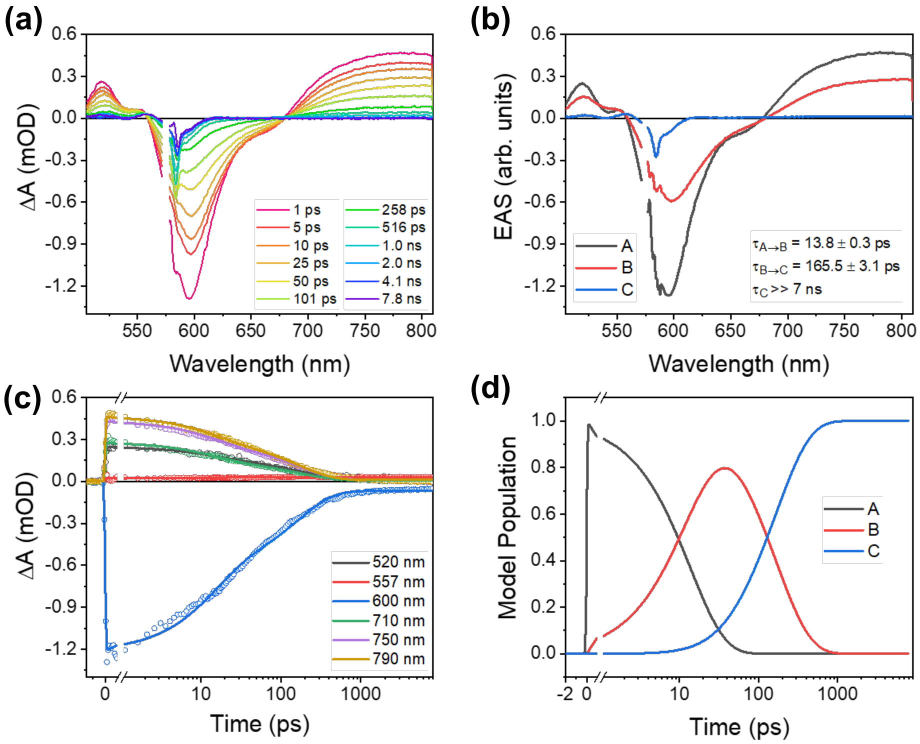

Figure 50. fsTA spectroscopy of neat Ph_4-C_8-PDI film excited at 574 nm: (a) raw spectra; (b) evolution associated spectra; (c) quality of global kinetic fit at fitting wavelengths; (d) evolution of populations over temporal range of experiment.

features appear at 530, 560, and >675 nm. The triplet absorptive features appear at 565 and 625 nm. FsTA spectra for the 1:1 Ph_4-C_8-PDI:*t*-Bu-ZnNc BHJ blend film are shown in Figure 51. Even though the Ph_4-C_8-PDI was supposed to be singly excited at 540 nm, state A appears to be the *t*-Bu-ZnNc singlet excited state. Within 12 ps, state B forms, which consists mostly of PDI anion ($PDI^{\cdot -}$) and *t*-Bu-ZnNc singlet as is evident with the red-shifting of the large absorptive peak to 700 nm. Unpictured NIR fsTA data also show formation of the *t*-Bu-ZnNc cation at 960 nm. 61 ps later, we see state C form which consists of *t*-Bu-ZnNc triplet <650 nm and $PDI^{\cdot -}$ between 700-750 nm. There is also evidence of PDI triplet growing in at 550 nm. The feature at 800 nm can be attributed to thermal effects in the *t*-Bu-ZnNc. Overall, charge transfer appears to dominate in this equal weight ratio blend film. While some triplet forms, we cannot conclude that any meaningful amount of it resulted from TET.

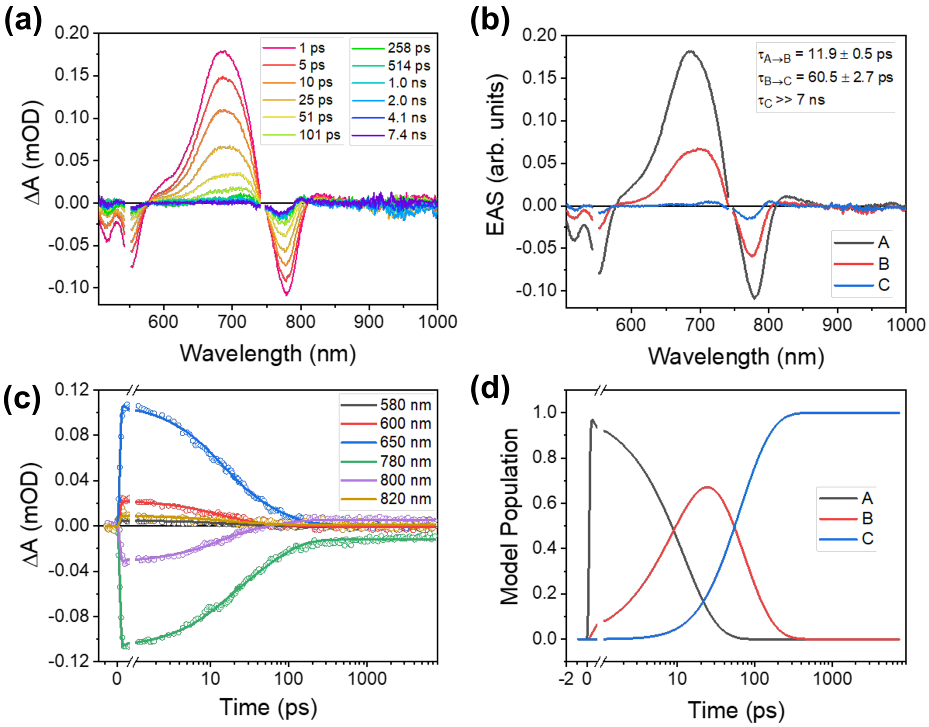

Figure 51. fsTA spectroscopy of neat 1:1 (by wt) Ph_4-C_8-PDI:*t*-Bu-ZnNc film excited at 540 nm: (a) raw spectra; (b) evolution associated spectra; (c) quality of global kinetic fit at fitting wavelengths; (d) evolution of populations over temporal range of experiment.

FsTA spectra for the 5:1 Ph_4-C_8-PDI:*t*-Bu-ZnNc BHJ blend film are shown in Figure 52. By increasing the amount of PDI in this film, I hoped to see clearer evidence of SF in the PDI and subsequent TET into the *t*-Bu-ZnNc. Upon initial excitation at 540 nm, Ph_4-C_8-PDI singlet excited state absorption is evident at 530 nm as well as some *t*-Bu-ZnNc singlet excited state at 650 nm. The system appears to undergo some rapid charge transfer as the PDI anion grows in at 700 nm, dominating in state B after 4 ps. Unpictured NIR fsTA data also shows the *t*-Bu-ZnNc cation growing in similarly within 8 ps. The long-lived state C forms after 44 ps showing character of PDI triplet at 550 nm, PDI anion, and possibly some ZnNc triplet between 600 and 650 nm. The heterogeneity of the BHJ blend film and the parallel kinetic transitions happening in the film again prevent any quantitative or mechanistic understanding of TET.

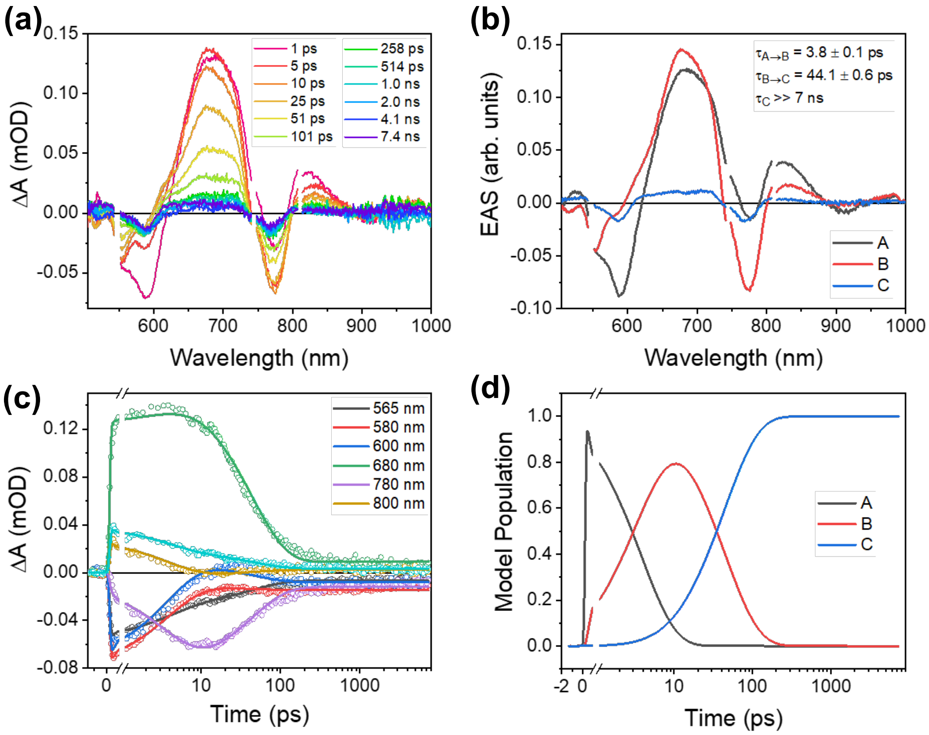

Figure 52. fsTA spectroscopy of neat 5:1 (by wt) Ph_4-C_8-PDI:*t*-Bu-ZnNc film excited at 540 nm: (a) raw spectra; (b) evolution associated spectra; (c) quality of global kinetic fit at fitting wavelengths; (d) evolution of populations over temporal range of experiment.

Finally, fsTA spectra for the 8:1 Ph_4-C_8-PDI:*t*-Bu-ZnNc BHJ blend film are shown in Figure 53. Similar to the other two films, we see charge transfer dominate early on with evidence of the PDI anion with some ZnNc singlet as well. The final kinetic transition from state C → D could possibly involve some amount of triplet transfer, but we cannot quantify it or confidently conclude the mechanism of *t*-Bu-ZnNc triplet formation. Overall, similarly to the previous systems, there is too much heterogeneity in the films with too slow of a SF rate in PDI for TET to be conclusively visible in bilayer or blend films.

CONCLUSIONS

From examining several electron donor/acceptor systems to evaluate if TET is possible from the SF chromophore, PDI, I do not think it is possible to visualize in a polycrystalline film. The

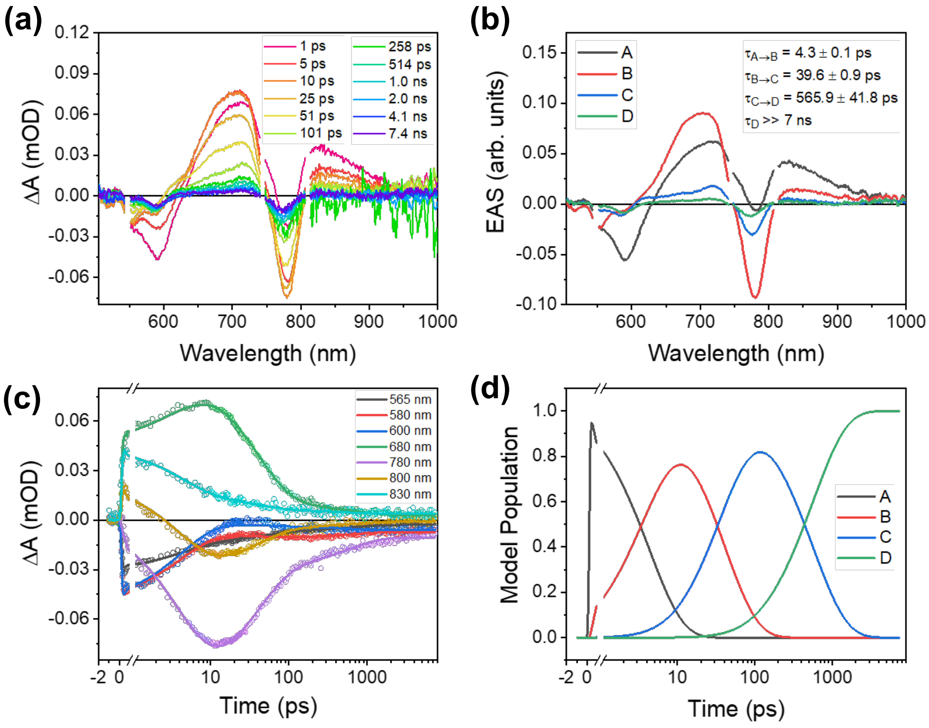

Figure 53. fsTA spectroscopy of neat 8:1 (by wt) Ph_4-C_8-PDI:*t*-Bu-ZnNc film excited at 540 nm: (a) raw spectra; (b) evolution associated spectra; (c) quality of global kinetic fit at fitting wavelengths; (d) evolution of populations over temporal range of experiment.

heterogeneity, wide distribution of kinetic rates, distribution of populations undergoing different photophysical transitions at different times, and the rapid Forster singlet energy transfer as well as charge transfer out-competing slower Dexter triplet energy transfer make this hypothesis very difficult to visualize in polycrystalline films using transient absorption spectroscopy. From my experiments, I have concluded that there is qualitative evidence of TET in a few of these systems, but I cannot find the triplet quantum yield from different mechanisms in this disordered of a system.

TET can be visualized in molecular dimers in solution as discussed in the introduction. It also could potentially be visualized in a co-crystal if charge transfer does not dominate entirely. The co-crystal order would minimize the distribution of kinetic rates and simplify the kinetic model.

This experiment is out of the scope of my work, but I hope TET can be realized in more systems to enhance our understanding of organic photovoltaics in the future.

Chapter 6: Policy Position - Without Environmental Justice, the Renewable Energy Transition Will Leave Low-Income and BIPOC Communities Behind[207]

Carolyn E. Ramírez

Published: *J. Sci. Pol. Gov.* 2021 Aug. 30, 18, 03 https://doi.org/10.38126/JSPG180306

Reproduced with permission: *Copyright 2022 © Journal of Science Policy & Governance, Inc*

EXECUTIVE SUMMARY

As extreme weather events become more common in the United States due to the worsening effects of climate change, access to utilities like electricity and water will be continually strained. Blackouts and intermittent utility interruptions impact low-income and communities of color most negatively. While renewable energy technologies promise alleviation of emissions and pollution, high cost and a lack of equitable energy infrastructure make it harder for low-income and communities of color to access renewable energy benefits. I propose a series of policies to address the cost barriers of renewable energy, improve reliability and access to power grids, and standardize household weatherization for people from all communities.

INTRODUCTION

On Sunday, February 14th, 2021, the Texas power grid failed. As a rare, but not unprecedented, winter storm rolled through the state, pipes burst, gas lines froze, lights and heaters shut off. At least 194 people died.[208] Many boil-water notices remained in place throughout the state until the end of the month, and the damage from broken water mains, flooded apartments and homes, and a lack of electricity left the region in a state of recovery as if a hurricane had just rolled through. The roads remained unusable for a week because the state had little road salt and very few plows. Even some hospitals lost power and water [209]. Additionally, several months later, many Texans are still dealing with sky-high utility bills from the week of the storm. A similar storm caused rampant blackouts in the state in 2011, but mitigation recommendations were largely ignored.[210]

While this sort of unreliable power and price gouging is incomprehensible to many Americans, it is not new to people of color or people in low-income communities. Black, Indigenous, and people of color (BIPOC) deal with larger proportionate energy bills and more frequent blackouts due to less reliable electricity.[211-212] The root of this issue is a long history of racist housing policies in the United States that led to profound disparities in the health and safety of different communities. The main lesson policymakers should take from the Texas blackouts is that **our energy grid needs urgent upgrades that center marginalized communities. Otherwise, racial disparities in energy access will continue to grow**.

Energy and environmental justice entered national and local science policy discourse over the last few decades following the advent of our modern understanding of anthropogenic climate change in the 1950s and the beginning of the environmental justice movement in the 1980s.[213-215] Modern science policy looks different than post-World War II when Vannevar Bush penned *The Endless Frontier*. Policy priorities in post-war times focused on fighting disease, increasing funding to university research, and recruiting more talented scientists.[216] These pillars are relevant today in different contexts, but Bush did not include environmental issues or racial inequities as policy concerns in 1945.

My proposed energy policy centers on environmental justice to fill in gaps from *The Endless Frontier*. **This policy is twofold: (1) reform the U.S. energy grid by focusing on improving energy infrastructure for BIPOC communities, providing government mechanisms to protect Americans from predatory utility companies, and implementing disaster-preparedness to prevent blackouts; and (2) face climate change head-on by transitioning to**

cleaner, renewable energy sources as soon as possible. Transitioning to renewable energy to address climate change without any changes to both the U.S. electric grid and utility structure will result in BIPOC communities still losing.

Racist legacies tilt climate change against BIPOC communities

The creation of the Federal Housing Administration (FHA) in 1934 federally formalized racial discrimination in loan lending for property purchase. The FHA perpetuated a policy known as "redlining" which created white-only neighborhoods because only white families could get loans from the FHA.[217] From 1934 to 1968, 98% of all loans the FHA awarded were given to white families.[218] This drastic gap in property ownership between white and Black families is a large contributor to the racial wealth gap due to differences in generational wealth. These racist housing laws also continue to impact Latino/x, Asian, and Native American families. Decreased wealth for BIPOC families combined with a historic lack of geographic mobility results in rural and suburban communities being mostly white while cities are mostly non-white.[219] Consequently, BIPOC communities are exposed to more pollution from industry and vehicle exhaust due to living in communities that border or are otherwise closer to industry and more concentrated emissions than white people.[220-221]

The resounding evidence that fossil fuel pollution and climate change disproportionately impact BIPOC communities should indicate that they have the most to gain from transitioning to renewable energy technologies and eliminating fossil fuel pollution. However, without an electric grid upgrade and changes in our utility infrastructure, renewable energy technologies like solar cells could increase the utility burden on BIPOC and low-income communities while also not remedying the lack of reliable electricity. People of color are more likely than white people to suffer from energy poverty, or inefficient utility infrastructure in their homes, which results in these households paying a larger portion of their income on utility bills.[222-223] Energy poverty has not been acknowledged by the U.S. government as a national crisis despite its consequences for BIPOC and low-income communities.[224] Renewable energy resources are expensive to install and can be intermittent energy suppliers without appropriate infrastructure, such as reliable storage and proper insulation.[225] Without implementing rigorous new energy policies at all levels of government, BIPOC communities could wind up hurting more during the renewable energy transition.

National progress on renewable energy and climate policy

With the beginning of the Biden administration in January of 2021, climate change became a central issue to American policy. On February 19th, 2021, the United States officially rejoined the Paris Agreement.[226] President Biden and Vice President Harris have a climate plan that involves making the U.S. run on 100% clean carbon-neutral energy by 2050.[227] A week into the new administration, President Biden signed a series of executive orders that centered climate change domestically and internationally, established new cabinet positions and committees focused on climate, eliminated fossil fuel subsidies, established intent to create new union jobs in clean energy, ended new oil and gas leases on public lands, and committed to center environmental justice in energy policy.[228]

Notably, President Biden has not signed onto the Green New Deal (GND), introduced to Congress in 2018 by Representative Alexandria Ocasio-Cortez and Senator Edward J. Markey.[229] The GND is a broad congressional resolution including many goals to divest the U.S. from fossil fuels, be carbon-neutral, and run on 100% clean energy by 2050 (similar to Biden's plan). The GND is more far-reaching than Biden's plan, detailing a more aggressive timeline to eliminate all fossil fuel usage in the U.S., and also includes more universal job and healthcare promises.[230]

Regardless of these differences, the Biden administration presents an opportunity to enact impactful environmental justice policy to alleviate climate burdens on underserved communities, although the currently polarized and relatively moderate political climate suggests passing effective climate legislation will be challenging.

Renewables are competitive, but dominant companies resemble big oil

While fossil fuels still dominate energy usage in the U.S., renewables have quickly gained ground.[231] The International Energy Agency declared last year that solar is the "cheapest … electricity in history."[232] This development does not come as a surprise to many renewable energy companies who have been quietly growing in wealth and power over the last few decades. NextEra Energy is one of those sky-rocketing corporations, challenging oil giants like ExxonMobil by increasing their market capitalization six-fold in the last decade.[233] While the success of renewable energy companies is great news for the transition to sustainable technologies, the prospect of multi-billion-dollar corporations controlling energy access across the country (and world) poses a risk of continued limited energy access and reliability for millions of Americans in BIPOC and low-income communities.

Large oil companies like ExxonMobil have a long history of prioritizing profits over people, highlighted by their denial of climate change over the last four decades.[234] Exxon, the American Petroleum Institute, and others formed the Global Climate Coalition (GCC) in 1989 to push pseudoscience around climate change and refute evidence that fossil fuel usage was contributing to climate change. They successfully lobbied the George W. Bush Administration to back out of the Kyoto Protocol.[235] The massive influence that multi-billion-dollar corporations have on the national energy landscape repeatedly puts corporate profits and prosperity over environmental justice interests. While renewable energy means deploying clean, carbon-neutral energy sources, **there is still a risk of corporate greed hurting the most marginalized communities**.

To date, there are many laws and statutes in place that regulate energy efficiency, set standards for carbon emissions reduction, and mandate integration of biofuels at both the federal and state levels.[236] However, one of the only laws that protects consumers from predatory utility companies is the Public Utility Holding Company Act of 1935, which prevents utility companies from forming a monopoly.[237] The Federal Energy Regulatory Commission, which oversees electric transmission nationally, also has statutes in place that require utility companies to provide equal energy access to consumers.[238] These regulations are non-specific and do not correct for systemic racism in housing and energy poverty. As the national energy landscape evolves and environmental justice drives policy changes, utility regulations need to be rewritten to center improvement in energy access and quality for BIPOC and low-income communities.

POLICY RECOMMENDATIONS

Recommendation 1: Need for consumer protections and utility weatherization upgrades

The general lack of updated and effective utility regulations allows systemic racism to perpetuate in housing and energy access. As evidenced by the destruction from annual natural disasters like the recent winter storm in Texas and hurricanes in the Gulf and on the East coast, our electric grids are not protected well enough to continue to provide vital power access.[239] The free market model without adequate regulations provides little incentive for weatherization and natural disaster protection. This unpreparedness is especially evident in Texas where the isolated state grid and extreme lack of grid regulations (perpetuated over decades) left millions without electricity and resulted in at least 194 people losing their lives.[240] The lack of electricity and water hits communities of color hardest, while disaster aid disproportionately benefits affluent white communities.[241]

Utility companies' excuses for not implementing more safety and weatherization measures usually focus on the uniqueness of each weather event and the supposed ineffectiveness and high costs associated with safety analyses. The main advantage of a free market for utility companies is that competition keeps prices generally low. Consumers can get very cheap rates via variable price options that depend on wholesale energy costs instead of having fixed cost rates. However, variable prices can result in predatory "emergency" price gouging which can make it harder for many Americans, especially BIPOC, to pay their energy bills and afford other necessities like food and shelter.[242] In extreme cases like the February 2021 winter storm in Texas, price gouging resulted in thousand-dollar utility bills that practically bankrupted consumers.[243]

Price gouging is an economic tactic that correlates with supply and demand. It ideally signals to consumers to reduce usage so that more people have access during crises. Some economists use this argument to defend price gouging and argue against price gouging laws that are in place to protect consumers.[244] However, this argument overlooks systemic racism and the need for environmental justice. Relying on price as an effective signal for resource conservation during emergencies results in wealthier people hoarding commodities and maintaining priority access to utilities like water and electricity. While price gouging laws are in place in 39 states (including Texas) and several U.S. territories, these laws are inconsistent and oftentimes not effective, as seen in Texas in February of 2021.[245]

The reality of climate change means extreme weather events are becoming more common, so catastrophes like the Texas winter storm will become more frequent.[246] To prepare for this reality, I propose instituting federally mandated price-gouging laws that prohibit predatory utility cost increases. The U.S. Department of Energy (DOE) has set a precedent for responding to price gouging during natural disasters following Hurricane Katrina in 2005 by investigating price gouging incidents.[247] States should revise the variable versus fixed cost model. Additionally, to make electricity access more equitable, I propose federally mandated minimum natural disaster preparation, including electricity backup supplies (identified sources of emergency fuel, generators, etc.) and weatherization plant upgrades for extreme temperatures, wildfires, and flood preparation. Expanding electricity capabilities by investing in sustainable energy generation and storage technologies like fuel cells and batteries will better serve communities nationwide as well. Federal funding for power plant weatherization and disaster preparedness should be overseen by the DOE and can be funded by reallocated fossil fuel subsidies.

Recommendation 2: Household weatherization upgrades for equitable electricity access

To make energy access equitable for all communities regardless of energy source, household utility infrastructures should be equal, and utility reliability should be standard. Black Americans and other people of color are more likely to have their utilities cut off, have less efficient household energy infrastructure, and face additional fees than white Americans.[248] In tandem with weatherization upgrades to utility plants, households with lower energy efficiency need to be upgraded. Some weatherization programs already exist including the DOE's Weatherization Assistance Program (WAP), established in 1976, which provides formula grants to all 50 states, the District of Columbia, Puerto Rico, Guam, Virgin Islands, American Samoa, Northern Mariana Islands, and Native American tribes.[249] In 2010, the DOE invested $2 billion in WAP with an additional $715 million invested from other agencies. The weatherization upgrades saved households an average of $3,803, including saving $223 per year on energy as of 2010.[250]

The individual and national economic fallout from the ongoing COVID-19 pandemic will take a long time to subside. As of early 2021, many people are still staying home, unemployment remains high, and national poverty has increased.[251] As more Americans struggle to pay their bills and federal stimulus relief lags behind, the impact of energy poverty will be higher. The Low-Income Home Energy Assistance Program (LIHEAP) is a federal program that provides help with utility bills, weatherization, and other expenses.[252] Additional federal assistance for LIHEAP, $900 million, was included in the CARES act passed in July of 2020, which is in addition to the 2020 budget for LIHEAP of about $3.3 billion.[253-254] However, as of 2016, when LIHEAP had a similar budget, only 20% of eligible households could participate in the program due to insufficient funding.[255]

To be eligible for WAP, a household must be at or below 200% of the federal poverty line, which is currently defined as a family of two making $17,420/year.[256] Other eligibility criteria include receiving supplemental security income or aid for dependents.[249] While eligibility based on household income is important, the main determinant of energy poverty is the *percentage* of that household income that people and families pay for utilities. Low-income families pay from 8% to 17% of their income on utilities, while other households pay about 3%.[224, 249]

I suggest modification of WAP to expand and redefine eligibility criteria to include and prioritize households that spend more than 7% of their income on utilities. Additionally, a current review of the program must be done to understand the expansion of the program from 2010 to 2021. As of 2017, the DOE reported spending about $2.1 billion on WAP with $678 million in additional investments from states and utilities.[257] This budget is not a significant increase from 2010. Without knowledge of the current valuation and success of WAP, I suggest significantly increasing the investment to reach more households in need. There is precedent for a budget increase based on President Biden's commitment to ensure 40% of investments in renewable energy-related projects are directed to historically disadvantaged communities.[228]

Recommendation 3: Environmental Justice Task Forces to ensure equity in the renewable energy transition

The renewable energy transition has been in progress for decades, but many policies still attempt to make sweeping changes without considering the complex impacts on historically underserved communities, including BIPOC and low-income communities. For example, in 2020, California implemented a mandate that all new buildings must have solar panels, which made many new homes and apartments too expensive for people who are low-income[258] Additionally, some proposed policies like cap-and-trade plans have not worked in California and have actually increased pollution in BIPOC and low-income communities because companies offset their local emissions by reducing emissions elsewhere instead of improving the local air quality.[259] Cap-and-trade policies proposed for the Northeastern U.S. are expected to increase the price of gasoline, adding an additional burden on low-income households.[260]

To more effectively incorporate environmental justice at the state and local level as part of the ongoing renewable energy transition, I propose the establishment of state-specific (or region-specific for U.S. territories, tribal nations, and District of Columbia) Environmental Justice Task Forces (EJTF) funded by the DOE. These task forces will allocate funding for renewable energy deployment in different parts of their region with a focus on funding the installation of renewable energy technologies (generation and storage) in and possibly transmission to BIPOC and low-income communities. The task forces would accept grant proposals from various local groups, including nonprofits, advocacy organizations, small renewable energy companies, or community groups for funding to install renewable energy technologies like solar cells. Funding would guarantee no upfront cost for consumers.

Having these task forces as a prerequisite for federal funds ensures that environmental justice is centered in all renewable technology implementation. These task forces would be made up of local experts in community development, local legislators, and community leaders. Their membership in the task force would be financially compensated as part of the federal funding per region. Measures would need to be implemented to ensure that renewable energy companies do not have more power or influence on these projects than community organizations. Adopting models similar to Illinois Solar For All (ISFA), which involves solar cell companies applying for the program and using funds to incentivize installation in low-income communities, would make sure the power remains in the hands of the communities [261]. All project proposals must specify and guarantee that 80% of renewable energy installation will directly benefit low-income and BIPOC communities.

The EJTF program would complement many existing state policies and programs that aim to increase environmental justice efforts in renewable energy deployment. California was the first state to establish low-income solar cell deployment initiatives with its Single-Family Affordable Solar Homes (SASH) and Multifamily Affordable Solar Housing (MASH) programs in 2009.[262] These programs provided funds for eligible households to install solar cells on their homes with a budget from the state of over $200 million. D.C. implemented a comprehensive low-income solar initiative called the Solar for All program in 2016 which folded in three main thrusts of solar deployment including single and multi-family homes, community solar, and job development. The multi-million-dollar program's goal is to deploy solar cells for 100,000 households by 2032.

The EJTF program could complement existing efforts like these by providing federal funding for state programs and providing representation for diverse communities across states and regions. Colorado, Illinois, Massachusetts, New York, and New Hampshire have all instituted relatively successful community solar programs, which provide solar to people who may not be able to install solar panels on their roofs (like renters).[261-262]

Renewable energy technologies use fewer resources to operate than energy-intensive sources like coal. In 2013, Texas utility customers saved $736 million in energy costs from using wind. Illinois consumers saved over $176 million in 2011 from the use of renewable energy sources.[263] To properly establish the EJTF program in all 50 states, U.S. territories, and Washington D.C., I suggest a federal budget of $3 billion, similar but higher than the WAP budget, with state and regional budget allocations based on population with an emphasis on the proportion of state or regional residents who live at or below 200% of the poverty level and/or who suffer from energy poverty. This budget should be facilitated by the DOE and can be made possible through President Biden's $2 trillion commitment to clean energy over four years.[264] The program should be evaluated externally on an annual basis and the budget should be increased based on these evaluations.

CONCLUSIONS

Environmental justice is critical to solving the climate crisis. Transitioning to renewable energy without considering equity will only further inequalities that plague our society. Climate change is already ravaging people's livelihoods as well as claiming lives every year. We still have a chance to preserve the planet for all members of future generations, but we have to act now. By reinforcing and supporting the renewable energy transition with rigorous and comprehensive weatherization and infrastructure upgrades for both utilities and households, we can improve energy equity across the country and mitigate severe consequences of climate change in the long term by prioritizing the needs of those on the frontline.

Conclusions and Outlook

Throughout my doctoral work, I have gained more confidence in the ability that organic chromophores have to make a positive impact in the renewable energy space. Robust pigments like perylene diimides (PDIs), naphthalocyanines (NCs), and bacteriochlorins (BCs) have a wide range of photophysical properties applicable as organic photovoltaic active/sensitizing layers, photocatalysts, and even medical imaging materials. Most of this work has just scratched the surface of experiments with these materials, both fundamental and applied.

PDIs are a promising, robust class of molecules. Specifically, with the advent of knowledge surrounding symmetry-breaking charge separation (SB-CS) in tetraphenoxy-PDI (tpPDI) films, future work with these materials is abundant. There is much to learn about the spin-dynamics of both the charge separated and triplet states which could be probed with electron paramagnetic resonance spectroscopy. Additionally, since we have discovered that HtpPDI undergoes quantitative SB-CS even at 80 K, the mechanism of this process with minimal enthalpic driving force in a nonpolar, low temperature environment has yet to be clarified. Different optical and vibrational spectroscopies could be used to further elucidate the molecular movement that contributes to this phenomenon. While we believe the quadrupolar nature of these molecules contributes significant driving force, we do not have a quantitative model of this process yet, and there is plenty of work to be done in this area. Our group has begun studies using 2D-transient absorption spectroscopy to get a larger picture of this process in tpPDI oligomers.

Additionally, realizing singlet fission (SF) in aggregated, rotated, parallel C_5PDI molecules and observing the quantitative trend of enhanced crystallinity leading to higher triplet quantum yields opens new doors for not only this molecule, but a wide range of other modified rylene diimides for SF applications. Our group has successfully challenged the notion that slip-stacked crystal structures were required for SF. Designing higher crystallinity films by vapor depositing C_5PDI on a variety of crystalline substrates at different temperatures could help to improve the triplet quantum yield, narrow the distribution of SB-CS kinetic rates, and may even make this molecule a candidate for charge separation or triplet exciton transfer studies, although my work has proven the latter to be rather challenging. Additionally, exploring the application of both HtpPDI and C_5PDI in organic photovoltaics is a critical next step to realizing their potential in the renewable energy space. The development of these devices would likely take several years at the research level and thus did not come to fruition during my doctoral research.

Finally, tetrapyrroles exhibit a variety of photophysical properties. Zinc 2,11,20,29-tetra-*tert*-butyl-2,3-naphthalocyanine (*t*-Bu-ZnNc) exhibits aggregation-enhanced properties including emission from its high energy S_2 state and rapid spin-orbit intersystem crossing (SO-ISC). These properties could be enhanced in different derivatives of similar molecules, exploring how different crystalline packing alters the radiative and nonradiative emissive properties. We also found that 13,23-diacetyl-8,8,18,18-tetra-methyl-12,22-diphenyl-bacteriochlorin (B-189) undergoes rapid SO-ISC, further supporting this notion of aggregation inducing energy level splitting/broadening. While triplet yields were low for both *t*-Bu-ZnNc and B-189, adding heavy metal centers like Pd or Zn to B-189 and exploring different substituent modifications for both molecules could help to tune both the SO-ISC rates and triplet quantum yields for use as triplet sensitizers or as molecules in various photoinduced applications in energy or medicine (with non-toxic metals).

Most importantly, upon the conclusion of my doctoral work I have learned the importance of environmental justice, even at the research stage of technology development. I hope my colleagues and successors in these fields and all research spaces will continue to learn about the social and political effects of the past, present, and future impacts of the work we do as engineers/scientists and consider policy implications often.

APPENDIX A: SUPPLEMENTAL INFORMATION FOR CH. 1

Additional single crystal images and molecular ordering data

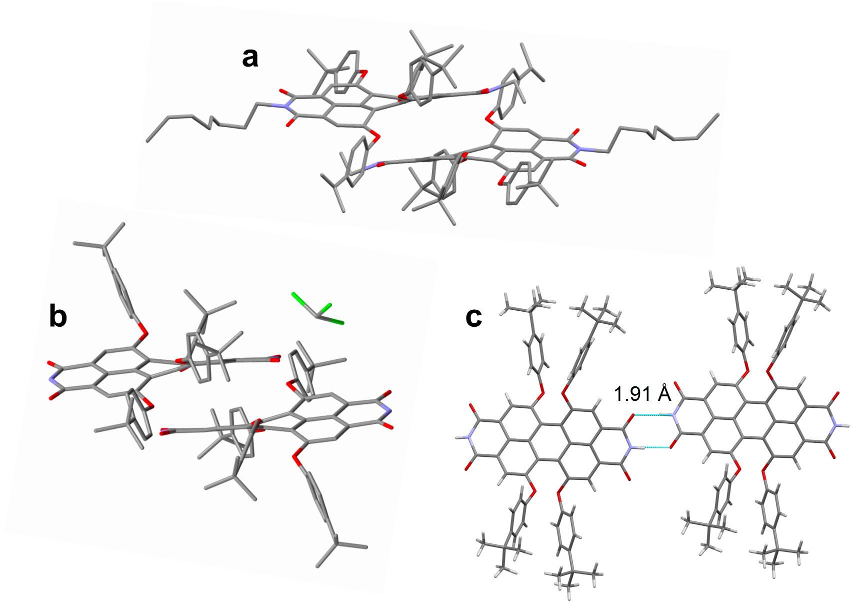

Figure A1. (a) Octyl-tpPDI dimer showing π-π and slip-stacking, (b) H-tpPDI dimer showing π-π and slip-stacking, and (c) H-tpPDI hydrogen-bonded dimer; the hydrogen bond distance is 1.91 Å.

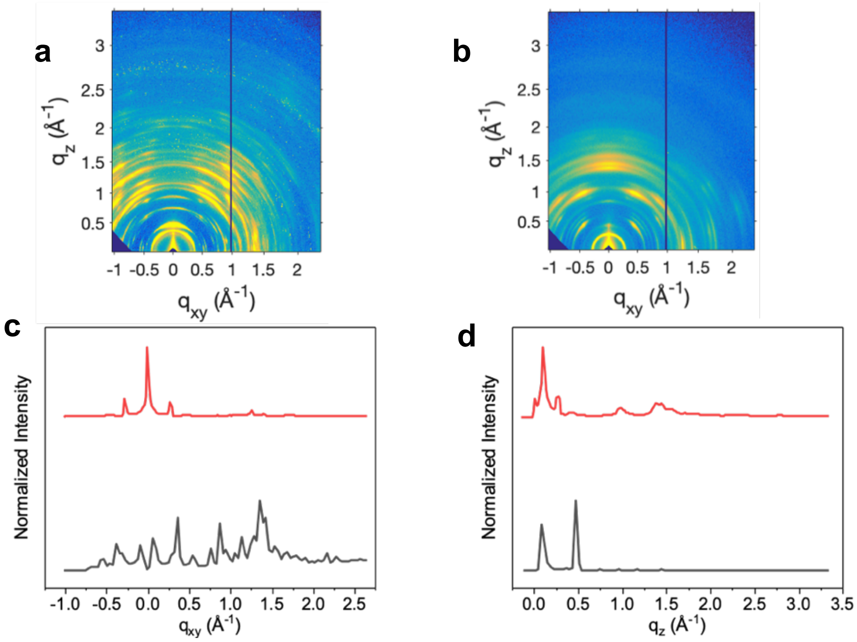

Figure A2. GIWAXS spectra of thermally annealed (a) octyl-tpPDI, (b) H-tpPDI, and the corresponding linecuts shown in (c) and (d) where gray is octyl-tpPDI and red is H-tpPDI.

Domain size analysis using atomic force microscopy (AFM)

Atomic force microscopy (AFM) images were taken using a laboratory-constructed AFM system. The AFM was operated in contact mode using a soft (force constant $k = 0.2$ N/m) cantilever (ContE-G, Budget Sensors). All scans were taken in air at room temperature. Some representative grains were detected manually.

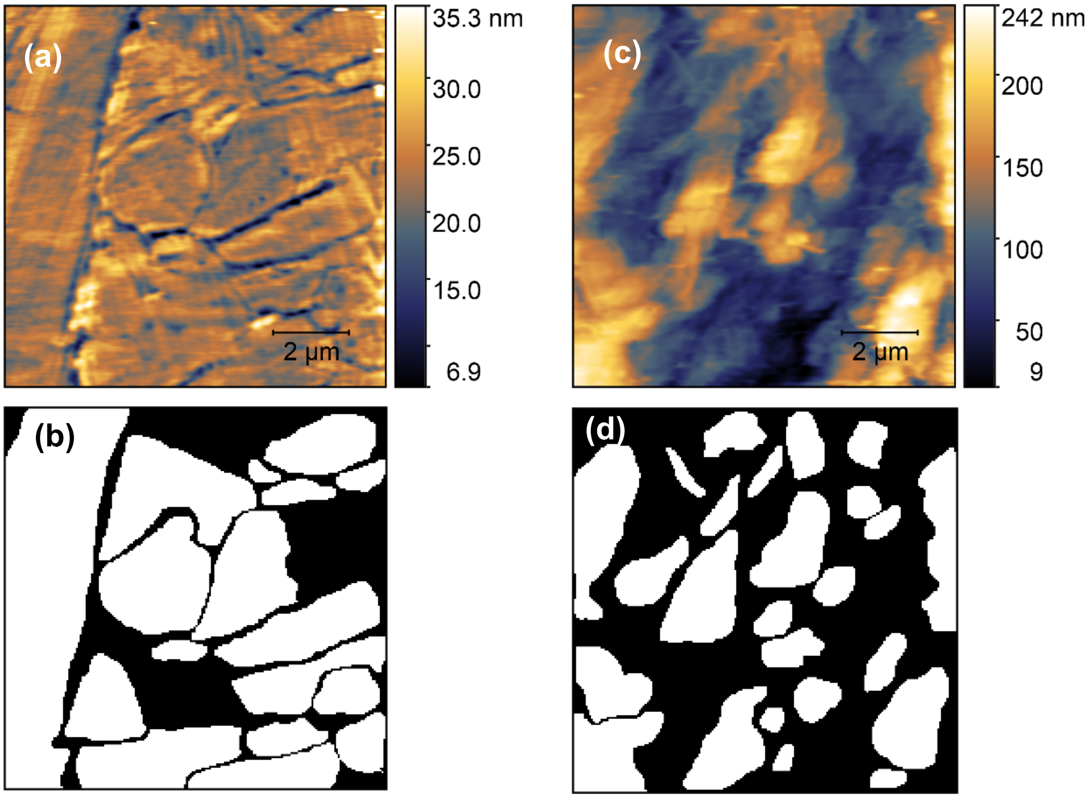

Figure A3. AFM images and manually applied grain masks of (a,b) octyl-tpPDI and (c,d) H-tpPDI films.

Figure A3 shows the topography and applied grain masks of the octyl-tpPDI (a,b) and the H-tpPDI films (c,d) at 10 × 10 μm^2. The calculated RMS roughness of the octyl-tpPDI and the H-tpPDI films over that area were 3 nm and 45 nm, respectively, signifying that the octyl-tpPDI was much smoother than its counterpart. Analysis of representative grains on the two samples shows that the grains in the octyl-tpPDI film are densely packed while those of the H-tpPDI are sparser. Concerning grain sizes, the octyl-tpPDI shows systematically larger grains with mean projected grain area of 4.1 μm^2 and mean equivalent disc radius of 0.99 μm, while the H-tpPDI shows mean projected grain area of 1.7 μm^2 and mean equivalent disc radius of 0.68 μm. It is interesting to note that almost all of the grains in the octyl-tpPDI film exhibit stripe patterns with stripe periodicity of around 100 nm. The stripes maintain their orientation within each grain but are randomly oriented for different grains. These nanostructures might reflect different packing of the PDI molecules within each grain.

Steady-state spectroscopy data

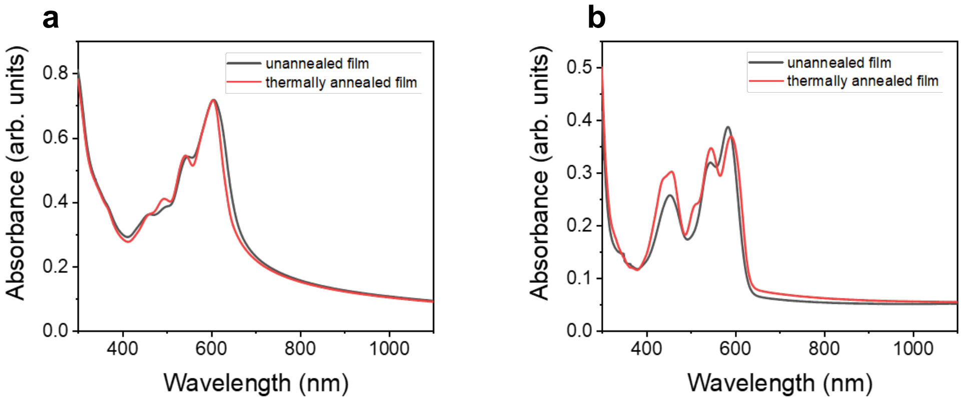

Figure A4. UV-vis of (a) H-tpPDI and (b) Octyl-tpPDI thermally annealed films where unannealed film absorbance is in gray and annealed absorbance is in red. Spectra are not scatter-corrected.

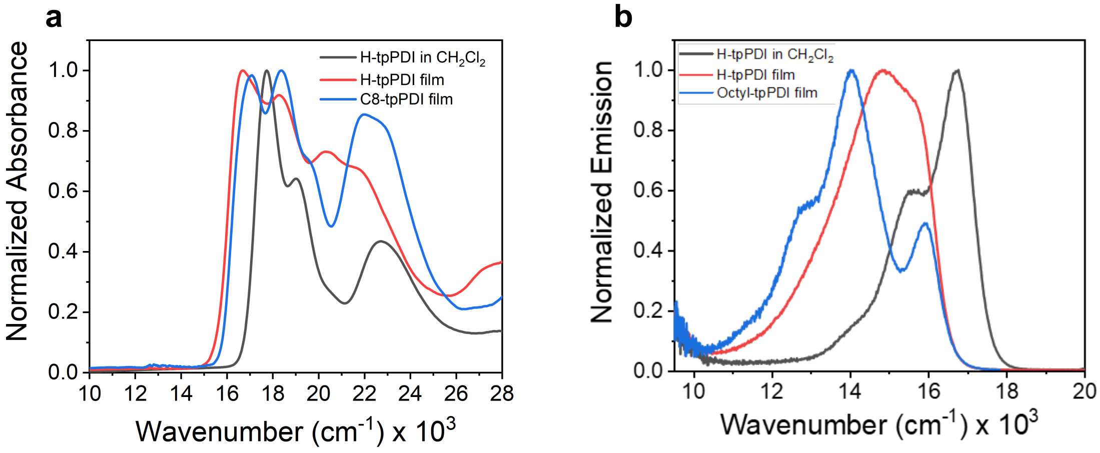

Figure A5. Steady-state (a) absorption and (b) emission spectra of H-tpPDI monomer, H-tpPDI film, and octyl-tpPDI film plotted versus wavenumber.

The emission intensity was adjusted using the Jacobian transformation method to properly represent signal per unit of frequency.[265]

Femtosecond and nanosecond transient absorption data for films

Femtosecond transient absorption (fsTA) data were fit using a previously described MATLAB fitting program[70] to a first order kinetic model. H-tpPDI and octyl-tpPDI film data were fit to A → B → C first order kinetic models shown in Figure 13 in the main text. Nanosecond transient absorption data (nsTA) were fit to first order kinetic models showing the decay of the triplet population to the singlet ground state. While recombination is a bimolecular process, the models employed here are first order as they yielded a sufficient fit.

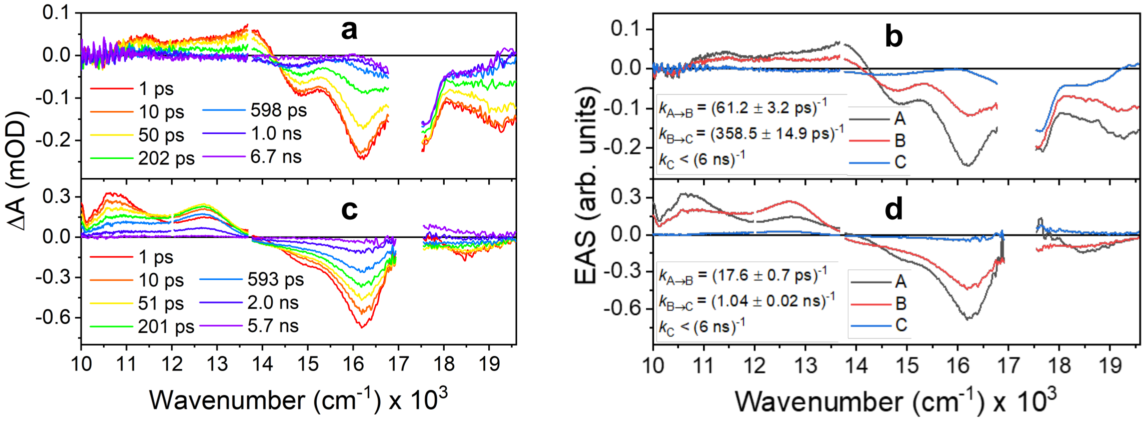

Figure A6. FsTA data plotted vs. wavenumber: (a) raw data for octyl-tpPDI film, (b) evolution associated spectra (EAS) for octyl-tpPDI film, (c) raw data for H-tpPDI film, (d) EAS for H-tpPDI film.

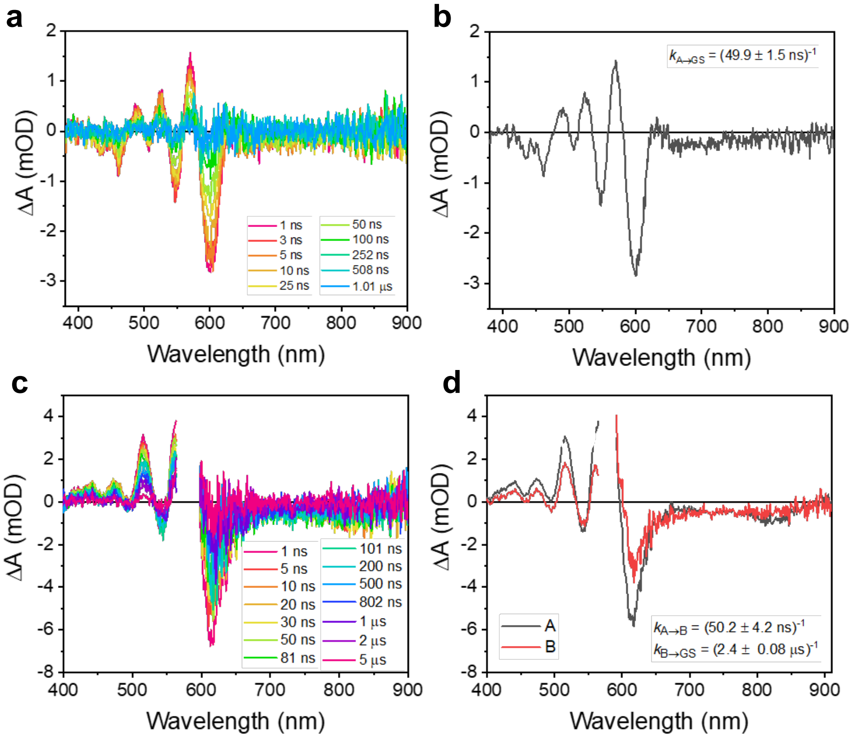

Figure A7. Nanosecond transient absorption (nsTA) spectra for (a) octyl-tpPDI and (c) H-tpPDI films; Evolution associated spectra (EAS) for nsTA of (b) octyl-tpPDI and (d) H-tpPDI films.

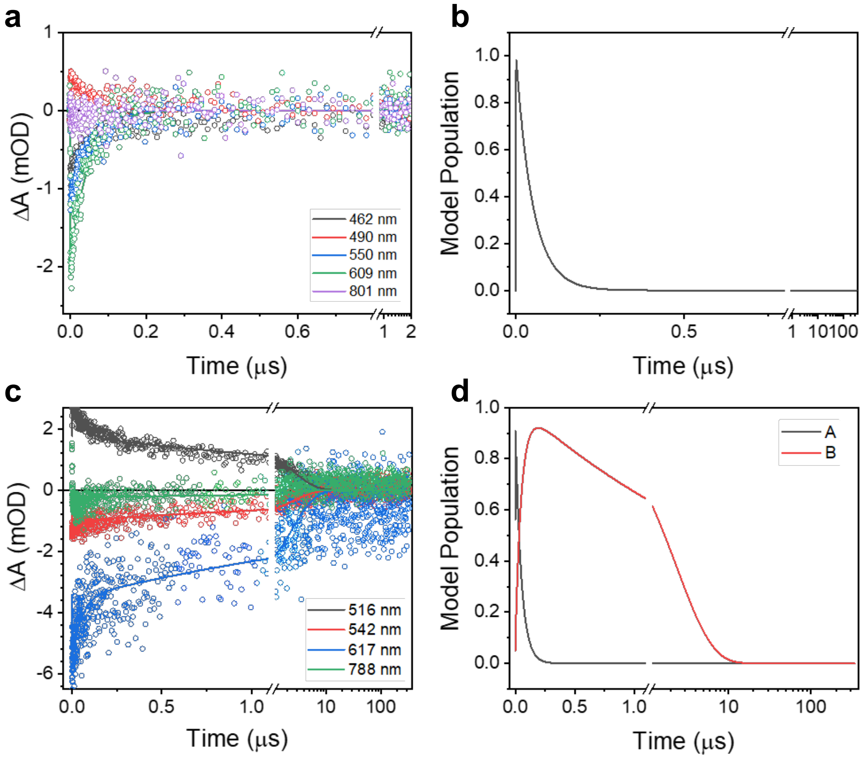

Figure A8. nsTA kinetic fits for (a) octyl-tpPDI and (c) H-tpPDI where raw data are shown as open circles and model fits are shown as solid lines; temporal evolution of populations for nsTA of (b) octyl-tpPDI and (d) H-tpPDI.

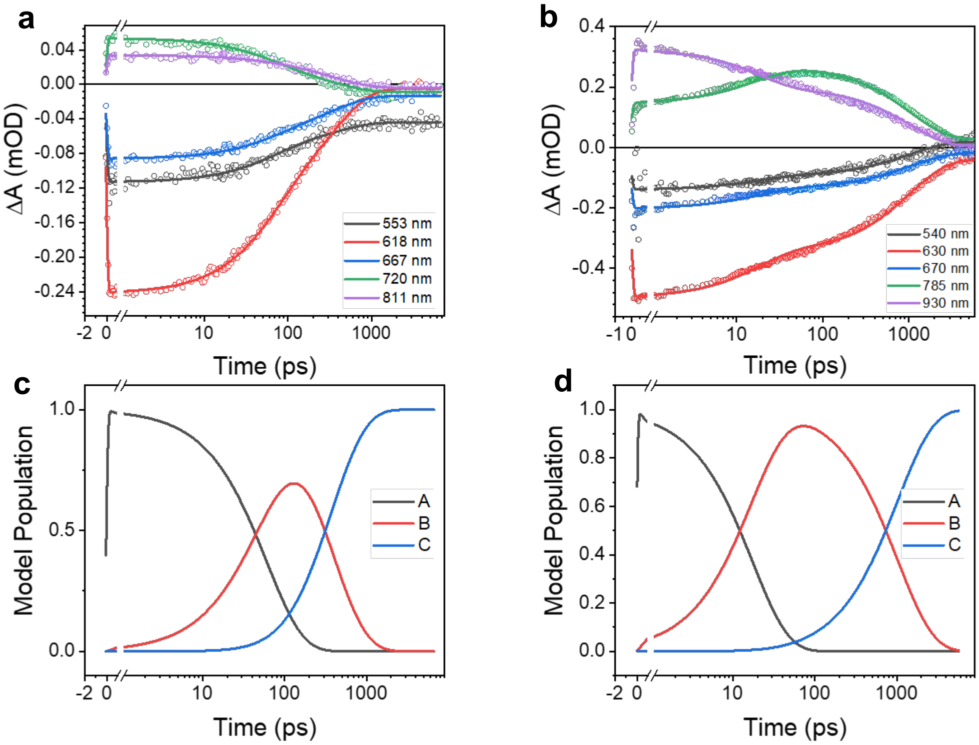

Figure A9. Kinetic fits for femtosecond transient absorption (fsTA) for (a) octyl-tpPDI and (b) H-tpPDI films where raw data are shown as open circles and model fits are shown as solid lines; temporal evolution of populations (states) for (c) octyl-tpPDI and (d) H-tpPDI films.

Tetraphenoxy-PDI extinction coefficients

Steady-state absorption spectra of H-tpPDI and octyl-tpPDI in chloroform ($CHCl_3$) with different concentrations were measured in a 1 cm quartz cuvette (Figure A10a,b). The absorbance at 550 nm for H-tpPDI and octyl-tpPDI at different concentrations were plotted (Figure S10c,d), and fitted using the Beer-Lambert law: $A = \varepsilon c l$ where A is absorbance, ε is extinction coefficient (M^{-1}·cm^{-1}), c is concentration (M), and l is path length (cm).[266] The slope of the linear fit is the molar extinction coefficient at 550 nm. For H-tpPDI, ε was determined to be 34007 ± 394 cm^{-1}·M^{-1}, while for octyl-tpPDI ε was found to be 32481 ± 306 cm^{-1}·M^{-1}.

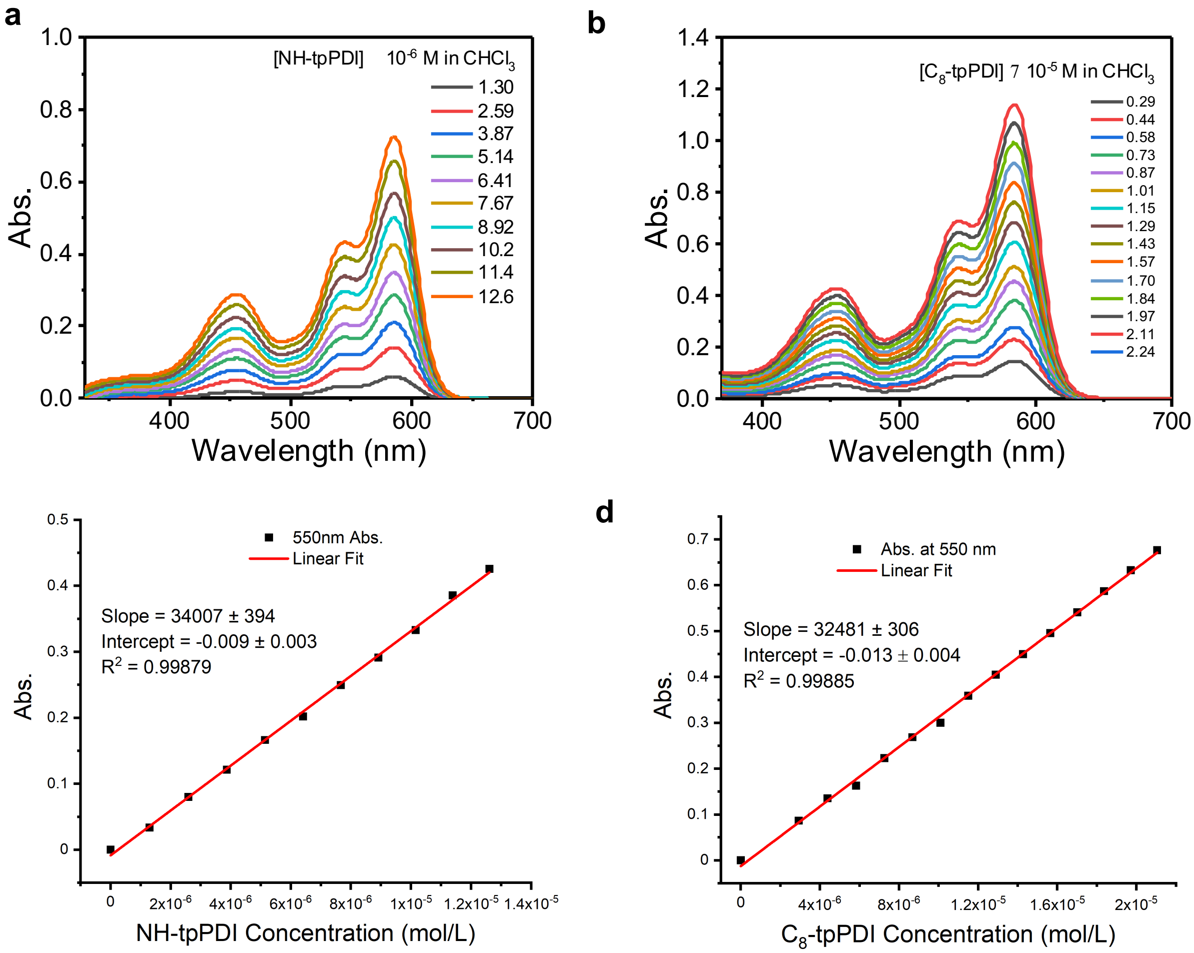

Figure A10. Molar extinction coefficient measurements for H-tpPDI and octyl-tpPDI. Steady state absorption spectra of a) H-tpPDI and b) octyl-tpPDI in $CHCl_3$ with different concentrations, and extinction coefficient calculation based on absorbance at 550 nm of c) H-tpPDI and d) octyl-tpPDI.

Triplet energy calculation methods: TDDFT

The optimized ground state S_0 coordinates of a simplified structure **Me-tpPDI** were obtained from literature.[267] TDDFT calculation of the triplet T_1 energy was performed based on the optimized S_0 state with B3LYP/6-31G(d). The calculated T_1 state energy is 1.17 eV.

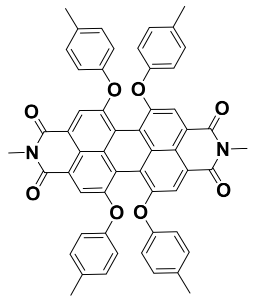

Me-tpPDI

Me-tpPDI singlet ground state

O	2.1680000000	-5.6741000000	-0.7031000000
O	-2.1903000000	-5.6721000000	0.6788000000
O	2.1942000000	5.6770000000	0.6616000000
O	-2.1682000000	5.6768000000	-0.7076000000
O	-3.4246000000	0.7586000000	-1.0832000000
O	-3.4292000000	-0.7320000000	1.0717000000
O	3.4322000000	0.7369000000	1.0637000000
O	3.4249000000	-0.7568000000	-1.0878000000
N	-0.0182000000	-5.6723000000	-0.0093000000
N	0.0201000000	5.6761000000	-0.0204000000
C	2.3064000000	-2.8594000000	-0.7064000000
C	2.3445000000	-1.4558000000	-0.6246000000
C	1.2368000000	-0.7192000000	-0.1576000000
C	-0.0040000000	-1.4199000000	-0.0072000000
C	-0.0088000000	-2.8432000000	-0.0071000000
C	1.1649000000	-3.5498000000	-0.3499000000
C	-1.2402000000	-0.7109000000	0.1428000000
C	-2.3533000000	-1.4391000000	0.6105000000
C	-2.3250000000	-2.8430000000	0.6922000000
C	-1.1879000000	-3.5399000000	0.3355000000
C	-1.2038000000	-5.0205000000	0.3600000000
C	1.1771000000	-5.0321000000	-0.3791000000
C	1.2420000000	0.7150000000	0.1390000000
C	0.0056000000	1.4237000000	-0.0098000000
C	-1.2355000000	0.7228000000	-0.1564000000
C	2.3561000000	1.4439000000	0.6032000000
C	2.3284000000	2.8480000000	0.6814000000
C	1.1905000000	3.5443000000	0.3259000000
C	0.0104000000	2.8470000000	-0.0124000000
C	-1.1642000000	3.5531000000	-0.3537000000
C	-2.3065000000	2.8620000000	-0.7066000000
C	-2.3440000000	1.4586000000	-0.6226000000
C	1.2066000000	5.0249000000	0.3469000000
C	-1.1764000000	5.0353000000	-0.3854000000
C	0.0583000000	7.1418000000	-0.0165000000
C	-0.0561000000	-7.1380000000	-0.0020000000
C	-4.6689000000	1.3708000000	-1.2023000000
C	-5.3188000000	1.9221000000	-0.0966000000
C	-6.5966000000	2.4515000000	-0.2557000000
C	-7.2473000000	2.4339000000	-1.4987000000
C	-6.5732000000	1.8656000000	-2.5851000000
C	-5.2880000000	1.3379000000	-2.4477000000
C	4.6750000000	1.3488000000	1.2026000000
C	5.2637000000	1.3378000000	2.4654000000
C	6.5395000000	1.8753000000	2.6275000000
C	7.2392000000	2.4303000000	1.5472000000
C	6.6203000000	2.4268000000	0.2907000000
C	5.3480000000	1.8861000000	0.1069000000
C	-7.2423000000	-2.4182000000	1.5338000000
C	-4.6727000000	-1.3436000000	1.2053000000
C	-5.3384000000	-1.8860000000	0.1057000000
C	-6.6126000000	-2.4211000000	0.2807000000
C	7.2405000000	-2.4479000000	-1.5068000000
C	6.5939000000	-2.4568000000	-0.2622000000
C	5.3186000000	-1.9204000000	-0.1013000000
C	4.6682000000	-1.3709000000	-1.2068000000
C	5.2855000000	-1.3427000000	-2.4539000000
C	6.5674000000	-1.8765000000	-2.5930000000
C	-6.5540000000	-1.8534000000	2.6142000000
C	-5.2735000000	-1.3206000000	2.4607000000
C	-8.6306000000	3.0218000000	-1.6556000000
C	8.6261000000	3.0003000000	1.7351000000
C	-8.6120000000	-3.0303000000	1.7144000000
C	8.6126000000	-3.0590000000	-1.6712000000
H	3.1718000000	-3.4186000000	-1.0392000000
H	-3.1942000000	-3.3972000000	1.0239000000
H	3.1987000000	3.4029000000	1.0092000000
H	-3.1728000000	3.4205000000	-1.0384000000
H	0.8309000000	7.4934000000	-0.7047000000
H	-0.9214000000	7.4993000000	-0.3252000000

H	-0.8299000000	-7.4914000000	-0.6880000000
H	0.9231000000	-7.4960000000	-0.3117000000
H	-7.1022000000	2.8777000000	0.6078000000
H	-7.0557000000	1.8370000000	-3.5590000000
H	-4.7641000000	0.8996000000	-3.2915000000
H	6.9952000000	1.8697000000	3.6151000000
H	7.1429000000	2.8495000000	-0.5638000000
H	4.8814000000	1.8744000000	-0.8726000000
H	-4.8653000000	-1.8748000000	-0.8707000000
H	-7.1309000000	-2.8416000000	-0.5779000000
H	7.1000000000	-2.8830000000	0.6009000000
H	4.8329000000	-1.9132000000	0.8690000000
H	4.7618000000	-0.9033000000	-3.2972000000
H	7.0480000000	-1.8520000000	-3.5681000000
H	4.7179000000	0.9143000000	3.3028000000
H	-4.8302000000	1.9206000000	0.8722000000
H	-7.0216000000	-1.8331000000	3.5956000000
H	-4.7382000000	-0.8859000000	3.2992000000
H	-0.2985000000	-7.4968000000	1.0014000000
H	0.3027000000	7.5028000000	0.9856000000
H	8.9414000000	3.5795000000	0.8616000000
H	9.3683000000	2.2061000000	1.8892000000
H	8.6738000000	3.6594000000	2.6098000000
H	9.1331000000	-2.6466000000	-2.5416000000
H	8.5503000000	-4.1463000000	-1.8119000000
H	9.2379000000	-2.8833000000	-0.7888000000
H	-9.0759000000	2.7412000000	-2.6151000000
H	-8.6076000000	4.1184000000	-1.6103000000
H	-9.3034000000	2.6810000000	-0.8599000000
H	-9.2322000000	-2.8941000000	0.8219000000
H	-9.1405000000	-2.5866000000	2.5646000000
H	-8.5439000000	-4.1105000000	1.9000000000

Solution tpPDI steady state and transient spectroscopy for triplet sensitization

Solution samples for triplet sensitization were prepared by co-dissolving both H-tpPDI and the triplet sensitizing compound (anthracene, PdPc(OBu)$_8$, or Pd-NDP) in CH$_2$Cl$_2$. These solutions were then degassed three times using a freeze-pump-thaw method to eliminate the presence of triplet-quenching oxygen.

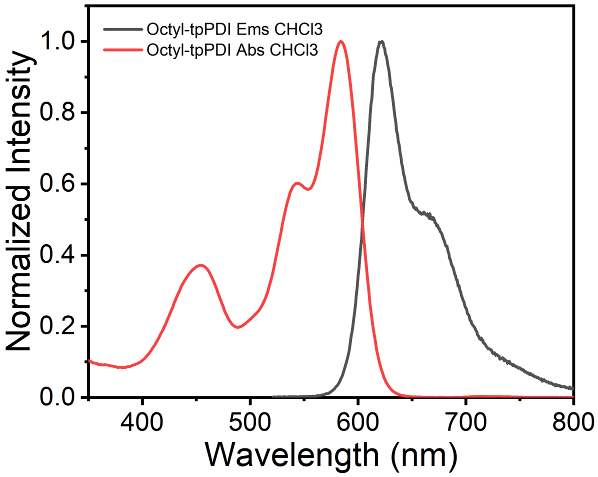

Figure A11. Normalized absorbance and emission of octyl-tpPDI in CHCl$_3$.

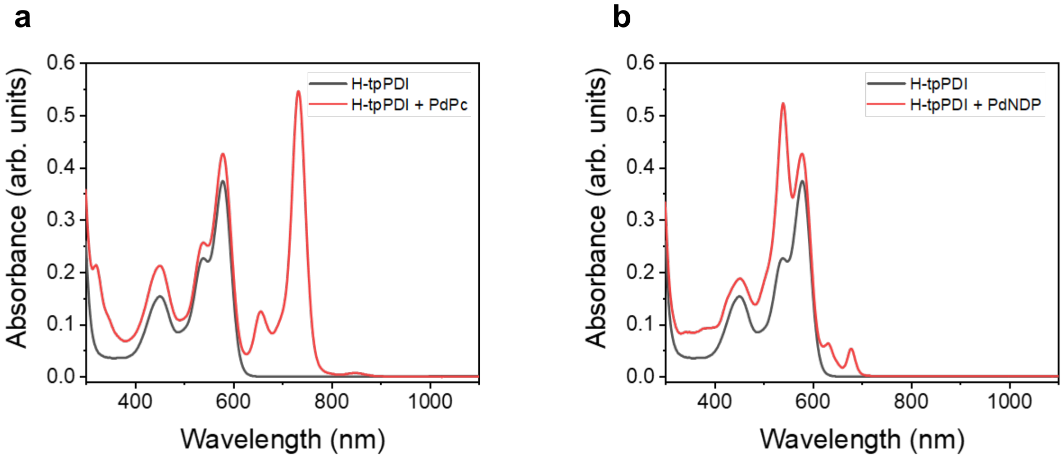

Figure A12. Solution samples prepared for nsTA where gray is H-tpPDI in CH_2Cl_2 and red is H-tpPDI monomer co-dissolved with triplet sensitizer (a) $PdPc(OBu)_8$ and (b) Pd-NDP in CH_2Cl_2.

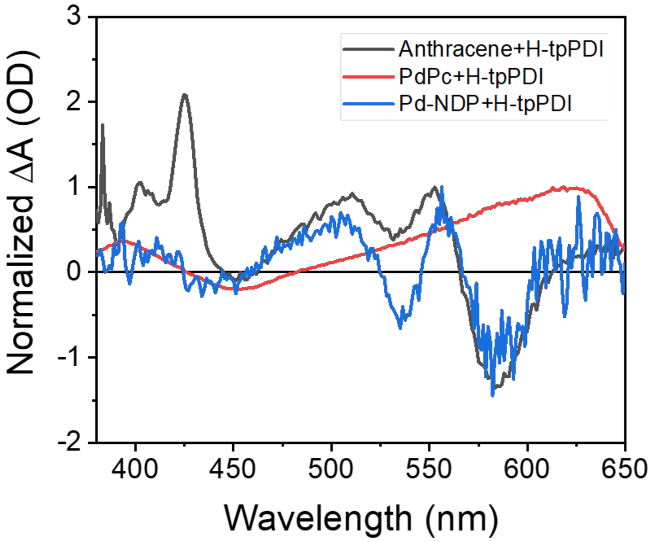

Figure A13. Normalized overlay of nsTA spectra for triplet sensitized H-tpPDI in CH_2Cl_2

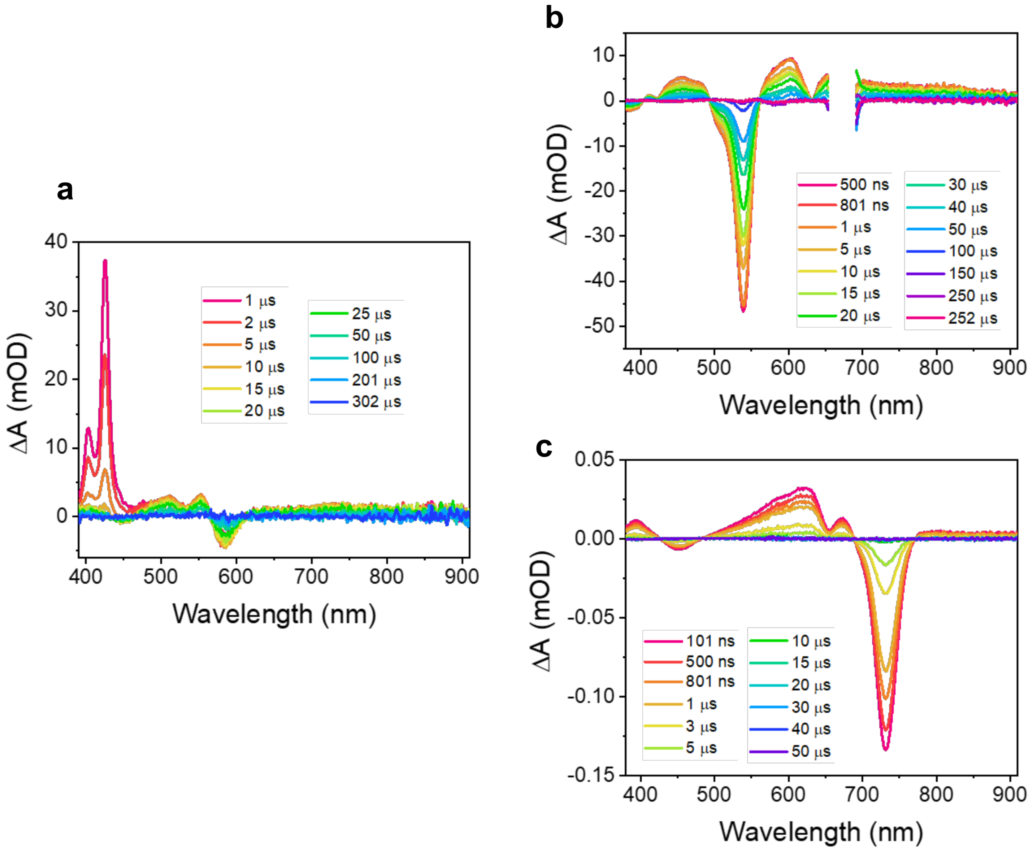

Figure A14. Raw nsTA spectra of triplet sensitized H-tpPDI: (a) H-tpPDI + anthracene (ex. 355 nm), (b) H-tpPDI + Pd-NDP (ex. 677 nm), (c) H-tpPDI + PdPc(OBu)$_8$ (ex. 710 nm).

Additional study: temperature dependence of symmetry-breaking charge separation in tetraphenoxy-perylenediimide films

Additional experimental methods

Transient Absorption Spectroscopy

Femtosecond transient absorption (fsTA) data were collected on a high repetition rate, low fluence system described previously.[24] Nanosecond transient absorption (nsTA) data were collected on a lower repetition rate, high fluence system published previously.[23] All film samples were excited at 580 nm, while the solution samples used to determine the triplet transient absorption spectra were excited at wavelengths resonant with the maximum absorption of the triplet sensitizer (see Supporting Information). Low temperature measurements were taken by mounting the film in a Janis VNF-100 cryostat (Janis Research Co. LLC) coupled to a Cryo-Con 32B (cryogenics Control Systems, Inc.) temperature controller. All data were fit and modeled using a previously described MATLAB fitting program.[70] Data were globally fit to a first order kinetic model.

Results and discussion

Steady-state spectroscopy

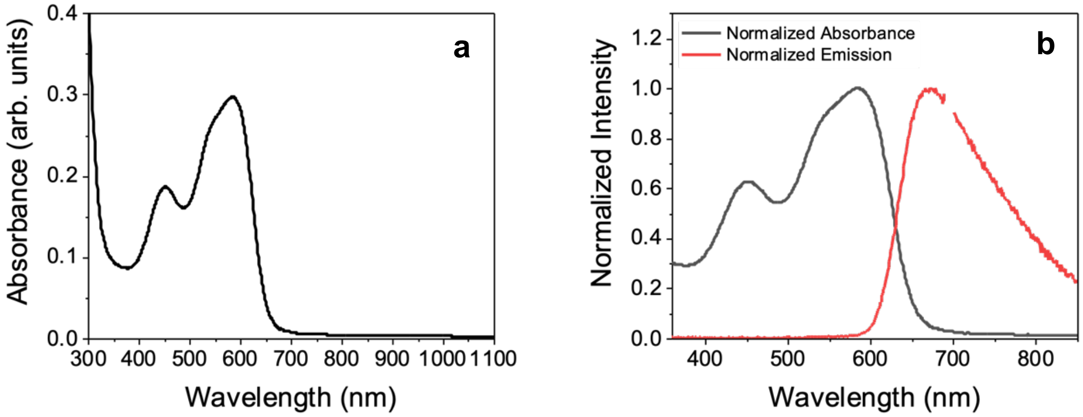

Figure A15. Steady-state (a) absorption and (b) normalized absorption vs. emission spectra of freshly spin-coated and annealed H-tpPDI film.

Absorption and emission data of the thermally annealed H-tpPDI spin-coated film shown in Figure A15 look similar to the spectra published and shown in Chapter 1. The lower energy Q-band vibronic peaks do not show as much distinction as previously synthesized films. Otherwise, the spectra resemble those previously collected and presented in Chapter 1.

Transient absorption spectroscopy

Transient absorption spectroscopy data were collected on the annealed film at a range of temperatures from 300-100 K. These data, shown below in Figures A16 – A20, show the same kinetic transitions as expected from room temperature studies shown in Chapter 1 with slowing kinetic rates as temperature decreases. These data fit best to an A → B → C → D model as opposed to the three species model the data fit best to in Chapter 1. I assign these four states identically across all five sets of data with the difference being the rate constants. State A is the singlet excited state following initial excitation. Even at 100 K, state A shows presence of the anion peak around 780 nm, indicating that SB-CS begins within the instrument response (<300 fs). The A → B transition is quantitative SB-CS in each spectrum, with τ_{AB} increasing as temperature decreases and the 780 nm peak growing in with the transition to state B. The B → C transition shows decreasing singlet absorption (redder than 850 nm) and vibrational relaxation with the PDI anion feature still dominating the spectra. Finally, C → D shows almost complete relaxation of the anion peak. In Chapter 1, we found that the long-lived state was the triplet state. There is not strong

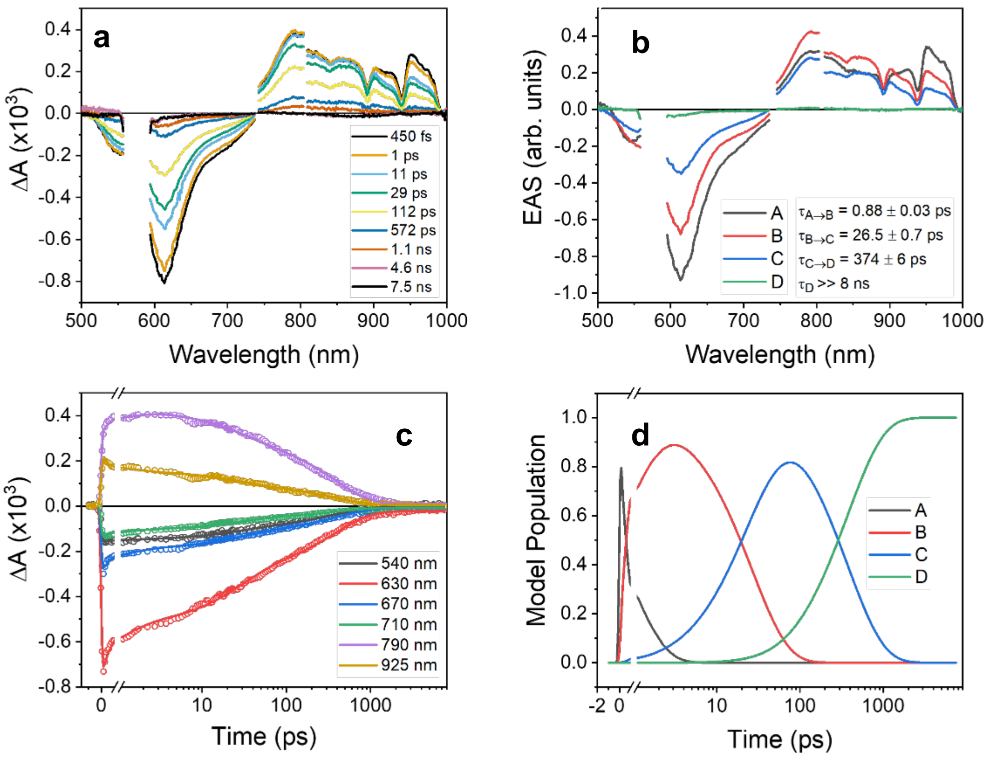

Figure A16. FsTA spectroscopy of thermally annealed H-tpPDI film at 300 K, pumped at 580 nm: spectral evolution of transient absorption signals; (b) Evolution-associated spectra; (c) Kinetic traces and fits at several key wavelengths; (d) Kinetic populations versus time.

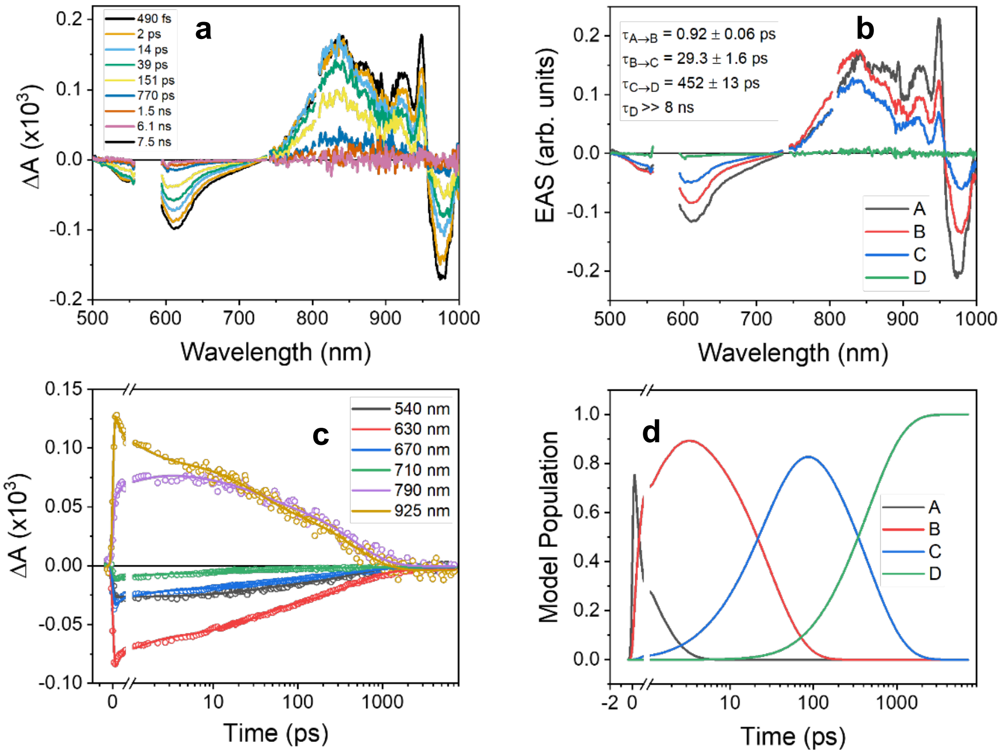

Figure A17. FsTA spectroscopy of thermally annealed H-tpPDI film at 250 K, pumped at 580 nm: spectral evolution of transient absorption signals; (b) Evolution-associated spectra; (c) Kinetic traces and fits at several key wavelengths; (d) Kinetic populations versus time.

spectral evidence that this state is the triplet in these spectra, but this state could be integral to the distributed kinetics of the SB-CS in the polycrystalline films.

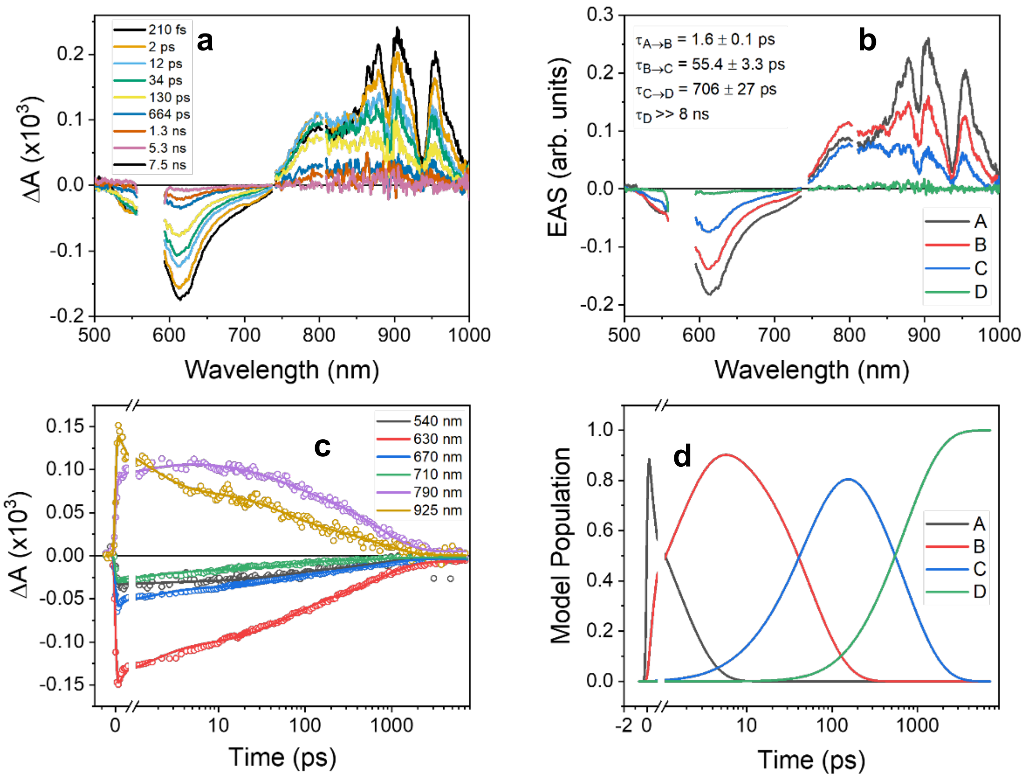

Figure A18. FsTA spectroscopy of thermally annealed H-tpPDI film at 200 K, pumped at 580 nm: spectral evolution of transient absorption signals; (b) Evolution-associated spectra; (c) Kinetic traces and fits at several key wavelengths; (d) Kinetic populations versus time.

Arrhenius fitting

In order to evaluate the temperature dependence of SB-CS, we fit the rate of SB-CS to an Arrhenius relationship[268] with an R^2 value of 0.82 showing a moderately good fit. This indicates that the SB-CS kinetics have a thermodynamic dependence as effectively modeled by the Arrhenius equation.

Conclusion

This follow up study shows that SB-CS does have a thermodynamic dependence as decreasing temperature does in fact decrease the rate of charge separation. Surprisingly, even at low temperatures, the SB-CS process is still very rapid. There is a lot more to learn about the mechanism for SB-CS because this process was initially thought to only be favored in polar

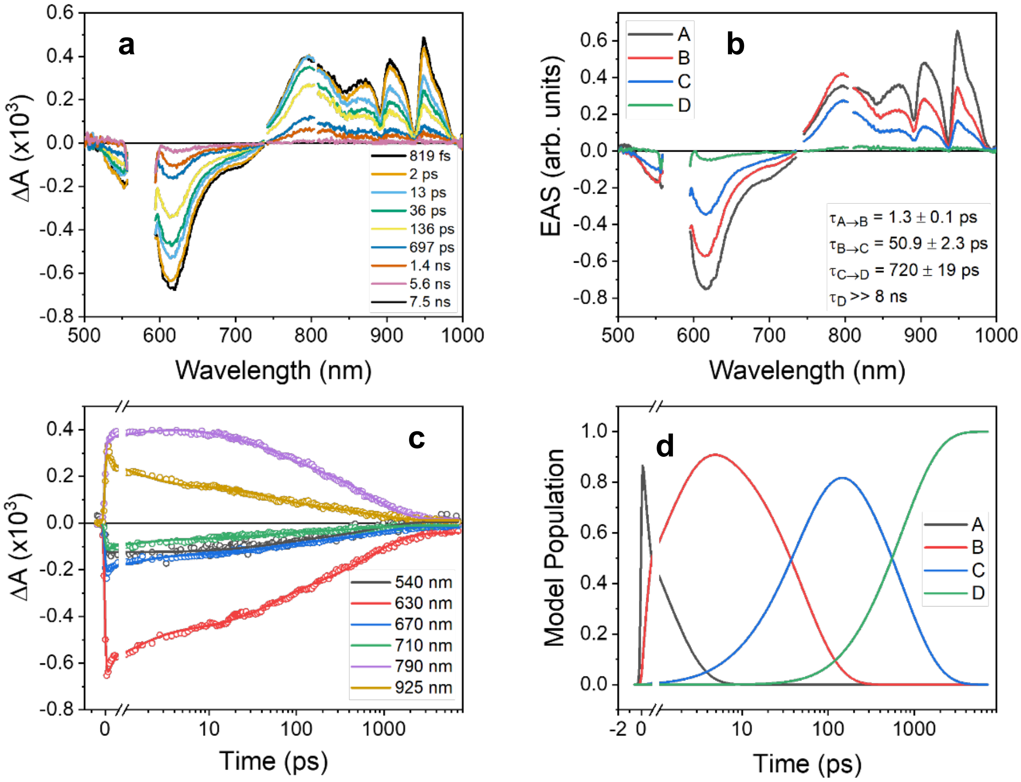

Figure A19. FsTA spectroscopy of thermally annealed H-tpPDI film at 150 K, pumped at 580 nm: spectral evolution of transient absorption signals; (b) Evolution-associated spectra; (c) Kinetic traces and fits at several key wavelengths; (d) Kinetic populations versus time.

environments due to the necessity of a strong driving force. However, we have found that not only is this process possible in nonpolar solid-state systems at room temperature—it is also possible in nonpolar solid-state systems at very low temperatures with a significant decrease in enthalpic driving force. While the SB-CS rate constant's temperature dependence shows an enthalpic Arrhenius relationship, perhaps SB-CS has more to do with entropic driving force induced by both the quadrupolar effect of the perylene cores and the vibrations of the core-twisted tpPDI molecules.

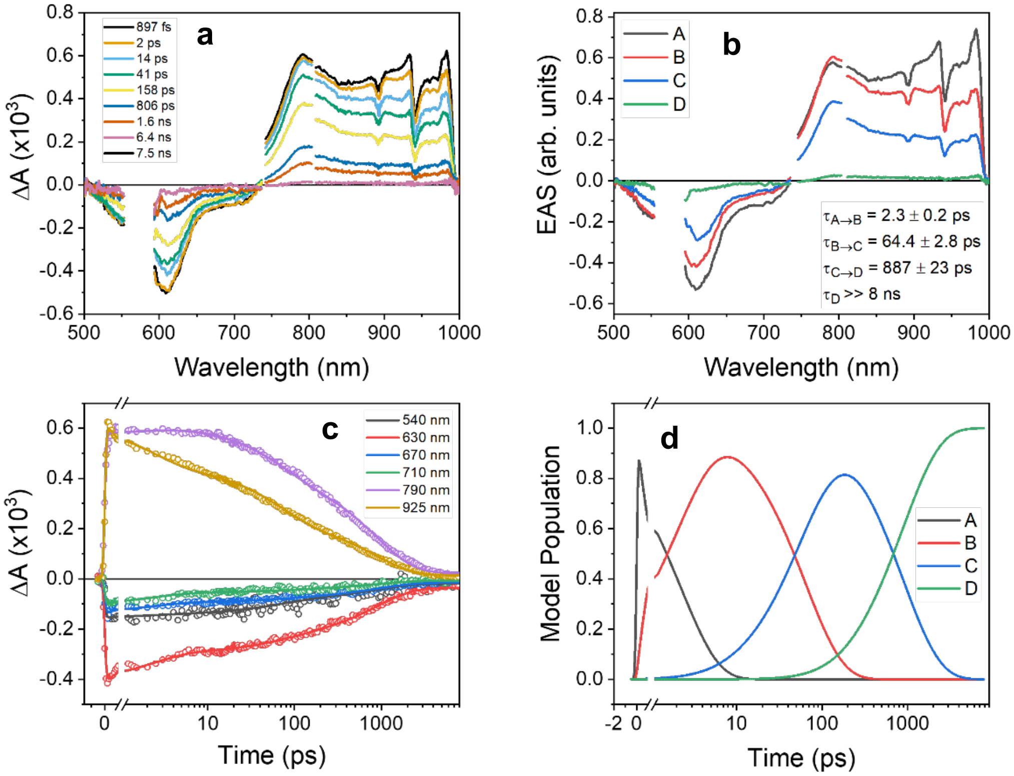

Figure A20. FsTA spectroscopy of thermally annealed H-tpPDI film at 100 K, pumped at 580 nm: spectral evolution of transient absorption signals; (b) Evolution-associated spectra; (c) Kinetic traces and fits at several key wavelengths; (d) Kinetic populations versus time.

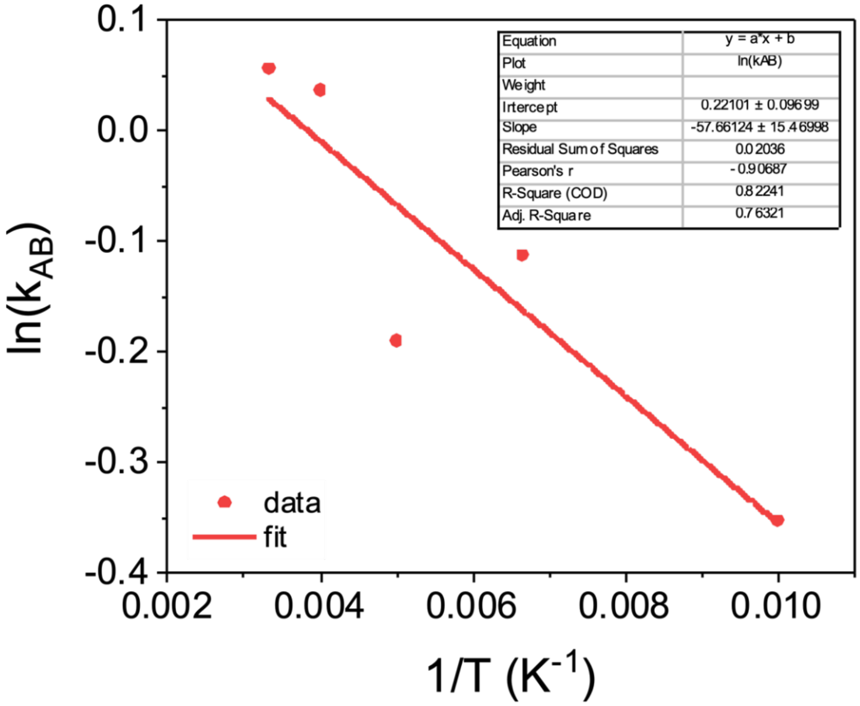

Equation	y = a*x + b
Plot	ln(kAB)
Weight	
Irtercept	0.22101 ± 0.09699
Slope	-57.66124 ± 15.46998
Residual Sum of Squares	0.02036
Pearson's r	-0.90687
R-Square (COD)	0.82241
Adj. R-Square	0.76321

Figure A21. Arrhenius fit of $k_{AB} = 1/\tau_{AB}$ values following the equation: $\ln\,(k_{AB}) = \ln(A) - \frac{E_a}{k_B T} * \frac{1}{T}$

APPENDIX B: SUPPLEMENTAL INFORMATION FOR CH. 2

Crystal Structure Determination of C_5PDI

Intensity data of a red needle single crystal of C_5PDI were collected at 100 K. A suitable single crystal with dimensions of 0.055×0.087×0.531 mm^3 was mounted on a MiTeGen loop with paratone oil on an XtaLAB Synergy diffractometer equipped with a micro-focus sealed X-ray tube PhotonJet (Cu) X-ray source and a Hybrid Pixel Array Detector (HyPix) detector. Temperature of the crystal was controlled with an Oxford Cryosystems low-temperature device. Data reduction was performed with the CrysAlisPro software using an empirical absorption correction. The structure was solved with the ShelXT structure solution program using the Intrinsic Phasing solution method and by using Olex2 as the graphical interface. The model was refined with ShelXL using least squares minimization. C0 experiences disorder out of the symmetry element it resides on, the disorder was modeled by splitting C0 using the splitSAME. The structure was deposited in the Cambridge Crystallographic Data Center (CCDC 2108992).

Identifier	**C_5PDI**
Formula	$C_{34}H_{30}N_2O_4$
Space Group	$P2_1/c$
Cell Lengths (Å)	a 33.8850(5) b 7.33970(10) c. 21.1476(3)
Cell Angles (°)	α 90 β 100.324(2) γ 90
Cell Volume ($Å^3$)	5174.38
Temperature (K)	100.15
Z	6
Crystal size (mm^3)	0.055×0.087×0.531

Radiation	CuKα (wavelength=1.54184 Å)

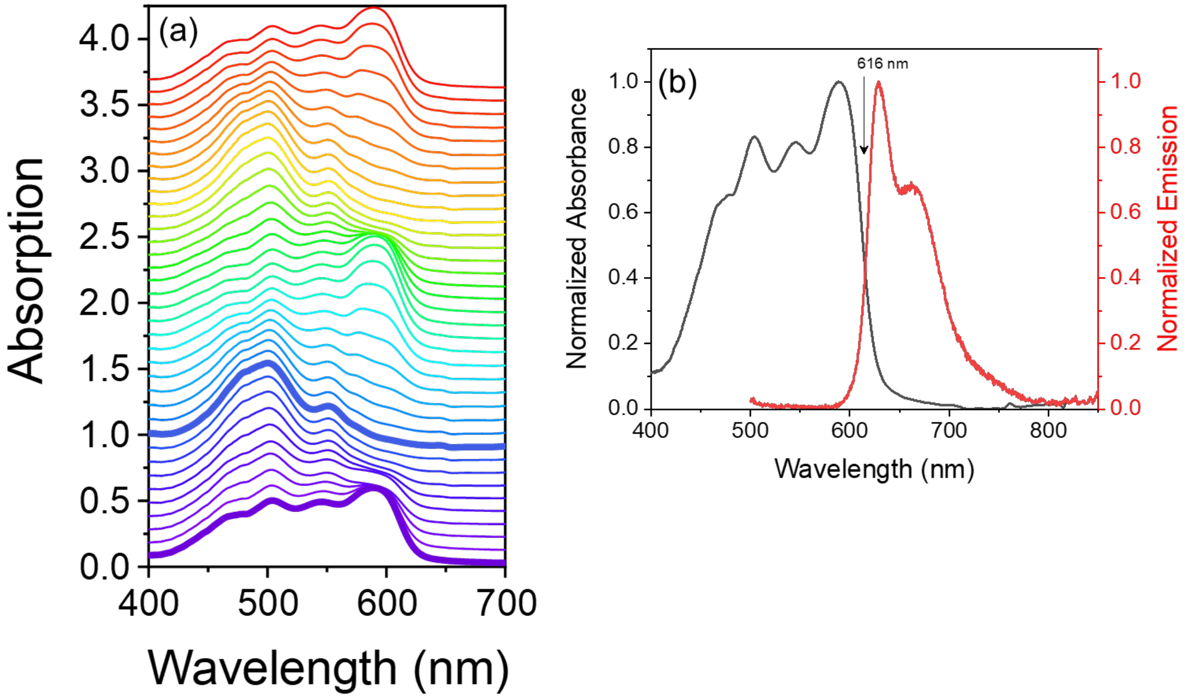

Figure B1. (a) Polarization dependence of single-crystal steady-state absorption from 0° to 360° in steps of 10°. Absorption spectra are shifted by 0.1 for clarity. Bold purple and blue spectra correspond to polarizations of 0° and 90°, respectively. (b) Overlay of the normalized polarization-averaged single crystal absorption spectra (black) and the unpolarized emission spectrum (red) normalized to the maximum of the polarization-averaged absorption spectrum.

Steady-State Single-Crystal UV-vis Absorption and Emission Spectra

The absorption at each wavelength in Figure 17 in the main text was fitted to an absorption model with two perpendicular components:[127]

$$A(\lambda) = -\log_{10}[10^{-A_{\cos}}\cos^2(\theta-\theta_0) + 10^{-A_{\sin}}\sin^2(\theta-\theta_0)], \qquad \text{(B1)}$$

where $A_{\cos}$, $A_{\sin}$ are the magnitudes of the two orthogonal components, and θ_0 is the laboratory-frame angle parallel to the cosine absorption component. The fits are overlaid on several key wavelengths in Figure 17b and confirm the presence of two perpendicularly polarized Davydov bands.

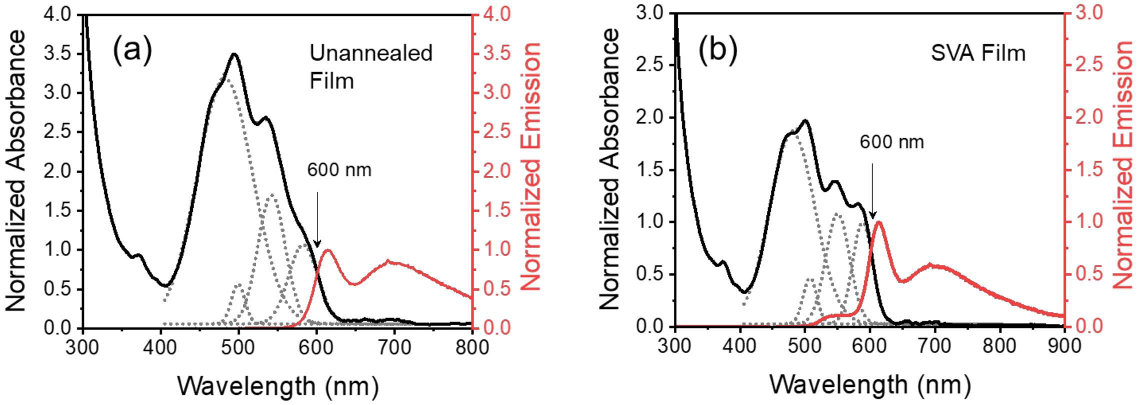

Figure B2. Scatter-corrected steady-state absorption and emission data overlaid for unannealed (a) and solvent-vapor annealed (b) films. Absorption spectra were normalized to the maxima of the 0-0 vibronic absorption bands identified using Gaussian fits (dotted lines). Crossing points are indicated at 600 nm.

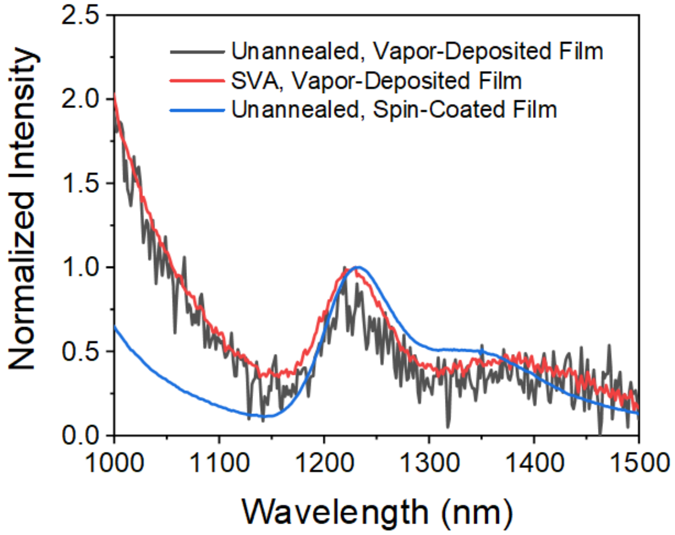

Figure B3. Near-infrared emission spectra of the C_5PDI films.

Triplet Sensitization Experiments

To verify the triplet spectrum, we doped C_5PDI with $PdPc(OBu)_8$ (10:1 w/w) in a spin-coated film. $PdPc(OBu)_8$ has a documented $E_T = 1.12$ eV,[39, 87] which upon photoexcitation, should transfer into the C_5PDI which has a lower $E_T = 1.1$ eV, as determined from phosphorescence shown in Figure S3. The sensitized nsTA C_5PDI triplet spectrum shown in Figure S4b in grey is overlaid with the C_5PDI film triplet spectra shown in red and blue (collected at different repetition rates and different pump pulse energies). The un-doped film triplet spectra show concomitant peaks with the doped film at 530 and 560 nm.

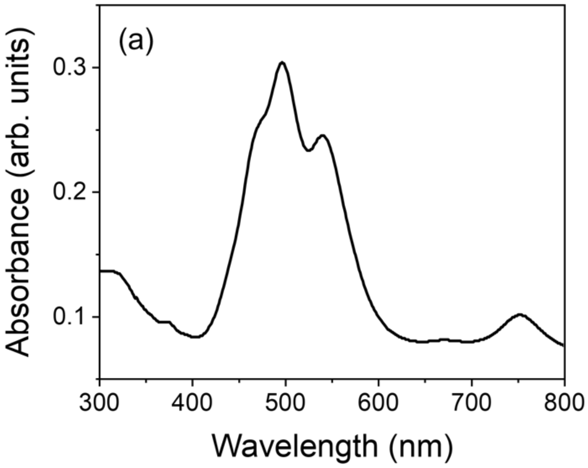

Figure B4. Triplet sensitization of C_5PDI film with $PdPc(OBu)_8$ (10:1 ratio w/w): (a) UV-vis absorbance spectrum of doped film showing C_5PDI absorbance blue of 630 nm and $PdPc(OBu)_8$ absorbance red of 630 nm (not scatter corrected); (b) sensitized nsTA (1.1 ns spectrum) overlaid with >7 ns fsTA raw spectra of C_5PDI SVA film. Positive absorption in gray trace red of 650 is from the $PdPc(OBu)_8$ triplet ESA that could not be subtracted out.

Time-Resolved Data Fitting Methodology

The femtosecond transient absorption microscopy data of the single crystals were globally fit to the following kinetic model:

$$\frac{dA}{dt} = -k_{A\to B}[A] \tag{B2}$$

$$\frac{dB}{dt} = k_{A\to B}[A] - k_{B\to C}[B]$$
$$\frac{dC}{dt} = k_{B\to C}[B] - k_{TTA}[C]^2$$

Singlet fission is taken occur unimolecularly to the correlated triplet pair state. Nanosecond transient absorption microscopy data fit only the single species present after the ~30 ns instrument response and treat this species with a bimolecular biexciton decay process:

$$\frac{dC}{dt} = k_{TTA}[C]^2 \tag{B3}$$

The femtosecond transient absorption data of the films was fit to a more complicated higher-order kinetic model that accounts for the singlet-singlet annihilation decay due to the higher laser fluence of the 1 kHz instrument:

$$\begin{aligned}\frac{dA}{dt} &= -k_{SSA}[A]^2 - k_{A\to B}[A]\\ \frac{dB}{dt} &= k_{A\to B}[A] - k_2[B]\\ \frac{dC}{dt} &= k_{B\to C}[B] - k_{C\to D}[C]\\ \frac{dD}{dt} &= k_{C\to D}[C]\end{aligned} \tag{B4}$$

For the low-fluence film TA data, the k_{SSA} constant in eq B4 is assumed to be zero. The nanosecond TA data of the films assumes two species, the latter of which relaxes back to the ground state via bimolecular decay, such as triplet-triplet annihilation:

$$\begin{aligned}\frac{dD}{dt} &= k_{C\to D}[C] - k_{D\to E}[D]\\ \frac{dD}{dt} &= k_{D\to E}[D] - k_{E\to GS}[E]^2\end{aligned} \tag{B5}$$

The time-resolved fluorescence data were acquired at the lowest relative energy density, and is only sensitive to emissive species, so it was not necessary to model bimolecular processes such as singlet-singlet annihilation and triplet-triplet annihilation. As such the time-resolved fluorescence data were fit to the following first order model

$$
\begin{aligned}
\frac{dA}{dt} &= -k_{A\to B}[A] \\
\frac{dB}{dt} &= k_{A\to B}[A] - k_{B\to GS}[B]
\end{aligned}
\tag{B6}
$$

Additional Transient Absorption Data for C₅PDI Films

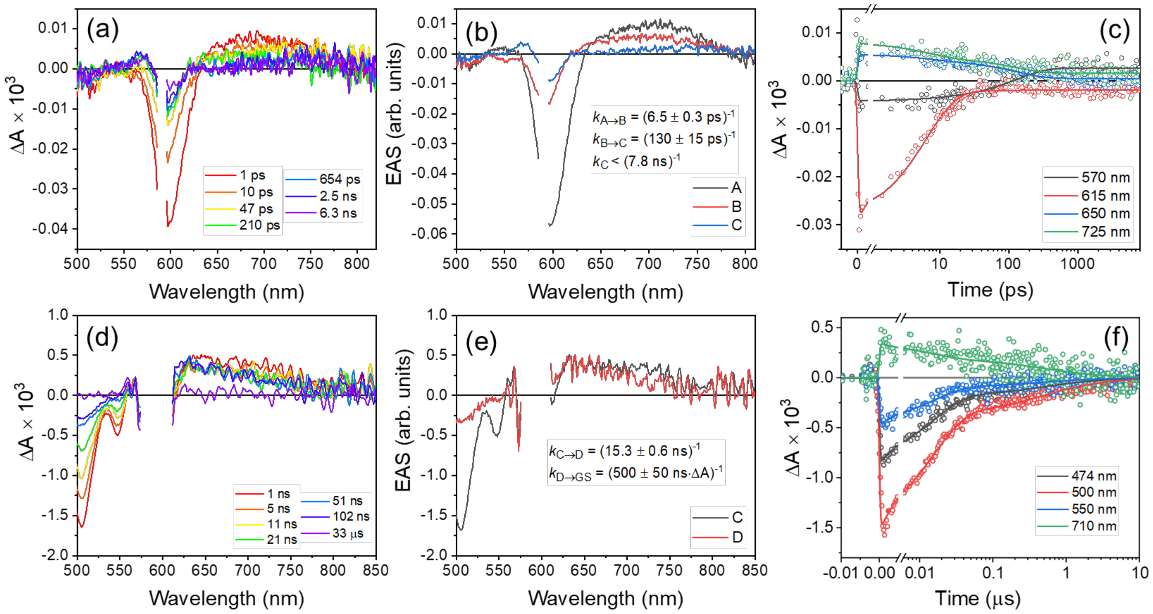

Figure B5. (a)-(c) fsTA and (d)-(f) nsTA spectra of the SVA C₅PDI film photoexcited at 590 nm @ 50 kHz pump repetition rate. (a) and (d): spectral evolution of transient absorption signals. (b) and (e): Evolution-associated spectra. (c) and (f): Kinetic traces and fits at several key wavelengths.

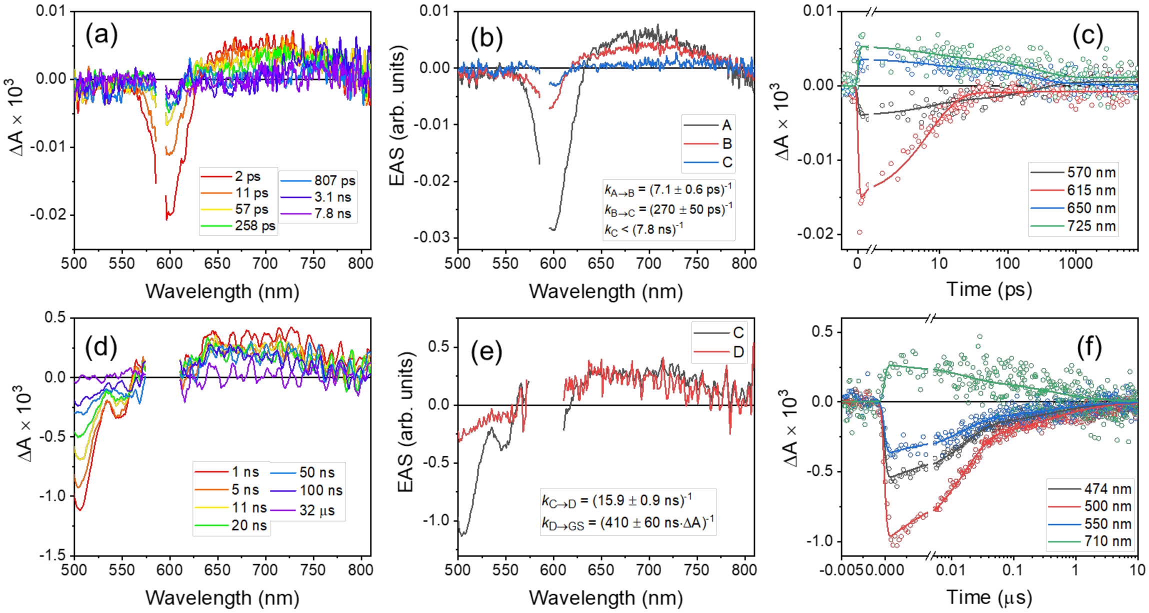

Figure B6. (a)-(c) fsTA and (d)-(f) nsTA spectra of the unannealed C5PDI film photoexcited at 590 nm @ 50 kHz pump repetition rate. (a) and (d): spectral evolution of transient absorption signals. (b) and (e): Evolution-associated spectra. (c) and (f): Kinetic traces and fits at several key wavelengths.

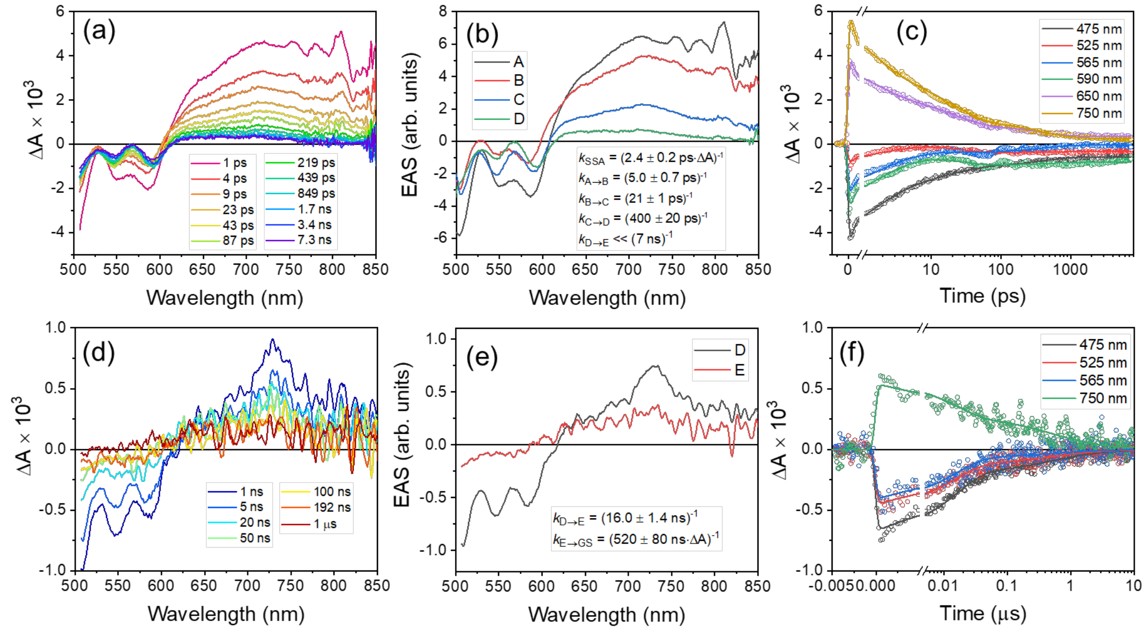

Figure B7. (a)-(c) fsTA and (d)-(f) nsTA spectra of the unannealed C5PDI film photoexcited at 500 nm @ 500 Hz pump repetition rate. (a) and (d): spectral evolution of transient absorption signals. (b) and (e): Evolution-associated spectra. (c) and (f): Kinetic traces and fits at several key wavelengths.

Laser-Induced Thermal Effects on the Films

In order to further confirm the triplet spectrum and determine whether thermal effects from the pump pulse could misconstrue the data, a thermal analysis was done on the C_5PDI film. Steady-state UV-vis absorption measurements were collected at different temperatures as shown in Figure B8c. The difference between these spectra and the room temperature spectra (taken at 20 °C) are shown plotted as ΔA vs. wavelength in Figure B8a,b. As evidenced from the ΔA plot, there is a distinct thermal effect absorptive-presenting feature at 440 nm, but this wavelength does not correspond to anything spectrally significant for C_5PDI films.

There is also a feature at 560-570 nm which does overlap directly with that of the triplet absorption in the **C_5PDI** film. In Figure B9, two selected thermal effect spectra are overlaid with

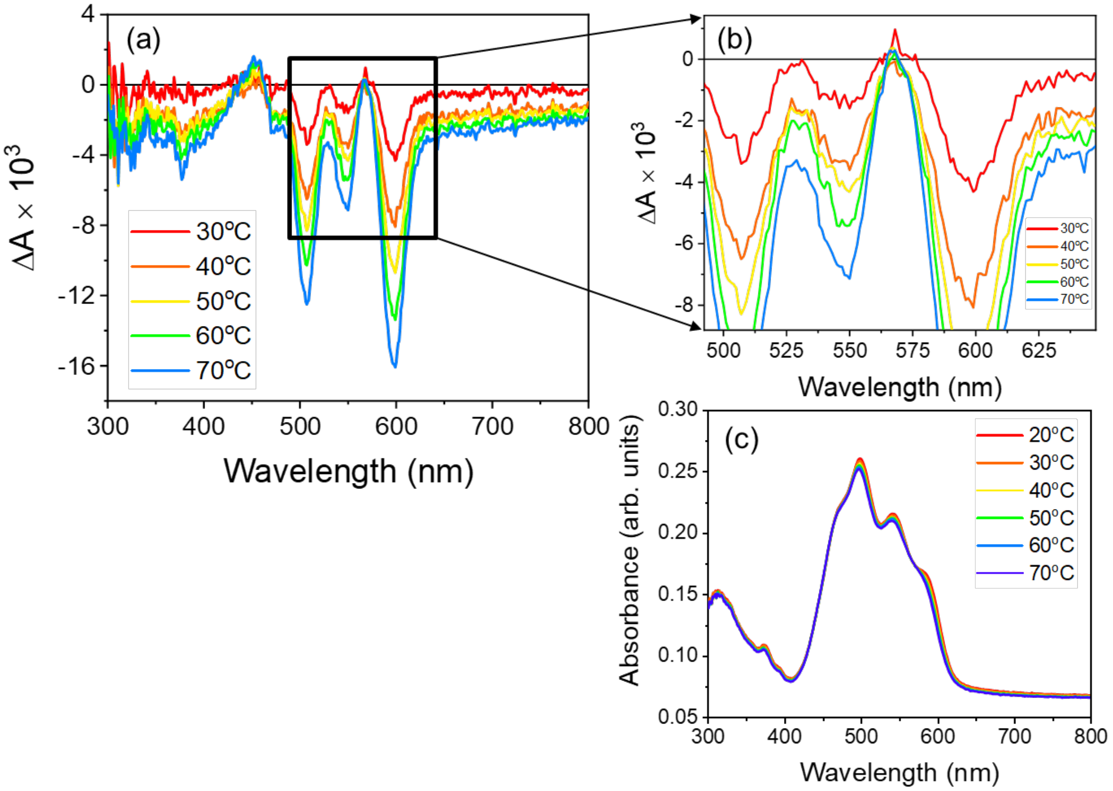

Figure B8. Temperature-dependent steady state UV-Vis absorption: (a) UV-vis data, (b) ΔA=A(T)-A(T=20 °C) comparison to study thermal effects, (c) zoomed in to wavelengths relevant to triplet absorption in TA.

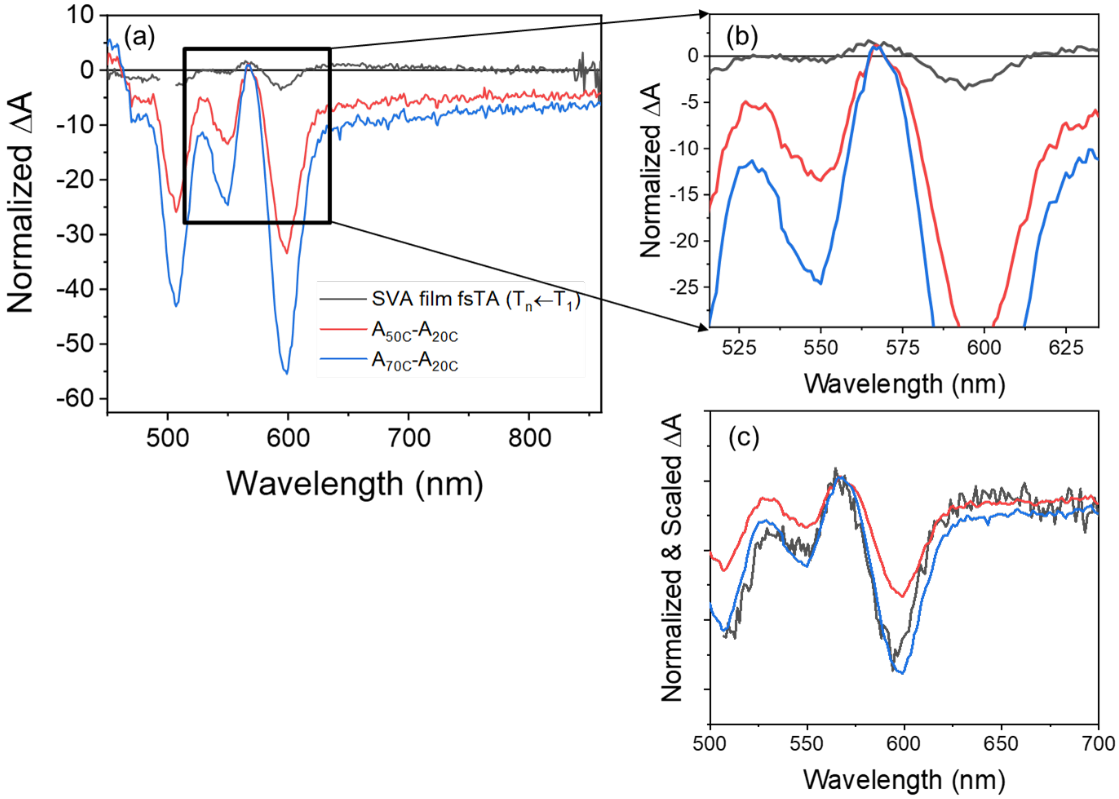

Figure B9. Temperature-dependent steady state UV-Vis absorption overlaid with fsTA triplet spectrum: (a) Selected ΔA = A(T)-A(T=20 ºC) spectra overlaid with the triplet fsTA spectrum, (b) zoomed in to wavelengths relevant to triplet absorption in TA, and (c) normalized to the peak at 570 nm.

the triplet ESA spectra from the SVA film pumped with 200 nJ/pulse of 500 nm light with a spot radius (1/*e*) of 0.5 mm. This excitation density is much higher than that of the data shown in Figure B5 where the sample was excited with 21 nJ/pulse of 590 nm light with a spot radius (1/*e*) of 0.59 mm. The pulse energy is an order of magnitude higher in the data shown in Figure B9, thus we can expect more dramatic thermal effects. However, as shown in the overlaid and normalized spectra, we can see that the triplet ESA is broader than the thermally induced absorption. We can conclude from this overlay that while thermal effects are certainly present, they do not fully obscure the triplet absorption.

Time-Resolved Fluorescence Spectroscopy of C_5PDI Films

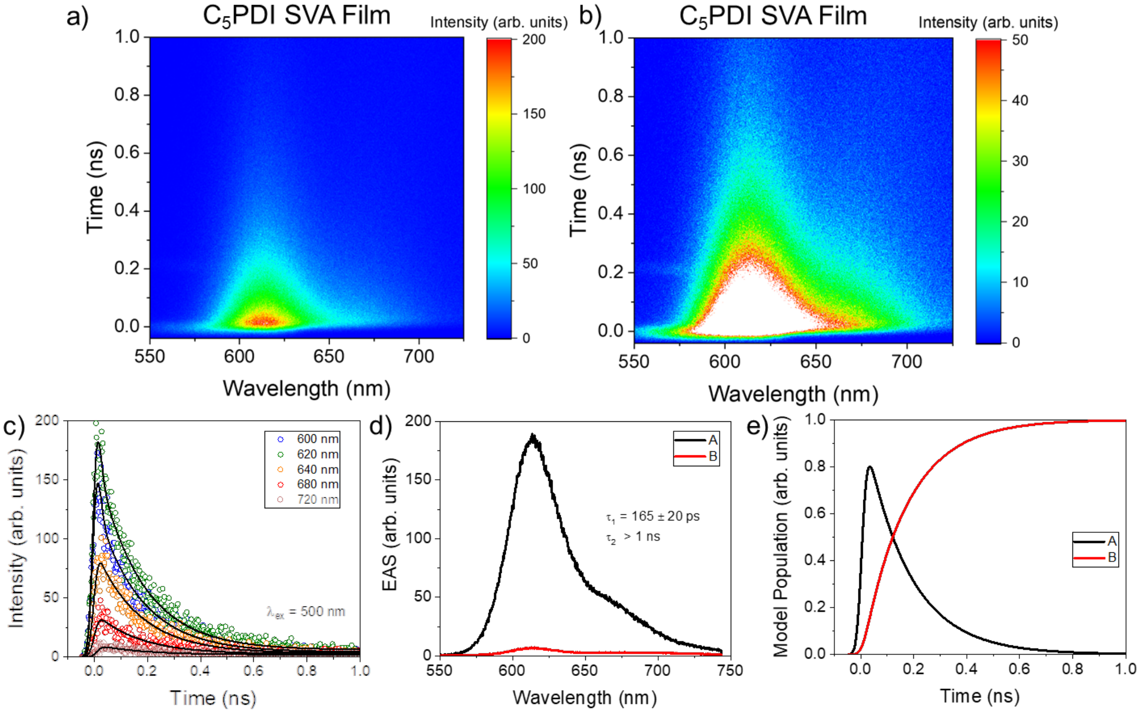

Figure B10. Time-resolved fluorescence data for the SVA C_5PDI film in a 1 ns window shown on two different intensity scales (a,b) highlighting the short- and long-lived components. c) Kinetics at several wavelengths fit to a sequential A→B model; d) evolution-associated spectra; e) model populations as functions of time.

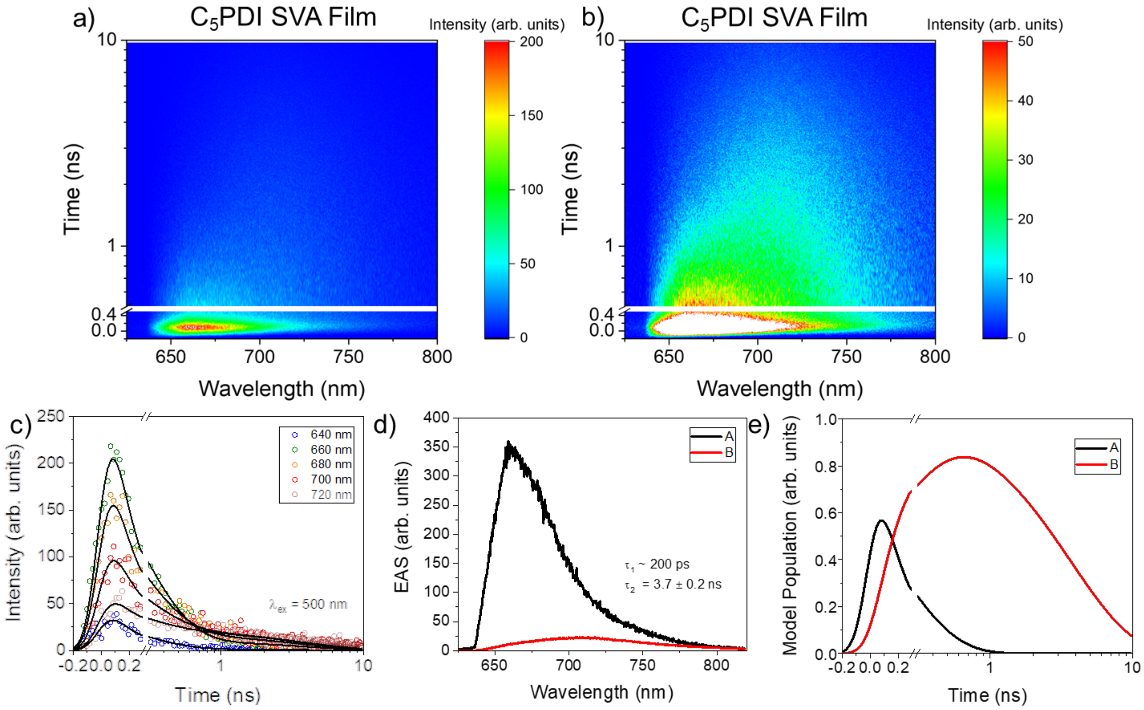

Figure B11. Time-resolved fluorescence data for the SVA C5PDI film in a 10 ns window shown on two different intensity scales (a,b) highlighting the short- and long-lived components. c) Kinetics at several wavelengths fit to a sequential A→B→GS model; d) evolution-associated spectra; e) model populations as functions of time.

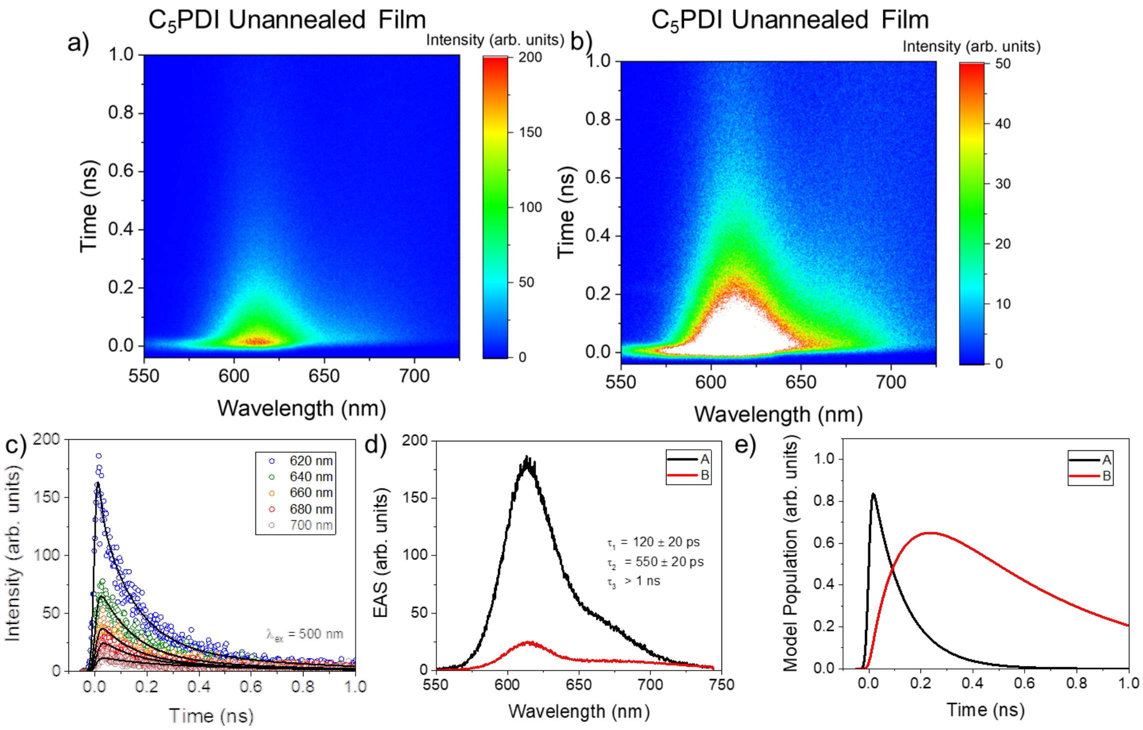

Figure B12. Time-resolved fluorescence data for the unannealed C5PDI film in a 1 ns window shown on two different intensity scales (a,b) highlighting the short- and long-lived components. c) Kinetics at several wavelengths fit to a sequential A→B→GS model; d) evolution-associated spectra; e) model populations as functions of time.

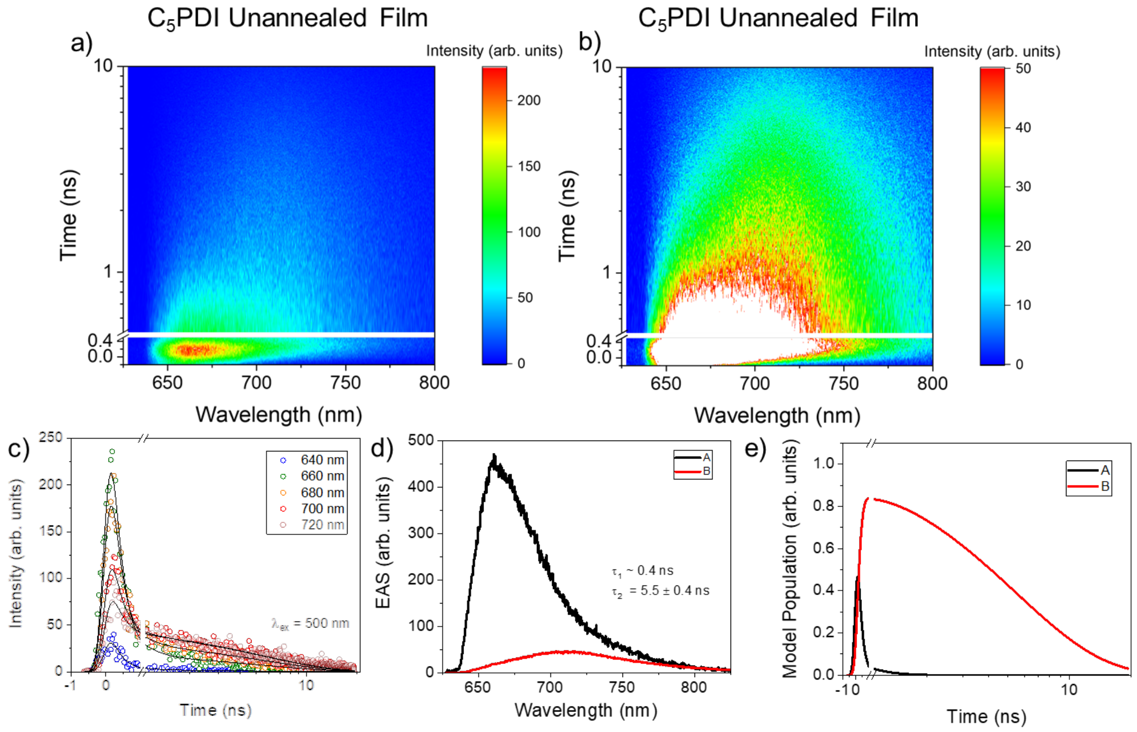

Figure B13. Time-resolved fluorescence data for the unannealed C_5PDI film in a 10 ns window shown on two different intensity scales (a,b) highlighting the short- and long-lived components. c) Kinetics at several wavelengths fit to a sequential A→B→GS model; d) evolution-associated spectra; e) model populations as functions of time.

Single Crystal and Film Triplet Yield Calculations: Spectral Deconvolution

To calculate the triplet quantum yield (Φ_T) of excitons generated in the crystal and film, spectral deconvolution, as described in detail previously,[40, 42] was used. Briefly, first, basis spectra were generated for the ground-state bleach (S_0), excited singlet state (S_1), and excited triplet state (T_1) from femtosecond transient absorption (fsTA) data with a pump pulse energy of 21 nJ for the film (to avoid artificial yield losses from singlet-singlet annihilation) and from femtosecond transient absorption microscopy data (fsTAM) data with a pump pulse energy of 40 pJ for the crystal. These spectra were normalized to the ground state bleach and are displayed in Figures B14a and B15a.

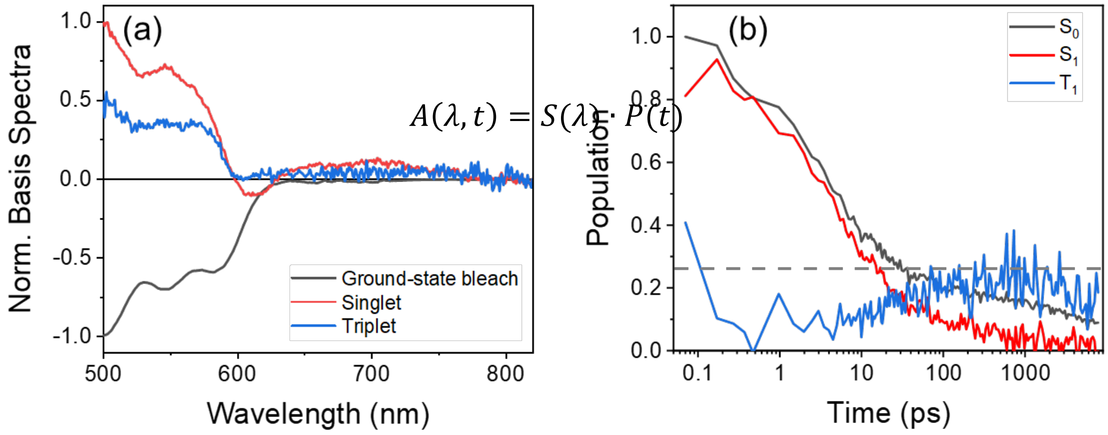

Figure B14. Spectral deconvolution and subsequent quantum yield populations for the solvent-vapor annealed **C_5PDI** film using fsTA data (21 nJ/pulse) data: (a) normalized basis spectra, (b) normalized populations calculated from linear regression in MATLAB showing a triplet yield of 29 ± 8%.

In order to determine the quantum yield of each state (S_0, S_1, and T_1), a linear regression was performed using MATLAB. Given the following relationship:

$$A(\lambda, t) = S(\lambda) \cdot P(t)$$

where A is absorbance, S is species (basis spectra), P is the population of the species, λ is wavelength, and t is time (in picoseconds), we perform a linear regression to solve for $P(t)$ of each state. The resulting population vs. time relationship is shown in Figures B14b and B15b.

This calculation was repeated in triplicate using different time points to determine the basis spectra and calculate the subsequent linear regression. This calculation results in a Φ_T of 70 ± 2% for the crystal and 29 ± 8% for the film. These values are appropriate to compare singlet fission efficiency between crystal vs. film of the same material because we made the same assumptions in each calculation. Typically, when finding the basis spectra for spectral deconvolution calculations, we would subtract the bleach (negative) features from the triplet and singlet absorption spectrums until we had smooth, positive absorptive features, as these excited state absorption spectra are well known for PDIs.[269] However, when comparing values for the Φ_T of C_5PDI in the crystal and film, subtracting this bleach would be arbitrary and would render the values incomparable due to significant overlap of GSB, singlet, and triplet features in the TA data. Thus, we elected to subtract the bleach so that the most negative feature in the TA time trace we chose as that basis spectrum went to zero. This allows us a basis to compare the Φ_T values and get a better understanding of how singlet fission efficiency depends on order and crystallinity. Because we know the PDI triplet absorption spectra is a smooth absorption between 500-600 nm with no bleach or negative features,[270-271] we can also assume that the values we calculated are lower-bound Φ_T values and

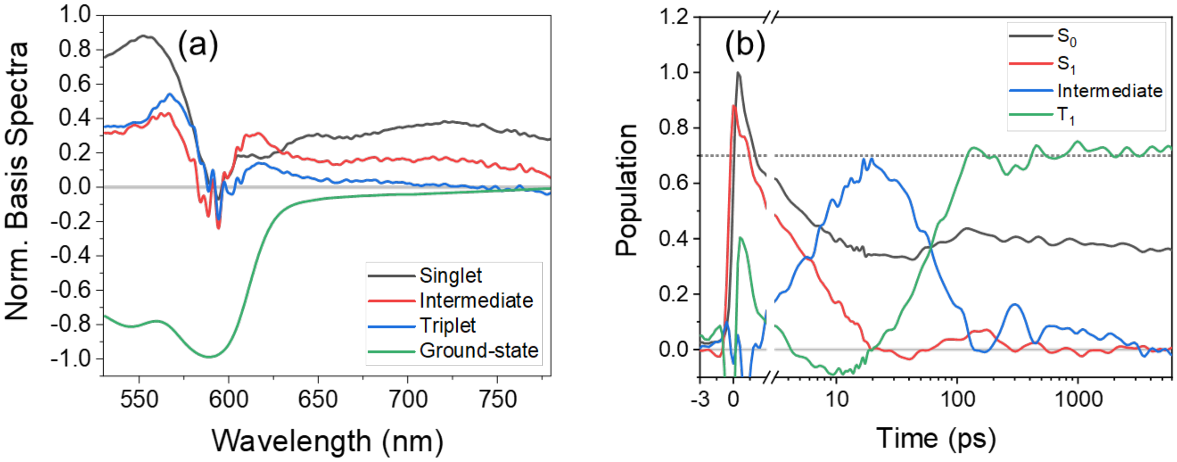

Figure B15. Spectral deconvolution and subsequent quantum yield populations for the **C_5PDI** single crystal using fsTAM data: (a) normalized basis spectra, (b) normalized populations calculated from linear regression in MATLAB showing a triplet yield of 70 ± 2 %.

the Φ_T might in fact exceed 100% in the crystal if we were able to make fewer assumptions and further deconvolute the singlet, triplet, and GSB spectra. While the large heterogeneity in the film may influence the triplet yield analysis, both the TA and steady-state absorption data were acquired over macroscopic volumes, 1 mm and ~1 cm, respectively, so the effects of heterogeneity are incorporated into the spectral separation and may also contribute to the relatively small values of these lower bounds.

Significant triplet-triplet annihilation within the correlated ^{1}(TT) state along with the presence of excimer-like trap states will dramatically reduce the triplet yield. Additionally, singlet fission in PDIs is endoergic and typically slower than in other singlet fission chromophores like TDIs, QDIs, or acenes, allowing for these competing kinetic pathways to occur before triplet formation. Additionally, while the single crystals present relatively monodisperse and homogeneous samples for spectral deconvolution, the film's structural heterogeneity and subsequent potential for different populations to undergo SF at different times may also contribute to the low triplet yield in the film. While this yield is low in the film, it is an interesting phenomenon to explore in materials with this crystal structure given the high triplet yield found in the C_5TDI analogue.[70]

Direct Triplet Yield Comparison between Single Crystal and Film Samples

Here we show a more direct way to compare the Φ_T of the different C_5PDI crystallinities (crystal, annealed film, unannealed film) albeit with a loss of the absolute value of Φ_T for each sample. For each sample we found the maximum amplitude in absolute value of the ground-state bleach on the TA surface (which occurs at earlier delays), $|\max(A_{GSB})|$, and the maximum amplitude of the triplet feature (which occurs at late delays), $|\max(A_T)|$, and calculated their ratio, $\xi \equiv |\max(A_T)|/|\max(A_{GSB})|$. This ratio is a good indicator for the number of triplets generated relative to the overall singlets generated. Since ξ is proportional to its sample's Φ_T, this method directly demonstrates that singlet fission is more efficient in the crystal than the film.

For the crystal, we chose the ground-state bleach feature at 592 nm ($\Delta t = 0.48$ ps) and the triplet feature at 566 nm ($\Delta t = 6$ ns). The ratio in the crystal is:

$$\xi_{crystal} = \frac{\left|\max\left(A_{T,crystal}\right)\right|}{\left|\max\left(A_{GSB,crystal}\right)\right|} = \frac{0.37}{3.7} = 0.1$$

For the films, we chose the ground-state bleach feature at 600 nm ($\Delta t = 0.07$ ps) and the triplet feature at 566 nm ($\Delta t = 5$ ns). The ratios in the annealed and unannealed films are:

$$\xi_{annealed\ film} = \frac{0.4}{6.7} = 0.06$$

$$\xi_{unannealed\ film} = \frac{0.05}{3.6} = 0.01$$

Thus, we see 0.1/0.06 = ×1.66 more triplets generated in the crystal than the annealed film. The observation of higher triplet production in the crystal than in the film is expected due to enhanced crystallinity and order.

Atomic force microscopy images of C_5PDI films

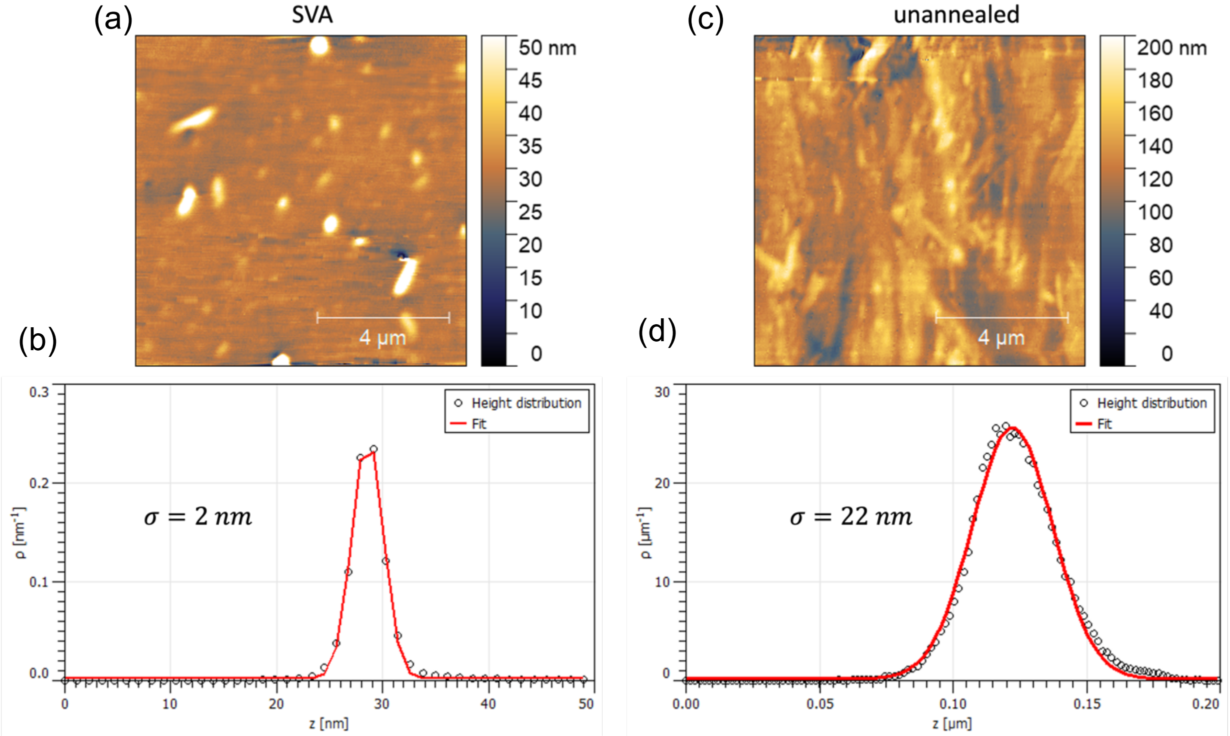

Figure B16. (a,c) atomic force microscopy images and (b,d) height distribution plots for (a,b) SVA film and (c,d) unannealed film.

Atomic force microscopy (AFM) images in Figure B16 of the annealed and unannealed films show the SVA film is much smoother than the unannealed film, as expected from the solvent vapor annealing process. The height distribution plots shown in Figure B16b,d show a larger distribution of film height in the unannealed film. The standard deviation of the height distribution is an order of magnitude smaller for the SVA film, additionally supporting the smoothing induced by the annealing process. The sigma of the Gaussian fit on the unannealed film also agrees well with the profilometry error.

APPENDIX C: SUPPLEMENTAL INFORMATION FOR CH. 3

X-ray Diffraction and Scattering Data

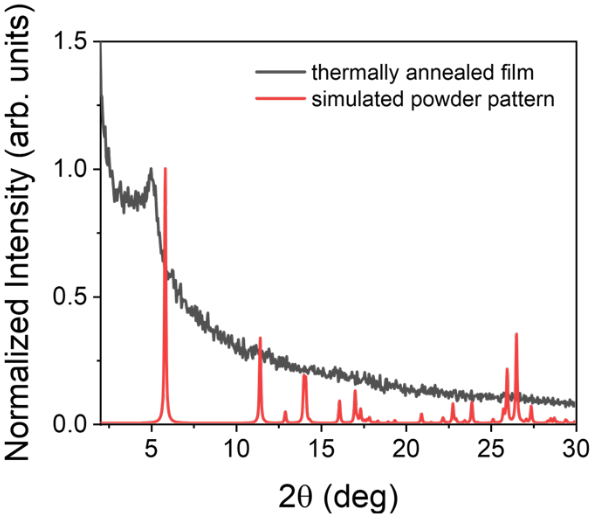

Figure C1. GIXRD pattern of ***t*-Bu-ZnNc** annealed film overlaid with simulated powder pattern from bare **ZnNc**.[149]

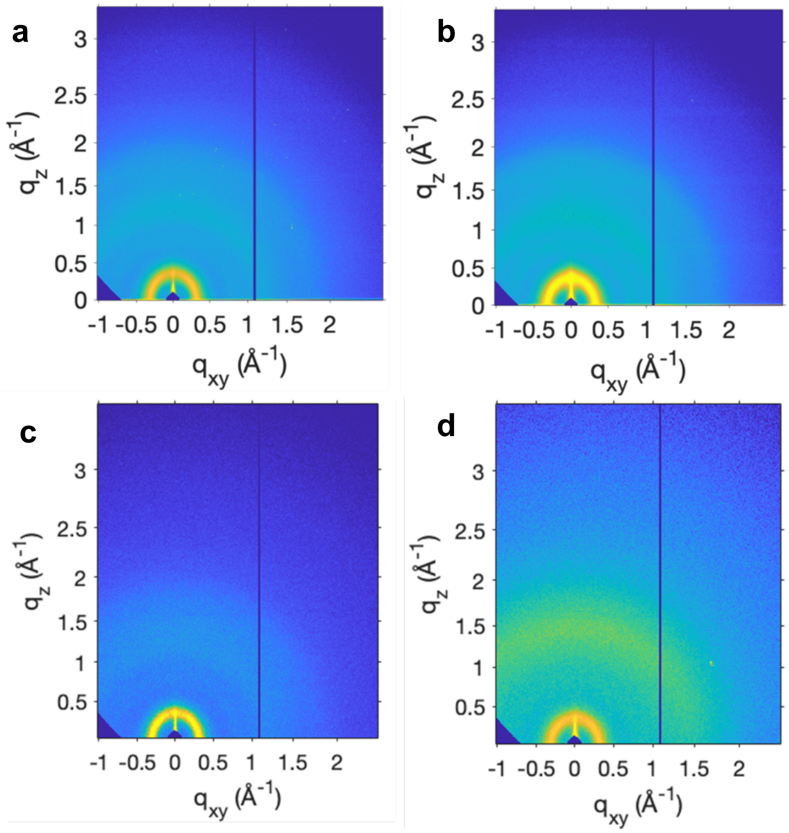

Figure C2. GIWAXS data for ***t*-Bu-ZnNc** films: (a) unannealed on sapphire, (b) thermally annealed on sapphire, (c) unannealed on quartz, (d) thermally annealed on quartz substrates.

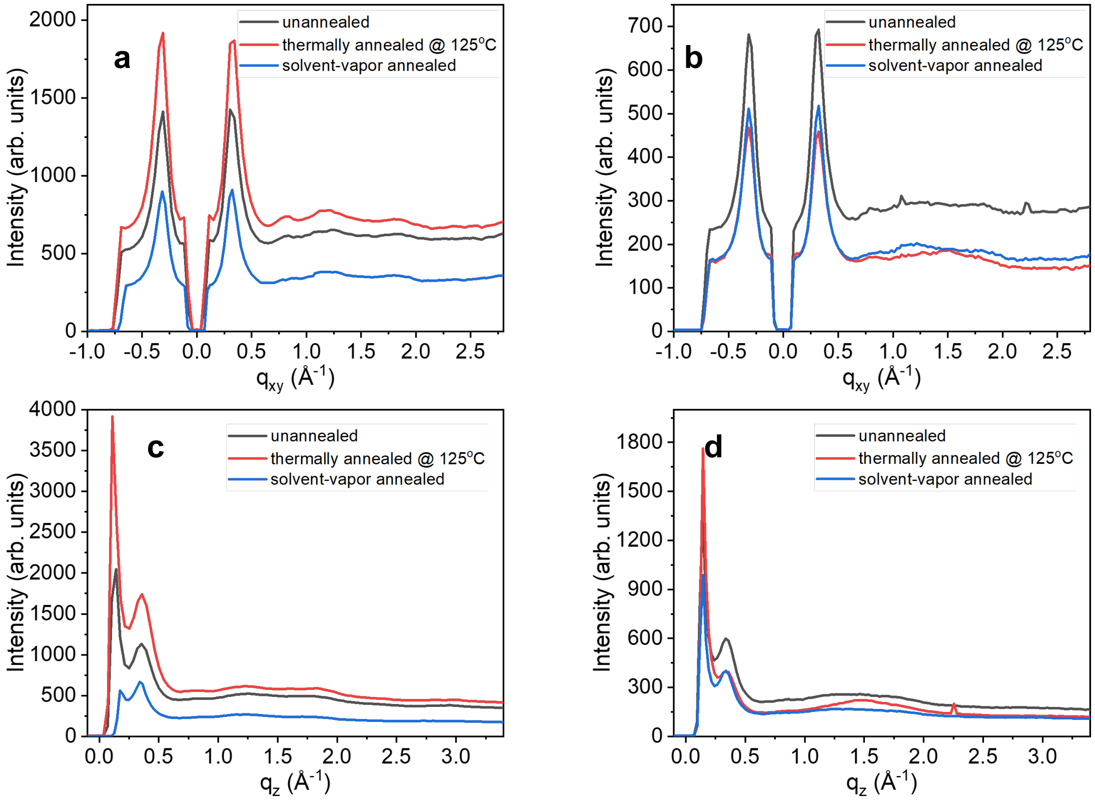

Figure C3. GIWAXS linecuts of ***t*-Bu-ZnNc** films on sapphire (a, c) and quartz (column, d).

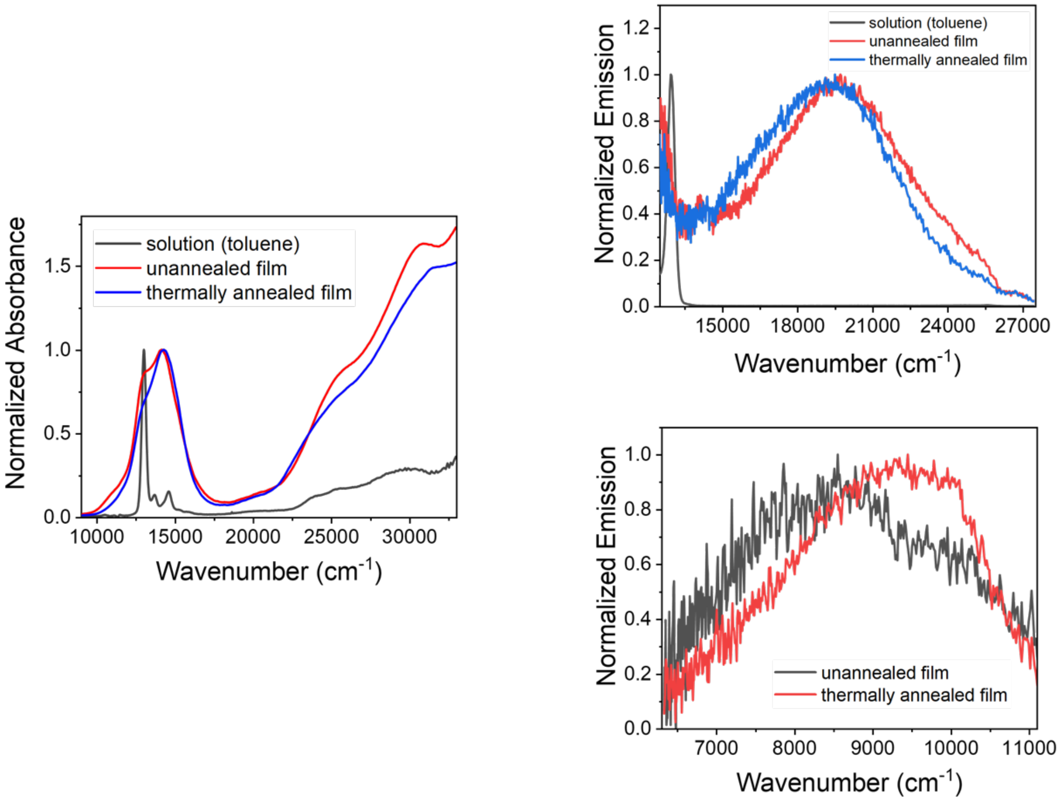

Figure C4. Steady-state UV-vis absorption and emission spectra of ***t*-Bu-ZnNc** in room-temperature toluene and spin-coated films shown versus wavenumber.

Additional Steady-State Spectroscopy Data & Analysis

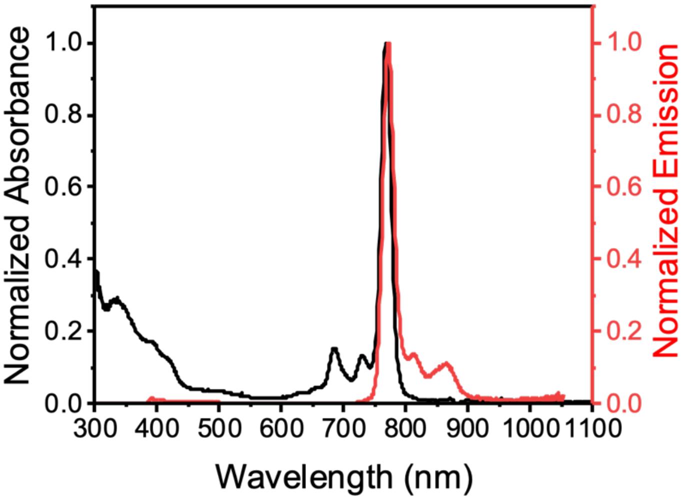

Figure C5. Steady-state UV-vis absorption and emission spectra of ***t*-Bu-ZnNc** in room-temperature toluene.

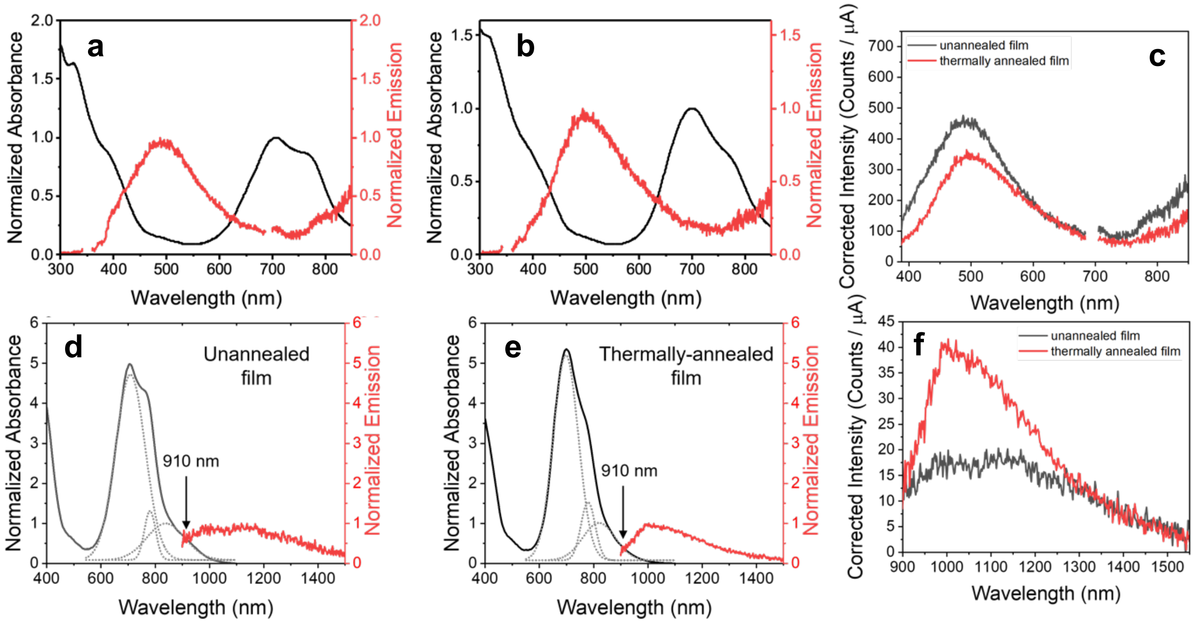

Figure C6. Steady-state UV-vis absorption and emission spectra of ***t*-Bu-ZnNc** (a),(d) unannealed film and (b),(e) thermally annealed film; (a),(b) visible absorption and emission showing S_2 energy; (d),(e) visible absorption and near-infrared emission showing S_1 energy; (c),(f) corrected un-normalized emission spectra.

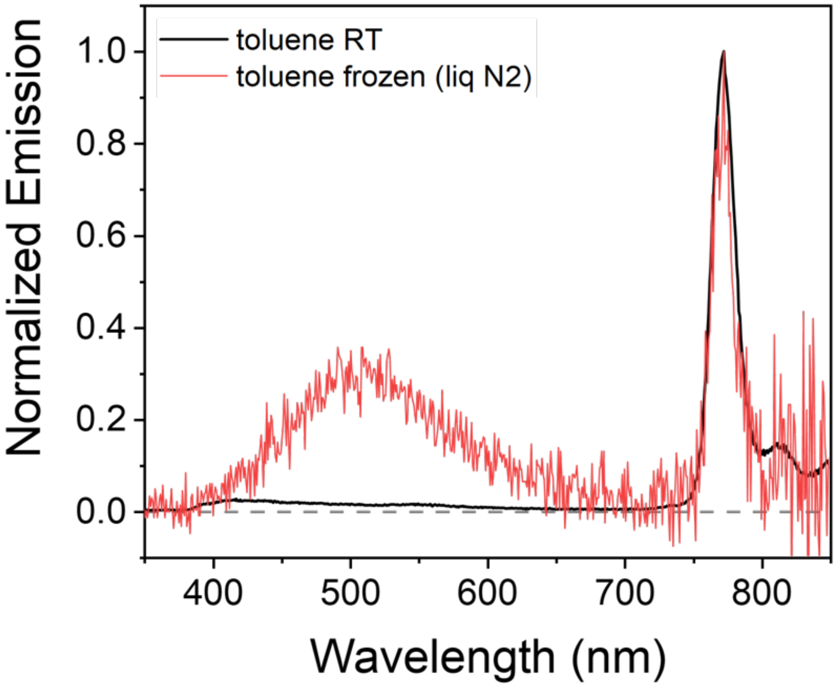

Figure C7. Emission spectra of ***t*-Bu-ZnNc** in toluene at room temperature (black) and frozen in liquid nitrogen (red)

Temperature-dependent emission measurements were taken of ***t*-Bu-ZnNc** in toluene in an optical cryostat in order to explore the role of molecular motion on the emission behavior. The solution was dilute with an optical density below 0.1 at the excitation wavelength (350 nm), as shown in Figure C8a, thereby minimizing the effects of aggregation, inner filter effects, and self-absorption. Measuring the emission of ***t*-Bu-ZnNc** over a range of temperatures from 220 K to 108 K, we observe that the S_2 emission increases as the temperature decreases, consistent with Figure C5. Using the measured energy gap between S_2 and S_1 (1.69 eV, see main text) we can show these data indeed follow the energy gap law. The integrated emission intensity, A, under the S_2 emission spectrum is proportional to the S_2 quantum yield (Φ_{S2}):

$$\Phi_{S2} = c * A \quad \text{(C1)}$$

where c is an arbitrary constant. Kinetically, Φ_{S2} can be expressed as:

$$\Phi_{S2} = \frac{k_f}{k_f + k_{IC}} \quad \text{(C2)}$$

where k_f is the radiative rate constant and k_{IC} is the rate constant for internal conversion between S_2 and S_1. From the energy gap law, k_{IC} is expressed as:[145]

$$k_{IC} = k_0 e^{-\Delta E / k_B T} \quad \text{(C3)}$$

where k_0 is the infinite-temperature rate limit, ΔE is the energy difference between S_2 and S_1, k_B is the Boltzmann constant, and T is temperature. If we substitute (C1) and (C3) into (C2) and rearrange, we have an Arrhenius-type relationship with which we can plot the fluorescence data:

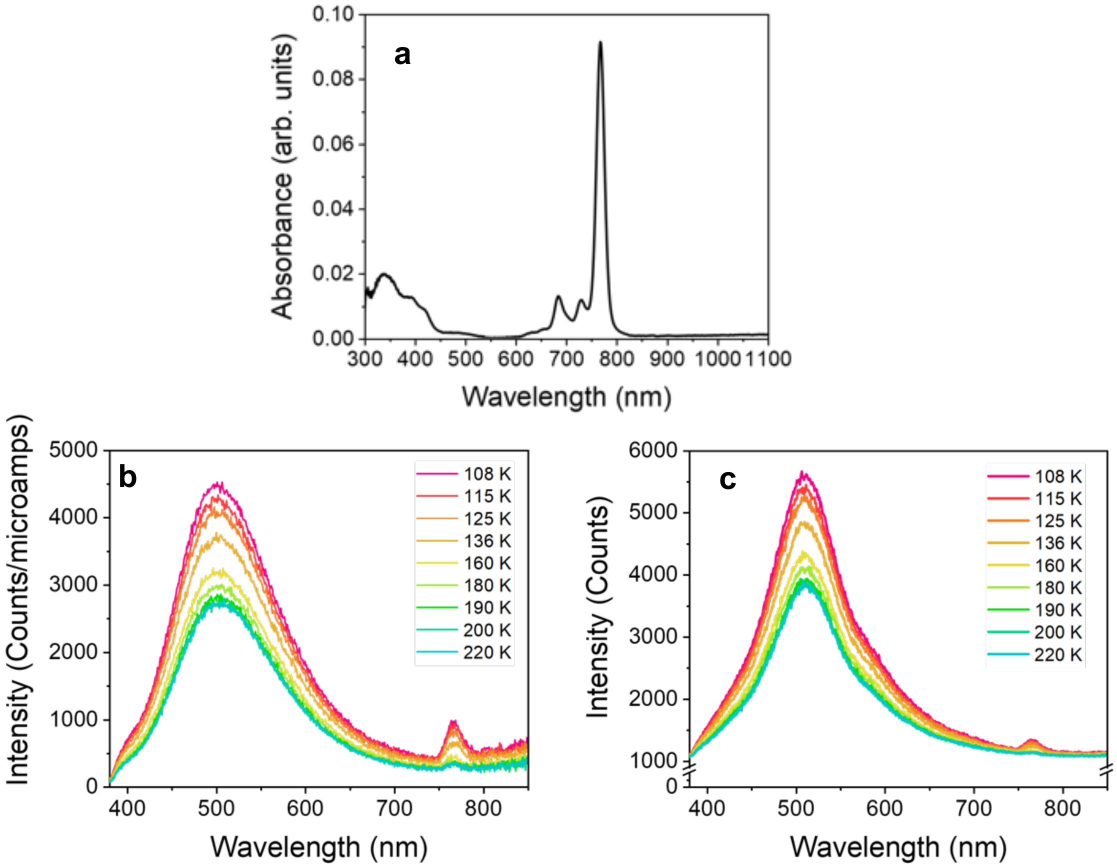

Figure C8. (a) Steady-state UV-vis absorption spectra of ***t*-Bu-ZnNc** in toluene; (b,c) steady-state emission spectra of ***t*-Bu-ZnNc** in toluene at different temperatures (corrected – b, uncorrected – c)

$$\ln\left(\frac{1}{c*A}-1\right)=\ln\left(\frac{k_f}{k_0}\right)-\frac{\Delta E}{k_B}*\frac{1}{T} \tag{C4}$$

where the ordinate-intercept is $\ln\left(\frac{k_f}{k_0}\right)$ and the slope is $-\frac{\Delta E}{k_B}$. Because we cannot accurately measure the quantum yield of S_2 emission in the optical cryostat, the system is underdetermined, and the value of c must be estimated. Given the short S_2 lifetime (6-21 ps in the films), the quantum yield is likely on the order of 1%, which from eq C1 gives an approximate value of $c = 1.0 \times 10^{-7}$ nm^{-1}. Figure C9 shows that with this value eq S4 does in fact give a linear trend with a high R^2 value of

0.97. We note that the choice of *c* does not affect the linearity of these data over this temperature range. Thus, the excited-state dynamics of ***t*-Bu-ZnNc** do obey the energy gap law and the rate of internal conversion is slowed at lower temperatures due to hindering of the rotational motion of the *t*-butyl groups in solution.

Table C1. Data and calculations for Arrhenius plot

Temperature (K)	1/T (1/K)	Area under S_2 Curve (nm)	1/(c*A)‡	ln[1/(c*A)-1] ‡
108	0.0092	591939	16.9	2.77
115	0.0087	538190	18.6	2.87
125	0.008	514115	19.5	2.92
136	0.0074	471114	21.2	3.01
160	0.0063	406772	24.6	3.16
180	0.0056	386103	25.9	3.21
190	0.0053	357657	28.0	3.29
200	0.005	355352	28.1	3.30
220	0.0046	364650	27.4	3.27

‡Evaluated with *c* estimated as $c = 1.0 \times 10^{-7}$ nm^{-1}

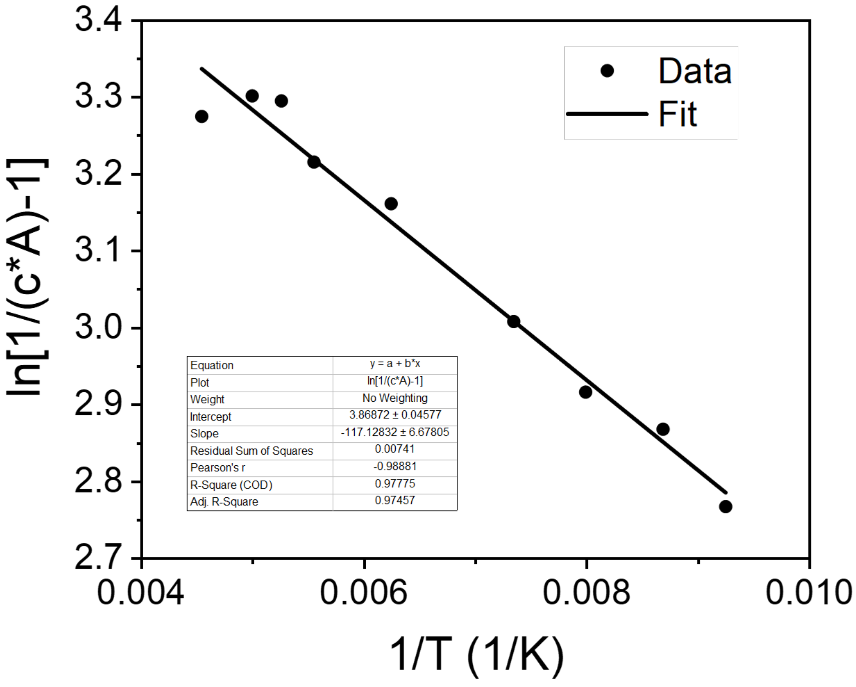

Equation	y = a + b*x
Plot	ln[1/(c*A)-1]
Weight	No Weighting
Intercept	3.86872 ± 0.04577
Slope	-117.12832 ± 6.67805
Residual Sum of Squares	0.00741
Pearson's r	-0.98881
R-Square (COD)	0.97775
Adj. R-Square	0.97457

Figure C9. Energy-gap law fit of the emission data for $c = 1.0 \times 10^{-7}$ nm^{-1}.

Additional Transient Absorption Spectra & Analysis

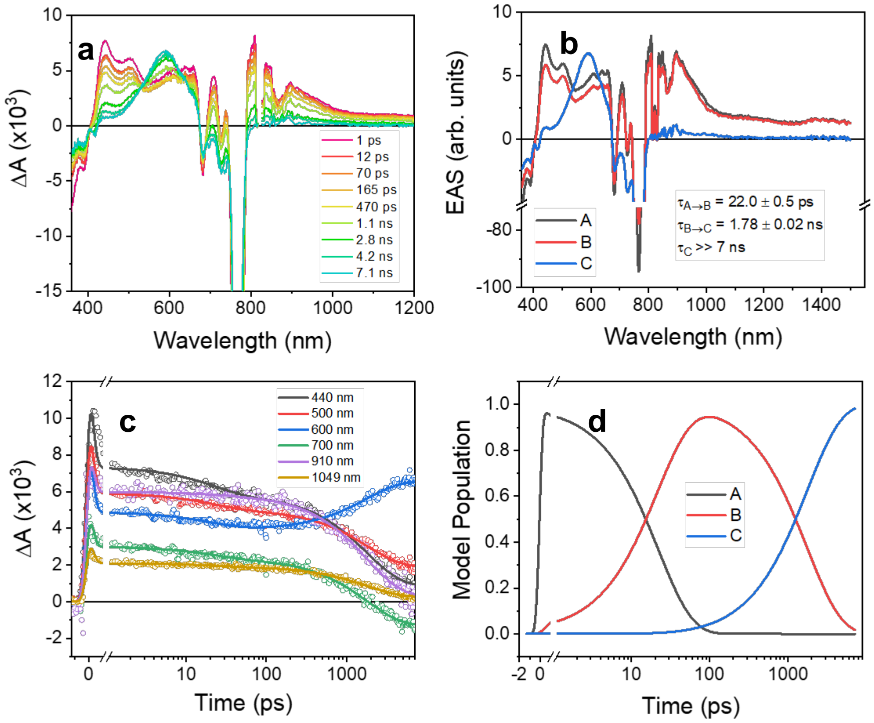

Figure C10. Femtosecond transient absorption spectroscopy of ***t*-Bu-ZnNc** in toluene excited at 765 nm: (a) raw spectra, (b) evolution-associated spectra, (c) quality of kinetic fit, (d) population of states versus time.

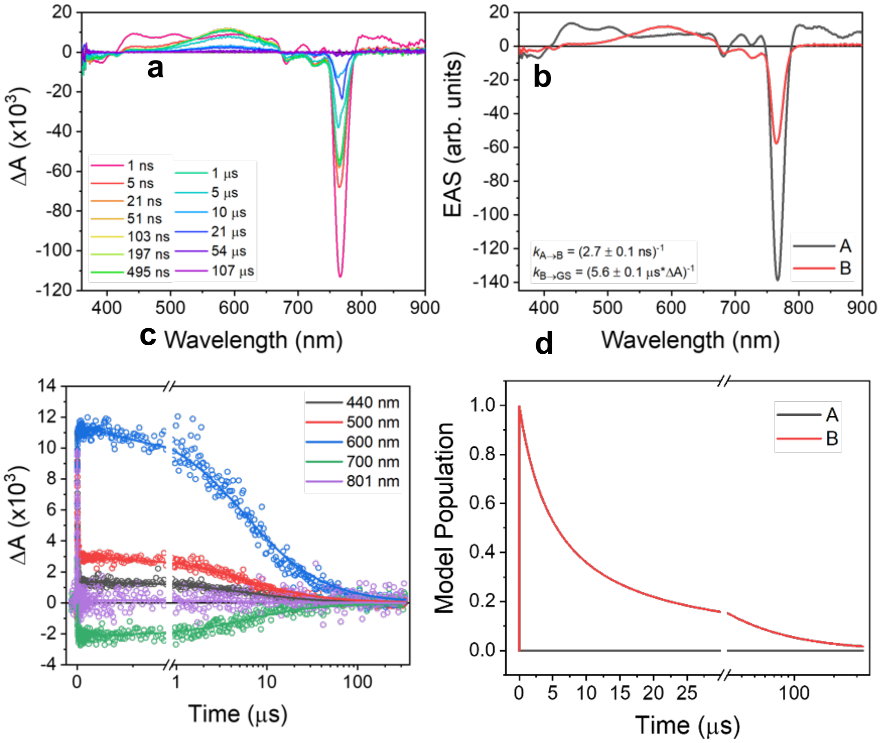

Figure C11. Nanosecond transient absorption spectroscopy of ***t*-Bu-ZnNc** in toluene excited at 765 nm: (a) raw spectra, (b) evolution-associated spectra, (c) quality of kinetic fit, (d) population of states versus time.

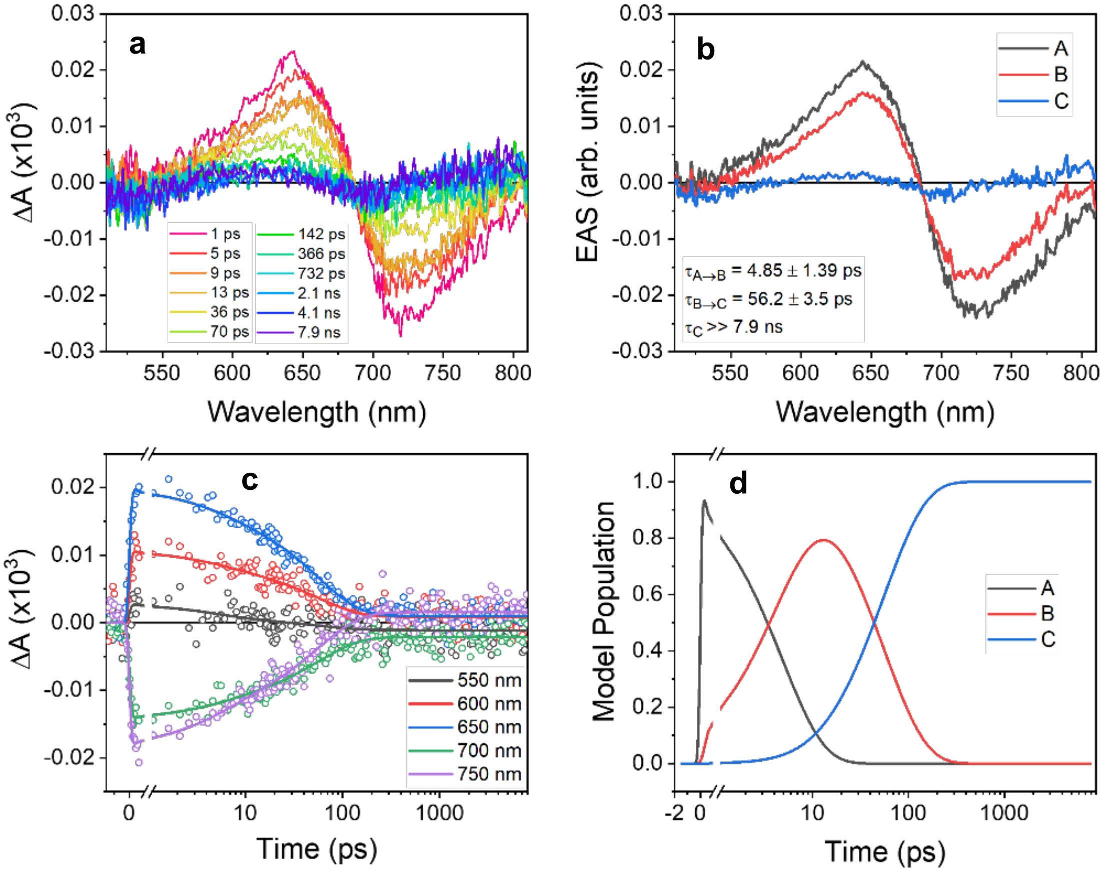

Figure C12. Femtosecond transient absorption spectroscopy of ***t*-Bu-ZnNc** unannealed film excited at 410 nm: (a) raw spectra, (b) evolution-associated spectra, (c) quality of kinetic fit, (d) evolution of population vs time.

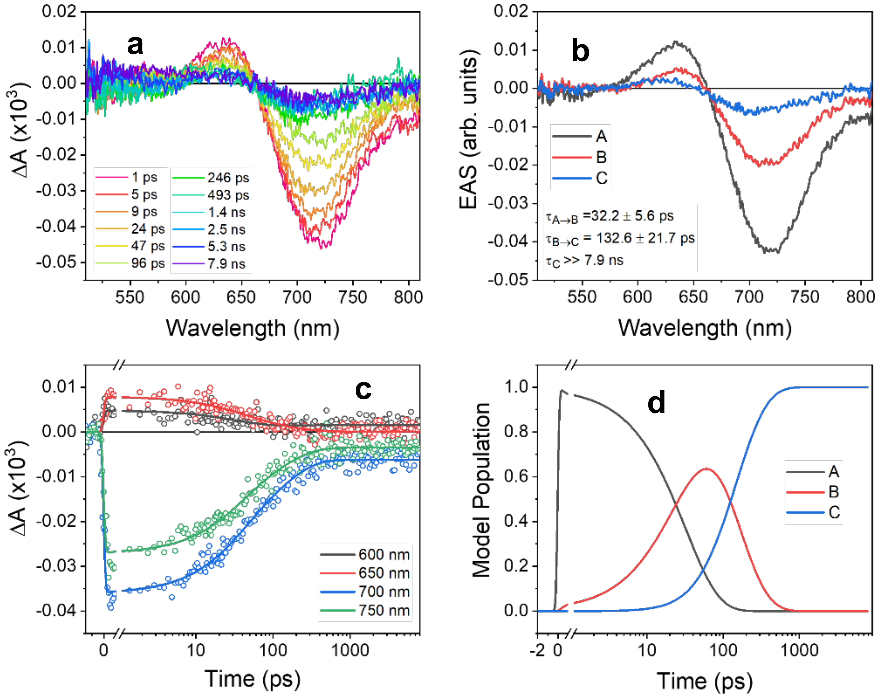

Figure C13. Femtosecond transient absorption spectroscopy of ***t*-Bu-ZnNc** thermally annealed film excited at 410 nm: (a) raw spectra, (b) evolution-associated spectra, (c) quality of kinetic fit, (d) evolution of population vs time.

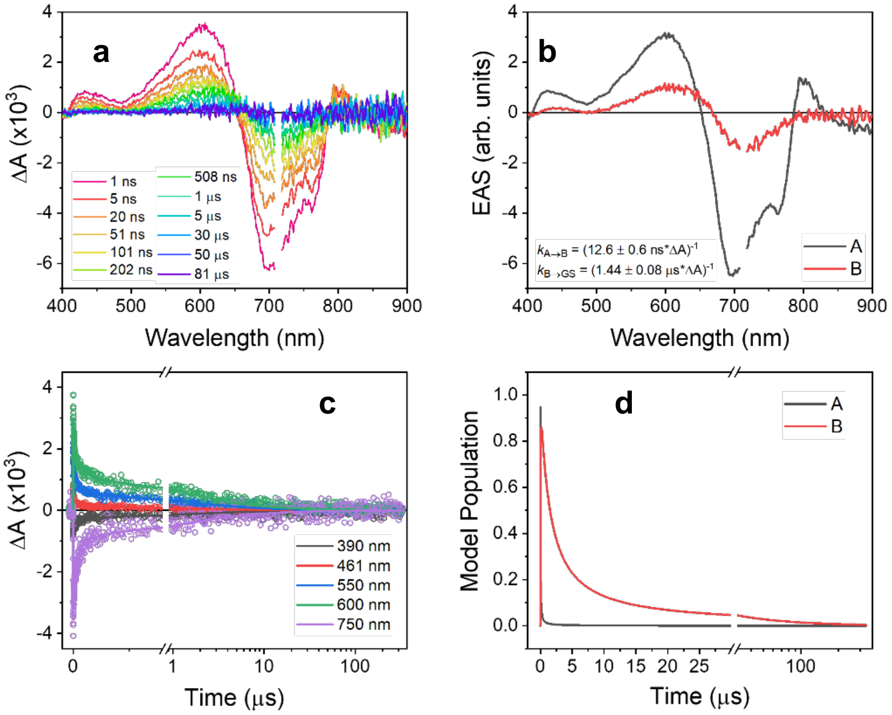

Figure C14. Nanosecond transient absorption spectroscopy of ***t*-Bu-ZnNc** unannealed film excited at 712 nm: (a) raw spectra, (b) evolution-associated spectra, (c) quality of kinetic fit, (d) evolution of population vs time.

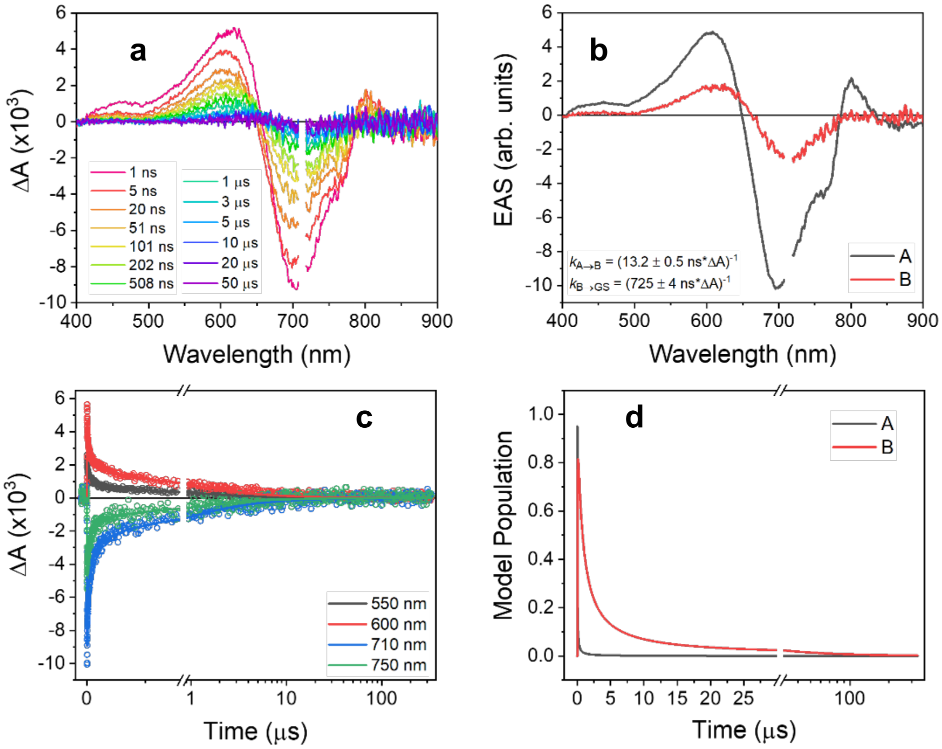

Figure C15. Nanosecond transient absorption spectroscopy of ***t*-Bu-ZnNc** thermally annealed film excited at 712 nm: (a) raw spectra, (b) evolution-associated spectra, (c) quality of kinetic fit, (d) evolution of population vs time.

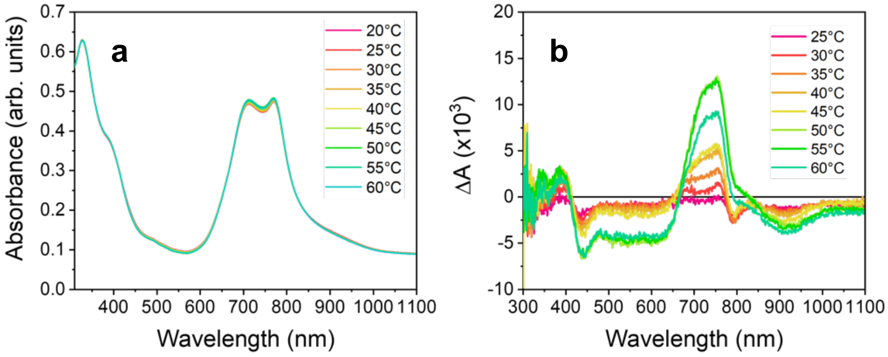

Figure C16. Thermal heating effects from laser on ***t*-Bu-ZnNc** films: (a) UV-vis absorption at different temperatures, (b) ΔA at different temperatures.

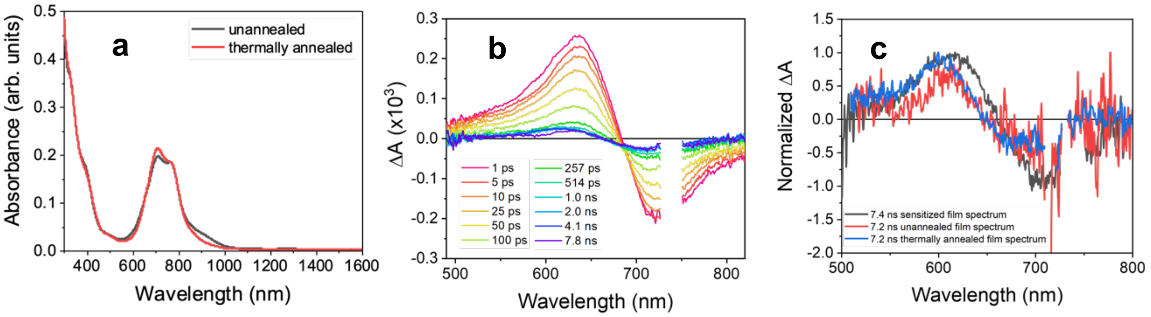

Figure C17. ***t*-Bu-ZnNc** film doped with $Pd(PPh_3)_2Cl_2$ (10:1 w/w, dissolved in $CHCl_3$ 15 mg/mL and spin-coated on clean sapphire at 1500 rpm): (a) UV-vis absorption of film, (b) raw data for fsTA of doped, annealed film (excited at 740 nm), (c) sensitized triplet spectrum overlaid with triplet spectra from fsTA of un-doped films.

Spectral Deconvolution for Triplet Yields

As described in the main text, spectral deconvolution,[40, 42] was employed to find the triplet quantum yield (Φ_T) in the annealed ***t*-Bu-ZnNc** film. First, we generated basis spectra for the ground-state bleach (S_0), excited singlet state (S_1), and excited triplet state (T_1) from femtosecond transient absorption (fsTA) data with an excitation pump pulse energy of 8.4 nJ at 712 nm. We assume no singlet-singlet annihilation due to the low pulse energy of excitation. Using the following mathematical relationship:

$$A(\lambda, t) = S(\lambda) \cdot P(t) \tag{C5}$$

where $A(\lambda, t)$ is the raw fsTA data, $S(\lambda)$ is the vector of basis spectra for each species of interest, and $P(t)$ is the vector of populations of each species, we find the populations as a function of time using a linear regression calculation in MATLAB with the inputs being the raw spectral data ($A(\lambda, t)$) and the calculated basis spectra shown in Figure 27a. The resulting populations versus time normalized to the singlet population reveals a maximum triplet quantum yield of 10 ± 2%.

In order to compare Φ_T values between the ***t*-Bu-ZnNc** in solution as well as the unannealed and annealed films, we employed a relative ratio calculation, ζ, which represents the number of triplets generated relative to other conformations of the same material system. The absolute maximum value of the absorbance of the triplet spectrum (at late time) is divided by the absolute maximum of the ground state bleach (at very early time). This ratio is thus comparable to other ***t*-Bu-ZnNc** samples. From this calculation, we find that the solution and unannealed films generate similar Φ_T, while the annealed film generates nine times more triplet-state excited molecules.

Time Dependent Density Functional Theory (TD-DFT) Calculations

The optimized coordinates for the S_0 ground state of the bare **ZnNc** molecule were found using geometry optimization DFT using the B3LYP exchange and 6-31G* basis set. The resulting optimized cartesian coordinates (shown below) were then used to run single point calculations using TD-DFT (B3LYP and 6-31G*). Ten roots were calculated and are shown below the coordinates. The S_1 energy was found to be 1.64 eV which is very similar to the solution value of 1.61 eV. The T_1 energy was found to be 0.85 eV, somewhat close to the previously experimentally determined energy of 0.98 eV (from literature).[162] Most notably, we found that there are many vibrational energy levels within both the singlet and triplet spin multiplicities that provide a pathway for rapid intersystem crossing provided increased spin-orbit coupling between neighboring chromophores (as is seen in a film). This relationship is shown in Figure 28.

Coordinates (Angstroms)

ATOM	X	Y	Z
1 C	0.7658263827	-4.1173893041	0.1506397705
2 C	-0.6190761273	-4.1460442177	0.1541796873
3 C	-1.0662770441	-2.7632433519	0.1383841076
4 C	1.1579117110	-2.7401261281	0.1443206415
5 N	0.0294637934	-1.9400676665	0.1233412297
6 N	2.4345749055	-2.3258150311	0.1511956247
7 C	2.8103820558	-1.0617812697	0.1463666435
8 N	2.0026575115	0.0615232422	0.1337961913
9 C	2.7709411496	1.1863294818	0.1277666410
10 C	4.2074674332	-0.6235286663	0.1525531259
11 C	4.1823114715	0.8022369922	0.1401708042
12 N	2.3575571691	2.4565773533	0.1151645859
13 C	1.0835960037	2.8247152447	0.1066421431
14 N	-0.0286095508	2.0182053133	0.1060349790
15 C	-0.7758133492	4.2011423151	0.0975696688
16 C	0.6491941757	4.2228192465	0.1002867809
17 C	-2.8042328100	1.1007394292	0.1167788528
18 N	-2.0008756329	-0.0009881044	0.1219858856
19 C	-2.7728182370	-1.1464995941	0.1341104995
20 C	-4.1818586456	-0.7540555206	0.1398649743
21 C	-4.2016442538	0.6724794425	0.1279498055
22 N	-2.3538818068	-2.4005596512	0.1410827778
23 N	-2.4276914689	2.3827973232	0.1067218587
24 C	-1.1670295617	2.7904624658	0.1023407455
25 C	1.5720026990	-5.3734929115	0.2613627637
26 C	-1.3614446807	-5.3690227475	0.2292396771
27 C	5.3962025868	-1.3155321709	0.1664994378
28 C	5.3432326171	1.5409648711	0.1409229819
29 C	-5.3487075979	-1.4832718618	0.1527120800
30 C	-5.3859247304	1.3737285965	0.1290736056
31 C	6.5875154946	0.8583156327	0.1543632668
32 C	6.6138217513	-0.5854146582	0.1677354115
33 C	1.3474897848	5.4073383025	0.0984879889
34 C	0.6222876317	6.6286240074	0.0931078345
35 C	-0.8211847953	6.6069156209	0.0903846932
36 C	-1.5093019279	5.3643034199	0.0930984713
37 C	0.7727402615	-6.5504598652	-0.3439859004
38 C	-0.7033788943	-6.5576942926	0.0788979181
39 C	-6.6075663768	0.6519693942	0.1419096825
40 C	-6.5884976907	-0.7920845341	0.1539852403
41 C	1.4621038124	-7.8749372224	-0.1336069209
42 C	0.7772911794	-9.0113960845	0.0896181099
43 C	-0.6713935415	-8.9992155033	0.2170574927
44 C	-1.3642011952	-7.8305293946	0.2217454068
45 C	-7.8287140197	-1.4884943536	0.1667432324
46 C	-9.0253359510	-0.8095542215	0.1675957998
47 C	-9.0439407040	0.6081053050	0.1555874367
48 C	-7.8650251706	1.3169610825	0.1431724162
49 C	-1.5208090399	7.8445475492	0.0852386531
50 C	-0.8442898263	9.0431405955	0.0828570505
51 C	0.5726418088	9.0644182224	0.0855295691
52 C	1.2845887473	7.8865712737	0.0905074894
53 C	7.8233098224	1.5625780233	0.1550638482
54 C	9.0239745938	0.8910000643	0.1682877150

55	C	9.0499123967	-0.5263961440	0.1817965524
56	C	7.8751058443	-1.2425249287	0.1814391065
57	Zn	0.0007613062	0.0269881079	0.0858248235
58	H	9.9582976773	1.4456425127	0.1685236586
59	H	7.8008528966	2.6497233975	0.1448256834
60	H	7.8934911817	-2.3296860495	0.1917489624
61	H	10.0041365896	-1.0459858516	0.1924645431
62	H	2.3718264552	7.9009103855	0.0925762669
63	H	1.0957176044	10.0167157726	0.0836282278
64	H	-2.6079961277	7.8263865595	0.0832095067
65	H	-1.3957728107	9.9792836034	0.0789090138
66	H	-9.9627241149	-1.3589675760	0.1775175397
67	H	-7.8129384121	-2.5757163841	0.1758264562
68	H	-7.8767740648	2.4042824455	0.1340113984
69	H	-9.9952882074	1.1329988200	0.1563042562
70	H	-2.4396469960	-7.8288110431	0.3872580228
71	H	-1.1924871313	-9.9425360749	0.3572503852
72	H	1.3006554001	-9.9586477559	0.1954453311
73	H	2.5470014535	-7.8862203241	-0.2197787805
74	H	1.7965219865	-5.5817591864	1.3216337511
75	H	2.5385415287	-5.2788261810	-0.2450601849
76	H	-2.4319740259	-5.3379630339	0.4129637144
77	H	5.4089640839	-2.4018887108	0.1762976452
78	H	5.3136267006	2.6269611982	0.1311754216
79	H	-5.3271133796	-2.5694731311	0.1614891748
80	H	-5.3913385004	2.4601541467	0.1200277770
81	H	2.4338807421	5.4148352348	0.1011466921
82	H	-2.5954093365	5.3390110748	0.0916480515
83	H	0.7565280166	-6.3707885431	-1.4392801015

```
   TDDFT Excitation Energies


Excited state   1: excitation energy (eV) =    0.8465
 Total energy for state  1:                  -4062.05587647
au
    Multiplicity: Triplet
    Trans. Mom.:  0.0000 X   0.0000 Y   0.0000 Z
    Strength   :     0.0000000000
    X: D(200) --> V(  1) amplitude =  0.9885

 Excited state   2: excitation energy (eV) =    1.1352
 Total energy for state  2:                  -4062.04526665
au
    Multiplicity: Triplet
    Trans. Mom.:  0.0000 X   0.0000 Y   0.0000 Z
    Strength   :     0.0000000000
    X: D(199) --> V(  1) amplitude =  0.3266
    X: D(199) --> V(  2) amplitude =  0.2199
    X: D(200) --> V(  2) amplitude =  0.8891

Excited state   3: excitation energy (eV) =    1.3453
 Total energy for state  3:                  -4062.03754651
au
    Multiplicity: Triplet
    Trans. Mom.:  0.0000 X   0.0000 Y   0.0000 Z
    Strength   :     0.0000000000
    X: D(199) --> V(  1) amplitude =  0.7968
    X: D(200) --> V(  2) amplitude = -0.3600

 Excited state   4: excitation energy (eV) =    1.6369
 Total energy for state  4:                  -4062.02682962
au
    Multiplicity: Singlet
    Trans. Mom.: -3.4266 X   0.4151 Y  -0.0280 Z
    Strength   :     0.4777994920
    X: D(199) --> V(  1) amplitude = -0.2699
    X: D(200) --> V(  1) amplitude =  0.9394

Excited state   5: excitation energy (eV) =    1.8558
 Total energy for state  5:                  -4062.01878431
au
    Multiplicity: Singlet
    Trans. Mom.:  0.2719 X  -2.5414 Y   0.0180 Z
    Strength   :     0.2970411338
    X: D(199) --> V(  1) amplitude =  0.3616
    X: D(199) --> V(  2) amplitude = -0.2176
    X: D(200) --> V(  2) amplitude =  0.8928

 Excited state   6: excitation energy (eV) =    1.8886
 Total energy for state  6:                  -4062.01758015
au
    Multiplicity: Triplet
    Trans. Mom.:  0.0000 X   0.0000 Y   0.0000 Z
    Strength   :     0.0000000000
    X: D(199) --> V(  1) amplitude =  0.3089
    X: D(199) --> V(  2) amplitude =  0.7569
    X: D(200) --> V(  3) amplitude =  0.2351

 Excited state   7: excitation energy (eV) =    1.9616
 Total energy for state  7:                  -4062.01489455
au
    Multiplicity: Singlet
    Trans. Mom.: -1.2112 X   1.5354 Y   0.0309 Z
    Strength   :     0.1838534681
    X: D(199) --> V(  1) amplitude =  0.8784
    X: D(200) --> V(  1) amplitude =  0.3002
    X: D(200) --> V(  2) amplitude = -0.3268

 Excited state   8: excitation energy (eV) =    2.0542
 Total energy for state  8:                  -4062.01149196
au
    Multiplicity: Triplet
    Trans. Mom.:  0.0000 X   0.0000 Y   0.0000 Z
    Strength   :     0.0000000000
    X: D(199) --> V(  1) amplitude = -0.3546
    X: D(199) --> V(  2) amplitude =  0.5700
    X: D(199) --> V(  4) amplitude = -0.2360
    X: D(199) --> V(  7) amplitude =  0.2201
    X: D(200) --> V(  3) amplitude = -0.3435
    X: D(200) --> V(  5) amplitude = -0.2316
 Excited state   9: excitation energy (eV) =    2.2060
 Total energy for state  9:                  -4062.00591617
au
    Multiplicity: Singlet
    Trans. Mom.: -1.6281 X  -2.0384 Y  -0.0081 Z
    Strength   :     0.3678084616
    X: D(199) --> V(  2) amplitude =  0.9523
    X: D(200) --> V(  2) amplitude =  0.2209

Excited state  10: excitation energy (eV) =    2.2346
 Total energy for state 10:                  -4062.00486491
au
    Multiplicity: Triplet
    Trans. Mom.:  0.0000 X   0.0000 Y   0.0000 Z
    Strength   :     0.0000000000
    X: D(198) --> V(  1) amplitude =  0.3155
    X: D(198) --> V(  6) amplitude = -0.2496
    X: D(199) --> V(  3) amplitude =  0.2258
    X: D(200) --> V(  3) amplitude =  0.5274
    X: D(200) --> V(  4) amplitude =  0.5396

 Excited state  11: excitation energy (eV) =    2.3321
 Total energy for state 11:                  -4062.00127989
au
    Multiplicity: Triplet
    Trans. Mom.:  0.0000 X   0.0000 Y   0.0000 Z
    Strength   :     0.0000000000
    X: D(197) --> V(  2) amplitude = -0.2820
    X: D(197) --> V(  3) amplitude = -0.3141
    X: D(197) --> V(  5) amplitude =  0.2781
   X: D(200) --> V(  3) amplitude = -0.3859
   X: D(200) --> V(  4) amplitude =  0.2564
   X: D(200) --> V(  5) amplitude =  0.5755
 Excited state  12: excitation energy (eV) =    2.3567

Total energy for state 12:                -4062.00037509
au
   Multiplicity: Triplet
   Trans. Mom.:  0.0000 X   0.0000 Y   0.0000 Z
   Strength   :     0.0000000000
   X: D(197) --> V(  1) amplitude =  0.3482
   X: D(198) --> V(  3) amplitude = -0.2241
   X: D(198) --> V(  4) amplitude = -0.3416
   X: D(199) --> V(  4) amplitude = -0.2310
   X: D(200) --> V(  4) amplitude = -0.2994
   X: D(200) --> V(  5) amplitude =  0.3031
   X: D(200) --> V(  6) amplitude =  0.4708

 Excited state  13: excitation energy (eV) =    2.5711
 Total energy for state 13:               -4061.99249706
au
   Multiplicity: Triplet
   Trans. Mom.:  0.0000 X   0.0000 Y   0.0000 Z
   Strength   :     0.0000000000
   X: D(197) --> V(  1) amplitude =  0.7684
   X: D(198) --> V(  2) amplitude = -0.2543
   X: D(200) --> V(  5) amplitude = -0.2436

 Excited state  14: excitation energy (eV) =    2.6545
 Total energy for state 14:               -4061.98943137
au
   Multiplicity: Triplet
   Trans. Mom.:  0.0000 X   0.0000 Y   0.0000 Z
   Strength   :     0.0000000000
   X: D(198) --> V(  1) amplitude =  0.8681
   X: D(200) --> V(  4) amplitude = -0.3609

Excited state  15: excitation energy (eV) =    2.6990
 Total energy for state 15:               -4061.98779736
au
   Multiplicity: Singlet
   Trans. Mom.: -0.3143 X   0.6595 Y  -0.0181 Z
   Strength   :     0.0353188857
   X: D(198) --> V(  1) amplitude = -0.3947
   X: D(200) --> V(  3) amplitude =  0.8040
   X: D(200) --> V(  4) amplitude =  0.4135

 Excited state  16: excitation energy (eV) =    2.7382
 Total energy for state 16:               -4061.98635593
au
   Multiplicity: Singlet
   Trans. Mom.: -0.7187 X   0.2036 Y  -0.0268 Z
   Strength   :     0.0374803583
   X: D(198) --> V(  1) amplitude =  0.6768
   X: D(200) --> V(  3) amplitude =  0.5479
   X: D(200) --> V(  4) amplitude = -0.3989
```

```
   X: D(200) --> V(  5) amplitude = -0.2226

 Excited state  17: excitation energy (eV) =    2.7713
 Total energy for state 17:               -4061.98514110
au
   Multiplicity: Singlet
   Trans. Mom.:  0.5117 X  -0.4144 Y   0.0246 Z
   Strength   :     0.0294805043
   X: D(198) --> V(  1) amplitude =  0.6058
   X: D(200) --> V(  4) amplitude =  0.7365
   X: D(200) --> V(  5) amplitude =  0.2494

 Excited state  18: excitation energy (eV) =    2.8014
 Total energy for state 18:               -4061.98403445
au
   Multiplicity: Singlet
   Trans. Mom.: -1.1201 X  -0.3194 Y  -0.0521 Z
   Strength   :     0.0932879306
   X: D(200) --> V(  4) amplitude = -0.3285
   X: D(200) --> V(  5) amplitude =  0.9169

 Excited state  19: excitation energy (eV) =    2.8350
 Total energy for state 19:               -4061.98280014
au
   Multiplicity: Singlet
   Trans. Mom.: -1.5161 X   0.1400 Y   0.0005 Z
   Strength   :     0.1609995989
   X: D(197) --> V(  1) amplitude =  0.9371
   X: D(200) --> V(  6) amplitude = -0.2832

Excited state  20: excitation energy (eV) =    2.8799
 Total energy for state 20:               -4061.98114910
au
   Multiplicity: Singlet
   Trans. Mom.: -0.0823 X   0.0512 Y  -0.0049 Z
   Strength   :     0.0006649067
   X: D(195) --> V(  1) amplitude = -0.9919
```

APPENDIX D: SUPPLEMENTAL INFORMATION FOR CH. 4

Steady-state absorption and emission data

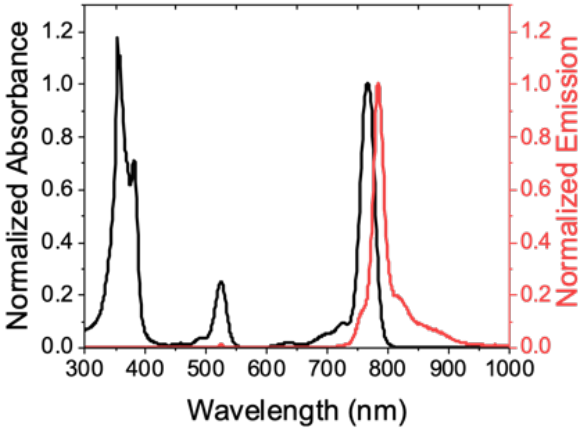

Figure D1. Steady-state UV-vis absorption (black) and steady-state emission spectra (red) for **B-189** in (a) solution.

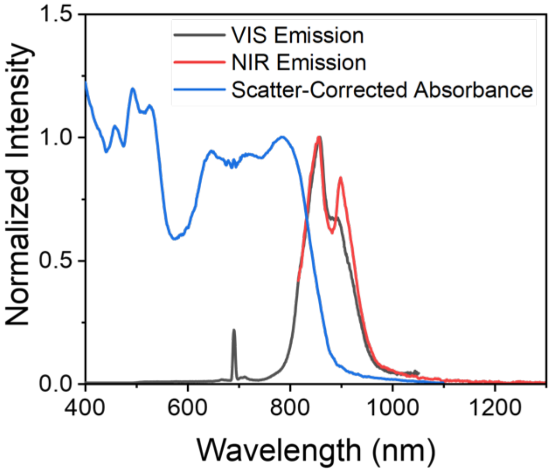

Figure D2. Steady-state UV-vis absorption (blue) and steady-state emission spectra (red, gray) for **B-189** spin-coated in toluene on sapphire at 700 rpm.

Additional transient absorption spectroscopy data

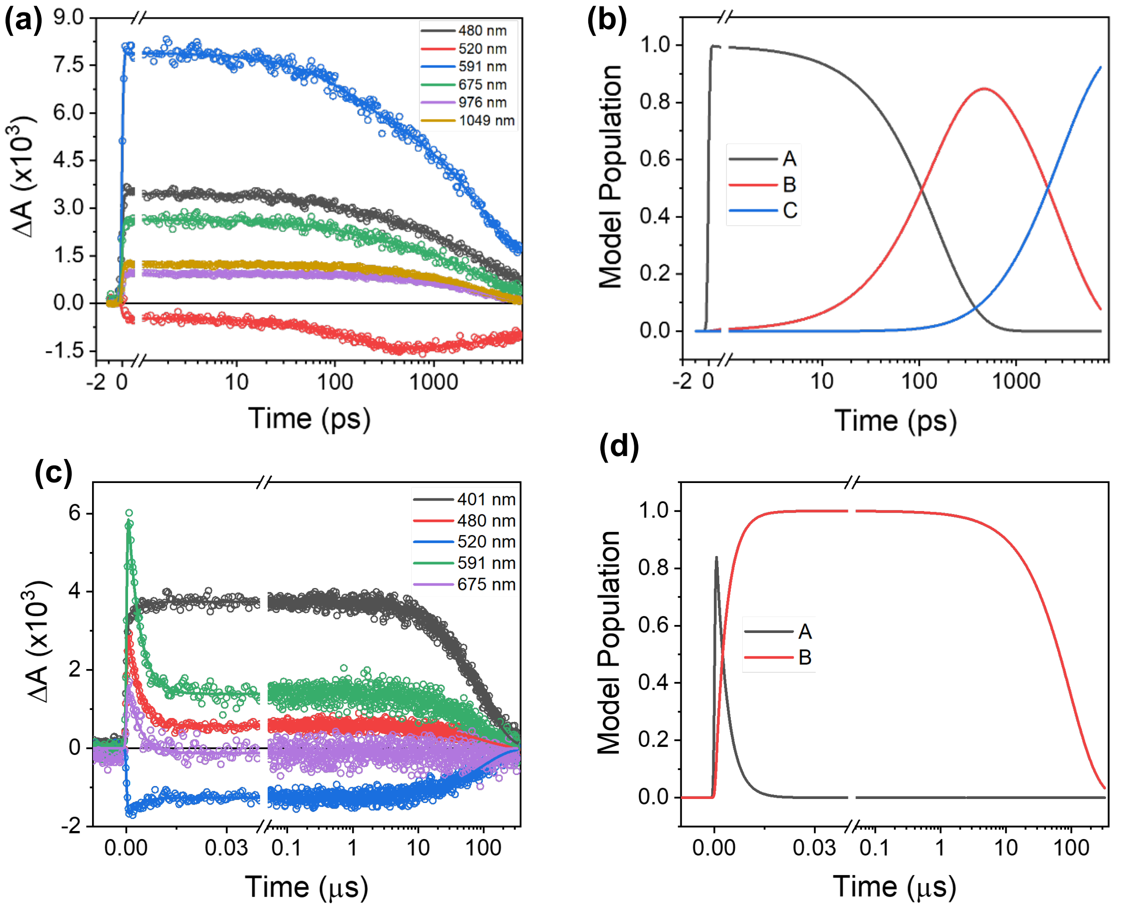

Figure D3. FsTA (a, b) and nsTA (c, d) data of **B-189** in toluene solution excited at 770 nm: (a, c) quality of kinetic fits, (b, d) evolution of kinetic populations with time.

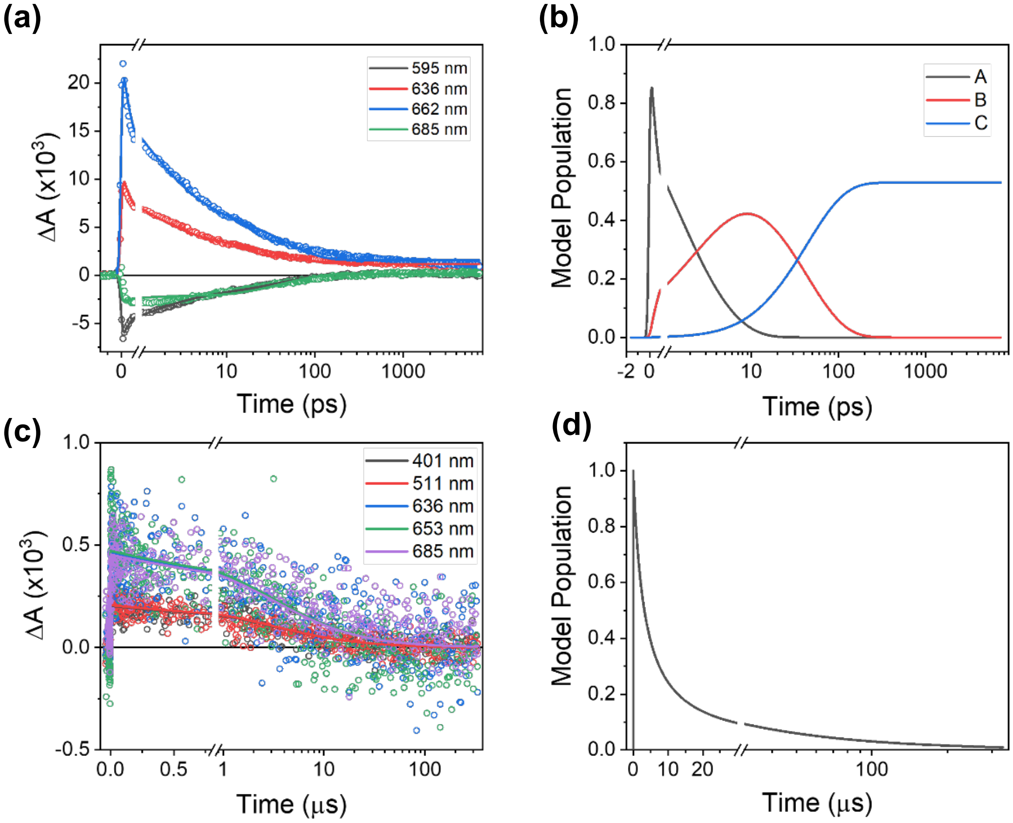

Figure D4. FsTA (a, b) and nsTA (c, d) data of **B-189** film spin-coated (700 rpm) in toluene excited at 780 nm: (a, c) quality of kinetic fits, (b, d) evolution of kinetic populations with time.

Time-resolved fluorescence (TRF) spectroscopy data

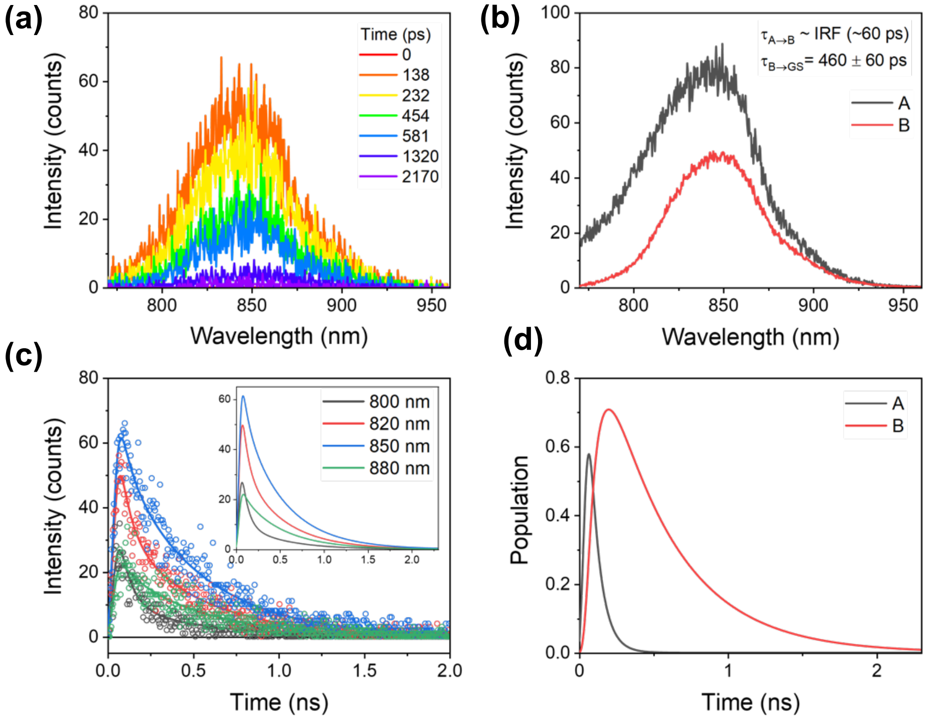

Figure D5. TRF data for **B-189** spin-coated (700 rpm) film in toluene excited at 650 nm collected in 2 ns temporal window: (a) raw data spectra; (b) evolution-associated spectra with kinetic parameters; (c) quality of kinetic fit; (d) evolution of populations with time.

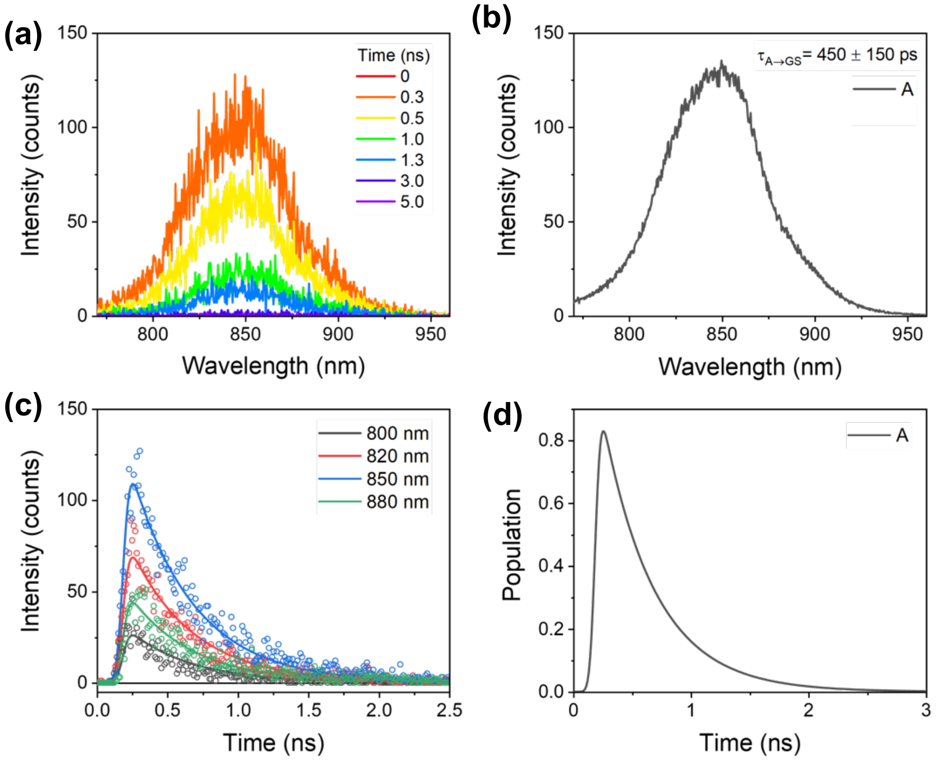

Figure D6. TRF data for **B-189** spin-coated (700 rpm) film in toluene excited at 650 nm collected in 5 ns temporal window: (a) raw data spectra; (b) evolution associated spectra with kinetic parameters; (c) quality of kinetic fit; (d) evolution of populations with time.

Spectral deconvolution triplet quantum yield calculations

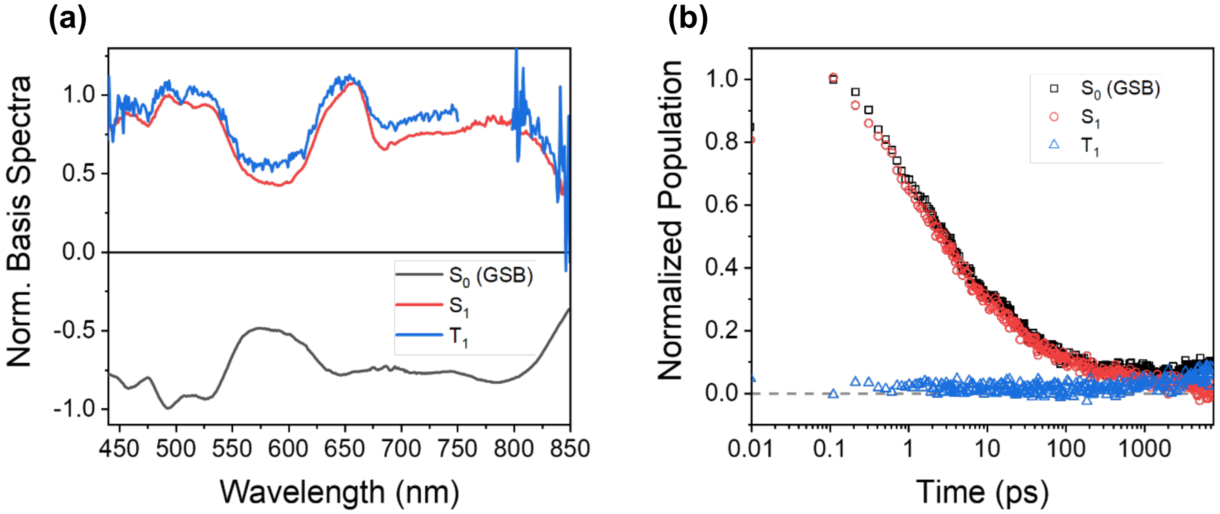

Figure D7. Spectral deconvolution for Φ_T calculations: (a) basis spectra and (b) species populations vs. time.

The triplet quantum yield (Φ_T) of **B-189** in the films was calculated to elucidate the mechanism for rapid SO-ISC using spectral deconvolution methods, described in detail previously.[40, 42] First, basis spectra are generated for the ground-state bleach (S_0), singlet excited state (S_1), and triplet excited state (T_1) from the femtosecond transient absorption (fsTA) data shown in Figure 34. These basis spectra are shown in Figure D7a. Because these fsTA data were collected on a high fluence/low repetition rate system, we consider the following calculation a lower-bound Φ_T because of the rapid singlet-singlet annihilation loss mechanism. Once we have the basis spectra, we use the following equation to perform a linear regression calculation in MATLAB:

$$A(\lambda, t) = S(\lambda) \cdot P(t)$$

where $A(\lambda, t)$ is the raw fsTA data, $S(\lambda)$ is the vector of basis spectra for each species of interest, and $P(t)$ is the vector of populations of each species. Solving for $P(t)$, we find the Φ_T was found to be 8.3 ± 2.2 %. The 27% error in the Φ_T result correlates with the 30% error in the profilometry measurements not in the methods of the main text.

Density functional theory (DFT) and time dependent density functional theory (TD-DFT) calculations

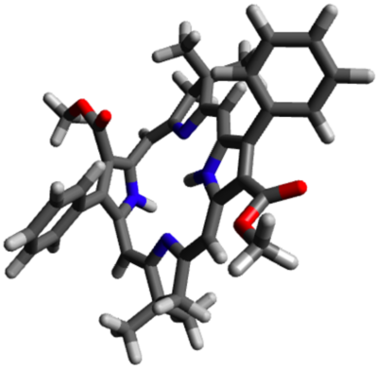

Figure D8. DFT optimized geometry of **B-189** monomer

The optimized coordinates for the S_0 ground state of the **B-189** molecule were found using geometry optimization DFT using the B3LYP exchange and 6-31G* basis set. The optimized geometry of the monomer is shown in Figure D8. The resulting optimized cartesian coordinates are shown below. Using this optimized geometry, we found the highest occupied molecular orbital (HOMO) and lowest occupied molecular orbital (LUMO) energies to be -4.98 eV and -2.61 eV, respectively, for the monomer.

The optimized coordinates were then used to run single point calculations using TD-DFT (B3LYP and 6-31G*). Ten roots were calculated and are shown below the coordinates. The S_1 energy was found to be 1.94 eV which is a bit larger than the solution value of 1.60 eV. The T_1 energy was found to be 0.92 eV. Most notably, we found that there are many vibrational energy levels within both the singlet and triplet spin multiplicities that may provide a pathway for rapid intersystem crossing provided increased spin-orbit coupling between neighboring chromophores (as is seen in a film). The series of energy diagrams shown in Figure 35 compares the TD-DFT energy values to those found experimentally in solution and film.

C	0.4870319551	-4.3427905899	1.2567102098
C	-0.9687605048	-4.4583538150	1.7914213472
C	-1.6042330427	-3.1702109775	1.3001608870
N	-0.6200335278	-2.2347909292	0.9904999756
C	0.5528201575	-2.8248852265	1.0072789584
C	3.0552639069	1.2257090107	0.4341709894
C	3.2654398055	-0.1353080945	0.4458451833
C	1.9594554779	-0.7762623440	0.6020332737
N	1.0228496456	0.2335147478	0.6402312164
C	1.6206061562	1.4755698797	0.5616011855
C	1.7737953537	-2.1328720773	0.7766787435
C	-2.4176070541	4.0883629455	1.4313304298
C	-0.9472186520	4.3614628152	1.0096366628
C	-0.3892416607	2.9599484053	0.8167397283
N	-1.3146948879	2.0278210021	0.7957355340
C	-2.5584902312	2.6169813075	1.0077339467
C	1.0022772513	2.7049734314	0.6623730242
C	-2.9664457699	-1.2654215978	-0.8386836134
C	-3.1867422372	0.1459366151	-0.9446587308
C	-3.6517188074	0.5692714465	0.3021289446
N	-3.7683039753	-0.5444879275	1.1078095370
C	-3.2934993801	-1.6586492966	0.4591714075
C	-2.9250812070	-2.8890908134	1.1541165991
C	-3.7132055279	1.9204973324	0.8568389840
C	-2.5674011838	4.2030151786	2.9631223442
C	-3.4215733908	5.0101136752	0.7237991160
C	-3.0134413982	1.0309763730	-2.1149258889
C	-2.3713991262	-2.1834046074	-1.8451000942
C	1.5271701887	-4.8536921952	2.2638524523
C	0.6388935453	-5.0774939836	-0.0945458284
C	4.5197306494	-0.9005733222	0.2750399291
C	4.1171754773	2.2475189655	0.2733639204
C	-4.0062930352	1.9741203306	-2.4372525990
C	-3.8488452668	2.8441398287	-3.5152692223
C	-2.6958946805	2.7850936814	-4.3008289704
C	-1.7053723845	1.8501789744	-3.9947322547
C	-1.8570709006	0.9827706362	-2.9131574714
C	5.6024335322	-0.7544600322	1.1564880651
C	6.7586639134	-1.5141615757	0.9856835523
C	6.8588037881	-2.4212477866	-0.0708305595
C	5.7911909813	-2.5700680258	-0.9576068149
C	4.6277384126	-1.8222211434	-0.7824745073
O	3.6963852270	3.3207739407	-0.4382502321
O	-3.0578208395	-3.3122198897	-2.1852317032
O	5.2496385038	2.1502541587	0.7028781738
O	-1.2870648446	-2.0136087631	-2.3608844767
C	-4.4466514927	-3.4640637484	-1.8810714479
C	4.6869367327	4.3423706423	-0.6432631226
H	-0.9694757007	-4.4884855513	2.8900379947
H	-1.4865899739	-5.3544053082	1.4360772422
H	0.0177573073	0.0915601884	0.7283495556
H	2.6804346118	-2.7256645459	0.7620364291
H	-0.8977050484	4.9213089135	0.0653747308
H	-0.3852123676	4.9383124522	1.7537642435
H	1.6542328770	3.5672560927	0.6152827662
H	-3.8405958021	-0.4849919415	2.1137912002
H	-3.6797106096	-3.5793262780	1.5274528949
H	-4.6640670086	2.3696386057	1.1382001564
H	-1.8474659400	3.5561464040	3.4773708389
H	-3.5736389671	3.9080406644	3.2820052476
H	-2.3961152162	5.2350902267	3.2937264002
H	-3.3620405874	4.8971313882	-0.3641573755

H	-3.2287507342	6.0605516101	0.9746768878
H	-4.4501373379	4.7821798362	1.0273868743
H	1.4655879175	-4.3115133750	3.2146288399
H	2.5493892463	-4.7511470166	1.8819993025
H	1.3620729698	-5.9180931411	2.4710025246
H	0.5188264950	-6.1589263236	0.0442150598
H	1.6306541872	-4.9000744734	-0.5259153823
H	-0.1074947598	-4.7344402016	-0.8189474835
H	-4.9138287653	2.0095727076	-1.8414154285
H	-4.6331324520	3.5604134259	-3.7486119486
H	-2.5735601855	3.4582550060	-5.1457359547
H	-0.8025049370	1.7966753061	-4.5980907404
H	-1.0831773503	0.2625433526	-2.6765406797
H	5.5352014957	-0.0391039467	1.9668241980
H	7.5863021693	-1.3917700080	1.6791404088
H	7.7645626435	-3.0070644139	-0.2038270729
H	5.8618225310	-3.2675000498	-1.7880676766
H	3.7997171525	-1.9380531338	-1.4760603638
H	-4.8245183578	-4.1976063751	-2.5974866217
H	-4.9913694034	-2.5228042935	-1.9962928954
H	-4.5896681722	-3.8429458650	-0.8643922140
H	5.0397116385	4.7362156340	0.3137119760
H	4.1852353781	5.1198044315	-1.2200726999
H	5.5391908415	3.9410819843	-1.19733637

```
TDDFT Excitation Energies
  Excited state   1: excitation energy (eV) =    0.9150
 Total energy for state  1:                 -2066.99154413 au
    Multiplicity: Triplet
    Trans. Mom.:  0.0000 X   0.0000 Y   0.0000 Z
    Strength   :     0.0000000000
    X: D(168) --> V(  1) amplitude =  0.9741
    Y: D(168) --> V(  1) amplitude =  0.2863
    X: D(169) --> V(  1) amplitude = -0.3162
 Excited state   2: excitation energy (eV) =    1.5426
 Total energy for state  2:                 -2066.96848028 au
    Multiplicity: Triplet
    Trans. Mom.:  0.0000 X   0.0000 Y   0.0000 Z
    Strength   :     0.0000000000
    X: D(168) --> V(  1) amplitude =  0.2979
    X: D(169) --> V(  1) amplitude =  0.9234
 Excited state   3: excitation energy (eV) =    1.9374
 Total energy for state  3:                 -2066.95397167 au
    Multiplicity: Singlet
    Trans. Mom.:  1.4371 X   0.4190 Y   0.2346 Z
    Strength   :     0.1089719459
    X: D(168) --> V(  1) amplitude =  0.2981
    X: D(169) --> V(  1) amplitude =  0.9385
 Excited state   4: excitation energy (eV) =    2.2946
 Total energy for state  4:                 -2066.94084396 au
    Multiplicity: Singlet
    Trans. Mom.: -0.8878 X   1.7287 Y   0.0332 Z
    Strength   :     0.2123719125
    X: D(168) --> V(  1) amplitude =  0.9363
    X: D(169) --> V(  1) amplitude = -0.3001
 Excited state   5: excitation energy (eV) =    2.3721
 Total energy for state  5:                 -2066.93799796 au
    Multiplicity: Triplet
    Trans. Mom.:  0.0000 X   0.0000 Y   0.0000 Z
    Strength   :     0.0000000000
    X: D(165) --> V(  1) amplitude = -0.3573
    X: D(166) --> V(  1) amplitude =  0.6138
    X: D(167) --> V(  1) amplitude =  0.5607
    X: D(168) --> V(  2) amplitude =  0.2388
 Excited state   6: excitation energy (eV) =    2.5867
 Total energy for state  6:                 -2066.93010940 au
    Multiplicity: Triplet
    Trans. Mom.:  0.0000 X   0.0000 Y   0.0000 Z
    Strength   :     0.0000000000
    X: D(165) --> V(  1) amplitude =  0.2817
    X: D(166) --> V(  1) amplitude = -0.4803
    X: D(167) --> V(  1) amplitude =  0.7857
 Excited state   7: excitation energy (eV) =    2.6338
 Total energy for state  7:                 -2066.92838078 au
    Multiplicity: Singlet
    Trans. Mom.: -0.3160 X  -0.4229 Y   0.0545 Z
    Strength   :     0.0181750906
    X: D(167) --> V(  1) amplitude =  0.9764
 Excited state   8: excitation energy (eV) =    2.8037
 Total energy for state  8:                 -2066.92213582 au
    Multiplicity: Triplet
    Trans. Mom.:  0.0000 X   0.0000 Y   0.0000 Z
    Strength   :     0.0000000000
    X: D(162) --> V(  1) amplitude =  0.2624
    X: D(163) --> V(  1) amplitude = -0.2249
    X: D(164) --> V(  1) amplitude =  0.6470
    X: D(165) --> V(  1) amplitude = -0.2547
    X: D(169) --> V(  2) amplitude =  0.3270
 Excited state   9: excitation energy (eV) =    2.8878
 Total energy for state  9:                 -2066.91904473 au
    Multiplicity: Triplet
    Trans. Mom.:  0.0000 X   0.0000 Y   0.0000 Z
    Strength   :     0.0000000000
    X: D(161) --> V(  1) amplitude =  0.2289
    X: D(162) --> V(  1) amplitude = -0.2512
    X: D(163) --> V(  1) amplitude =  0.5151
    X: D(164) --> V(  1) amplitude =  0.5324
    X: D(169) --> V(  2) amplitude = -0.2800
 Excited state  10: excitation energy (eV) =    3.0164
 Total energy for state 10:                 -2066.91431967 au
    Multiplicity: Singlet
    Trans. Mom.: -0.8538 X  -0.3938 Y   0.1886 Z
    Strength   :     0.0679660465
    X: D(166) --> V(  1) amplitude =  0.9474
 Excited state  11: excitation energy (eV) =    3.1045
 Total energy for state 11:                 -2066.91108079 au
    Multiplicity: Triplet
    Trans. Mom.:  0.0000 X   0.0000 Y   0.0000 Z
    Strength   :     0.0000000000
    X: D(165) --> V(  1) amplitude =  0.6193
    X: D(166) --> V(  1) amplitude =  0.5618
    X: D(168) --> V(  2) amplitude = -0.3647
    X: D(169) --> V(  2) amplitude =  0.3213
 Excited state  12: excitation energy (eV) =    3.1639
 Total energy for state 12:                 -2066.90889786 au
    Multiplicity: Triplet
    Trans. Mom.:  0.0000 X   0.0000 Y   0.0000 Z
    Strength   :     0.0000000000
    X: D(159) --> V(  1) amplitude = -0.4371
    X: D(163) --> V(  1) amplitude =  0.4270
    X: D(164) --> V(  1) amplitude = -0.2679
    X: D(165) --> V(  1) amplitude = -0.4162
    X: D(168) --> V(  2) amplitude = -0.4493
    X: D(169) --> V(  2) amplitude =  0.2679
 Excited state  13: excitation energy (eV) =    3.1747
 Total energy for state 13:                 -2066.90850232 au
    Multiplicity: Singlet
    Trans. Mom.:  0.4900 X  -0.0003 Y  -0.2364 Z
    Strength   :     0.0230171337
    X: D(165) --> V(  1) amplitude =  0.9655
 Excited state  14: excitation energy (eV) =    3.1921
 Total energy for state 14:                 -2066.90786393 au
    Multiplicity: Triplet
    Trans. Mom.:  0.0000 X   0.0000 Y   0.0000 Z
    Strength   :     0.0000000000
    X: D(160) --> V(  1) amplitude =  0.5068
    X: D(161) --> V(  1) amplitude =  0.2235
    X: D(162) --> V(  1) amplitude = -0.3120
    X: D(163) --> V(  1) amplitude =  0.3285
    X: D(168) --> V(  2) amplitude =  0.2979
    X: D(169) --> V(  2) amplitude =  0.3848
 Excited state  15: excitation energy (eV) =    3.2525
 Total energy for state 15:                 -2066.90564384 au
    Multiplicity: Triplet
    Trans. Mom.:  0.0000 X   0.0000 Y   0.0000 Z
    Strength   :     0.0000000000
    X: D(159) --> V(  1) amplitude = -0.5155
    X: D(162) --> V(  1) amplitude =  0.4117
    X: D(163) --> V(  1) amplitude =  0.2386
```

```
   X: D(165) --> V(  1) amplitude =  0.2755
   X: D(168) --> V(  2) amplitude =  0.5001
Excited state  16: excitation energy (eV) =    3.3181
Total energy for state 16:                 -2066.90323242 au
   Multiplicity: Singlet
   Trans. Mom.: -0.6066 X   0.3333 Y   0.1046 Z
   Strength   :     0.0398268827
   X: D(164) --> V(  1) amplitude =  0.9600
Excited state  17: excitation energy (eV) =    3.4124
Total energy for state 17:                 -2066.89976623 au
   Multiplicity: Singlet
   Trans. Mom.: -0.0468 X   0.0002 Y  -0.0143 Z
   Strength   :     0.0002002178
   X: D(160) --> V(  1) amplitude =  0.4483
   X: D(163) --> V(  1) amplitude =  0.8087
Excited state  18: excitation energy (eV) =    3.4642
Total energy for state 18:                 -2066.89786182 au
   Multiplicity: Singlet
   Trans. Mom.: -0.1046 X   0.0813 Y  -0.0906 Z
   Strength   :     0.0021855527
   X: D(159) --> V(  1) amplitude = -0.4206
   X: D(160) --> V(  1) amplitude = -0.2445
   X: D(161) --> V(  1) amplitude = -0.2716
   X: D(162) --> V(  1) amplitude =  0.7062
   X: D(163) --> V(  1) amplitude =  0.3317
Excited state  19: excitation energy (eV) =    3.5900
Total energy for state 19:                 -2066.89323999 au
   Multiplicity: Singlet
   Trans. Mom.: -0.1176 X   0.0834 Y   0.0907 Z
   Strength   :     0.0025515285
   X: D(161) --> V(  1) amplitude =  0.9041
   X: D(162) --> V(  1) amplitude =  0.3983
Excited state  20: excitation energy (eV) =    3.6557
Total energy for state 20:                 -2066.89082750 au
   Multiplicity: Singlet
   Trans. Mom.: -0.1230 X   0.6826 Y   0.0759 Z
   Strength   :     0.0435966983
   X: D(159) --> V(  1) amplitude =  0.2617
   X: D(160) --> V(  1) amplitude = -0.4714
   X: D(168) --> V(  3) amplitude =  0.3212
   X: D(169) --> V(  2) amplitude =  0.7
```

References

1. U.S. Dept. of Energy. *Annual Energy Outlook 2022 with projections to 2050*; 2022; pp 13, 48.
2. Hall, R. N., Silicon photovoltaic cells. *Solid-State Electronics* **1981,** *24* (7), 595-616.
3. Louwen, A.; van Sark, W.; Schropp, R.; Faaij, A., A cost roadmap for silicon heterojunction solar cells. *Sol. Energy Mater. Sol. Cells* **2016,** *147*, 295-314.
4. Hoppe, H.; Sariciftci, N. S., Organic solar cells: An overview. *J. Mater. Res.* **2004,** *19* (7), 1924-1945.
5. Strümpel, C.; McCann, M.; Beaucarne, G.; Arkhipov, V.; Slaoui, A.; Švrček, V.; del Cañizo, C.; Tobias, I., Modifying the solar spectrum to enhance silicon solar cell efficiency—An overview of available materials. *Solar Energy Materials and Solar Cells* **2007,** *91* (4), 238-249.
6. Guillaume Alombert-Goget, D. R., Alessandro Chiasera, Stefano Varas, Maurizio Ferrari, Giancarlo C. Righini, Belto Dieudonne, Brigitte Boulard, Rare-earth doped materials enhance silicon solar cell efficiency. *The International Society for Optics and Photonics* 2011.
7. Einzinger, M.; Wu, T.; Kompalla, J. F.; Smith, H. L.; Perkinson, C. F.; Nienhaus, L.; Wieghold, S.; Congreve, D. N.; Kahn, A.; Bawendi, M. G.; Baldo, M. A., Sensitization of silicon by singlet exciton fission in tetracene. *Nature* **2019,** *571* (7763), 90-94.
8. Shockley, W.; Queisser, H. J., Detailed balance limit of efficiency of p-n junction solar cells. *J. Appl. Phys.* **1961,** *32*, 510-19.
9. Hanna, M. C.; Nozik, A. J., Solar conversion efficiency of photovoltaic and photoelectrolysis cells with carrier multiplication absorbers. *J. Appl. Phys.* **2006,** *100* (7), 074510/1-074510/8.
10. Anslyn, E. V.; Dougherty, D. A., *Modern Physical Organic Chemistry*. University Science Books: 2006.
11. Bialas, A. L.; Spano, F. C., A Holstein–Peierls Approach to Excimer Spectra: The Evolution from Vibronically Structured to Unstructured Emission. *The Journal of Physical Chemistry C* **2022,** *126* (8), 4067-4081.
12. Mauck, C. M.; Hartnett, P. E.; Margulies, E. A.; Ma, L.; Miller, C. E.; Schatz, G. C.; Marks, T. J.; Wasielewski, M. R., Singlet Fission via an Excimer-Like Intermediate in 3,6-Bis(thiophen-2-yl)diketopyrrolopyrrole Derivatives. *J. Am. Chem. Soc.* **2016,** *138* (36), 11749-11761.
13. Wu, Y.; Young, R. M.; Frasconi, M.; Schneebeli, S. T.; Spenst, P.; Gardner, D. M.; Brown, K. E.; Wurthner, F.; Stoddart, J. F.; Wasielewski, M. R., Ultrafast Photoinduced Symmetry-Breaking Charge Separation and Electron Sharing in Perylenediimide Molecular Triangles. *J. Am. Chem. Soc.* **2015,** *137* (41), 13236-13239.
14. Smith, M. B.; Michl, J., Singlet Fission. *Chemical Reviews* **2010,** *110* (11), 6891-6936.
15. Chen, M.; Bae, Y. J.; Mauck, C. M.; Mandal, A.; Young, R. M.; Wasielewski, M. R., Singlet Fission in Covalent Terrylenediimide Dimers: Probing the Nature of the Multiexciton State Using Femtosecond Mid-Infrared Spectroscopy. *J. Am. Chem. Soc.* **2018,** *140* (29), 9184-9192.

16. Congreve, D. N.; Lee, J.; Thompson, N. J.; Hontz, E.; Yost, S. R.; Reusswig, P. D.; Bahlke, M. E.; Reineke, S.; Van Voorhis, T.; Baldo, M. A., External Quantum Efficiency Above 100% in a Singlet-Exciton-Fission-Based Organic Photovoltaic Cell. *Science (Washington, DC, U. S.)* **2013,** *340* (6130), 334-337.
17. Cook, R. E.; Phelan, B. T.; Kamire, R. J.; Majewski, M. B.; Young, R. M.; Wasielewski, M. R., Excimer Formation and Symmetry-Breaking Charge Transfer in Cofacial Perylene Dimers. *J. Phys. Chem. A* **2017,** *121* (8), 1607-1615.
18. Vauthey, E., Photoinduced Symmetry-Breaking Charge Separation. *ChemPhysChem* **2012,** *13* (8), 2001-2011.
19. Spenst, P.; Young, R. M.; Wasielewski, M. R.; Wuerthner, F., Guest and solvent modulated photo-driven charge separation and triplet generation in a perylene bisimide cyclophane. *Chem. Sci.* **2016,** *7* (8), 5428-5434.
20. Bartynski, A. N.; Gruber, M.; Das, S.; Rangan, S.; Mollinger, S.; Trinh, C.; Bradforth, S. E.; Vandewal, K.; Salleo, A.; Bartynski, R. A.; Bruetting, W.; Thompson, M. E., Symmetry-Breaking Charge Transfer in a Zinc Chlorodipyrrin Acceptor for High Open Circuit Voltage Organic Photovoltaics. *J. Am. Chem. Soc.* **2015,** *137* (16), 5397-5405.
21. Huang, C.; Barlow, S.; Marder, S. R., Perylene-3,4,9,10-tetracarboxylic Acid Diimides: Synthesis, Physical Properties, and Use in Organic Electronics. *The Journal of Organic Chemistry* **2011,** *76* (8), 2386-2407.
22. Elles, C. https://ellesgroup.ku.edu/ta_spectroscopy.
23. Young, R. M.; Dyar, S. M.; Barnes, J. C.; Juríček, M.; Stoddart, J. F.; Co, D. T.; Wasielewski, M. R., Ultrafast Conformational Dynamics of Electron Transfer in ExBox4+⊂Perylene. *The Journal of Physical Chemistry A* **2013,** *117* (47), 12438-12448.
24. Hartnett, P. E.; Margulies, E. A.; Mauck, C. M.; Miller, S. A.; Wu, Y.; Wu, Y.-L.; Marks, T. J.; Wasielewski, M. R., Effects of Crystal Morphology on Singlet Exciton Fission in Diketopyrrolopyrrole Thin Films. *The Journal of Physical Chemistry B* **2016,** *120* (7), 1357-1366.
25. Bragg, W. H.; Bragg, W. L., The reflection of X-rays by crystals. *Proceedings of the Royal Society of London. Series A, Containing Papers of a Mathematical and Physical Character* **1913,** *88* (605), 428-438.
26. The Advanced Photon Source: Research Techniques. https://www.aps.anl.gov/Beamlines/Research-Techniques.
27. Mehta, A. Introduction to Reciprocal Space: 7th X-ray Scattering School. https://www-ssrl.slac.stanford.edu/conferences/workshops/sxst2014/documents/intro_to_reciprocal_space.pdf.
28. Smith, M. B.; Michl, J., Recent Advances in Singlet Fission. *Annual Review of Physical Chemistry* **2013,** *64* (1), 361-386.
29. Baldacchino, A. J.; Collins, M. I.; Nielsen, M. P.; Schmidt, T. W.; McCamey, D. R.; Tayebjee, M. J. Y., Singlet fission photovoltaics: Progress and promising pathways. *Chemical Physics Reviews* **2022,** *3* (2), 021304.
30. Ehrler, B.; Musselman, K. P.; Böhm, M. L.; Friend, R. H.; Greenham, N. C., Hybrid pentacene/a-silicon solar cells utilizing multiple carrier generation via singlet exciton fission. *Applied Physics Letters* **2012,** *101* (15), 153507.
31. Pazos-Outón, L. M.; Lee, J. M.; Futscher, M. H.; Kirch, A.; Tabachnyk, M.; Friend, R. H.; Ehrler, B., A Silicon–Singlet Fission Tandem Solar Cell Exceeding 100% External

Quantum Efficiency with High Spectral Stability. *ACS Energy Letters* **2017,** *2* (2), 476-480.

32. Wu, T. C.; Thompson, N. J.; Congreve, D. N.; Hontz, E.; Yost, S. R.; Van Voorhis, T.; Baldo, M. A., Singlet fission efficiency in tetracene-based organic solar cells. *Applied Physics Letters* **2014,** *104* (19), 193901.
33. Ehrler, B.; Walker, B. J.; Böhm, M. L.; Wilson, M. W. B.; Vaynzof, Y.; Friend, R. H.; Greenham, N. C., In situ measurement of exciton energy in hybrid singlet-fission solar cells. *Nature Communications* **2012,** *3* (1), 1019.
34. Willems, R. E. M.; Meskers, S. C. J.; Wienk, M. M.; Janssen, R. A. J., Effect of Charge-Transfer State Energy on Charge Generation Efficiency via Singlet Fission in Pentacene–Fullerene Solar Cells. *The Journal of Physical Chemistry C* **2019,** *123* (16), 10253-10261.
35. Niu, M.-S.; Yang, X.-Y.; Qin, C.-C.; Bi, P.-Q.; Lyu, C.-K.; Feng, L.; Qin, W.; Gao, K.; Hao, X.-T., Competition between singlet fission and singlet exciton dissociation at the interface in TIPS-pentacene:IT-4F blend. *Organic Electronics* **2019,** *71*, 296-302.
36. Schrauben, J. N.; Zhao, Y.; Mercado, C.; Dron, P. I.; Ryerson, J. L.; Michl, J.; Zhu, K.; Johnson, J. C., Photocurrent Enhanced by Singlet Fission in a Dye-Sensitized Solar Cell. *ACS Applied Materials & Interfaces* **2015,** *7* (4), 2286-2293.
37. Hartnett, P. E.; Margulies, E. A.; Matte, H. S. S. R.; Hersam, M. C.; Marks, T. J.; Wasielewski, M. R., Effects of Crystalline Perylenediimide Acceptor Morphology on Optoelectronic Properties and Device Performance. *Chemistry of Materials* **2016,** *28* (11), 3928-3936.
38. Hartnett, P. E.; Timalsina, A.; Matte, H. S. S. R.; Zhou, N.; Guo, X.; Zhao, W.; Facchetti, A.; Chang, R. P. H.; Hersam, M. C.; Wasielewski, M. R.; Marks, T. J., Slip-Stacked Perylenediimides as an Alternative Strategy for High Efficiency Nonfullerene Acceptors in Organic Photovoltaics. *Journal of the American Chemical Society* **2014,** *136* (46), 16345-16356.
39. Bae, Y. J.; Christensen, J. A.; Kang, G.; Zhou, J.; Young, R. M.; Wu, Y.-L.; Van Duyne, R. P.; Schatz, G. C.; Wasielewski, M. R., Substituent effects on energetics and crystal morphology modulate singlet fission in 9,10-bis(phenylethynyl)anthracenes. *J. Chem. Phys.* **2019,** *151* (4), 044501/1-044501/10.
40. Bae, Y. J.; Kang, G.; Malliakas, C. D.; Nelson, J. N.; Zhou, J.; Young, R. M.; Wu, Y.-L.; Van Duyne, R. P.; Schatz, G. C.; Wasielewski, M. R., Singlet Fission in 9,10-Bis(phenylethynyl)anthracene Thin Films. *Journal of the American Chemical Society* **2018,** *140* (45), 15140-15144.
41. Basel, B. S.; Zirzlmeier, J.; Hetzer, C.; Phelan, B. T.; Krzyaniak, M. D.; Reddy, S. R.; Coto, P. B.; Horwitz, N. E.; Young, R. M.; White, F. J.; Hampel, F.; Clark, T.; Thoss, M.; Tykwinski, R. R.; Wasielewski, M. R.; Guldi, D. M., Unified model for singlet fission within a non-conjugated covalent pentacene dimer. *Nature Communications* **2017,** *8* (1), 15171.
42. Margulies, E. A.; Wu, Y.-L.; Gawel, P.; Miller, S. A.; Shoer, L. E.; Schaller, R. D.; Diederich, F.; Wasielewski, M. R., Sub-Picosecond Singlet Exciton Fission in Cyano-Substituted Diaryltetracenes. *Angewandte Chemie International Edition* **2015,** *54* (30), 8679-8683.
43. Chen, M.; Powers-Riggs, N. E.; Coleman, A. F.; Young, R. M.; Wasielewski, M. R., Singlet Fission in Quaterrylenediimide Thin Films. *The Journal of Physical Chemistry C* **2020,** *124* (5), 2791-2798.

44. Eaton, S. W.; Shoer, L. E.; Karlen, S. D.; Dyar, S. M.; Margulies, E. A.; Veldkamp, B. S.; Ramanan, C.; Hartzler, D. A.; Savikhin, S.; Marks, T. J.; Wasielewski, M. R., Singlet Exciton Fission in Polycrystalline Thin Films of a Slip-Stacked Perylenediimide. *Journal of the American Chemical Society* **2013,** *135* (39), 14701-14712.
45. Margulies, E. A.; Miller, C. E.; Wu, Y.; Ma, L.; Schatz, G. C.; Young, R. M.; Wasielewski, M. R., Enabling singlet fission by controlling intramolecular charge transfer in π-stacked covalent terrylenediimide dimers. *Nature Chemistry* **2016,** *8* (12), 1120-1125.
46. Bae, Y. J.; Zhao, X.; Kryzaniak, M. D.; Nagashima, H.; Strzalka, J.; Zhang, Q.; Wasielewski, M. R., Spin Dynamics of Quintet and Triplet States Resulting from Singlet Fission in Oriented Terrylenediimide and Quaterrylenediimide Films. *The Journal of Physical Chemistry C* **2020,** *124* (18), 9822-9833.
47. Chen, M.; Krzyaniak, M. D.; Nelson, J. N.; Bae, Y. J.; Harvey, S. M.; Schaller, R. D.; Young, R. M.; Wasielewski, M. R., Quintet-triplet mixing determines the fate of the multiexciton state produced by singlet fission in a terrylenediimide dimer at room temperature. *Proceedings of the National Academy of Sciences* **2019,** *116* (17), 8178.
48. Mandal, A.; Chen, M.; Foszcz, E. D.; Schultz, J. D.; Kearns, N. M.; Young, R. M.; Zanni, M. T.; Wasielewski, M. R., Two-Dimensional Electronic Spectroscopy Reveals Excitation Energy-Dependent State Mixing during Singlet Fission in a Terrylenediimide Dimer. *Journal of the American Chemical Society* **2018,** *140* (51), 17907-17914.
49. Le, A. K.; Bender, J. A.; Arias, D. H.; Cotton, D. E.; Johnson, J. C.; Roberts, S. T., Singlet Fission Involves an Interplay between Energetic Driving Force and Electronic Coupling in Perylenediimide Films. *Journal of the American Chemical Society* **2018,** *140* (2), 814-826.
50. Le, A. K.; Bender, J. A.; Roberts, S. T., Slow Singlet Fission Observed in a Polycrystalline Perylenediimide Thin Film. *The Journal of Physical Chemistry Letters* **2016,** *7* (23), 4922-4928.
51. Hausch, J.; Berges, A. J.; Zeiser, C.; Rammler, T.; Morlok, A.; Bredehöft, J.; Hammer, S.; Pflaum, J.; Bardeen, C. J.; Broch, K., Distinguishing between Triplet-Pair State and Excimer Emission in Singlet Fission Chromophores Using Mixed Thin Films. *The Journal of Physical Chemistry C* **2022**.
52. Zhang, Z.; Ni, W.; Ma, L.; Sun, L.; Gurzadyan, G. G., Enhancement of Singlet Fission Yield by Hindering Excimer Formation in Perylene Film. *The Journal of Physical Chemistry C* **2022,** *126* (1), 396-403.
53. Paul, S.; Karunakaran, V., Excimer Formation Inhibits the Intramolecular Singlet Fission Dynamics: Systematic Tilting of Pentacene Dimers by Linking Positions. *The Journal of Physical Chemistry B* **2022,** *126* (5), 1054-1062.
54. Ramirez, C. E.; Chen, S.; Powers-Riggs, N. E.; Schlesinger, I.; Young, R. M.; Wasielewski, M. R., Symmetry-Breaking Charge Separation in the Solid State: Tetra(phenoxy)perylenediimide Polycrystalline Films. *Journal of the American Chemical Society* **2020,** *142* (42), 18243-18250.
55. Perez, M. D.; Borek, C.; Forrest, S. R.; Thompson, M. E., Molecular and Morphological Influences on the Open Circuit Voltages of Organic Photovoltaic Devices. *Journal of the American Chemical Society* **2009,** *131* (26), 9281-9286.
56. Erwin, P.; Thompson, M. E., Elucidating the interplay between dark current coupling and open circuit voltage in organic photovoltaics. *Applied Physics Letters* **2011,** *98* (22), 223305.

57. Das, S.; Thornbury, W. G.; Bartynski, A. N.; Thompson, M. E.; Bradforth, S. E., Manipulating Triplet Yield through Control of Symmetry-Breaking Charge Transfer. *The Journal of Physical Chemistry Letters* **2018,** *9* (12), 3264-3270.
58. Young, R. M.; Wasielewski, M. R., Mixed Electronic States in Molecular Dimers: Connecting Singlet Fission, Excimer Formation, and Symmetry-Breaking Charge Transfer. *Acc. Chem. Res.* **2020,** *53* (9), 1957-1968.
59. Powers-Riggs, N. E.; Zuo, X.; Young, R. M.; Wasielewski, M. R., Symmetry-Breaking Charge Separation in a Nanoscale Terrylenediimide Guanine-Quadruplex Assembly. *Journal of the American Chemical Society* **2019,** *141* (44), 17512-17516.
60. Coleman, A. F.; Chen, M.; Zhou, J.; Shin, J. Y.; Wu, Y.; Young, R. M.; Wasielewski, M. R., Reversible Symmetry-Breaking Charge Separation in a Series of Perylenediimide Cyclophanes. *The Journal of Physical Chemistry C* **2020,** *124* (19), 10408-10419.
61. Dereka, B.; Vauthey, E., Solute–Solvent Interactions and Excited-State Symmetry Breaking: Beyond the Dipole–Dipole and the Hydrogen-Bond Interactions. *J. Phys. Chem. Lett.* **2017,** *8* (16), 3927-3932.
62. Sugie, A.; Han, W.; Shioya, N.; Hasegawa, T.; Yoshida, H., Structure-Dependent Electron Affinities of Perylene Diimide-Based Acceptors. *The Journal of Physical Chemistry C* **2020,** *124* (18), 9765-9773.
63. Wurthner, F.; Thalacker, C.; Sautter, A., Hierarchical organization of functional perylene chromophores to mesoscopic superstructures by hydrogen bonding and π-π interactions. *Adv. Mater. (Weinheim, Ger.)* **1999,** *11* (9), 754-758.
64. Quante, H.; Schlichting, P.; Rohr, U.; Geerts, Y.; Muellen, K., Novel perylene-containing polymers. *Macromol. Chem. Phys.* **1996,** *197* (12), 4029-4044.
65. Li, Y.; Wang, N.; Gan, H.; Liu, H.; Li, H.; Li, Y.; He, X.; Huang, C.; Cui, S.; Wang, S.; Zhu, D., Synthesis and Characterization of 3,5-Bis(2-hydroxyphenyl)-1,2,4-triazole Functionalized Tetraaryloxy Perylene Bisimide and Metal-Directed Self-Assembly. *The Journal of Organic Chemistry* **2005,** *70* (24), 9686-9692.
66. Dolomanov, O. V.; Bourhis, L. J.; Gildea, R. J.; Howard, J. A. K.; Puschmann, H., OLEX2: a complete structure solution, refinement and analysis program. *J. Appl. Crystallogr.* **2009,** *42* (2), 339-341.
67. Sheldrick, G. M., SHELXT - Integrated space-group and crystal-structure determination. *Acta Crystallogr., Sect. A: Found. Adv.* **2015,** *71* (1), 3-8.
68. Sheldrick, G. M., A short history of SHELX. *Acta Crystallogr., Sect. A: Found. Crystallogr.* **2008,** *64* (1), 112-122.
69. Jiang, Z., GIXSGUI: a MATLAB toolbox for grazing-incidence X-ray scattering data visualization and reduction, and indexing of buried three-dimensional periodic nanostructured films. *Journal of Applied Crystallography* **2015,** *48* (June 2015), 917-926.
70. Margulies, E. A.; Logsdon, J. L.; Miller, C. E.; Ma, L.; Simonoff, E.; Young, R. M.; Schatz, G. C.; Wasielewski, M. R., Direct Observation of a Charge-Transfer State Preceding High-Yield Singlet Fission in Terrylenediimide Thin Films. *J. Am. Chem. Soc.* **2017,** *139* (2), 663-671.
71. Gsänger, M.; Oh, J. H.; Könemann, M.; Höffken, H. W.; Krause, A.-M.; Bao, Z.; Würthner, F., A Crystal-Engineered Hydrogen-Bonded Octachloroperylene Diimide with a Twisted Core: An n-Channel Organic Semiconductor. *Angew. Chem. Int. Ed.* **2010,** *49* (4), 740-743.

72. Li, W.; Chen, M.; Cai, J.; Spooner, E. L. K.; Zhang, H.; Gurney, R. S.; Liu, D.; Xiao, Z.; Lidzey, D. G.; Ding, L.; Wang, T., Molecular Order Control of Non-fullerene Acceptors for High-Efficiency Polymer Solar Cells. *Joule* **2019,** *3* (3), 819-833.
73. Mativetsky, J. M.; Wang, H.; Lee, S. S.; Whittaker-Brooks, L.; Loo, Y.-L., Face-on stacking and enhanced out-of-plane hole mobility in graphene-templated copper phthalocyanine. *Chemical Communications* **2014,** *50* (40), 5319-5321.
74. Brown, K. E.; Salamant, W. A.; Shoer, L. E.; Young, R. M.; Wasielewski, M. R., Direct Observation of Ultrafast Excimer Formation in Covalent Perylenediimide Dimers Using Near-Infrared Transient Absorption Spectroscopy. *The Journal of Physical Chemistry Letters* **2014,** *5* (15), 2588-2593.
75. Giaimo, J. M.; Lockard, J. V.; Sinks, L. E.; Scott, A. M.; Wilson, T. M.; Wasielewski, M. R., Excited Singlet States of Covalently Bound, Cofacial Dimers and Trimers of Perylene-3,4:9,10-bis(dicarboximide)s. *J. Phys. Chem. A* **2008,** *112* (11), 2322-2330.
76. Myong, M. S.; Zhou, J.; Young, R. M.; Wasielewski, M. R., Charge-Transfer Character in Excimers of Perylenediimides Self-Assembled on Anodic Aluminum Oxide Membrane Walls. *The Journal of Physical Chemistry C* **2020,** *124* (8), 4369-4377.
77. Sung, J.; Nowak-Król, A.; Schlosser, F.; Fimmel, B.; Kim, W.; Kim, D.; Würthner, F., Direct Observation of Excimer-Mediated Intramolecular Electron Transfer in a Cofacially-Stacked Perylene Bisimide Pair. *Journal of the American Chemical Society* **2016,** *138* (29), 9029-9032.
78. Lefler, K. M.; Brown, K. E.; Salamant, W. A.; Dyar, S. M.; Knowles, K. E.; Wasielewski, M. R., Triplet State Formation in Photoexcited Slip-Stacked Perylene-3,4:9,10-bis(dicarboximide) Dimers on a Xanthene Scaffold. *J. Phys. Chem. A* **2013,** *117* (40), 10333-10345.
79. Mauck, C. M.; Young, R. M.; Wasielewski, M. R., Characterization of Excimer Relaxation via Femtosecond Shortwave- and Mid-Infrared Spectroscopy. *J. Phys. Chem. A* **2017,** *121* (4), 784-792.
80. Kaufmann, C.; Kim, W.; Nowak-Król, A.; Hong, Y.; Kim, D.; Würthner, F., Ultrafast Exciton Delocalization, Localization, and Excimer Formation Dynamics in a Highly Defined Perylene Bisimide Quadruple π-Stack. *Journal of the American Chemical Society* **2018,** *140* (12), 4253-4258.
81. Singh, R.; Kim, M.; Lee, J.-J.; Ye, T.; Keivanidis, P. E.; Cho, K., Excimer formation effects and trap-assisted charge recombination loss channels in organic solar cells of perylene diimide dimer acceptors. *Journal of Materials Chemistry C* **2020,** *8* (5), 1686-1696.
82. Closs, G. L.; Miller, J. R., Intramolecular Long-Distance Electron Transfer in Organic Molecules. *Science* **1988,** *240* (4851), 440-447.
83. Lefler, K. M.; Co, D. T.; Wasielewski, M. R., Self-Assembly-Induced Ultrafast Photodriven Charge Separation in Perylene-3,4-dicarboximide-Based Hydrogen-Bonded Foldamers. *The Journal of Physical Chemistry Letters* **2012,** *3* (24), 3798-3805.
84. Mallia, A. R.; Hariharan, M., Self-Assembled Donor–Acceptor Trefoils: Long-Lived Charge Separated State through Aggregation. *The Journal of Physical Chemistry C* **2017,** *121* (9), 4778-4788.
85. Liang, N.; Zhu, X.; Zheng, Z.; Meng, D.; Liu, G.; Zhang, J.; Li, S.; Li, Y.; Hou, J.; Hu, B.; Wang, Z., Tuning Charge Generation Process of Rylene Imide-Based Solar Cells via Chalcogen-Atom-Annulation. *Chemistry of Materials* **2019,** *31* (10), 3636-3643.

86. Zhylitskaya, H.; Cybińska, J.; Chmielewski, P.; Lis, T.; Stępień, M., Bandgap Engineering in π-Extended Pyrroles. A Modular Approach to Electron-Deficient Chromophores with Multi-Redox Activity. *Journal of the American Chemical Society* **2016,** *138* (35), 11390-11398.

87. Rihter, B. D.; Kenney, M. E.; Ford, W. E.; Rodgers, M. A. J., Synthesis and photoproperties of diamagnetic octabutoxyphthalocyanines with deep red optical absorbance. *Journal of the American Chemical Society* **1990,** *112* (22), 8064-8070.

88. Monkman, A.; Burrows, H.; Miguel, M.; Hamblett, I.; Navaratnam, S., Triplet state spectroscopy of conjugated polymers studied by pulse radiolysis. *Synthetic Metals* **2001**, 75-79.

89. Hestand, N. J.; Spano, F. C., Interference between Coulombic and CT-mediated couplings in molecular aggregates: H- to J-aggregate transformation in perylene-based π-stacks. *The Journal of Chemical Physics* **2015,** *143* (24), 244707.

90. Xia, J.; Sanders, S. N.; Cheng, W.; Low, J. Z.; Liu, J.; Campos, L. M.; Sun, T., Singlet Fission: Progress and Prospects in Solar Cells. *Adv. Mater.* **2017,** *29* (20), 1601652.

91. Lee, J.; Jadhav, P.; Reusswig, P. D.; Yost, S. R.; Thompson, N. J.; Congreve, D. N.; Hontz, E.; Van Voorhis, T.; Baldo, M. A., Singlet Exciton Fission Photovoltaics. *Acc. Chem. Res.* **2013,** *46* (6), 1300-1311.

92. Fallon, K. J.; Budden, P.; Salvadori, E.; Ganose, A. M.; Savory, C. N.; Eyre, L.; Dowland, S.; Ai, Q.; Goodlett, S.; Risko, C.; Scanlon, D. O.; Kay, C. W. M.; Rao, A.; Friend, R. H.; Musser, A. J.; Bronstein, H., Exploiting Excited-State Aromaticity To Design Highly Stable Singlet Fission Materials. *J. Am. Chem. Soc.* **2019,** *141* (35), 13867-13876.

93. Busby, E.; Xia, J.; Wu, Q.; Low, J. Z.; Song, R.; Miller, J. R.; Zhu, X. Y.; Campos, Luis M.; Sfeir, M. Y., A design strategy for intramolecular singlet fission mediated by charge-transfer states in donor–acceptor organic materials. *Nat. Mater.* **2015,** *14* (4), 426-433.

94. Walker, B. J.; Musser, A. J.; Beljonne, D.; Friend, R. H., Singlet exciton fission in solution. *Nat. Chem.* **2013,** *5* (12), 1019-1024.

95. Ullrich, T.; Munz, D.; Guldi, D. M., Unconventional singlet fission materials. *Chem. Soc. Rev.* **2021,** *50* (5), 3485-3518.

96. Ma, L.; Zhang, K.; Kloc, C.; Sun, H.; Michel-Beyerle, M. E.; Gurzadyan, G. G., Singlet fission in rubrene single crystal: direct observation by femtosecond pump–probe spectroscopy. *Physical Chemistry Chemical Physics* **2012,** *14* (23), 8307-8312.

97. Renaud, N.; Sherratt, P. A.; Ratner, M. A., Mapping the Relation between Stacking Geometries and Singlet Fission Yield in a Class of Organic Crystals. *J. Phys. Chem. Lett.* **2013,** *4* (7), 1065-1069.

98. Zimmerman, P. M.; Bell, F.; Casanova, D.; Head-Gordon, M., Mechanism for Singlet Fission in Pentacene and Tetracene: From Single Exciton to Two Triplets. *J. Am. Chem. Soc.* **2011,** *133* (49), 19944-19952.

99. Dillon, R. J.; Piland, G. B.; Bardeen, C. J., Different Rates of Singlet Fission in Monoclinic versus Orthorhombic Crystal Forms of Diphenylhexatriene. *J. Am. Chem. Soc.* **2013,** *135* (46), 17278-17281.

100. Zhao, T.; Ni, W.; Kloc, C.; Sun, L.; Gurzadyan, G. G., Singlet Fission, Polaron Formation, and Energy Transfer in Indolo[3,2-b]carbazole Thin Films and Single Crystals. *J. Phys. Chem. C* **2021,** *125* (34), 18827-18833.

101. Aryanpour, K.; Shukla, A.; Mazumdar, S., Theory of Singlet Fission in Polyenes, Acene Crystals, and Covalently Linked Acene Dimers. *J. Phys. Chem. C* **2015,** *119* (13), 6966-6979.

102. Zirzlmeier, J.; Lehnherr, D.; Coto, P. B.; Chernick, E. T.; Casillas, R.; Basel, B. S.; Thoss, M.; Tykwinski, R. R.; Guldi, D. M., Singlet fission in pentacene dimers. *Proc. Natl. Acad. Sci. USA* **2015,** *112* (17), 5325-5330.

103. Liu, H.; Wang, Z.; Wang, X.; Shen, L.; Zhang, C.; Xiao, M.; Li, X., Singlet exciton fission in a linear tetracene tetramer. *J. Mater. Chem. C* **2018,** *6* (13), 3245-3253.

104. Zukun, W.; Wu, R.; Chen, Z.; Ye, L.; Li, H.; Zhu, H., Ultrafast Electron Transfer Before Singlet Fission and Slow Triplet State Electron Transfer in Pentacene Single Crystal/C60 Heterostructure. *J. Phys. Chem. A* **2020,** *124* (21), 4185-4192.

105. Hart, Stephanie M.; Silva, W. R.; Frontiera, R. R., Femtosecond stimulated Raman evidence for charge-transfer character in pentacene singlet fission. *Chem. Sci.* **2018,** *9* (5), 1242-1250.

106. Broch, K.; Dieterle, J.; Branchi, F.; Hestand, N. J.; Olivier, Y.; Tamura, H.; Cruz, C.; Nichols, V. M.; Hinderhofer, A.; Beljonne, D.; Spano, F. C.; Cerullo, G.; Bardeen, C. J.; Schreiber, F., Robust singlet fission in pentacene thin films with tuned charge transfer interactions. *Nat. Commun.* **2018,** *9* (1), 954.

107. Wang, R.; Zhang, C.; Zhang, B.; Liu, Y.; Wang, X.; Xiao, M., Magnetic dipolar interaction between correlated triplets created by singlet fission in tetracene crystals. *Nat. Commun.* **2015,** *6* (1), 8602.

108. Piland, G. B.; Bardeen, C. J., How Morphology Affects Singlet Fission in Crystalline Tetracene. *J. Phys. Chem. Lett.* **2015,** *6* (10), 1841-1846.

109. Arias, D. H.; Ryerson, J. L.; Cook, J. D.; Damrauer, N. H.; Johnson, J. C., Polymorphism influences singlet fission rates in tetracene thin films. *Chem. Sci.* **2016,** *7* (2), 1185-1191.

110. Roberts, S. T.; McAnally, R. E.; Mastron, J. N.; Webber, D. H.; Whited, M. T.; Brutchey, R. L.; Thompson, M. E.; Bradforth, S. E., Efficient Singlet Fission Discovered in a Disordered Acene Film. *J. Am. Chem. Soc.* **2012,** *134* (14), 6388-6400.

111. Wilson, M. W. B.; Rao, A.; Ehrler, B.; Friend, R. H., Singlet Exciton Fission in Polycrystalline Pentacene: From Photophysics toward Devices. *Acc. Chem. Res.* **2013,** *46* (6), 1330-1338.

112. Macedo, A. G.; Christopholi, L. P.; Gavim, A. E. X.; de Deus, J. F.; Teridi, M. A. M.; Yusoff, A. R. b. M.; da Silva, W. J., Perylene derivatives for solar cells and energy harvesting: a review of materials, challenges and advances. *J. Mater. Sci.: Mater. Electron.* **2019,** *30* (17), 15803-15824.

113. Bialas, D.; Kirchner, E.; Röhr, M. I. S.; Würthner, F., Perspectives in Dye Chemistry: A Rational Approach toward Functional Materials by Understanding the Aggregate State. *J. Am. Chem. Soc.* **2021,** *143* (12), 4500-4518.

114. Geng, Y.; Li, H.-B.; Wu, S.-X.; Su, Z.-M., The interplay of intermolecular interactions, packing motifs and electron transport properties in perylene diimide related materials: a theoretical perspective. *J. Mater. Chem.* **2012,** *22* (39), 20840-20851.

115. Aulin, Y. V.; Felter, K. M.; Günbas, D. D.; Dubey, R. K.; Jager, W. F.; Grozema, F. C., Morphology-Independent Efficient Singlet Exciton Fission in Perylene Diimide Thin Films. *ChemPlusChem* **2018,** *83* (4), 230-238.

116. Feng, X.; Kolomeisky, A. B.; Krylov, A. I., Dissecting the Effect of Morphology on the Rates of Singlet Fission: Insights from Theory. *J. Phys. Chem. C* **2014,** *118* (34), 19608-19617.
117. Farag, M. H.; Krylov, A. I., Singlet Fission in Perylenediimide Dimers. *J. Phys. Chem. C* **2018,** *122*, 25753–25763.
118. Abbel, R.; Galagan, Y.; Groen, P., Roll-to-Roll Fabrication of Solution Processed Electronics. *Advanced Engineering Materials* **2018,** *20* (8), 1701190.
119. Schulze, M.; Steffen, A.; Würthner, F., Near-IR Phosphorescent Ruthenium(II) and Iridium(III) Perylene Bisimide Metal Complexes. *Angew. Chem., Int. Ed.* **2015,** *54* (5), 1570-1573.
120. Stoll, S.; Schweiger, A., EasySpin, a comprehensive software package for spectral simulation and analysis in EPR. *Journal of Magnetic Resonance* **2006,** *178* (1), 42-55.
121. Kasha, M.; Rawls, H. R.; El-Bayoumi, M. A., Exciton model in molecular spectroscopy. *Pure Appl. Chem.* **1965,** *11* (3-4), 371-392.
122. Margulies, E. A.; Shoer, L. E.; Eaton, S. W.; Wasielewski, M. R., Excimer formation in cofacial and slip-stacked perylene-3,4:9,10-bis(dicarboximide) dimers on a redox-inactive triptycene scaffold. *Phys. Chem. Chem. Phys.* **2014,** *16* (43), 23735-23742.
123. Brown, K. E.; Salamant, W. A.; Shoer, L. E.; Young, R. M.; Wasielewski, M. R., Direct Observation of Ultrafast Excimer Formation in Covalent Perylenediimide Dimers Using Near-Infrared Transient Absorption Spectroscopy. *J. Phys. Chem. Lett.* **2014,** *5* (15), 2588-2593.
124. Hestand, N. J.; Spano, F. C., Molecular Aggregate Photophysics beyond the Kasha Model: Novel Design Principles for Organic Materials. *Acc. Chem. Res.* **2017,** *50* (2), 341-350.
125. Hestand, N. J.; Spano, F. C., Expanded Theory of H- and J-Molecular Aggregates: Effects of Vibronic Coupling and Intermolecular Charge Transfer. *Chem. Rev. (Washington, DC, U. S.)* **2018,** *118* (15), 7069-7163.
126. Nečas, D.; Klapetek, P., Gwyddion: an open-source software for SPM data analysis. *Open Physics* **2012,** *10* (1), 181-188.
127. Austin, A.; Hestand, N. J.; McKendry, I. G.; Zhong, C.; Zhu, X.; Zdilla, M. J.; Spano, F. C.; Szarko, J. M., Enhanced Davydov Splitting in Crystals of a Perylene Diimide Derivative. *J. Phys. Chem. Lett.* **2017,** *8* (6), 1118-1123.
128. Alzola, J. M.; Tcyrulnikov, N. A.; Brown, P. J.; Marks, T. J.; Wasielewski, M. R.; Young, R. M., Symmetry-Breaking Charge Separation in Phenylene-Bridged Perylenediimide Dimers. *The Journal of Physical Chemistry A* **2021,** *125* (35), 7633-7643.
129. Kong, J.; Zhang, W.; Li, G.; Huo, D.; Guo, Y.; Niu, X.; Wan, Y.; Tang, B.; Xia, A., Excited-State Symmetry-Breaking Charge Separation Dynamics in Multibranched Perylene Diimide Molecules. *J. Phys. Chem. Lett.* **2020,** *11* (24), 10329-10339.
130. Wu, Y.; Young, R. M.; Frasconi, M.; Schneebeli, S. T.; Spenst, P.; Gardner, D. M.; Brown, K. E.; Würthner, F.; Stoddart, J. F.; Wasielewski, M. R., Ultrafast Photoinduced Symmetry-Breaking Charge Separation and Electron Sharing in Perylenediimide Molecular Triangles. *J. Am. Chem. Soc.* **2015,** *137* (41), 13236-13239.
131. Kircher, T.; Löhmannsröben, H. G., Photoinduced charge recombination reactions of a perylene dye in acetonitrile. *Physical Chemistry Chemical Physics* **1999,** *1* (17), 3987-3992.

132. Schlesinger, I.; Zhao, X.; Powers-Riggs, N. E.; Wasielewski, M. R., Singlet Fission in Terrylenediimide Single Crystals: Competition between Biexciton Annihilation and Free Triplet Exciton Formation. *J. Phys. Chem. C* **2021,** *125* (25), 13946-13953.
133. Zeidan, T. A.; Carmieli, R.; Kelley, R. F.; Wilson, T. M.; Lewis, F. D.; Wasielewski, M. R., Charge-Transfer and Spin Dynamics in DNA Hairpin Conjugates with Perylenediimide as a Base-Pair Surrogate. *J. Am. Chem. Soc.* **2008,** *130* (42), 13945-13955.
134. Dance, Z. E. X.; Mi, Q.; McCamant, D. W.; Ahrens, M. J.; Ratner, M. A.; Wasielewski, M. R., Time-Resolved EPR Studies of Photogenerated Radical Ion Pairs Separated by p-Phenylene Oligomers and of Triplet States Resulting from Charge Recombination. *J. Phys. Chem. B* **2006,** *110* (50), 25163-25173.
135. Bayliss, S. L.; Weiss, L. R.; Kraffert, F.; Granger, D. B.; Anthony, J. E.; Behrends, J.; Bittl, R., Probing the Wave Function and Dynamics of the Quintet Multiexciton State with Coherent Control in a Singlet Fission Material. *Physical Review X* **2020,** *10* (2), 021070.
136. Gosztola, D.; Niemczyk, M. P.; Svec, W.; Lukas, A. S.; Wasielewski, M. R., Excited Doublet States of Electrochemically Generated Aromatic Imide and Diimide Radical Anions. *J. Phys. Chem. A* **2000,** *104* (28), 6545-6551.
137. Schultz, J. D.; Shin, J. Y.; Chen, M.; O'Connor, J. P.; Young, R. M.; Ratner, M. A.; Wasielewski, M. R., Influence of Vibronic Coupling on Ultrafast Singlet Fission in a Linear Terrylenediimide Dimer. *J. Am. Chem. Soc.* **2021,** *143* (4), 2049-2058.
138. Korovina, N. V.; Das, S.; Nett, Z.; Feng, X.; Joy, J.; Haiges, R.; Krylov, A. I.; Bradforth, S. E.; Thompson, M. E., Singlet Fission in a Covalently Linked Cofacial Alkynyltetracene Dimer. *Journal of the American Chemical Society* **2016,** *138* (2), 617-627.
139. Kasha, M., Characterization of electronic transitions in complex molecules. *Discussions of the Faraday Society* **1950,** *9* (0), 14-19.
140. Shevyakov, S. V.; Li, H.; Muthyala, R.; Asato, A. E.; Croney, J. C.; Jameson, D. M.; Liu, R. S. H., Orbital Control of the Color and Excited State Properties of Formylated and Fluorinated Derivatives of Azulene. *The Journal of Physical Chemistry A* **2003,** *107* (18), 3295-3299.
141. Schwarzer, D.; Troe, J.; Schroeder, J., S1-Lifetime of Azulene in Solution. *Berichte der Bunsengesellschaft für physikalische Chemie* **1991,** *95* (8), 933-934.
142. Rentzepis, P. M., Emission from the lowest singlet and triplet states of azulene. *Chemical Physics Letters* **1969,** *3* (9), 717-720.
143. Beer, M.; Longuet-Higgins, H. C., Anomalous Light Emission of Azulene. *J. Chem. Phys.* **1955,** *23* (8), 1390-1391.
144. Sidman, J. W.; McClure, D. S., Electronic and Vibrational States of Azulene. *The Journal of Chemical Physics* **1956,** *24* (4), 757-763.
145. Englman, R.; Jortner, J., The energy gap law for radiationless transitions in large molecules. *Molecular Physics* **1970,** *18* (2), 145-164.
146. Turro, N. J., Ramamurthy, V., Scaiano, J.C., *Modern molecular photochemistry of organic molecules*. Sausalito, Calif. : University Science Books: 2010.
147. Viswanath, G.; Kasha, M., Confirmation of the Anomalous Fluorescence of Azulene. *The Journal of Chemical Physics* **1956,** *24* (3), 574-577.
148. Steer, R. P., Photophysics of molecules containing multiples of the azulene carbon framework. *Journal of Photochemistry and Photobiology C: Photochemistry Reviews* **2019,** *40*, 68-80.

149. Awuku, S.; Bradley, S. J.; Ghiggino, K. P.; Steer, R. P.; Stevens, A. L.; White, J. M.; Yeow, C., Photophysics and spectroscopy of 1,2-Benzazulene. *Chemical Physics Letters* **2021,** *784*, 139114.
150. del Valle, J. C.; Catalán, J., Kasha's rule: a reappraisal. *Physical Chemistry Chemical Physics* **2019,** *21* (19), 10061-10069.
151. Zhao, Z.; Zhang, H.; Lam, J. W. Y.; Tang, B. Z., Aggregation-Induced Emission: New Vistas at the Aggregate Level. *Angewandte Chemie International Edition* **2020,** *59* (25), 9888-9907.
152. Guo, J.; Fan, J.; Lin, L.; Zeng, J.; Liu, H.; Wang, C.-K.; Zhao, Z.; Tang, B. Z., Mechanical Insights into Aggregation-Induced Delayed Fluorescence Materials with Anti-Kasha Behavior. *Advanced Science* **2019,** *6* (3), 1801629.
153. Qian, H.; Cousins, M. E.; Horak, E. H.; Wakefield, A.; Liptak, M. D.; Aprahamian, I., Suppression of Kasha's rule as a mechanism for fluorescent molecular rotors and aggregation-induced emission. *Nature Chemistry* **2017,** *9* (1), 83-87.
154. Qi, Q.; Huang, L.; Yang, R.; Li, J.; Qiao, Q.; Xu, B.; Tian, W.; Liu, X.; Xu, Z., Rhodamine-naphthalimide demonstrated a distinct aggregation-induced emission mechanism: elimination of dark-states via dimer interactions (EDDI). *Chemical Communications* **2019,** *55* (10), 1446-1449.
155. Zhao, W.; He, Z.; Peng, Q.; Lam, J. W. Y.; Ma, H.; Qiu, Z.; Chen, Y.; Zhao, Z.; Shuai, Z.; Dong, Y.; Tang, B. Z., Highly sensitive switching of solid-state luminescence by controlling intersystem crossing. *Nat. Commun.* **2018,** *9* (1), 3044.
156. Stojanović, L.; Crespo-Otero, R., Aggregation-Induced Emission in the Tetraphenylthiophene Crystal: The Role of Triplet States. *J. Phys. Chem. C* **2020,** *124* (32), 17752-17761.
157. Xu, J.; Zhu, X.; Guo, J.; Fan, J.; Zeng, J.; Chen, S.; Zhao, Z.; Tang, B. Z., Aggregation-Induced Delayed Fluorescence Luminogens with Accelerated Reverse Intersystem Crossing for High-Performance OLEDs. *ACS Materials Letters* **2019,** *1* (6), 613-619.
158. Zhang, J.; Mukamel, S.; Jiang, J., Aggregation-Induced Intersystem Crossing: Rational Design for Phosphorescence Manipulation. *J. Phys. Chem. B* **2020,** *124* (11), 2238-2244.
159. McGlynn, S. P.; Daigre, J.; Smith, F. J., External Heavy-Atom Spin—Orbital Coupling Effect. IV. Intersystem Crossing. *The Journal of Chemical Physics* **1963,** *39* (3), 675-679.
160. Rao, A.; Friend, R. H., Harnessing singlet exciton fission to break the Shockley–Queisser limit. *Nature Reviews Materials* **2017,** *2* (11), 17063.
161. Hanson, K.; Roskop, L.; Djurovich, P. I.; Zahariev, F.; Gordon, M. S.; Thompson, M. E., A Paradigm for Blue- or Red-Shifted Absorption of Small Molecules Depending on the Site of π-Extension. *Journal of the American Chemical Society* **2010,** *132* (45), 16247-16255.
162. El-Khouly, M. E.; Gutiérrez, A. M.; Sastre-Santos, Á.; Fernández-Lázaro, F.; Fukuzumi, S., Light harvesting zinc naphthalocyanine–perylenediimide supramolecular dyads: long-lived charge-separated states in nonpolar media. *Physical Chemistry Chemical Physics* **2012,** *14* (10), 3612-3621.
163. Morishige, K.; Araki, K., Crystal structures of nickel, copper and zinc naphthalocyaninates. *Journal of the Chemical Society, Dalton Transactions* **1996,** (22), 4303-4305.
164. Yanagi, H.; Kouzeki, T.; Ashida, M.; Noguchi, T.; Manivannan, A.; Hashimoto, K.; Fujishima, A., Molecular orientation of vacuum-deposited thin films of zincnaphthalocyanine. *Journal of Applied Physics* **1992,** *71* (10), 5146-5153.

165. Manivannan, A.; Nagahara, L. A.; Yanagi, H.; Kouzeki, T.; Ashida, M.; Maruyama, Y.; Hashimoto, K.; Fujishima, A., Scanning tunneling microscopy observations of zincnaphthalocyanine on MoS2. *Thin Solid Films* **1993,** *226* (1), 6-8.
166. Yanagi, H.; Kouzeki, T.; Ashida, M., Epitaxial growth of naphthalocyanine thin films vacuum deposited on alkali halides. *Journal of Applied Physics* **1993,** *73* (8), 3812-3819.
167. Dhanya, I.; Menon, C. S., Optoelectric properties of amorphous Tert-Butyl substituted Zinc Naphthalocyanine thin films. *Optoelectronics and Advanced Materials, Rapid Communications* **2010,** *4*, 2085-2087.
168. de Souza, T. F. M., Antonio, F. C. T.; Zanotto, M.; Homem-de-Mello, P.; Ribeiro, A. O., Photophysical and Photochemical Properties and Aggregation Behavior of Phthalocyanine and Naphthalocyanine Derivatives. *Journal of the Brazilian Chemical Society* **2018,** *29* (6), 1199-1209.
169. Bialas, A. L.; Spano, F. C., A Holstein–Peierls Approach to Excimer Spectra: The Evolution from Vibronically Structured to Unstructured Emission. *The Journal of Physical Chemistry C* **2022**.
170. Kasha, M.; Rawls, H. R.; Ashraf El-Bayoumi, M., The exciton model in molecular spectroscopy. *Pure and Applied Chemistry* **1965,** *11* (3-4), 371-392.
171. Prlj, A.; Begušić, T.; Zhang, Z. T.; Fish, G. C.; Wehrle, M.; Zimmermann, T.; Choi, S.; Roulet, J.; Moser, J.-E.; Vaníček, J., Semiclassical Approach to Photophysics Beyond Kasha's Rule and Vibronic Spectroscopy Beyond the Condon Approximation. The Case of Azulene. *Journal of Chemical Theory and Computation* **2020,** *16* (4), 2617-2626.
172. Domcke, W.; Köppel, H.; Cederbaum, L. S., Spectroscopic effects of conical intersections of molecular potential energy surfaces. *Molecular Physics* **1981,** *43* (4), 851-875.
173. Keller, N.; Calik, M.; Sharapa, D.; Soni, H. R.; Zehetmaier, P. M.; Rager, S.; Auras, F.; Jakowetz, A. C.; Görling, A.; Clark, T.; Bein, T., Enforcing Extended Porphyrin J-Aggregate Stacking in Covalent Organic Frameworks. *Journal of the American Chemical Society* **2018,** *140* (48), 16544-16552.
174. Akselrod, G. M.; Deotare, P. B.; Thompson, N. J.; Lee, J.; Tisdale, W. A.; Baldo, M. A.; Menon, V. M.; Bulović, V., Visualization of exciton transport in ordered and disordered molecular solids. *Nature Communications* **2014,** *5* (1), 3646.
175. Tabachnyk, M.; Ehrler, B.; Bayliss, S.; Friend, R. H.; Greenham, N. C., Triplet diffusion in singlet exciton fission sensitized pentacene solar cells. *Applied Physics Letters* **2013,** *103* (15), 153302.
176. Sternlicht, H.; Nieman, G. C.; Robinson, G. W., Triplet—Triplet Annihilation and Delayed Fluorescence in Molecular Aggregates. *The Journal of Chemical Physics* **1963,** *38* (6), 1326-1335.
177. Bodunov, E. N.; Berberan-Santos, M. N.; Martinho, J. M. G., Effect of dimensionality and size on triplet–triplet annihilation. *Chemical Physics* **2005,** *316* (1), 217-224.
178. Nichols, V. M.; Broch, K.; Schreiber, F.; Bardeen, C. J., Excited-State Dynamics of Diindenoperylene in Liquid Solution and in Solid Films. *The Journal of Physical Chemistry C* **2015,** *119* (23), 12856-12864.
179. Ishii, K.; Abiko, S.; Kobayashi, N., Time-Resolved Electron Spin Resonance of Gallium and Germanium Porphyrins in the Excited Triplet State. *Inorganic Chemistry* **2000,** *39* (3), 468-472.

180. Barbon, A.; Brustolon, M.; van Faassen, E. E., Photoexcited spin triplet states in zinc phthalocyanine studied by transient EPR. *Physical Chemistry Chemical Physics* **2001,** *3* (23), 5342-5347.
181. Kreger, K.; Schmidt, H.-W.; Hildner, R., Tailoring the excited-state energy landscape in supramolecular nanostructures. *Electronic Structure* **2021,** *3* (2), 023001.
182. Ortí, E.; Brédas, J. L.; Clarisse, C., Electronic structure of phthalocyanines: Theoretical investigation of the optical properties of phthalocyanine monomers, dimers, and crystals. *The Journal of Chemical Physics* **1990,** *92* (2), 1228-1235.
183. Diers, J. R.; Kirmaier, C.; Taniguchi, M.; Lindsey, J. S.; Bocian, D. F.; Holten, D., A perspective on the redox properties of tetrapyrrole macrocycles. *Physical Chemistry Chemical Physics* **2021,** *23* (35), 19130-19140.
184. Hood, D.; Niedzwiedzki, D. M.; Zhang, R.; Zhang, Y.; Dai, J.; Miller, E. S.; Bocian, D. F.; Williams, P. G.; Lindsey, J. S.; Holten, D., Photophysical Characterization of the Naturally Occurring Dioxobacteriochlorin Tolyporphin A and Synthetic Oxobacteriochlorin Analogues. *Photochemistry and Photobiology* **2017,** *93* (5), 1204-1215.
185. Fujita, H.; Jing, H.; Krayer, M.; Allu, S.; Veeraraghavaiah, G.; Wu, Z.; Jiang, J.; Diers, J. R.; Magdaong, N. C. M.; Mandal, A. K.; Roy, A.; Niedzwiedzki, D. M.; Kirmaier, C.; Bocian, D. F.; Holten, D.; Lindsey, J. S., Annulated bacteriochlorins for near-infrared photophysical studies. *New Journal of Chemistry* **2019,** *43* (19), 7209-7232.
186. Liu, Y.; Allu, S.; Nagarjuna Reddy, M.; Hood, D.; Diers, J. R.; Bocian, D. F.; Holten, D.; Lindsey, J. S., Synthesis and photophysical characterization of bacteriochlorins equipped with integral swallowtail substituents. *New Journal of Chemistry* **2017,** *41* (11), 4360-4376.
187. Jiang, J.; Matula, A. J.; Swierk, J. R.; Romano, N.; Wu, Y.; Batista, V. S.; Crabtree, R. H.; Lindsey, J. S.; Wang, H.; Brudvig, G. W., Unusual Stability of a Bacteriochlorin Electrocatalyst under Reductive Conditions. A Case Study on CO2 Conversion to CO. *ACS Catalysis* **2018,** *8* (11), 10131-10136.
188. Diers, J. R.; Tang, Q.; Hondros, C. J.; Chen, C.-Y.; Holten, D.; Lindsey, J. S.; Bocian, D. F., Vibronic Characteristics and Spin-Density Distributions in Bacteriochlorins as Revealed by Spectroscopic Studies of 16 Isotopologues. Implications for Energy- and Electron-Transfer in Natural Photosynthesis and Artificial Solar-Energy Conversion. *The Journal of Physical Chemistry B* **2014,** *118* (27), 7520-7532.
189. Faries, K. M.; Diers, J. R.; Springer, J. W.; Yang, E.; Ptaszek, M.; Lahaye, D.; Krayer, M.; Taniguchi, M.; Kirmaier, C.; Lindsey, J. S.; Bocian, D. F.; Holten, D., Photophysical Properties and Electronic Structure of Chlorin-Imides: Bridging the Gap between Chlorins and Bacteriochlorins. *The Journal of Physical Chemistry B* **2015,** *119* (24), 7503-7515.
190. Liu, M.; Chen, C.-Y.; Hood, D.; Taniguchi, M.; Diers, J. R.; Bocian, D. F.; Holten, D.; Lindsey, J. S., Synthesis, photophysics and electronic structure of oxobacteriochlorins. *New Journal of Chemistry* **2017,** *41* (10), 3732-3744.
191. Zhang, S.; Kim, H.-J.; Tang, Q.; Yang, E.; Bocian, D. F.; Holten, D.; Lindsey, J. S., Synthesis and photophysical characteristics of 2,3,12,13-tetraalkylbacteriochlorins. *New Journal of Chemistry* **2016,** *40* (7), 5942-5956.
192. Kim, H.-J.; Lindsey, J. S., De Novo Synthesis of Stable Tetrahydroporphyrinic Macrocycles: Bacteriochlorins and a Tetradehydrocorrin. *The Journal of Organic Chemistry* **2005,** *70* (14), 5475-5486.

193. Krayer, M.; Ptaszek, M.; Kim, H.-J.; Meneely, K. R.; Fan, D.; Secor, K.; Lindsey, J. S., Expanded Scope of Synthetic Bacteriochlorins via Improved Acid Catalysis Conditions and Diverse Dihydrodipyrrin-Acetals. *The Journal of Organic Chemistry* **2010,** *75* (4), 1016-1039.

194. Giaimo, J. M.; Gusev, A. V.; Wasielewski, M. R., Excited-state symmetry breaking in cofacial and linear dimers of a green perylenediimide chlorophyll analogue leading to ultrafast charge separation. *J. Am. Chem. Soc.* **2002,** *124* (29), 8530-8531.

195. Ma, S.; Du, S.; Pan, G.; Dai, S.; Xu, B.; Tian, W., Organic molecular aggregates: From aggregation structure to emission property. *Aggregate* **2021,** *2* (4), e96.

196. Penfold, T. J.; Gindensperger, E.; Daniel, C.; Marian, C. M., Spin-Vibronic Mechanism for Intersystem Crossing. *Chemical Reviews* **2018,** *118* (15), 6975-7025.

197. Papadopoulos, I.; Zirzlmeier, J.; Hetzer, C.; Bae, Y. J.; Krzyaniak, M. D.; Wasielewski, M. R.; Clark, T.; Tykwinski, R. R.; Guldi, D. M., Varying the Interpentacene Electronic Coupling to Tune Singlet Fission. *Journal of the American Chemical Society* **2019,** *141* (15), 6191-6203.

198. Zirzlmeier, J.; Lehnherr, D.; Coto, P. B.; Chernick, E. T.; Casillas, R.; Basel, B. S.; Thoss, M.; Tykwinski, R. R.; Guldi, D. M., Singlet fission in pentacene dimers. *Proceedings of the National Academy of Sciences* **2015,** *112* (17), 5325.

199. Hudson, R. J.; Stuart, A. N.; Huang, D. M.; Kee, T. W., What Next for Singlet Fission in Photovoltaics? The Fate of Triplet and Triplet-Pair Excitons. *The Journal of Physical Chemistry C* **2022,** *126* (12), 5369-5377.

200. Roberts, S. T., Singlet to triplet and back again. *Nature Chemistry* **2015,** *7* (10), 764-765.

201. Dexter, D. L., A Theory of Sensitized Luminescence in Solids. *The Journal of Chemical Physics* **1953,** *21* (5), 836-850.

202. Tabachnyk, M.; Ehrler, B.; Gélinas, S.; Böhm, M. L.; Walker, B. J.; Musselman, K. P.; Greenham, N. C.; Friend, R. H.; Rao, A., Resonant energy transfer of triplet excitons from pentacene to PbSe nanocrystals. *Nature Materials* **2014,** *13* (11), 1033-1038.

203. Davis, N. J. L. K.; Allardice, J. R.; Xiao, J.; Petty, A. J.; Greenham, N. C.; Anthony, J. E.; Rao, A., Singlet Fission and Triplet Transfer to PbS Quantum Dots in TIPS-Tetracene Carboxylic Acid Ligands. *The Journal of Physical Chemistry Letters* **2018,** *9* (6), 1454-1460.

204. Tritsch, J. R.; Chan, W.-L.; Wu, X.; Monahan, N. R.; Zhu, X. Y., Harvesting singlet fission for solar energy conversion via triplet energy transfer. *Nature Communications* **2013,** *4* (1), 2679.

205. Pandey, A. K., Highly efficient spin-conversion effect leading to energy up-converted electroluminescence in singlet fission photovoltaics. *Scientific Reports* **2015,** *5* (1), 7787.

206. Soldatova, A. V.; Kim, J.; Rizzoli, C.; Kenney, M. E.; Rodgers, M. A. J.; Rosa, A.; Ricciardi, G., Near-Infrared-Emitting Phthalocyanines. A Combined Experimental and Density Functional Theory Study of the Structural, Optical, and Photophysical Properties of Pd(II) and Pt(II) α-Butoxyphthalocyanines. *Inorganic Chemistry* **2011,** *50* (3), 1135-1149.

207. Ramirez, C. E., Without Environmental Justice, the Renewable Energy Transition Will Leave Low-Income and BIPOC Communities Behind. *Journal of Science Policy and Governance* **2021,** *18* (03).

208. Despart, Z.; Serrano, A.; Lamm, S., Analysis reveals nearly 200 died in Texas cold storm and blackouts, almost double the official count. *Houston Chronicle* April 1, 2021, 2021.

209. Jervis, R., 'Just crippling': Texans devastated by ice storm are now hunting empty shelves for food and water. *USA Today* February 18, 2021, 2021.

210. Price, A.; Sechler, B., Winter storm blackouts plagued Texas in 2011, too. Recommendations made afterward went unenforced. *Austin American-Statesman* February 18, 2021, 2021.

211. Franklin, M.; Kurtz, C.; Alksnis, M.; Steichen, L.; Younger, C.; Patterson, J.; *Lights Out in the Cold: Reforming Utility Shut-Off Policies as if Human Rights Matter*; NAACP Environmental and Climate Justice Program: March 2017, 2017.

212. Drehobl, A.; Ross, L., *Lifting the High Energy Burden in America's Largest Cities: How Energy Efficiency Can Improve Low-Income and Underserved Communities*; American Council for an Energy-Efficient Economy, April 20, 2016, 2016.

213. History.com Editors, Climate Change History. https://www.history.com/topics/natural-disasters-and-environment/history-of-climate-change.

214. EPA Environmental Justice. https://www.epa.gov/environmentaljustice.

215. Skelton, R.; Miller, V., The Environmental Justice Movement. March 17, 2016, 2016.

216. Bush, V. *Science The Endless Frontier*; Office of Scientific Research and Development: United States Government Printing Office, Washington, July 1945, 1945.

217. Madrigal, A. C., The Racist Housing Policy That Made Your Neighborhood. *The Atlantic* May 22, 2014, 2014.

218. Fulwood III, S. *The United States' History of Segregated Housing Continues to Limit Affordable Housing*; Center for American Progress, December 15, 2016, 2016.

219. Parker, K.; Horowitz, J. M.; Brown, A.; Fry, R.; Cohn, D.; Igielnik, R., *Demographic and economic trends in urban, suburban and rural communities*; Pew Research Center: May 22, 2018, 2018.

220. UCS, In the Northeast, Communities of Color Breathe 66% More Air Pollution from Vehicles. Union of Concerned Scientists: 2019.

221. Fleischman, L.; Franklin, M., *Fumes Across the Fence-Line: The Health Impacts of Air Pollution from Oil & Gas Facilities on African American Communities*; National Association for the Advancement of Colored People (NAACP) and Clean Air Task Force (CATF): November 2017, 2017; pp 3-7, 12, 23.

222. Energy justice towards racial justice. *Nature Energy* **2020,** *5* (8), 551-551.

223. Mock, B., Neighborhoods With More People of Color Pay Higher Energy Bills. *Bloomberg CityLab* November 25, 2019, 2019.

224. Bednar, D. J.; Reames, T. G., Recognition of and response to energy poverty in the United States. *Nature Energy* **2020,** *5* (6), 432-439.

225. Thompson, A., Switching to Renewables Can Hurt Vulnerable Groups—Unless Utilities Plan Ahead. *Scientific American* December 18, 2019, 2019.

226. Blinken, A. J., The United States Officially Rejoins the Paris Agreement. U.S. Department of State: 2021.

227. Murphy, D., Renewables chief hails 'crucial' Biden climate agenda as administration plans massive energy overhaul. *CNBC* 2021.

228. The White House, FACT SHEET: President Biden Takes Executive Actions to Tackle the Climate Crisis at Home and Abroad, Create Jobs, and Restore Scientific Integrity Across Federal Government. 2021.

229. Recognizing the duty of the Federal Government to create a Green New Deal. In *H.Res.109*, 2019.

230. Berardelli, J., How Joe Biden's climate plan compares to the Green New Deal. *CBS News* October 5, 2020, 2020.
231. Desilver, D., Renewable energy is growing fast in the U.S., but fossil fuels still dominate. January 15, 2020, 2020.
232. Evans, S., Solar is now 'cheapest electricity in history', confirms IEA. *Carbon Brief Clear on Climate* October 13, 2020, 2020.
233. Blunt, K.; McFarlane, S., The New Green Energy Giants Challenging Exxon and BP. *The Wall Street Journal* December 11, 2020, 2020.
234. Lavelle, M., Former Exxon Scientists Tell Congress of Oil Giant's Climate Research Before Exxon Turned to Denial. *Inside Climate News* 2019.
235. Banerjee, N.; Song, L.; Hasemyer, D., Exxon's Own Research Confirmed Fossil Fuels' Role in Global Warming Decades Ago. *Inside Climate News* September 16, 2015, 2015.
236. EIA, U. S. *Summary of Legislation and Regulations Included in the Annual Energy Outlook 2021*; Independent Statistics and Analysis, 2021.
237. UCS Public Utility Holding Company Act (PUHCA). https://www.ucsusa.org/resources/public-utility-holding-company-act.
238. Sundback, M. F., Rappolt, B.; Mina, A. P., *Electricity regulation in the United States: overview*; Sheppard Mullin LLP: July 1, 2020, 2020.
239. Ferman, M., Winter storm could cost Texas more money than any disaster in state history. *The Texas Tribune* February 25, 2021, 2021.
240. Schwartz, J.; Collier, K.; Davila, V., "Power companies get exactly what they want": How Texas repeatedly failed to protect its power grid against extreme weather. *The Texas Tribune* February 22, 2021, 2021.
241. Yancey-Bragg, N.; Jervis, R., Texas' winter storm could make life worse for Black and Latino families hit hard by power outages. *USA Today* February 20, 2021, 2021.
242. Ingber, S., 31 Percent Of U.S. Households Have Trouble Paying Energy Bills. *National Public Radio* September 19, 2018, 2018.
243. McDonnell Nieto del Rio, G.; Bogel-Burroughs, N.; Penn, I., His Lights Stayed on During Texas' Storm. Now He Owes $16,752. *The New York Times* February 20, 2021, 2021.
244. Carden, A., Price Gouging Laws Are Knowledge Embargoes That Should Be Repealed. *Forbes* August 31, 2019, 2019.
245. Morton, H. Price Gouging State Statutes. https://www.ncsl.org/research/financial-services-and-commerce/price-gouging-state-statutes.aspx.
246. Kaplan, S., The undeniable link between weather disasters and climate change. *The Washington Post* October 22, 2020, 2020.
247. U.S. Secretary of Energy, Fact Sheet: Department of Energy Response to Hurricane Katrina. U.S. Department of Energy: 2005.
248. Kowalski, K. M., Racial disparities persist in electric service. Is 'willful blindness' to blame? *Energy News Network* July 1, 2020, 2020.
249. U.S. DOE, About the Weatherization Assistance Program. https://www.energy.gov/eere/wap/about-weatherization-assistance-program.
250. U.S. DOE, *Weatherization Assistance Program National Evaluations: Summary of Results*; U.S. Department of Energy Office of Energy Efficiency & Renewable Energy, August 2015, 2015.
251. Boghani, P., How COVID Has Impacted Poverty in America. *Frontline* December 8, 2020, 2020.

252. Low Income Home Energy Assistance Program (LIHEAP). https://www.acf.hhs.gov/ocs/low-income-home-energy-assistance-program-liheap.
253. Shields, L. Bolstering Federal Energy Assistance and Weatherization With State Clean Energy Programs. https://www.ncsl.org/research/energy/bolstering-federal-energy-assistance-and-weatherization-with-state-clean-energy-programs.aspx.
254. LIHEAP and WAP Funding. https://liheapch.acf.hhs.gov/Funding/funding.htm.
255. Clearinghouse, L. *Leveraging and LIHEAP: Providing Non-Federal Funds for Energy Assistance*; U.S. Department of Health & Human Services, 2015.
256. U.S. ASPE, HHS Poverty Guidelines for 2021. https://aspe.hhs.gov/poverty-guidelines.
257. U.S. DOE, Weatherization Works! https://www.energy.gov/sites/prod/files/2019/07/f64/WAP-Fact-Sheet-2019.pdf.
258. Chatlani, S., Will Low-Income Communities Be Left Out Of California's Clean Energy Transition? *KPBS* October 18, 2019, 2019.
259. Cushing, L. J.; Wander, M.; Morello-Frosch, R.; Pastor, M.; Zhu, A.; Sadd, J., *A Preliminary Environmental Equity Assessment of California's Cap-and-trade Program*; University of Southern California, University of California, Berkeley, Occidental College Los Angeles: USC Dornsife Program for Environmental and Regional Equity, September 2016, 2016.
260. Murphy, M., Study Points To Greater Gas Price Impacts From Transpo Pact. *State House News Service* November 19, 2020, 2020.
261. IPA Illinois Solar For All. https://www.illinoissfa.com/.
262. *Low-Income Solar Policy Guide*; GRID Alternatives, Vote Solar, Center for Social Inclusion: March 11, 2016, 2016.
263. McCormick, K. *Bridging the Clean Energy Divide: Affordable Clean Energy Solutions for Today and Tomorrow*; Natural Resources Defense Council (NRDC): April 2015, 2015; p 14.
264. Glueck, K.; Friedman, L.; Biden Announces $2 Trillion Climate Plan. *The New York Times* July 14, 2020, 2021.
265. Mooney, J.; Kambhampati, P., Get the Basics Right: Jacobian Conversion of Wavelength and Energy Scales for Quantitative Analysis of Emission Spectra. *The Journal of Physical Chemistry Letters* **2013,** *4* (19), 3316-3318.
266. Swinehart, D. F., Beer-Lambert law. *J. Chem. Educ.* **1962,** *39*, 333-5.
267. Schultz, J. D.; Coleman, A. F.; Mandal, A.; Shin, J. Y.; Ratner, M. A.; Young, R. M.; Wasielewski, M. R., Steric Interactions Impact Vibronic and Vibrational Coherences in Perylenediimide Cyclophanes. *J. Phys. Chem. Lett.* **2019,** *10* (23), 7498-7504.
268. Laidler, K. J., The development of the Arrhenius equation. *Journal of Chemical Education* **1984,** *61* (6), 494.
269. Sanders, S. N.; Kumarasamy, E.; Pun, A. B.; Trinh, M. T.; Choi, B.; Xia, J.; Taffet, E. J.; Low, J. Z.; Miller, J. R.; Roy, X.; Zhu, X. Y.; Steigerwald, M. L.; Sfeir, M. Y.; Campos, L. M., Quantitative Intramolecular Singlet Fission in Bipentacenes. *Journal of the American Chemical Society* **2015,** *137* (28), 8965-8972.
270. Nagarajan, K.; Mallia, A. R.; Reddy, V. S.; Hariharan, M., Access to Triplet Excited State in Core-Twisted Perylenediimide. *The Journal of Physical Chemistry C* **2016,** *120* (16), 8443-8450.

271. Yu, Z.; Wu, Y.; Peng, Q.; Sun, C.; Chen, J.; Yao, J.; Fu, H., Accessing the Triplet State in Heavy-Atom-Free Perylene Diimides. *Chemistry – A European Journal* **2016,** *22* (14), 4717-4722.